Dissertation submitted in partial satisfaction of the requirements for the degree of Doctor of Philosophy in Physics

Visualizing the influence of defects and impurities on pncitide and chalcogenide superconductors

Antón G. Fente Hernández

March 2017

Thesis advisers
Hermann Suderow and Isabel Guillamón
Universidad Autónoma de Madrid

Contents

List of Figures

Abstract

By the time I was starting my master a small bench for solution growth was set up in the Low Temperature Laboratory with the collaboration of Prof. Paul Canfield from the Ames Laboratory (Ames, Ia, USA). In the following months I became familiar with the technique. In the following summer I made a three month stay in Prof. Canfield's laboratory learning more about solution growth and applying this knowledge back in Madrid to study single crystals and collaborate with different groups.

High quality single crystals are the best choice to study intrinsic properties of a material. They are free of structural domain anisotropies, have a controlled composition and a low concentration of defects. In this sense, they are the perfect environment to study the effect of isolated imperfections on the properties of the material. Furthermore disorder (such as dopants or impurities) can be introduced in a very controlled way producing small modifications in pressure, charge or introducing local magnetic moments.

As mentioned in the title, the thesis project is mainly focused on the study of impurities and defects in superconductors, particularly a dichalcogenide superconductor (S doped 2H-$NbSe_2$) and two iron based superconductors: Co doped $CaFe_2As_2$ and $CaKFe_4As_4$. To access the local electronic properties of this materials we use a scanning tunneling microscope (STM) and by cooling it to very low temperature ($0.1\,K$) we get the necessary energy resolution for the study.

The Fermi surface of FeBSC is formed by the $3d$ electrons of Fe with a contribution of the p orbitals of the chalcogenide atoms. The distance between these two elements strongly affects the overlapping of the orbital and thus, the Fermi surface which varies strongly with pressure. $Ca(Fe_{0.965}Co_{0.035})_2As_2$ is an iron based compound with extremely high sensitivity to pressure and strain. Due to the steric pressure of the Ca ion, small pressures result in dramatic changes in the ground state of the system. In this compound the effect of pressure can be mimic with post growth thermal treatments, allowing experiments like STM to access groundstates that would be impossible to study otherwise. Thanks to this we can characterize the local effect of strain in the superconducting phase of the system.

We have also focused on the recently discovered $CaKFe_4As_4$, performing the first tunneling measurements in this material. This FeBSC was found to be superconducting with a T_c of $35\,K$, which is by far the largest among stoichiometric compounds.

It shows no structural transition down to the lowest measured temperature, being also free of domains associated with this transition. This material gives a great opportunity to study the superconducting mechanism in a non doped compound, that is, removing the disorder coming from doping and from structural domains. We have characterize in this material the effects of topographic defects on superconductivity and the vortex lattice.

2H-$NbSe_2$ is considered by many to be a reference material for the study of superconductivity with STM, which makes it a good framework to study the effect of magnetic impurities. It shows, however, a strong in-plane anisotropy. This can be reduced by substituting Se by S. We show that $NbSe_{1.8}S_{0.2}$ is nearly in-plane isotropic. Adding a small amount of Fe impurities, we identify Shiba states and study the density of states around isolated impurities and groups of impurities of Fe ions that act as embedded localized magnetic moments. We study the effects of this impurities in the LDOS, investigating isolated and nearby ones.

STM is a widely used technique in the field of superconductivity, specially on the vortex matter. It allows to map with detail not only the vortex lattice but also individual vortices, being an ideal tool to study their individual and collective behavior. Despite this strong presence in the filed of vortex physics, there was not a well established method to extract the characteristic size of the vortex with STM. In chapter 3 we show how, in collaboration with Dr. Vladimir Kogan from the Ames Laboratory, we were able to provide such method using data from this thesis.

Resumen de la tesis

Al la vez que comenzaba mis estudios de máster se montó, en colaboración con el Prof. Paul Canfield del *Ames Laboratory* (Ames, IA, EEUU), un pequeño banco para crecimiento de materiales por flujo el en Laboratorio de bajas temperaturas de la UAM. Durante los meses posteriores, me familiaricé con dicha técnica, centrando en ella mi trabajo de fin de máster y en el verano siguiente, realicé una estancia de tres meses en el laboratorio del profesor Canfield para aprender más sobre esta técnica de crecimiento de materiales y poder aplicar estos conocimientos de vuelta en Madrid, donde establecimos colaboraciones con otros grupos para el estudio de monocristales.

Los monocristales de alta calidad son la mejor elección para el estuido de propiedades intrínsecas de un material. Carecen de anisotropías provocadas por dominios estructurales, su composición está bien controlada y tienen un número bajo de defectos. En este sentido, son el marco perfecto para el estudio de los efectos de imperfecciones aisladas en las propiedades del material. Además, puede introducirse en ellos desorden de una manera controlada (como con sustitución o impurezas), produciendo pequeñas modificaciones en la presión, la carga o introduciendo momentos magnéticos localizados.

Como figura en el título, este proyecto está centrado en el estudio de impurezas y defectos en superconductores, en concreto en un dicalcogenuro (2H-$NbSe_2$ dopado con azufre) y dos superconductores basados en hierro: $CaFe_2As_2$ dopado con cobalto y $CaKFe_4As_4$. Para estudiar las propiedades electrónicas de estos materiales usamos un microscopio de efecto túnel (STM por sus siglas en inglés) el cual, al ser enfriado a muy bajas temperaturas ($0.1\,K$), nos proporciona la resolución en energía necesaria para dicho estudio.

La superficie de Fermi de los superconductores basados en hierro (FeBSC por sus siglas en inglés) está formada fundamentalmente por los electrones $3d$ del hierro, junto a cierta contribución de los orbitales p de los átomos de la columna del nitrógeno / calcogenuros. La distancia entre estos dos elementos afecta fuertemente el solapamiento entre orbitales, por lo que la superficie de Fermi varía mucho con la presión. El $Ca(Fe_{0.965}Co_{0.035})_2As_2$ es un compuesto basado en hierro con una sensibilidad a la presión y a las deformaciones extremadamente alta. Debido a la presión estérica del ion Ca, un pequeño cambio de presión puede traducirse en un cambio drástico en el estado fundamental del sistema. En este compuesto, los efectos de la presión pueden ser reproducidos con un tratamiento térmico posterior al crecimiento de la muestra, permi-

tiendo de esta manera que experimentos como el STM accedan a estados fundamentales que de otra forma no podrían. Gracias a ello podemos caracterizar a escala local los efectos de las deformaciones en el estado superconductor de este sistema.

También nos hemos centrado en el estudio del recientemente descubierto $CaKFe_4As_4$, realizando las primeras medidas de espectroscopía túnel en este material. En este FeBSC se encuentra superconductividad con una temperatura crítica de $53\,K$, con mucho la más elevada etre los FeBSC estequiométricos. Carece de transición estructural entre temperatura ambiente hasta la temperatura más baja medida, encontrándose por tanto libre de dominios estructurales asociados a este tipo de transición. Este material proporciona una oportunidad excepcional para estudiar el mecanismo de la superconductividad en un compuesto sin dopaje, es decir, eliminando los efectos del desorden originado por el dopaje y los dominios estructurales. Hemos caracterizado en este material los efectos de los defectos en la superficie sobre la red de vórtices.

2H-$NbSe_2$ está considerado como un material de referencia en el estudio de la superconductividad con STM, lo que lo convierte en un buen marco para el estudio de los efectos de impurezas magnéticas. Este compuesto muestra, sin embarigo, una fuerte anisotropía del gap en el plano. Dicha anisotropía puede reducirse sustituyendo Se por S. Hemos visto que $NbSe_{1.8}S_{0.2}$ es casi completamente isótropo en el plano. Añadiendo una pequela cantidad de átomos de hierro, hemos identificado estados de Shiba y estudiado la densidad de estados alrededor de impurezas aisladas y pequeños grupos de impurezas de hierro que actúan como momentos magnéticos localizadas embebidas en el material. Estudiamos los efectos de estas impurezas en la densidad local de estados, investigando impurezas individuales y cercanas.

El STM es una técnica muy utilizada en el campo de la superconductividad, especialmente en el estudio de los vórtices. Permite realizar observaciones, no solo de la red de vórtices, sino también de vórtices individuales, siendo una herramienta idal para el estudio de comportamientos tanto individuales como colectivos. Pese a sus gran presencia en el campo, no había hasta ahora un método establecido para extraer el tamaño característico del vórtice con STM. En el capítulo 3 mostramos como, en colaboración con el Dr. Vladimir Kogan del *Ames Laboratory*, hemos sido capaces de proporcionar un método para ello utilizando datos obtenidos en esta tesis.

CHAPTER 1

Introduction

1.1 Motivation of the thesis

Understanding materials helps us to use them in existing applications and to design new applications that use some of their properties. Superconductors are characterized by their ability to carry an electric current without dissipation. The goal is to achieve such property at temperatures and magnetic fields as high as possible. To this end, we want to increase the critical temperature and optimize dissipation in presence of a current. The critical temperature is related to the electronic properties of the material, while dissipation with motion of vortices. When I started my PhD, I set myself to work on these problems and provide some, hopefully relevant, answers.

I have been studying single crystals because these allow separating effects intrinsic to the material from extrinsic effects such as disorder. Another advantage is that we can study the anisotropy due to the crystal lattice, which is sometimes useful to understand the results better. However, even perfect crystals have defects such as lattice dislocations, missing atoms, interstitial atoms or even other elements that have accidentally been introduced into the growth. Controlling these defects (their type, position and concentration), we can use them to actually probe the material at hand and better understand some of their properties. Here, I focus on the impurities and defects in dichalcogenide and pnictide superconductors. I will show how defects can be used to measure the electronic properties of pnictide materials and, for the first time, how these produce vortex pinning. I will also discuss magnetic defects inside chalcogenide superconductors. Although these do not influence vortex pinning, they produce interesting electronic effects at the local scale.

1.2 Some remarks on superconductivity

Superconductivity[1] was discovered more than a hundred years ago in 1911 at the Leiden Laboratory. After achieving the liquefaction of helium, Heike Kamerlingh Onnes was studying the behavior of electrical resistivity of metals with decreasing temperature.

[1]For de development of this part I will follow Schmidt [1997] and Tinkham [1996]

For mercury, he observed a sudden drop to zero (Fig.1.1) somewhere around $4\,K$. For all temperatures below $4\,K$ he could attain, the value of the resistivity remained unmeasurable. A new term, "superconducting" system, was soon coined. In the following years superconductivity was found in many other materials.

Figure 1.1: Photograph of Kamerlingh Onnes (right) and Gerrit Flim, his chief technician, at the helium liquefier at the Leiden laboratory (around 1911). Historic plot of the resistivity of mercury versus temperature showing the superconducting transition at $4.2\,K$. Adapted from van Delft and Kes [2011].

The temperature at which the resistivity of a material dropped to zero was called critical temperature T_c. It was soon realized that superconductivity was destroyed when the temperature was increased above the material's T_c but also when the magnetic field was increased above a certain value, called H_c. The observed variation of the critical field with temperature is well characterized by the empirical formula:

$$H_c(T) = H_c(0)\left[1 - (T/T_c)^2\right]. \tag{1.1}$$

We can write the difference in the free energies of the normal and superconducting states in terms of H_c as

$$\mu_0 \frac{H_c(T)}{2} = f_n(T) - f_s(T). \tag{1.2}$$

Being f_n and f_s the free energies per unit volume of the normal and superconducting state respectively.

During the years after the discovery of H. Kamerlingh Onnes it was was generally believed that superconductors were no more than perfect conductors with zero resistance. Next step came with the experiments of Meissner and Ochsenfeld [1933]. According to Maxwell equations, a perfect conductor reacts to a magnetic field in such a way that $dH/dt = 0$, therefore if a magnetic field $H_0 < H_c$ is applied to a perfect conductor at $T < T_c$ the magnetic field inside the perfect conductor is $H = 0$. However, if the field is

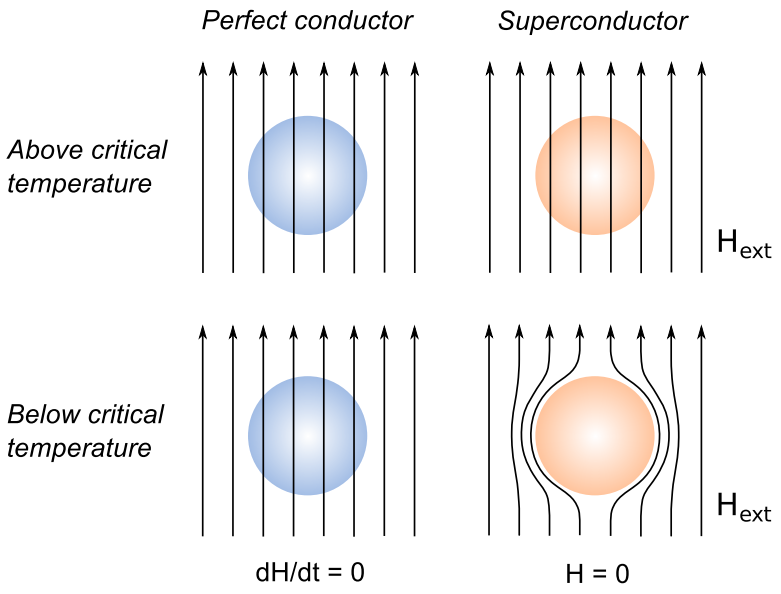

Figure 1.2: Schematic draw of the discovery from Meissner and Ochsenfeld [1933]. When a magnetic field is applied to a perfect conductor or a superconductor at temperature $T > T_c$ the field penetrates into the material. In this situation, when temperature is lowered below T_c the field inside the perfect conductor with remain the same ($dH/dt = 0$) while the superconductor completely expels the magnetic field ($H = 0$).

applied at $T > T_c$ and then the temperature is lowered, $dH/dt = 0$ gives $H = H_0$ inside the perfect conductor. The observation of Meissner and Ochsenfeld [1933] was that superconductors always expel the magnetic field from the inside as long as $H < H_c$ (see Fig.1.2). This perfect diamagnetism of superconductors was called *Meissner effect*.

London and London [1935] proposed a phenomenological theory with two equations that was suitable for describing the electrodynamics superconductors. Using a two fluid model of superconducting (n_S) and normal electrons (n_n), this theory succeeded in explaining the two phenomena described above, zero electrical resistivity and perfect diamagnetism. Supercurrents that flow in a small region at the surface can screen the magnetic field applied on the sample, which decays exponentially with a characteristic length – the London penetration depth λ_L – explaining the Meissner effect.

1.2.1 Ginzburg-Landau theory

The first phenomenological quantum theory of superconductivity was developed by Landau and Ginzburg [1950]. According to Landau's theory of phase transitions, a phase transition of second order occurs when the state of the body changes gradually while its symmetry changes discontinuously at the transition temperature, being the low temperature phase the one of reduced symmetry, meaning the most ordered one. Within this theory, Ginzburg and Landau described the superconducting state expanding the free energy as a function of the macroscopic wavefunction $\Psi(\vec{r})$, defined below

the critical temperature and write the free energy of the superconducting state as power expansion of $\Psi(\vec{r})$. A macroscopic amount of Cooper pairs can be described by a single wavefunction with fixed modulus and phase, implying that they are in a coherent quantum mechanical state. The wavefunction is related to the density of superconducting electrons by $|\Psi(\vec{r})|^2 = n_s$. Following their description, the free energy density f of a superconductor can be written as:

$$f = f_{n0} + \alpha |\Psi|^2 + \frac{\beta}{2} |\Psi|^4 + \frac{1}{2m^*} \left| \left(i\hbar\nabla + e^* \vec{A} \right) \Psi \right|^2 + \frac{h^2}{8\pi} \tag{1.3}$$

where f_{n0} is the free energy density of the normal state, α and β are parameters that depend on the material, h the magnetic field per unit volume, $\vec{A}$ the vector potential and m^* and e^* are respectively the mass and charge of the superconducting electrons. Minimizing the free energy with respect to Ψ and $\vec{A}$ one gets to Ginzburg-Landau (GL) differential equations:

$$\alpha\Psi + \beta |\Psi|^2 \Psi + \frac{1}{2m^*} \left(i\hbar\nabla + e^* \vec{A} \right)^2 \Psi = 0 \tag{1.4}$$

$$\vec{J} = \frac{-i\hbar e^*}{2m^*} \left(\Psi^* \nabla\Psi - \Psi \nabla\Psi^* \right) - \frac{e^{*2}}{m^* c} \Psi^* \Psi \vec{A} \tag{1.5}$$

With these two equations, GL theory succeed in describing the spatial variation of the superconducting state by means of two characteristic lengthscales: the penetration depth λ that characterizes the distance over which the magnetic field decays inside the superconducting region (and is related to the London penetration depth) and the coherent length ξ that characterizes the distance over which the order parameter can vary. Both lengths have a dependence of temperature near T_c of the type: $\lambda, \xi \propto (T_c - T)^{-1/2}$. The ratio of these two lengths defines the Ginzburg-Landau parameter $\kappa = \lambda/\xi$.

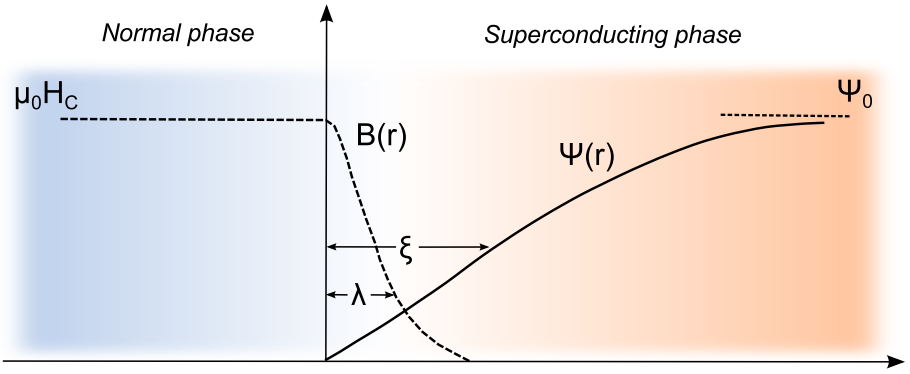

Figure 1.3: Schematic draw of the variation of the magnetic field and the superconducting order parameter with the characteristic lengthscales of Ginzburg-Landau theory.

Some years later Abrikosov [1957] predicted the existence of a new type of superconductors based on the value of the Ginzburg-Landau parameter. He proposed to make the difference between $\xi > \lambda$ ($\kappa = 1/\sqrt{2}$), which leads to a positive surface energy in the interface between normal and superconducting state and $\xi < \lambda$ where the creation of an interface becomes energetically favorable. This means that for this second type of superconductors – called "type II" superconductors – the magnetic flux can penetrate the superconducting material through normal state domains known as vortices.

So, for type II superconductors, instead the first order transition at H_c that happens in what we will call now on "type I" superconductors, there is a lower critical field H_{c1} at which magnetic flux starts to penetrate in the superconductor until it reaches $B = \mu_0 H$ at an upper critical field $H = H_{c2}$. Due to this partial flux penetration, the energy cost of expelling the magnetic field from the superconducting region is reduced and the thermodynamical critical field of the superconductor is increased.

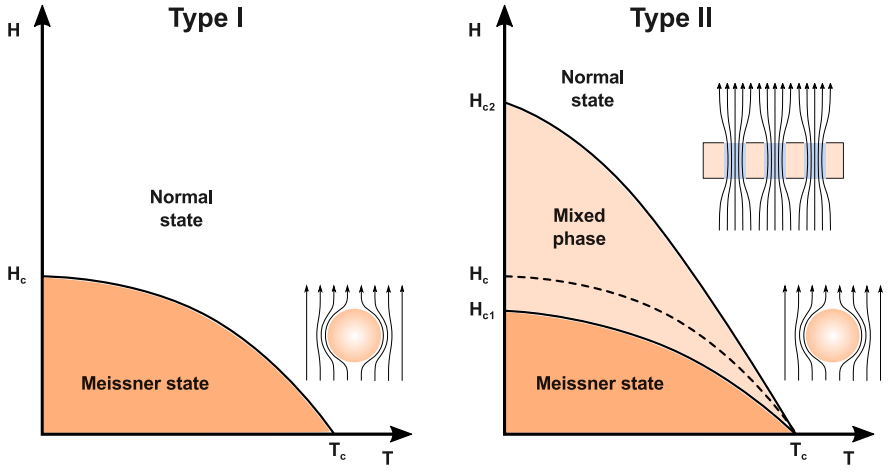

Figure 1.4: Cartoon of the applied magnetic field versus temperature phase diagram of type I and type II superconductors.

Abrikosov [1957] also found that the penetration on the magnetic flux in the superconductor in the *mixed state* or *Schubnikov phase* – that is, for fields between H_{c1} and H_{c2} – should happen in regular arrays of flux tubes or *vortices* each one carrying a quantum of flux

$$\Phi_0 = \frac{h}{2e} = 20.7 \times 10^{-15}\, Wb, \tag{1.6}$$

being h Plank's constant and e the electron charge. Fig.1.4 shows the magnetic field versus temperature phase diagrams for the type I and type II superconductors. Type II superconductors show Meissner effect below the critical field H_{c1}. Above this field, magnetic flux starts to penetrate the superconductor through vortex lines (mixed state) until above H_{c2} superconductivity is destroyed.

1.2.2 Microscopic theory of superconductivity

The phenomenological theories mentioned were successful in explaining many aspects of superconductors. However, a microscopic explanation for the mechanism of superconductivity did not appear until Bardeen, Cooper, and Schrieffer [1957a,b] published the today well known BCS theory.

The discovery of the isotope effect [Maxwell, 1950; Reynolds *et al.*, 1950] revealed the importance of the crystal lattice for superconductivity. It was seen that the use of different isotopes in a metal altered the critical temperature in such a way that $T_c \propto M^{-\alpha}$, with $\alpha \approx 1/2$ sometimes. Fröhlich [1950] explained the lattice contribution to the electron - electron interaction in the following way: an electron moving near the lattice interacts with the positive ions deforming the lattice which creates a local accumulation of positive charge. A second electron would feel this positive charge accumulation and would be attracted to it, absorbing the phonon associated to the lattice vibration. A schematic draw of this explanation can be seen in Fig.1.5.

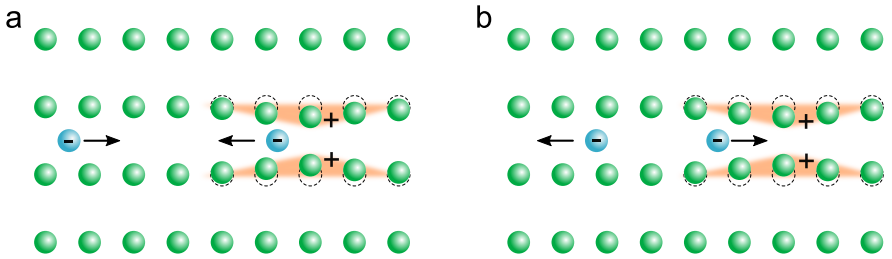

Figure 1.5: Schematic draw of the phonon mediated pairing proposed by Fröhlich [1950]. a) As the electron (blue) coming from the right passes near the lattice it interacts with it slightly distorting the lattice and creating an area with accumulation of positive charge (orange shade area). b) Another electron coming from the left *feels* the accumulation of positive charge and is attracted to it. Both electrons are in this way coupled through a lattice excitation, a phonon.

Cooper [1956] demonstrated that the Fermi sea is unstable to even a weak attractive potential, that leads to the formation of bound states consisting of pairs of electrons with opposite momenta and spin. These paired electrons are called *Cooper pairs*. The attractive interaction can be due to phonons, as explained above, or it can be the bare Coulomb interaction or through magnons [Kohn and Luttinger, 1965; Miyake and Sato, 2001]. The BCS theory extends this proposal for two electrons to all conduction electrons.

The BCS description of the superconducting ground state leads to a relation for the excited states of the system of the form

$$E_k = \sqrt{\epsilon_k^2 + \Delta^2}, \tag{1.7}$$

where ϵ_k is the kinetic energy measured with respect to the Fermi level and Δ is a constant. A look into Eq.1.7 reveals that any excitation, for an arbitrary small ϵ will

have an energy Δ above the Fermi level. Δ represents a region in which no states are allowed, a gap in the energy spectrum (Fig.1.6.a). However, since the electrons close to the Fermi level are forming Cooper pairs, the minimum energy needed to break a pair and create an excitation is of 2Δ. For energies $\epsilon_k \gg \Delta$ the usual metallic bandstruscture is recovered.

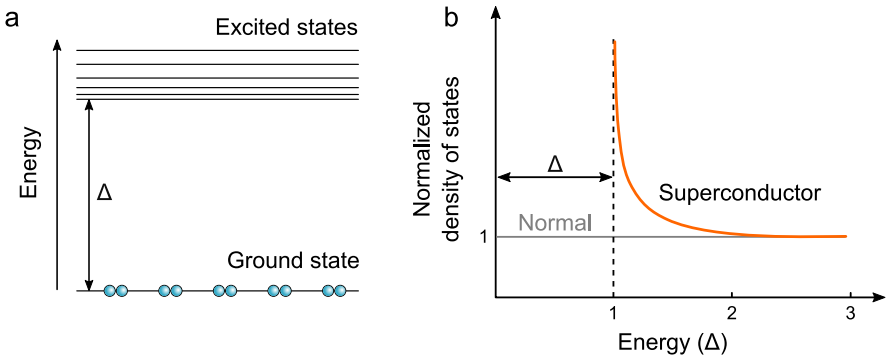

Figure 1.6: a) Adapted from Schmidt [1997]. Schematic representation of the ground state and the first excited states in a superconductor. b) Adapted from Tinkham [1996]. BCS normalized density of states of states of a superconductor near the Fermi level compared to that of a normal metal.

The density of states of the superconducting state compared to that of the normal state is given by

$$\frac{N_s(E)}{N_n(0)} = \begin{cases} 0 & E < \Delta \\ \frac{E}{\sqrt{E^2+\Delta^2}} & E > \Delta. \end{cases} \tag{1.8}$$

Where we have taken $N_n(E \gg \Delta) \approx N_n(0)$. As can be seen from Fig.1.6.b and from Eq.1.8, there are no states for energies smaller than Δ. BCS theory also establishes a relation between the value of the superconducting gap and the critical temperature being $\Delta = 1.76\, k_B T_c$.

Fig.1.7.b shows the calculated temperature dependence of the superconducting gap as obtained from BCS theory. For the lowest temperatures it is nearly constant an equal to that at zero temperature. Fig.1.7.a shows the effect of the temperature smearing in the BCS density of states as the temperature is going from 0 to T_c. Colorscale matches that of the points in Fig.1.7.b.

Phenomenological and microscopic theories of superconductivity were reconciled when Gor'kov [1959] proved that the results from Ginzburg - Landau theory could be obtained from the BCS model for temperatures near T_c (near the second order transition) where the order parameter Ψ is the macroscopic wave function of the superconducting electrons, and directly related to the superconducting gap Δ.

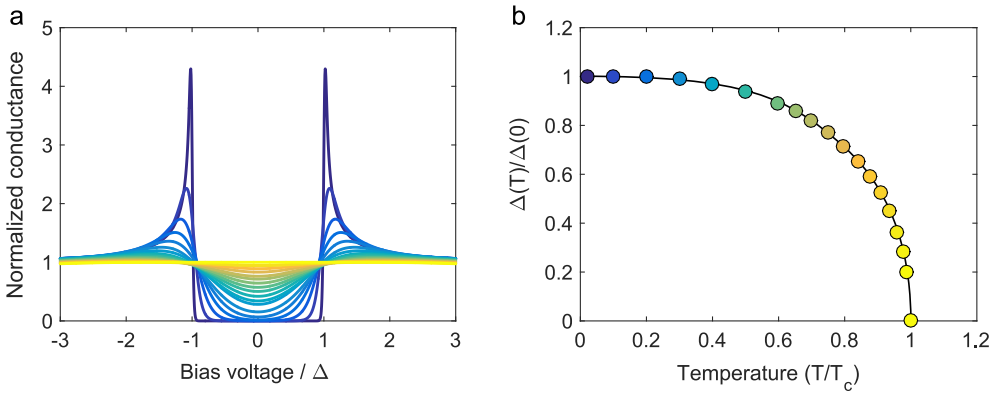

Figure 1.7: a) Calculation BCS density of states for a superconductor including the effect of temperature through the convolution with the derivative of the Fermi function. b) Temperature dependence of the superconducting gap with temperature in BCS theory. Curves in a match the points highlighted in the curve in b with the same color.

Multiband superconductivity

The Fermi surface of a material can be formed not just by one band but by contributions of several ones. This was first considered by Suhl, Matthias, and Walker [1959], who predicted theoretically the existence of two band superconductors. In one band superconductors, pairing occurs only between electrons of the same band. In the case of multiband superconductors, gaps of different sizes might open on different parts of the Fermi surfaces with different attractive interaction. This situation can usually be simplified to the case of effective two-band superconductivity. That is, if there are multiple sheets crossing the Fermi surfaces with each one showing a different gap, it often occurs that the gaps are centered around two gap values Δ_1 and Δ_2. For many multiband superconductors, the main features of the Fermi surface can be described considering just two groups of electrons of two effective bands. Strongly differing intraband interactions in each band will lead to strongly differing gap values. On the other hand, interband interactions generally lead to less different gap values. This has been considered in detail in many theoretical works, particularly in the case of MgB_2 and the FeBSC [Brandt and Das, 2011].

In a hypothetical two band superconductor without interband scattering each band would have separated superconducting properties, defining two well defined superconducting gaps and critical temperatures. In real materials bands are always coupled and although there might be two gap values there is only one T_c. Fig.1.8 shows the dependence of the superconducting gap associated with two different bands in a two gap superconductor as calculated by Suhl, Matthias, and Walker [1959].

The prototypical two band superconductor is MgB_2. Its Fermi surface has two main contributions, one as two-dimensional cylinders arising from σ-orbitals due to p_x and p_y electrons of B atoms and the other, more two-dimensinal coming from π-orbitals due to p_z electrons of B atoms. Fig.1.9.a shows a first principle calculation of the Fermi surface including in color code the gap associated to each sheet.

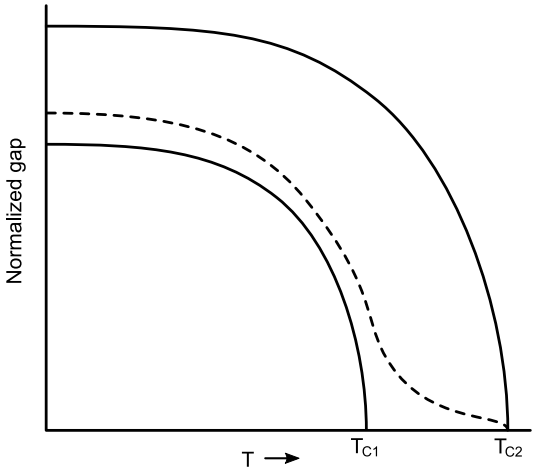

Figure 1.8: a) From Suhl, Matthias, and Walker [1959]. Temperature dependence of the superconducting gaps in a two band superconductor. Since both bands are coupled, the band with the largest gap induces superconductivity in that of the smaller one, leading it to a not BCS-like dependence. As a result, two gap superconductors show only one critical temperature.

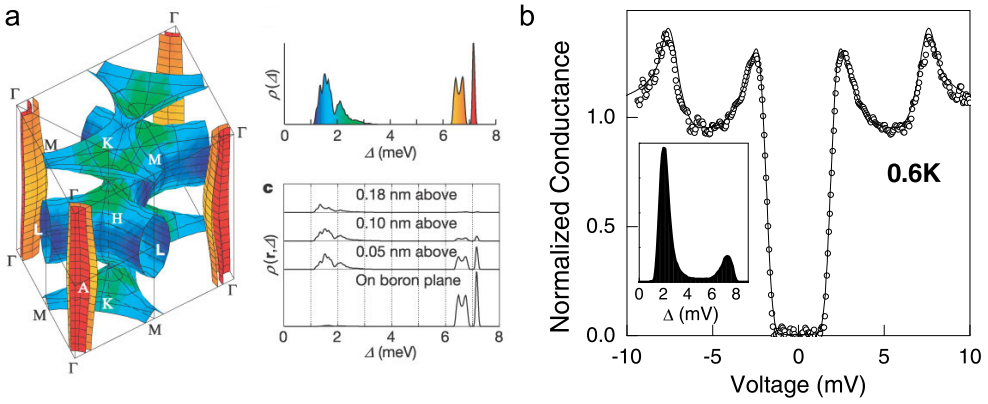

Figure 1.9: a) From Choi *et al.* [2002]. Left panel: first principle calculation of the Fermi surface of MgB_2 with the gap present at each part of the surface added as a colorcode. Right panel includes the gap distribution and the contribution of different surface planes to it. b) Normalized conductance of MgB_2 measured by Martinez-Samper *et al.* [2003] showing a clear two gap structure. Superconducting gap values are extracted using the model in Eq.1.9 using the distribution function in the inset.

The contribution of the different parts of the DOS to the tunneling conductance will vary depending on the tunneling matrix elements (see section 2.2.1). This behavior can be modeled with a gap distribution instead a single value where

$$LDOS \propto \sum_{\Delta_i} \gamma_i \, \mathrm{Re}\left(\frac{E}{\sqrt{E^2 - \Delta_i^2}}\right). \tag{1.9}$$

Where Δ_i are the different gap values and γ_i their corresponding weight in the distribution. To include the effect of temperature the result is convoluted with the derivative of the Fermi function. This procedure has been used to obtain the gap values in MgB_2 in the experiments of Choi *et al.* [2002]; Martinez-Samper *et al.* [2003] giving good results like in Fig.1.9.b. It has also been previously used for other superconductors like $NbSe_2$ in Rodrigo and Vieira [2004]; Guillamón [2009].

1.2.3 Superconducting vortices

The vortex lattice

Thus, in the intermediate state of type II superconductors, the magnetic flux penetrates as quantized "cylinders" named *vortices*. Each of these vortices has a normal core where the order parameter goes to zero as sketched in Fig.1.10.a. Around the vortex core, superconducting electrons circulate forming suppercurrents with a direction such that the field generated by it coincides with the applied magnetic field. These supercurrents circulate within an area of the order of λ around the core. We should keep in mind that for type II superconductors usually $\lambda \gg \xi$. The vortex radius, as any other spatial variation of the order parameter is strongly related to the coherence length and it is of the same order. More details regarding this last aspect will be given in chapter 3.

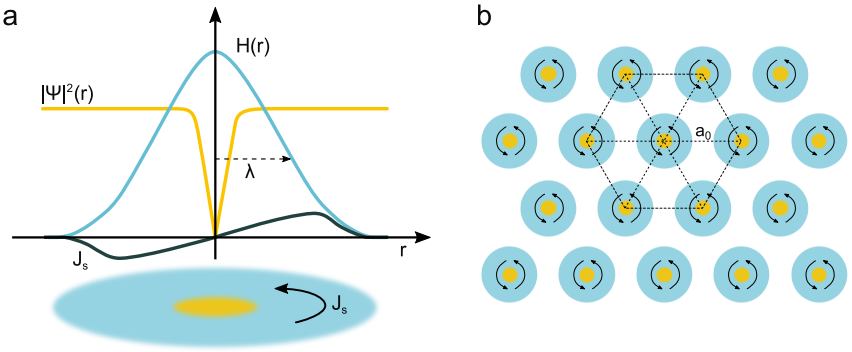

Figure 1.10: a) Cartoon of the variation of the order parameter, the magnetic field and the supercurrents at a superconducting vortex. b) Schematic top view of the vortex triangular Abrikosov lattice in a superconductor.

The interaction between vortices is repulsive. Abrikosov showed that they arrange into a triangular lattice with hexagonal symmetry. This type of lattice is called Abrikosov lattice after him. Most studied superconductors show this arrangement. However, a square vortex lattice can be found in some materials [Canfield, Gammel, and Bishop, 1998]. Intervortex distance in the case of a triangular and a square lattice are given by

$$d_{\triangle} = \left(\frac{4}{3}\right)^{1/4} \left(\frac{\Phi_0}{B}\right)^{1/2} \quad ; \quad d_{\square} = \left(\frac{\Phi_0}{B}\right)^{1/2}. \tag{1.10}$$

Fig.1.11.a shows one of the images taken by Essmann and Träuble [1967] where the triangular arrangement of the vortex lattice is clear.

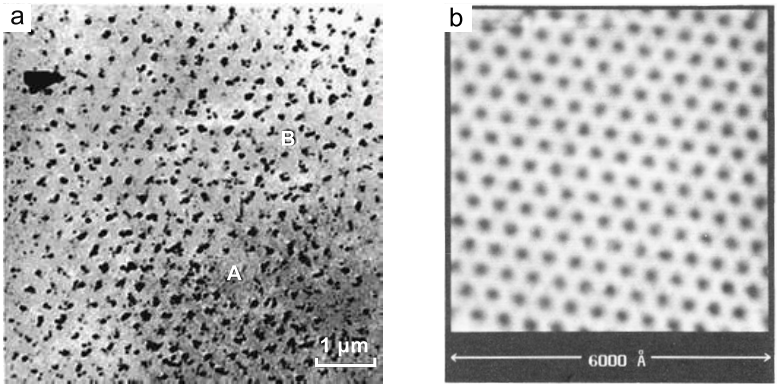

Figure 1.11: a) Adapted from Essmann and Träuble [1967]. Magnetic decoration image of a triangular vortex lattice in Pb with $4\,\%$ indium taken at $1.1\,K$. A and B in the image represent a hole and a dislocation in the lattice b) Adapted from Hess *et al.* [1989]. STM image of the vortex lattice in 2H-$NbSe_2$ taken at $1.8\,K$ with an applied field of $1\,T$.

During the last decades, scanning tunneling microscopy has become more and more important in the study of superconducting vortices, being today a fundamental probe in the field. STM/S can map variations of the superconducting density of states in the real space. Due to its spatial an energy resolution it can easily map changes of the order of the coherence length ξ, and therefore resolve details of the lattice or individual vortices. The first images of the vortex lattice taken with STM were performed by Hess *et al.* [1989] on 2H-$NbSe_2$ (see Fig.1.11). Since then, vortex lattices have been imaged in many superconductors studying their static and dynamic behavior, revealing properties of the superconducting gap and the Fermi surface [see Fischer *et al.*, 2007; Hoffman, 2011; Suderow *et al.*, 2014, for more detailed reviews on the use of STM to image the vortex matter].

Andreev reflection

Elementary excitations in a superconductor are formed by quasi-partiles of hole-like or electron-like character. Fig.1.12.a shows the dispersion relation E_k for a superconductor. In region 3, the quasi-particle is near the hole branch of the spectra and behaves accordingly. Similar, in region 1, the quasi-particle will behave as an electron. In the middle, however, its character will be defined by the corresponding coherence factors. The change between hole-like and electron-like happens gradually, which implies that the charge of the quasi-particle changes continuously from $+1$ to -1 (Fig.1.12.b).

In the intermediate state of superconductors, there are interfaces between regions of normal metal and superconducting regions (NS interface). When an elementary excitation of the superconductor approaches the interface, a process know as Andreev

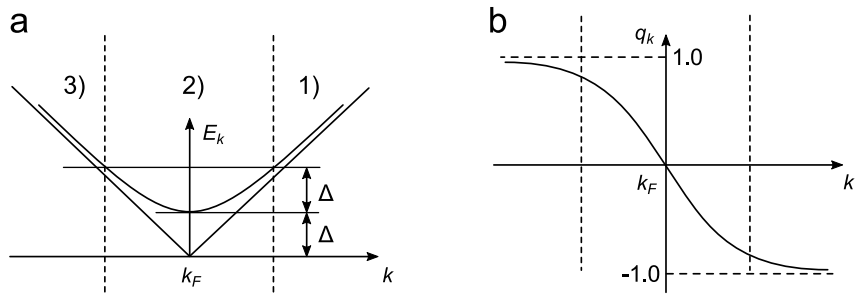

Figure 1.12: Adapted from Schmidt [1997]. Energy espectrum E_k (a) of quasi-particles in a superconductor and their charge q_k (b). In region 1, the quasiparticle charge is close to -1, in region 3 it is close to 1 and in region 2 it might assume any value from -1 to $+1$.

reflection occurs.

Andreev reflection is important to understand many behaviors in superconductors. Let us consider an electron approaching a NS interface from the normal state with energy $E_k < \Delta(T)$. It moves towards the NS interface as shown schematically in Fig.1.13. When the electron reaches an area with a finite – but small – value of Δ ($x = x_1$) it becomes an electron-like quasi-particle of the superconductor, filling the appropriate $\vec{k}$ state for its energy E_k. As the quasi-particle moves closer to the superconducting region ($x = x_2$) the value of the gap increases and it moves into another $\vec{k}$ state closer to $\vec{k_F}$ resulting in an increase of the quasi-particle charge.

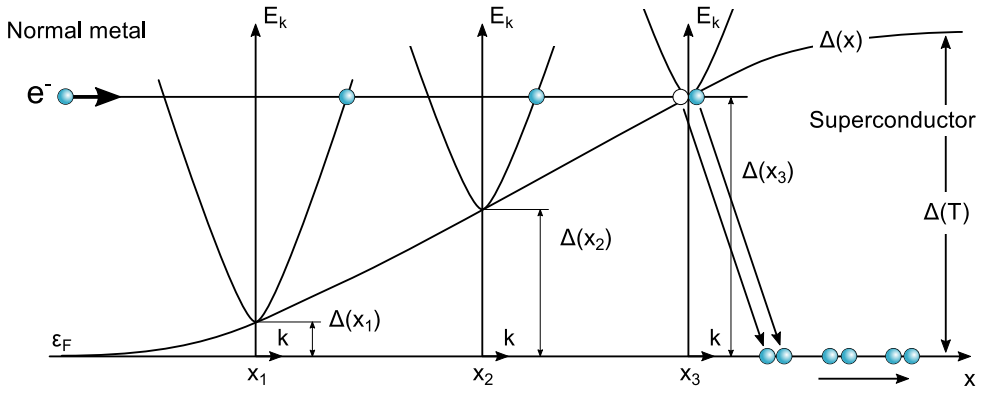

Figure 1.13: Adapted from Schmidt [1997]. Schematic representation of the process of the Andreev reflection. In the vicinity of the NS interface, a quasiparticle (electron) moves from one $\vec{k}$ state to another, gradually changing its charge as it moves closer to the superconducting region.

Thus, as moving into the superconducting region, the quasi-particle reduces its charge and reduces its momenta towards $\vec{k_F}$. When the energy of the quasi-particle becomes equal to that of the superconducting gap ($x = x_3$), the charge of the quasi-particle becomes zero and its momenta is $k = k_F$. At this point it is reflected back from the interface and, in momentum space, it moves to the left hand branch, which is popu-

lated by holes. Its group velocity is inverted, now it moves from the superconducting to the normal metal region, and its charge becomes positive. Propagation of a positive charge to the left is equal to the propagation of a negative charge to the right. Therefore, this process involves a transfer of charge from the normal to the superconducting region, that is, a current. This process was first considered by Andreev [1964] and it is called *Andreev reflection*.

The Andreev reflection implies that once the quasi-particle reaches the interface it couples to another electron and enters the superconducting condensate while the hole left by the other electron moves back into the normal region. So this process accounts for charge transfer between the normal and superconducting regions for electron with energies below the energy gap [Cuevas, Martín-Rodero, and Yeyati, 1996; Suderow *et al.*, 2014].

Caroli-deGennes-Matricon states inside vortex cores

Caroli, deGennes, and Matricon [1964] calculated the energy spectra inside a vortex line in a pure type II superconductor. They realized that the spatially varying pair potential inside the core should lead to the formation of bound Andreev states localized in the vortex core. Using Bogolubov-deGennes they found that the spectra inside the core were formed by quantized levels with a spacing in energy of $\delta \approx \Delta^2/E_F$.

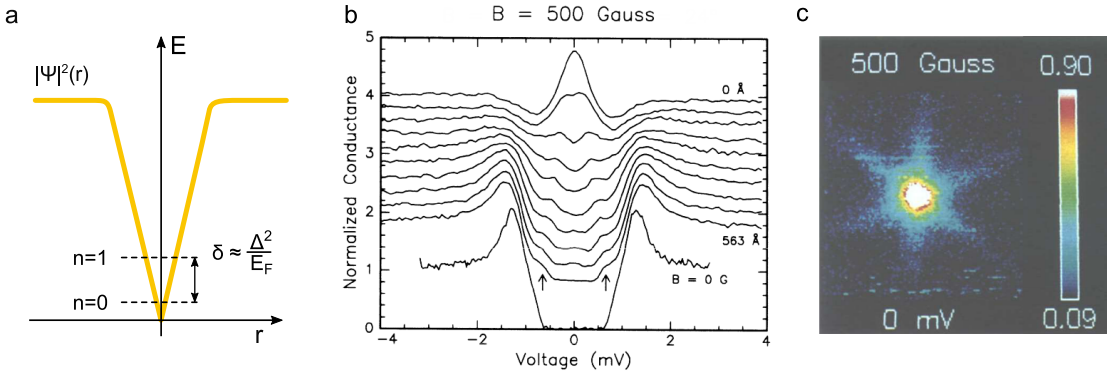

Figure 1.14: a) Schematic representation of the variation of the level spacing inside the vortex core. b-c) Adapted from Hess, Robinson, and Waszczak [1990]. b) Conductance curves going from the center of a vortex (upper curve) into the superconducting region (bottom curve) in $NbSe_2$. The peak at the vortex core center was interpreted as the first experimental evidence of the Caroli-deGennes-Matricon boundstates. c) Zero bias conductance map of a single vortex reflecting the gap anisotropy in 2H-$NbSe_2$.

In their STM experiments in 2H-$NbSe_2$, Hess *et al.* [1989]; Hess, Robinson, and Waszczak [1990, 1991] measured a peak in the density of states at the vortex core center. This peak split as moving away from the core center. They interpreted this as the experimental observation of the bound states predicted by Caroli, deGennes, and Matricon [1964]. Since then such localized states have been seen in many compounds

through STM [Fischer *et al.*, 2007; Hoffman, 2011; Suderow *et al.*, 2014].

There is an important difference between bound states in a quantum well and Andreev levels in a superconducting vortex. Whereas, in a quantum well, the states are truly confined in the well, in a superconducting vortex, the pair wavefunction vanishes only at a single point. Excitations are quasi-particles created on top of a spatially varying finite superconducting background through the Andreev exchange process described above.

1.2.4 Impurities in superconductors: Abrikosov-Gor'kov

Matthias, Suhl, and Corenzwit [1958, 1960]; Matthias [1962] made systematic studies on the superconducting transition temperature of La when introducing small percentages of other rare earths. They observed sharp drops of T_c when small amounts ($< 1\,\%$) of magnetic atoms were added to the compound (see for instance, Fig.1.15.a). They further relate the drop in T_c with the spin of the magnetic impurity, suggesting that it was due o a exchange interaction.

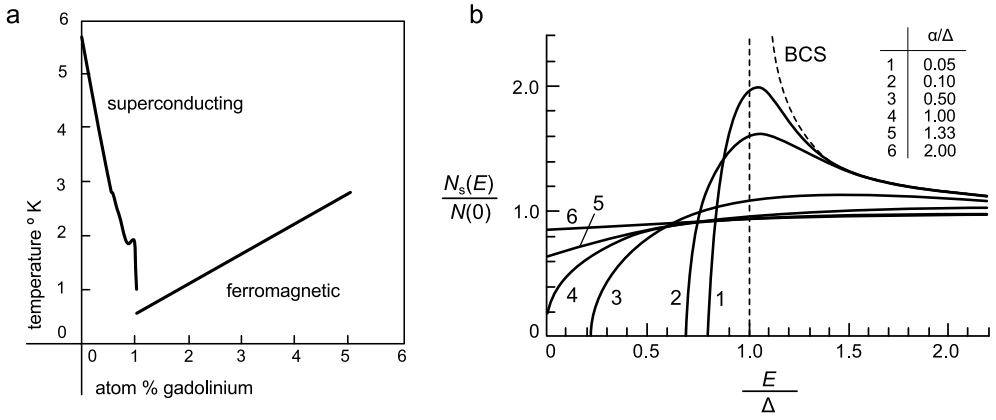

Figure 1.15: a) Superconducting and ferromagnetic transition temperatures of La-Gd alloys. adapted form deGennes [1966] and this after Matthias [1962]. Superconducting transition temperature shows a sharp drop as magnetic impurities of Gd are added to the compound. b) Density of states as a function of the reduced energy gap for different values of the pair breaking strength α/Δ. Adapted from Tinkham [1996] and this after [Skalski, Betbeder-Matibet, and Weiss, 1964].

Anderson [1959] showed for dirty superconductors (those where the mean free path l is smaller than the coherence length ξ) that if pairing states are invariant under time-reversal operators, equilibrium properties of the superconductor, such as T_c, H_{c2} or Δ, are independent of the electronic mean free path. For the case of magnetic impurities, Abrikosov and Gor'kov [1961] developed a theory based on exchange interactions that explain the reduction of T_c observed by Matthias and coworkers. This theory predicts as well strong modifications in the density of states of the superconductor (which eventually become gapless) due to scattering processes. Within the theory, the pair

breaking produced by impurities is characterized through the typical energy difference 2α it causes between the two time-reversed electrons. Fig.1.15.b contains the density of states calculated for several values of α.

It can be seen from Fig.1.15.b that as α increases the density of state is smeared, introducing states inside the superconducting gap and eventually closing it for energies of two times the BCS superconducting gap Δ. Woolf and Reif [1965] performed tunneling experiments on lead and indium superconducting films containing different magnetic impurities. They found good agreement with the Abrikosov-Gor'kov (AG) theory for impurities with strong localized moments.

It should be mentioned that the effect of magnetic impurities in the AG theory can be extended to any other perturbation that breaks time-reversal symmetry: external magnetic fields, currents, rotations, spin exchange and hyperfine fields [see deGennes, 1966; Tinkham, 1996].

1.3 Iron based superconductors

The paradigm of superconductivity changed in the 80's with the discovery of superconductivity in high T_c cuprates by Bednorz and Müller [1986]. These materials generated huge expectations due to their critical temperatures, much higher than those known at the moment. The BCS phonon-mediated coupling was not able to explain the formation of pairs in this new type of superconductors and they were named *unconventional* superconductors. A deeper understanding of superconductivity was – and despite all efforts and findings still is – needed to understand these compounds.

The next breakthrough in the field of high temperature (unconventional) superconductors came with the discovery of superconductivity in iron based superconductors (FeBSC). It was first discover in LaFePO by Kamihara *et al.* [2006] with a $T_c \approx 4\,K$ and in LaNiAsO at $2.4\,K$ by Watanabe *et al.* [2007]. However, it is another work from the same group which is usually considered as the key paper for the discovery of iron superconductors, where Kamihara *et al.* [2008] found superconductivity at a T_c as high as $26\,K$ in $LaFeAsO_{1-x}F_x$.

The first surprise was that of having a superconductor with iron. Iron is a well known magnetic material and magnetism was thought to strongly damage superconductivity. In fact superconductivity and magnetism are considered to be competing phenomena. For this reason, the discovery of a superconductor with iron and with such a high T_c had so much relevance in the community. Furthermore, the pairing mechanism of these materials is not conventional phonon coupling, but rather repulsive electron - electron interaction as in cuprates, so they soon were recognized as a new opportunity to understand how superconductivity is developed in high T_c materials.

At first glance there are similarities between cuprates and FeBSC. They both have 2D

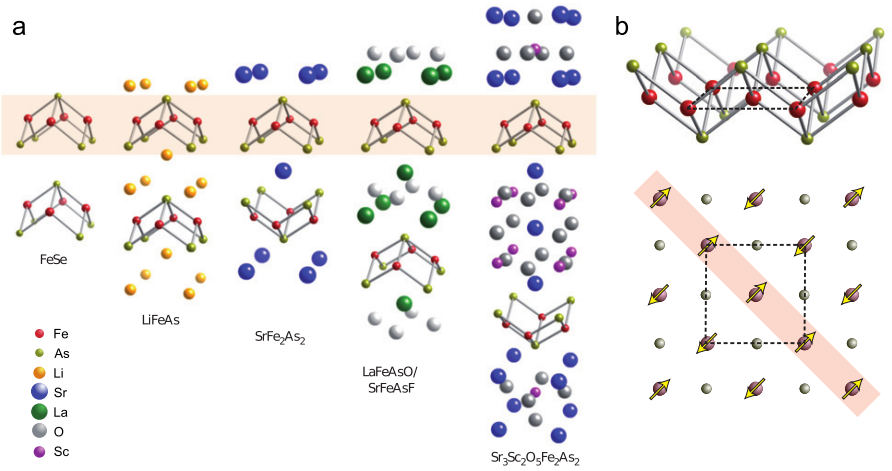

Figure 1.16: a) Crystal structures of different families of the iron pnictides. Fe-As planes are highlighted as common features in all structures. From Paglione and Greene [2010]. Blue square indicates the structure of the 122 materials, which would be the more relevant for the compounds studied in this work. b) Detail of the FeAs plane and top view of the same plane. As can be seen in the figure, Fe spins are aligned ferromagnetically in one direction and antiferromagnetically in the other showin what is called *stripe like* antiferromagnetic order.

lattices of $3d$ transition metal ions as the building blocks and orthorhombic distortions can be present upon small doping. They have also similar phase diagrams with a magnetic ordered phase in the parent compound and a superconducting dome developing with doping either with holes or electrons with the higher T_c where the magnetic order disappears. However, while in the cuprates the Cu in plane d orbitals dominate at the Fermi surface, in FeBSC, not only the d orbitals of Fe contribute, but the out of plane orbital of the As, with which iron is in tetrahedral coordination, relevant for the Fermi surface. Regarding the phase diagrams, in cuprates magnetic order vanishes before superconductivity appears. For FeBSC there is no general behavior. Some compounds, like for instance LaFeAsO, show a first order transition between magnetic and superconducting phases, whereas other compounds like the 122 family both groundstates coexist for certain doping levels. In the magnetic phase, cuprates are Mott insulators and in the normal phase above the superconducting transition they show a pseudogap phase. FeBSC magnetic phases are metallic and in the normal phase they show linear dependence of resistivity with temperature. Finally, in high T_c cuprates, the mechanism of doping and the symmetry of the order parameter (d-wave) are now well known. The pairing mechanism, however, is still unknown. In FeBSC the symmetry of the order parameter, despite it seems to agree with multiband $s_{\pm}$ in most cases, it might be different in others. Nevertheless, the community seems to agree that the ultimate source of the pairing interaction in both systems might be fundamentally similar [Hirschfeld, Korshunov, and Mazin, 2011].

FeBSC are by themselves very interesting materials with unique properties and researchers have found almost every phenomena associated with strongly correlated systems in these materials. They are multiband materials with a new symmetry of the order parameter. Their phase diagrams are rich showing simultaneously different phe-

nomena as magnetic order, superconductivity and electronic nematicity and they provide a new framework for the study of quantum critical points. For the study of all these phenomena they present an advantage over cuprates, that is, very pure single crystalline samples can be grown by flux methods providing very high quality and homogeneous materials.

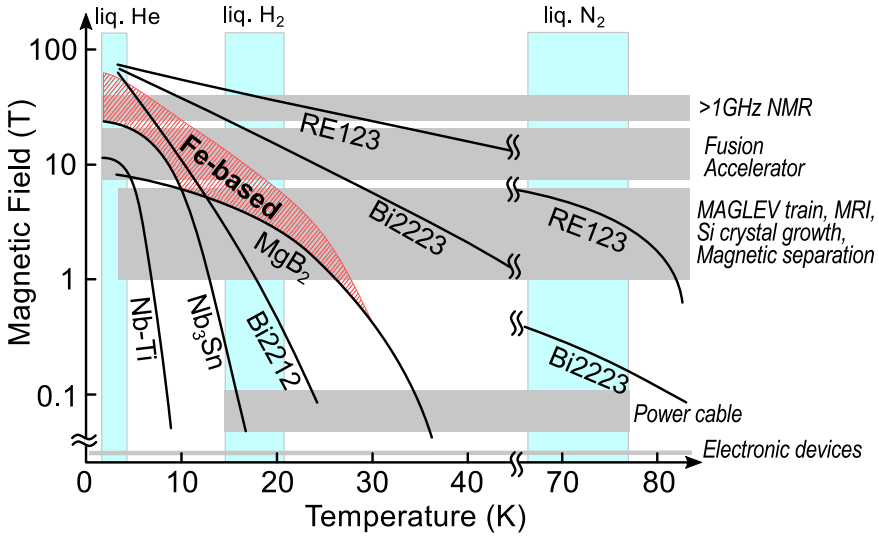

Figure 1.17: Applicable conditions for $J_e > 10^4\, A\, cm^{-2}$ for various superconducting tapes and wires From Shimoyama [2014].

Fig.1.17 shows the temperature-field range of application of FeBSC. It can be seen from the figure that FeBSC can introduce performance improvements (higher T_c and higher critical fields) in almost all areas. Furthermore, when comparing to cuprates FeBSC wires have much lower potential cost since they are metallic in the normal state and superconductivity is less affected by impurities or defects. All these characteristics make them particularly interesting for wire applications [Hosono and Kuroki, 2015; Shimoyama, 2014].

Regarding the Fermi surface, the main contribution to the electronic properties of the FeBSC is from the five Fe d states. Fermi surface consists of orbitals from the d_{xy}, d_{yz} and d_{xz} orbitals and the hopping between Fe sites occurs primarily via a pnictogen (chalcogen) ion which with is in tetrahedral coordination as can be seen from the structures in Fig.1.16. Generally, the Fermi surface consists of at least four quasi 2D electron and hole cylinders: two hole sheets (often called pockets due to their small size) centered at the Brillouin zone center (Γ point) and two electron pockets centered at the M point, $(0, \pi)$ and $(\pi, 0)$, in the tetragonal unit cell (see Fig.1.18.b). The two non-equivalent As positions in the magnetic phase (above and below the Fe lattice as indicated in Fig.1.16.a) result in a folding of the BZ to include two Fe atoms per unit cell (Fig.1.16.c). The folding vector (indicated in Fig.1.16.c) sets the electron pockets at the point (π, π) with respect to the new unit cell, the same direction of the AFM ordering vector. A fifth hole band is also proposed to sit at $(0, \pi)$ in the folded BZ, and

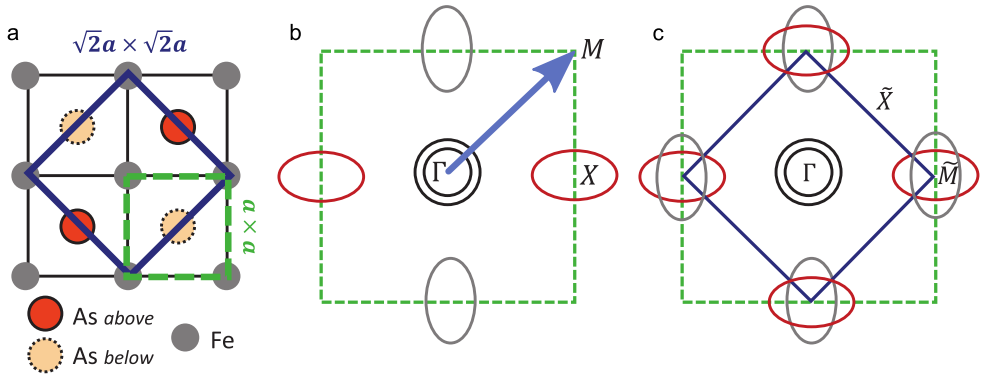

Figure 1.18: a) Schematic draw of the top view of the crystallographic unit cell of the FeAs plane. Dashed green and solid blue squares indicate 1-Fe and 2-Fe unit cells, respectively. b) Schematic 2D Fermi surface in the 1-Fe BZ whose boundaries are indicated by a green dashed square. The arrow indicates folding wave vector Q_F. c) Fermi sheets in the folded BZ whose boundaries are now shown by a solid blue square. From Hirschfeld, Korshunov, and Mazin [2011].

its presence may be very sensitive to structural details.

In multiband materials, the superconducting gap can be different in each pocket of the Fermi surface. In fact, this is a fundamental aspect of unconventional superconductors. In order to satisfy the self consistent gap equation with a repulsive (positive) potential, the order parameter should change sign between different parts of the Fermi surface.

1.3.1 Generic phase diagram

Generally phase diagrams are dome-shaped with magnetic ordered parent compound. Magnetic order is *stripe like*, meaning that spins are aligned parallel in one direction and antiparallel in the other (see Fig.1.16.b). They also show a structural phase transition which is often but not always coupled to the magnetic phase transition. Above them there might be a nematic transition (or a region with nematic fluctuations) of electronic order which has been reported in many compounds. This state is, however a subject of controversy since nematic, structural and magnetic order parameters are strongly coupled. It is therefore difficult to separate their effects. Superconductivity emerges as a dome at finite doping/pressure with the optimal doping near to where the magnetic transition extrapolates to zero temperature. For some materials there is a region with coexistence of magnetic order and superconductivity. There is also experimental evidence for quantum criticality inside the superconducting region and non Fermi liquid behavior is observed close to optimal doping. For instance, some compound show linear temperature dependence of resistivity [Analytis *et al.*, 2010] and divergence of superfluid density, effective mass, and jump in heat capacity in the SC transition at T_c when approaching optimal doping.

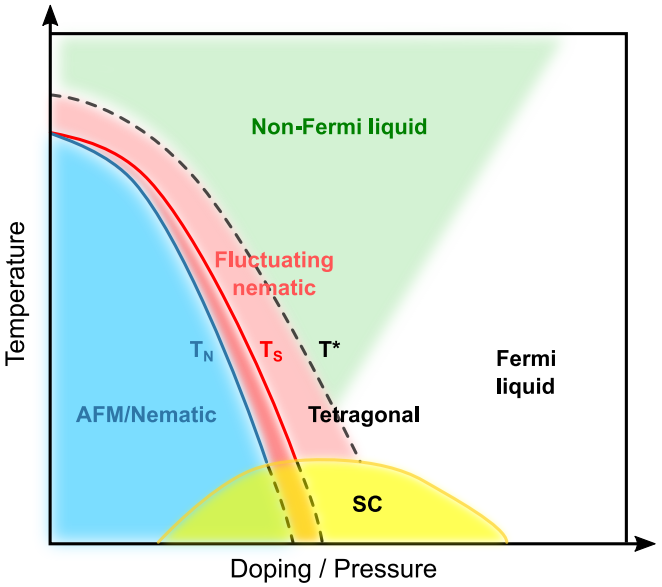

Figure 1.19: Generic temperature versus doping / pressure phase diagram for the FeBSC. The parent compound usually presents a structural / magnetic transition that reduces its temperature with incresing doping / pressure. The structural and magnetic transitions are coupled or separated depending on the compound. Above the structural transition and usually coupled to it and to the magnetic one there is an electronic nematic phase. Superconductivity emerges in a dome-shape with finite doping / pressure with the optimal doping usually coinciding with the extrapolation of the magnetic phase to zero temperature.

The first FeBSC discovered were part of the 1111 family like LaFePO, LaNiAsO, or $LaFeAsO_{1-x}F_x$ [Kamihara *et al.*, 2006; Watanabe *et al.*, 2007; Kamihara *et al.*, 2008] and have some of the highest critical temperatures, but large single crystals proved challenging to grow and therefore properties such as intrinsic anisotropy or inhomogeneity could not be studied.

A lot of work has been done in the 122 family of the FeBSC, specially in the compounds derived from $BaFe_2As_2$. The reason is that soon after their discovery there were large single crystals available [Ni *et al.*, 2008a] allowing for any type of experiment and suitable for the study of anisotropies. Nematicity, for instance, was first reported in an STM study of cobalt doped $CaFe_2As_2$ [Chuang *et al.*, 2010]. In the same year, Chu *et al.* [2010] showed the electronic nature of this state performing resistivity measurements on detwinned single crystals of $Ba(Fe_{1-x}Co_x)_2As_2$.

111 and 11 materials such as LiFeAs or Fe(Te,Se), came out as very interesting compounds. LiFeAs is a shoichiometric material with a relatively high T_c ($18\,K$) that allows for the study of superconductivity without dopant-induced disorder. Nematicity has also been observed in the vortex state of FeSe. Monolayers of this material show the highest T_C among FeBSC getting above $100\,K$.

The number of FeBSC compounds is already large and still increasing. Growth groups are continuously adding new compounds to the scene and improving sample

quality. In fact, during the development of this thesis a new family of FeBSC was discovered including stoichiometric 1144 compounds with T_c's as high as $35\,K$ [Iyo *et al.*, 2016; Meier *et al.*, 2016], which will hopefully give some new insight about superconductivity in FeBSC.

1.3.2 Order parameter in FeBSC superconductors

The symmetry of the order and the pairing interaction remain as open questions in the case of FeBSC. There are lots of review articles on the matter as those done by Mazin and Schmalian [2009]; Hirschfeld, Korshunov, and Mazin [2011]; Chubukov and Hirschfeld [2015]; Hirschfeld [2016]; Bascones, Valenzuela, and Calderón [2016]. Here we pretend to give a short and general overview on this matter to introduce some concepts that will come in hand later.

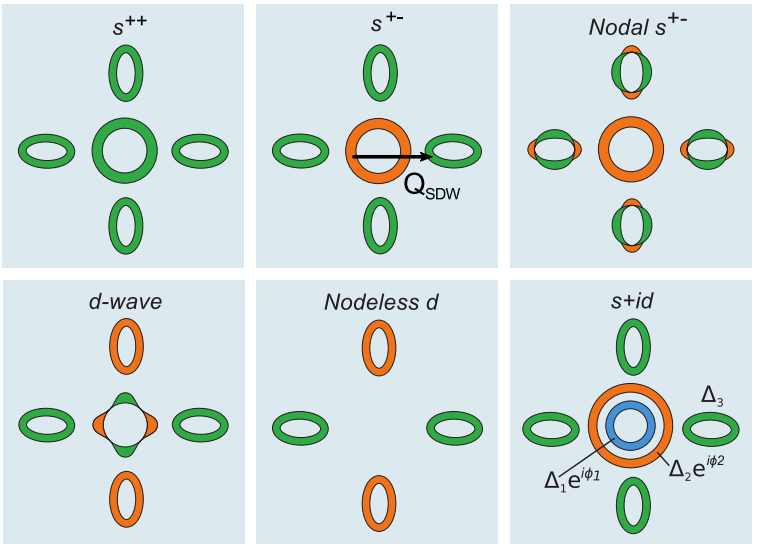

Figure 1.20: Schematic representation of the different scenarios proposed for the pairing symmetries in FeBSC, colors represent the phase of the order parameter at each pocket. From Chubukov and Hirschfeld [2015].

There have been proposals for different types of symmetry, being the most relevant ones the $s_{\pm}$, the s_{++} and the d symmetries. $s_{\pm}$ is favored by spin fluctuations, which have been related to interband interaction instead of intraband. s_{++}, mediated by an attractive interband interaction to nematic fluctuations. d-wave proposal dominates for intraband repulsive intractions. Among this three, $s_{\pm}$ and d-wave are most debated candidates [Hosono and Kuroki, 2015; Hirschfeld, 2016].

$s_{\pm}$ symmetry was proposed in Mazin *et al.* [2008]. In favor of this type of symmetry, there are theoretical calculation showing that interpocket and intrapocket interaction are of repulsive character. This would imply that, in order to have a bound pair, the order parameter must change sign between pockets, leading to $s_{\pm}$ symmetry. However,

given the differences between the size of the pockets and the vector connecting them, a mechanism to connect electron and hole pockets and enhance interpocket interaction would be needed. The most popular scenario is pairing mediated by spin fluctuations with the antiferromagnetic spin density wave (SDW) vector $\vec{Q}_{SDW}$ connecting electron and hole pockets (see Fig.1.20). In this case, when magnetic fluctuation grow, they favor interpocket interaction which eventually becomes larger than the intrapocket.

The existence of accidental nodes (not imposed by symmetry) has also been discussed for $s_{\pm}$ causing a sign change in the electron pockets (see Fig.1.20. Nodal $s^{\pm}$). Nodes might appear on either type of pocket if higher harmonics in the angular expansion of the order parameter are sufficiently large. In real space, nodeless $s_{\pm}$ the pairing would be between electrons of the next - nearest - neighbor (NNN), the interaction would be mediated by the pnictogen (or chalcogen) atom giving rise to a SDW. If the pairing occurs between Fe nearest neighbors (NN) nodes would be necessary to minimize the energy. Regarding this matter, a lot of work have been done in the effect of the distance between pnictogen (chalcogen) atom and Fe plane [see for instance Calderón, Valenzuela, and Bascones, 2009]. Several studies show that this height can act as a switch from a high T_c nodeless pairing (LaFeAsO) to a lower T_c nodal pairing with smaller height (LaFePO) [Kuroki *et al.*, 2009].

$d_{x^2-y^2}$ symmetry may emerge from repulsive interaction between two electron pockets. It implies that the sign of the order parameter varies between two electron pockets changing sign under $\pi/2$ rotations. For weakly and moderately electron doped FeBSC d wave is a close second candidate behind $s_{\pm}$, however, for higher dopant concentrations, in which interaction between electron and hole pockets is rather small, it appears as the leading instability. It has also been proposed for strongly hole-doped compounds.

1.3.3 Pair breaking in FeBSC

Despite there is still no experiment that would unambiguously determine the symmetry of the order parameter, there have been several approaches. One is the fact that in conventional superconductors, a non magnetic impurity have no effect in the LDOS of the condensate, however, the same type of impurity in $s_{\pm}$ superconductors produces scattering between parts of the Fermi surface with different sign, leading to a finite value of the LDOS due to pair breaking [Hirschfeld, 2016]. Nevertheless, one should bare in mind that the lack of a boundstate or the non observation of a finite LDOS in the case of non magnetic impurities does not allow to conclude that the superconducting gap does not change sign and therefore $s_{\pm}$ symmetry cannot be excluded. Chen *et al.* [2016] studied the effects of incipient bands in the pairing symmetry proposing different scenarios in which $s_{\pm}$ leads to no boundstate.

1.4 Scope of this work

By the time I was starting my master a small bench for solution growth was set up in the Low Temperature Laboratory with the collaboration of Prof. Paul Canfield from the Ames Laboratory (Ames, Ia, USA). In the following months I became familiar with the technique. In the following summer I made a three month stay in Prof. Canfield's laboratory learning more about solution growth and applying this knowledge back in Madrid to study single crystals and collaborate with different groups.

High quality single crystals are the best choice to study intrinsic properties of a material. They are free of structural domain anisotropies, have a controlled composition and a low concentration of defects. In this sense, they are the perfect environment to study the effect of isolated imperfections on the properties of the material. Furthermore disorder (such as dopants or impurities) can be introduced in a very controlled way producing small modifications in pressure, charge or introducing local magnetic moments.

As mentioned in the title, the thesis project is mainly focused on the study of impurities and defects in superconductors, particularly a dichalcogenide superconductor (S doped 2H-$NbSe_2$) and two iron based superconductors: Co doped $CaFe_2As_2$ and $CaKFe_4As_4$. To access the local electronic properties of this materials we use a scanning tunneling microscope (STM) and by cooling it to very low temperature ($0.1\,K$) we get the necessary energy resolution for the study.

The Fermi surface of FeBSC is formed by the $3d$ electrons of Fe with a contribution of the p orbitals of the chalcogenide atoms. The distance between these two elements strongly affects the overlapping of the orbital and thus, the Fermi surface which varies strongly with pressure. $Ca(Fe_{0.965}Co_{0.035})_2As_2$ is an iron based compound with extremely high sensitivity to pressure and strain. Due to the steric pressure of the Ca ion, small pressures result in dramatic changes in the ground state of the system. In this compound the effect of pressure can be mimic with post growth thermal treatments, allowing experiments like STM to access groundstates that would be impossible to study otherwise. Thanks to this we can characterize the local effect of strain in the superconducting phase of the system.

We have also focused on the recently discovered $CaKFe_4As_4$, performing the first tunneling measurements in this material. This FeBSC was found to be superconducting with a T_c of $35\,K$, which is by far the largest among stoichiometric compounds. It shows no structural transition down to the lowest measured temperature, being also free of domains associated with this transition. This material gives a great opportunity to study the superconducting mechanism in a non doped compound, that is, removing the disorder coming from doping and from structural domains. We have characterize in this material the effects of topographic defects on superconductivity and the vortex lattice.

2H-$NbSe_2$ is considered by many to be a reference material for the study of supercon-

ductivity with STM, which makes it a good framework to study the effect of magnetic impurities. It shows, however, a strong in-plane anisotropy. This can be reduced by substituting Se by S. We show that $NbSe_{1.8}S_{0.2}$ is nearly in-plane isotropic. Adding a small amount of Fe impurities, we identify Shiba states and study the density of states around isolated impurities and groups of impurities of Fe ions that act as embedded localized magnetic moments. We study the effects of this impurities in the LDOS, investigating isolated and nearby ones.

STM is a widely used technique in the field of superconductivity, specially on the vortex matter. It allows to map with detail not only the vortex lattice but also individual vortices, being an ideal tool to study their individual and collective behavior. Despite this strong presence in the filed of vortex physics, there was not a well established method to extract the characteristic size of the vortex with STM. In chapter 3 we show how, in collaboration with Dr. Vladimir Kogan from the Ames Laboratory, we were able to provide such method using data from this thesis.

1.5 Resumen de la tesis

Al la vez que comenzaba mis estudios de máster se montó, en colaboración con el Prof. Paul Canfield del *Ames Laboratory* (Ames, IA, EEUU), un pequeño banco para crecimiento de materiales por flujo el en Laboratorio de bajas temperaturas de la UAM. Durante los meses posteriores, me familiaricé con dicha técnica, centrando en ella mi trabajo de fin de máster y en el verano siguiente, realicé una estancia de tres meses en el laboratorio del profesor Canfield para aprender más sobre esta técnica de crecimiento de materiales y poder aplicar estos conocimientos de vuelta en Madrid, donde establecimos colaboraciones con otros grupos para el estudio de monocristales.

Los monocristales de alta calidad son la mejor elección para el estuido de propiedades intrínsecas de un material. Carecen de anisotropías provocadas por dominios estructurales, su composición está bien controlada y tienen un número bajo de defectos. En este sentido, son el marco perfecto para el estudio de los efectos de imperfecciones aisladas en las propiedades del material. Además, puede introducirse en ellos desorden de una manera controlada (como con sustitución o impurezas), produciendo pequeñas modificaciones en la presión, la carga o introduciendo momentos magnéticos localizados.

Como figura en el título, este proyecto está centrado en el estudio de impurezas y defectos en superconductores, en concreto en un dicalcogenuro (2H-$NbSe_2$ dopado con azufre) y dos superconductores basados en hierro: $CaFe_2As_2$ dopado con cobalto y $CaKFe_4As_4$. Para estudiar las propiedades electrónicas de estos materiales usamos un microscopio de efecto túnel (STM por sus siglas en inglés) el cual, al ser enfriado a muy bajas temperaturas ($0.1\,K$), nos proporciona la resolución en energía necesaria para dicho estudio.

La superficie de Fermi de los superconductores basados en hierro (FeBSC por sus siglas en inglés) está formada fundamentalmente por los electrones $3d$ del hierro, junto a cierta contribución de los orbitales p de los átomos de la columna del nitrógeno / calcogenuros. La distancia entre estos dos elementos afecta fuertemente el solapamiento entre orbitales, por lo que la superficie de Fermi varía mucho con la presión. El $Ca(Fe_{0.965}Co_{0.035})_2As_2$ es un compuesto basado en hierro con una sensibilidad a la presión y a las deformaciones extremadamente alta. Debido a la presión estérica del ion Ca, un pequeño cambio de presión puede traducirse en un cambio drástico en el estado fundamental del sistema. En este compuesto, los efectos de la presión pueden ser reproducidos con un tratamiento térmico posterior al crecimiento de la muestra, permitiendo de esta manera que experimentos como el STM accedan a estados fundamentales que de otra forma no podrían. Gracias a ello podemos caracterizar a escala local los efectos de las deformaciones en el estado superconductor de este sistema.

También nos hemos centrado en el estudio del recientemente descubierto $CaKFe_4As_4$, realizando las primeras medidas de espectroscopía túnel en este material. En este FeBSC se encuentra superconductividad con una temperatura crítica de $53\,K$, con mucho la más elevada etre los FeBSC estequiométricos. Carece de transición estructural entre temperatura ambiente hasta la temperatura más baja medida, encontrándose por tanto libre de dominios estructurales asociados a este tipo de transición. Este material proporciona una oportunidad excepcional para estudiar el mecanismo de la superconductividad en un compuesto sin dopaje, es decir, eliminando los efectos del desorden originado por el dopaje y los dominios estructurales. Hemos caracterizado en este material los efectos de los defectos en la superficie sobre la red de vórtices.

2H-$NbSe_2$ está considerado como un material de referencia en el estudio de la superconductividad con STM, lo que lo convierte en un buen marco para el estudio de los efectos de impurezas magnéticas. Este compuesto muestra, sin embarigo, una fuerte anisotropía del gap en el plano. Dicha anisotropía puede reducirse sustituyendo Se por S. Hemos visto que $NbSe_{1.8}S_{0.2}$ es casi completamente isótropo en el plano. Añadiendo una pequela cantidad de átomos de hierro, hemos identificado estados de Shiba y estudiado la densidad de estados alrededor de impurezas aisladas y pequeños grupos de impurezas de hierro que actúan como momentos magnéticos localizadas embebidas en el material. Estudiamos los efectos de estas impurezas en la densidad local de estados, investigando impurezas individuales y cercanas.

El STM es una técnica muy utilizada en el campo de la superconductividad, especialmente en el estudio de los vórtices. Permite realizar observaciones, no solo de la red de vórtices, sino también de vórtices individuales, siendo una herramienta idal para el estudio de comportamientos tanto individuales como colectivos. Pese a sus gran presencia en el campo, no había hasta ahora un método establecido para extraer el tamaño característico del vórtice con STM. En el capítulo 3 mostramos como, en colaboración con el Dr. Vladimir Kogan del *Ames Laboratory*, hemos sido capaces de proporcionar un método para ello utilizando datos obtenidos en esta tesis.

CHAPTER 2

Experimental methods

STM is a very powerful tool for the study of materials that has been successfully applied to several fields in condensed matter research and its relevance in all of them is today undeniable[1].

Superconductivity is a low temperature phenomenon, discovered by H. K. Onnes in 1911. To study superconductivity, cryogenic methods are needed. Here I will describe methods that I have been using during my Ph.D. I will also explain the working principle of STM and explain, throughout the chapter, where I have made improvements in the system.

But in order to perform a good experiment, not only a good experimental setup is needed but also a high quality sample. All the measurements done during this work were performed on single crystals. I will also discuss in this chapter the techniques I have learned during my stay at Prof. Canfield laboratory in Ames (IA, USA) and the growths we have successfully carried out in the Low Temperature Laboratory in Madrid involving pnictide superconductors. This Ph.D. thesis is the first in the laboratory where the student has both, grown a complex crystal and measured it with the STM.

I would also like to mention that almost all our experimental equipment, from the cryostat and the control electronics to the STM itself, has been designed and assembled together with the workshops of our university (SEGAINVEX[2]).

2.1 Cooling to millikelvin temperatures with dilution refrigeration

A dilution refrigerator is a particularly good choice for our experiment not only because it can cool down to temperatures of a few tens of mK but also because it can maintain those temperatures with high cooling power without interruption. This is very convenient for STM experiments that take advantage of the low thermal noise (which is of the order of k_BT) for the electronic measurements, the perfect cryogenic

[1] APS collection for the the 35^{th} anniversary of scanning tunneling microscopy
[2] https://www.uam.es/segainvex

vacuum, which serves both to preserve the surface and as the most simple tunneling barrier and the time the equipment can be running, which is useful for long spectroscopic measurements that need measurements several days long. In particular, in this Ph.D. thesis I will describe spectroscopic measurements that need very long acquisition times.

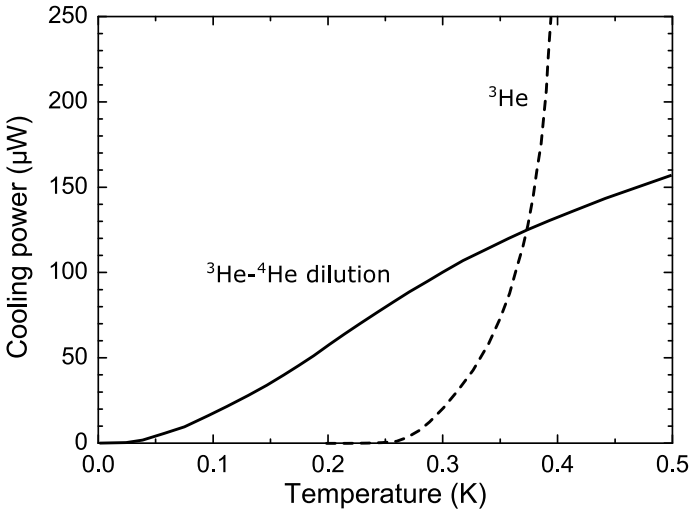

Figure 2.1: Cooling power of the dilution refrigerator compared to a ^{3}He evaporation system. Adapted from Lounasmaa [1974]

Figure 2.1 shows a comparison between the cooling power in a conventional ^{3}He cryostat and in a ^{3}He-^{4}He dilution refrigerator. We see that the former decays exponentially and goes to zero just below $0.3\,K$ while the latter decays as T^2 and remains finite to much lower temperatures allowing to keep temperatures of the order of mK.

2.1.1 Principle of operation

The principle of operation of dilution refrigerators, proposed for the first time by London [1951] and London, Clarke, and Mendoza [1962], is based on the quantum properties of a mixture of ^{3}He and ^{4}He.

In order to illustrate this, figure 2.2 shows the binary ^{3}He-^{4}He phase diagram. We can distinguish three important regions, left and right sides of the λ-curve where the mixture behaves respectively as a superfluid or a normal fluid and the lower part of the diagram, below the coexistence curve where the mixture is spontaneously separated into two phases, one richer in ^{4}He – or dilute (D) from the point of view of ^{3}He – and one richer in ^{3}He – concentrated (C) – that will float on the top of the other due to its lower density.

Lowering the temperature of the mixture for a certain concentration x from T to T' over the coexistence curve, will result into the phase separation. If the temperature is further decreased to T'' the ^{3}He content of the concentrated phase will increase from x'_C to x''_C following the coexistence curve. In the dilute phase ^{3}He concentration will

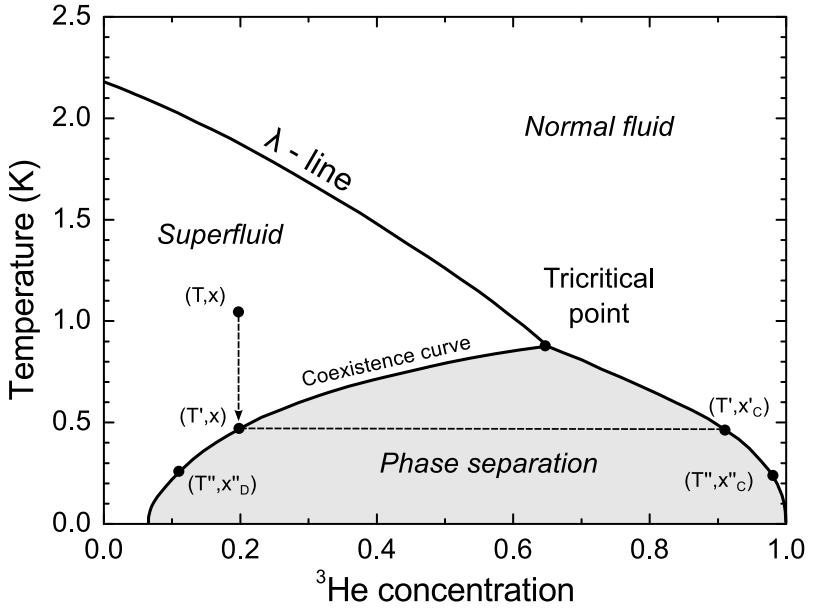

Figure 2.2: Temperature vs ^{3}He concentration phase diagram at saturated vapor pressure for a mixture of ^{3}He-^{4}He. In the diagram $x = n_3/(n_3 + n_4)$, being n_3, n_4 the number of moles of ^{3}He and ^{4}He respectively. Subindices D and C stand for dilute and concentrated ^{3}He phases.

be reduced from x to x''_D. If the temperature is decreased even more, x_C would keep increasing until $x_C \simeq 1$ and $x_D \simeq 0.064$ below 0.1 K.

It is of utter importance for the performance of the dilution refrigerator the fact that x_D remains finite even at zero temperature. This characteristic property of the coexistence curve discovered by Edwards *et al.* [1965] is what allows avoiding the exponential decay of the cooling power.

The explanation for this effect is of quantum nature and lays on the different statistics that ^{4}He and ^{3}He follow. ^{4}He has zero nuclear spin (it is a boson) and because the dilute phase stays below the λ-curve, it is also superfluid. Therefore ^{4}He is effectively in its quantum mechanical ground state, it has no excitations and remains thermodynamically inert. On the other hand, ^{3}He has a half integer nuclear spin and obeys Fermi-Dirac statistics and for practical purposes, above the λ-curve it can be regarded as a normal Fermi liquid in the range of temperatures where the dilution refrigerator works. So, in this model, the system of ^{3}He atoms in a superfluid ^{4}He background is described by free ^{3}He quasi-particles with a higher effective mass (m^*).

In the mixing chamber at a fixed temperature, the equilibrium condition is given by the equality of the chemical potentials of dilute and concentrated phases:

$$\mu_{3C}(T, x_C) = \mu_{3D}(T, x_D), \tag{2.1}$$

where $\mu_{3C} = \mu_3 \equiv g_3 \equiv h_3 - Ts_3$ and $\mu_3 D = (\partial G_D/\partial n_3)$ [3]. At zero temperature,

[3]Capital letters stand for extensive quantities while molar quantities are represented by lower case letters. Subscripts 3, 4, D and C refer respectively to pure ^{3}He, pure ^{4}He, dilute phase and concentrated

the chemical potential is related to the latent heat through $L_3(0) = -\mu_3(0)$, where $L_3(0) = L_{3C}(0)$. The energy needed to remove one ^{3}He atom from the concentrated phase into the vacuum is $L_3(0)/N_0 = -\mu_3(0)/N_0$, being N_0 Avogadro's number. This is also the energy needed to remove one ^{3}He atom from the concentrated to the dilute phase. In the dilute phase the binding energy of a ^{3}He atom is $\mu_{3D}(0,0)/N_0$ which is larger of that of the concentrated phase. This means that ^{3}He atoms are more strongly bound to ^{4}He atoms than among them and thus, they can pass from the concentrated to the dilute phase. However, this happens only to a certain extend because as x_D increases the binding energy decreases. It can be understood recalling that ^{3}He follows Fermi statistics. In calculating μ_{3D} the variation of the binding energy $\epsilon_{3D}(0, x_D)$ with the concentration and the increase of the kinetic energy $kT_F(x_D)$ should be taken into account. Substituting in Eq.2.1 one gets for the equilibrium

$$-L_3(0)/N_0 = -\epsilon_{3D}(0, x_D) + kT_F(x_D). \tag{2.2}$$

As shown in Lounasmaa [1974], the concentration at which it is no longer energetically favorable to dilute more ^{3}He into ^{4}He is of $x_D = 6.4\ \%$.

This finite equilibrium concentration provides a finite amount of particles in the dilute phase. In usual evaporation, this does not occur, the amount of particles in the gas phase exponentially drops to zero when decreasing temperature. If the concentration of ^{3}He atoms in the dilute phase is reduced, given the difference in binding energy of ^{3}He atoms at both sides of the interphase, some ^{3}He atoms from the concentrated phase will cross the interface into the dilute phase in order to maintain equilibrium. Since the enthalpy of ^{3}He in the dilute phase is larger than that in the concentrated phase due to the difference in the Fermi energy, cooling will occur.

Figure 2.3 shows a scheme of the dilution refrigerator. The process can be separated into a series of different stages, each one with characteristic temperature and pressure. The first one is the $1\,K$ pot, a small cavity where a small amount of ^{4}He extracted from the bath is pumped in order to cool down to $1.5\,K$. The mixture that comes down the injection line goes through the pot (without direct contact with the ^{4}He) and it is condensed and cooled. In order to further cool the liquid before it reaches the phase separation (that occurs down in the mixing chamber) it goes through a series of heat exchangers of different kinds. Those exchangers use the enthalphy of the outgoing mixture to reduce the temperature of the incoming ^{3}He. The cooling power of the dilution refrigerator depends in a non trivial way of those heat exchangers, therefore their design and number play a mayor role in the performance of the refrigerator.

The mixing chamber is the coldest part of the cryostat, where the phase separation takes place. Here the concentrated phase, richer in the lighter isotope, is floating over the dilute one. The mixing chamber is connected through the heat exchangers to the evaporator or still (short for distillation pot), where the liquid-gas interface is located. The design of the still, mixing chamber and connecting lines determines the amount of ^{3}He needed and the total volume of the mixture. A proper design leaves free room for

phase.

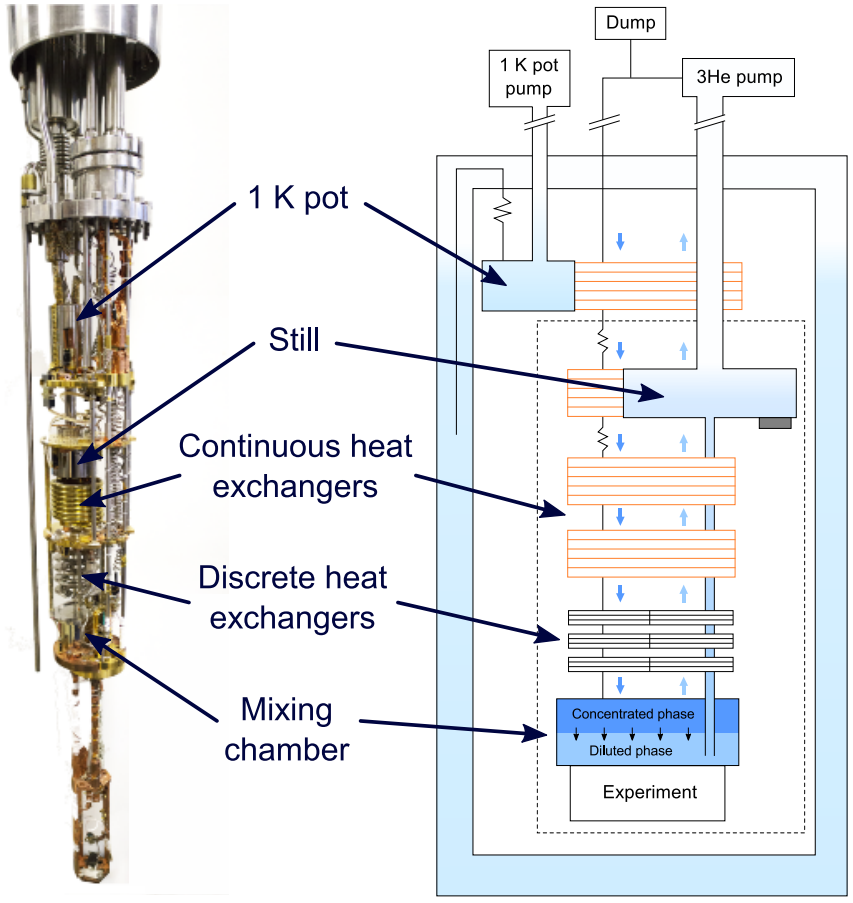

Figure 2.3: Photograph of the dilution refrigerator used in this thesis and schematic picture of the dilution refrigerator. Different parts of the refrigerator are indicated in both figures.

the process to work with a wide range of ^{3}He.

The temperature gradient between the mixing chamber and the still provides a large difference of equilibrium concentrations of ^{3}He in the dilute phase. When ^{3}He is pumped from the still, the ^{3}He concentration at the still is reduced, which creates an osmotic pressure gradient that acts against gravity and Fountain pressure, driving the ^{3}He from the mixing chamber up to the still. Due to the difference in the vapor pressures of superfluid ^{4}He and ^{3}He, if the still is pumped, the gas that goes out is practically pure ^{3}He. In order to maintain the equilibrium concentration in the mixing chamber ^{3}He is continuously going from the concentrated to the dilute phase giving the necessary cooling power for the continuous operation of the dilution refrigerator.

2.2 Scanning tunneling microscopy

The Scanning Tunneling Microscope (STM) was designed and developed at the IBM laboratories by Binning and Rohrer [Binnig *et al.*, 1982c,b; Binning and Rohrer, 1982;

Binnig *et al.*, 1982a; Binnig and Rohrer, 1983]. It is based on the quantum tunneling phenomena occurring between two conductors separated by an isolating layer. The impact of this tool for the community is reflected in the Nobel prize award received by these two scientist in 1986, only five years after their invention[4]. It allows the study of the surface and electronic properties near the Fermi surface with great resolution.

2.2.1 Principle of operation

In 1961 Bardeen applied time dependent perturbation theory to evaluate the tunneling matrix elements in the pursuit of understanding tunneling junction experiments [Bardeen, 1961]. He showed that the amplitude of electron transfer depends on the overlap of the wavefunctions of the two electrodes (treated as separated subsystems) in the space between them. Very soon after the invention of Binning and Roher, a modified Bardeen's theory was applied to STM by Tersoff and Hamann [1983, 1985] using typical distances and sizes found in experiments.

The tunneling current (I), or the electron transition rate, is obtained through the Fermi golden rule,

$$I = \frac{4\pi e}{\hbar} \int_{-\infty}^{\infty} \left[f\left(\epsilon + eV\right) - f\left(\epsilon\right) \right] N_s\left(\epsilon + eV\right) N_t\left(\epsilon\right) |M|^2 d\epsilon, \tag{2.3}$$

where $f(E)$ is the Fermi distribution function and N_s and N_t are respectively the densities of states (DOS) of the two electrodes [5]. To simplify the equation, the Fermi energy is set as reference, meaning $E_F = 0$. In the case when $k_B T$ is small with respect to the resolution of the experiment, the Fermi distribution can be considered as a step and therefore, Eq.2.3 becomes:

$$I = \frac{4\pi e}{\hbar} \int_{-\infty}^{\infty} N_s\left(\epsilon + eV\right) N_t\left(\epsilon\right) |M|^2 d\epsilon. \tag{2.4}$$

We assume that the matrix element can be considered as constant through the tunneling process and energy independent [Bardeen, 1961]. Thus, tunneling current is proportional to the convolution of the DOS of the two electrodes.

In the case of our particular experiment we use a gold tip to study superconducting samples at very low temperatures. We are in the range where $k_B T$ is small ($8.6\ \mu eV$ at 100 mK) and the tip is made of gold, which is metallic, meaning its DOS is $N_t(\epsilon) = constant$. Taking the derivative, we obtain the tunneling conductance which is directly proportional to the density of states of the sample,

$$\frac{dI}{dV} \propto N_s\left(eV\right). \tag{2.5}$$

Thus, with STM one can directly access the normalized density of states of our sample. Measurements of the DOS as function of the position are called scanning tunneling

[4] 1986 Nobel prize award.

[5] The use of subindex s and t corresponding to sample and tip is justified to adapt notation for STM.

spectroscopy (STS).

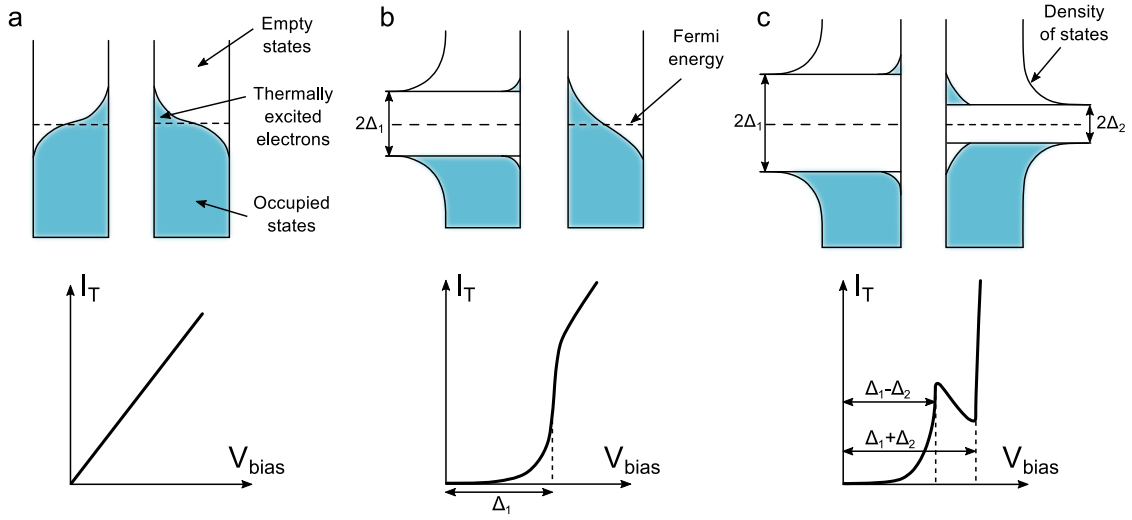

Figure 2.4: From Tinkham [1996]. Characteristic I-V curves in tunneling junctions between two metals (a), a metal and a superconductor (b) and two superconductors (c).

On the other hand, as said, wavefunctions of each of the subsystems decay exponentially with the distance inside the barrier. Assuming one-dimensional tunneling, we can write

$$\Psi_s \propto e^{-\kappa z} \;\; ; \;\; \Psi_t \propto e^{-\kappa(d-z)} \;\; ; \;\; \kappa = \sqrt{\frac{2m\phi}{\hbar^2}} \approx 0.5\sqrt{\phi}\ \text{Å}^{-1}, \tag{2.6}$$

where m is the electron mass, ϕ the mean value of the tip and sample workfunction in eV. Using this wavefunctions in Bardeen's formalism it is found that

$$I \propto e^{-2\kappa d}. \tag{2.7}$$

This means that the change of the measured current is very high for small changes in heights at short distances, giving STM a very high sensitivity of the distance between tip and sample. Usually, as a rule of thumb, we can assume that the current changes by an order of magnitude when the tip-sample distance is changed by an Angstrom.

The tunneling effect is the basis of the STM but for the operation of the microscope it is necessary to control sub nanometric displacements which we do thanks to the existence of the piezoelectric effect. Materials that exhibit this effect allow for controlled motion through the application of voltages. For the ceramics used in the construction of our STMs deformations are of the order of some nm/V and we applied voltages differences up to 260 V [6]. The maximum scanning window is between 1 and 2 μm.

The configuration we use is a piezotube with six electrodes to which we attached the tip of our STM. Applying voltages in the different electrodes allows movement in X,Y

[6]For simplicity I would use now on the word piezo to refer to this type of materials.

and Z directions in a sub-nm scale with reproducibility.

2.2.2 Measurements with STM/STS

As explained, the tunneling current is very sensitive to the changes in the tip-sample distance, which allows to measure the electronic density over the surface of a sample. This can be done basically in two modes of operation, the constant height and the constant current modes. The former keeps the voltage applied to the Z electrode of the piezotube during the scan and reads the variations in the tunneling current as a function of the position $I_T(X,Y)$. The constant current mode – used in all measurements presented here – sets a constant value of the tunneling current and using a feedback loop with a proportional-integral (PI) control. This feedback loop controls the voltage applied to the Z electrode and records the variation of this voltage as a function of the position $V_Z(X,Y)$ (see Fig.2.5).

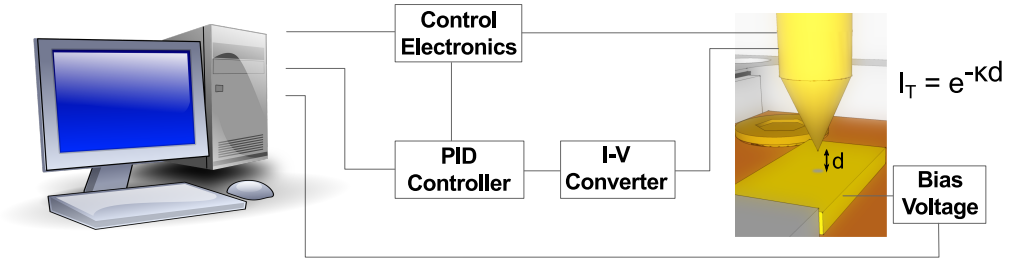

Figure 2.5: Schematic representation of the feedback loop used in the constant current method in our experimental system.

When storing the variation of the Z electrode while keeping the tunneling current constant we get a signal that is a mixture of the integrated density of states up to the applied voltage at that point (see Eq.2.4) and the distance between tip and sample (see Eq. 2.7). The largest contribution to the signal comes usually from the changes in the exponential and thus, this type of imaging is commonly refereed to as topography.

In order to perform spectroscopic measurements the tip of the microscope is moved using the control loop described above and an spectroscopic curve is measured at every point of the image. For this, the feedback loop is opened keeping the distance between tip and sample constant while the variation of the tunneling current $I_T(V_B)$ with the bias voltage is stored. An STS measurement gives therefore the tunneling current as a function of the position and the bias voltage $I_T(X,Y,V_B)$. Taking for each point the normalized conductance through a numerical derivative gives the normalized DOS at each point of the scanning window as a function of the energy, for filled and empty states.

Unless otherwise specify we normalize our spectroscopic curves to their value outside the gap, as far as possible from the quasi-particle peaks in order to use the normal state of the material as reference. In the case of spectroscopic measurements we average

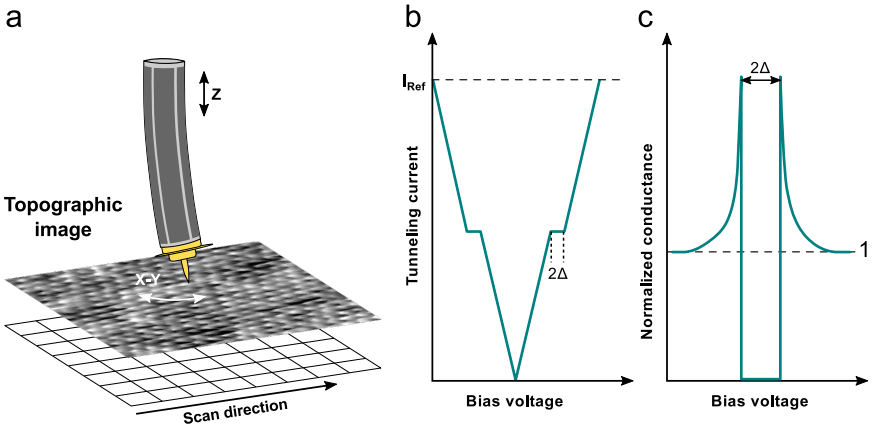

Figure 2.6: Schematic draw of how a spectroscopic measurement is done. The piezotube scans over the surface (a) and at each point (each pixel of the topography) it opens the feedback loop and performs a spectroscopic curve (b) storing the tunneling current value as the voltage is ramped down and up. To extract the normalized dos (c) we take the numerical derivative tunneling current curves and normalize it to its value above the quasi-particle peaks.

the normalization value for all curves and use the same value in all of them. The example curves presented in this chapter are all depicted in such a way.

Spectroscopic measurements can have very long acquisition times depending on the parameters used (number of points and data rate in the topographic image and number of points and data rate in the spectroscopic curves). In order to get good quality data one should reach a compromise between the available time for measuring, typically set by the time between helium transfers, the energy range in which the phenomena we are interested in manifests and spatial extension of these phenomena. Particular conditions of the measurement, electrical or mechanical noises affecting the signal or the quality of the scanning window will also influence the ultimate choice for measuring parameters. Typical spectroscopic images taken during this thesis take place overnight (10 to 14 hours) or during weekends (20 - 50 hours) in order to avoid class periods when the building has more activity. Below we provide a more detailed discussion on the reasons for needing such long acquisition times.

2.2.3 Visualizing the vortex lattice

STS is quite useful to study superconductors. Superconductivity is a low energy phenomenon, where most of the assumptions made above (energy independent tip DOS, energy independent matrix elements) usually work well. The opening of the superconducting gap provides a neat signal in the DOS to study as a function of the position. In type II superconductors, the vortex lattice gives a clear pattern of changes in the superconducting DOS as a function of the position with variations at a lengths scale of the superconducting coherence length.

The first studies of the vortex lattice using STM were performed by Hess *et al.* [1989];

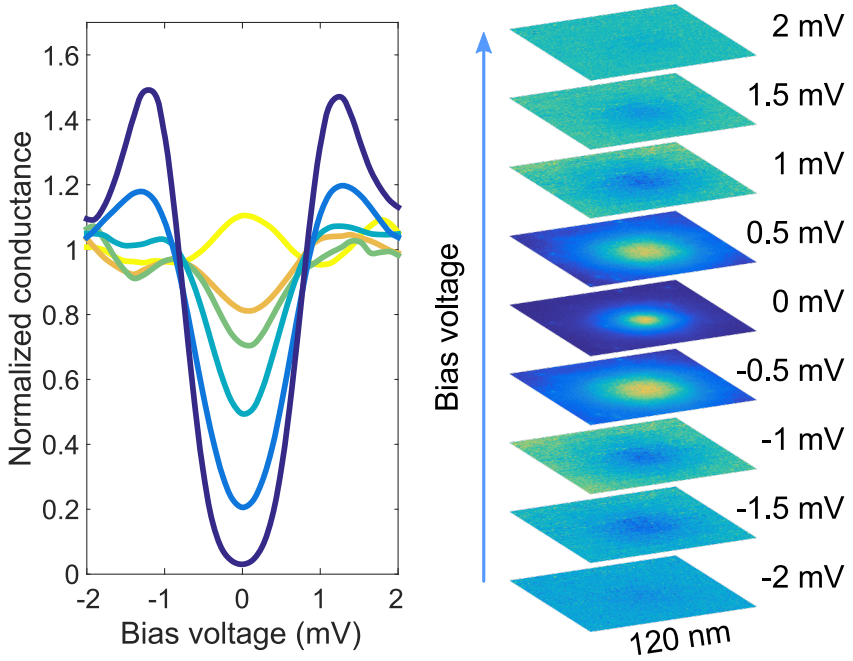

Figure 2.7: Left panel: normalized conductance curves going from the center of a vortex to outside in 2H-$NbSe_{1.8}S_{0.2}$. Right panel: conductance maps of the vortex taken at different bias voltages. Color code of the curves in the left panel corresponds to the $0\,mV$ map. Measurements were done at $0.05\,T$ and at $800\,mK$.

Hess, Robinson, and Waszczak [1990]. In those works they image the vortex lattice in $NbSe_2$ and study the variation of the DOS inside the vortex core, finding a peak at the center of the vortex core (see chapter 1). Fig.2.7 shows how vortices are visualized using STM. Curves in the left panel show typical conductance curves measured from the vortex core (yellow) to away from the vortex (dark blue). Taking for each voltage the contrast given by these curves we can assemble the conductance maps in the right panel.

The work of Hess *et al.* was the first of many that used STM to visualize the superconducting vortex lattice. Due to its resolution and the possibility to perform simultaneous topographic and spectroscopic maps makes STM is nowadays a fundamental tool in the study of vortex physics.

2.2.4 Quasi-particle interference

Electronic states in the conduction band of a metal are described by Bloch functions $\psi_{\vec{k}}(\vec{r},\epsilon)$. .The local density of states ($LDOS$) is related to the momentum eigenstates through

$$LDOS(E,\vec{r}) \propto \sum_{\vec{k}} |\Psi(\vec{r_k})|^2 \delta(E-\epsilon(\vec{k})). \tag{2.8}$$

In which can be seen that introducing Bloch states does not produce any observable

spatial modulation with wavevector $\vec{k}$. However, in the presence of impurities, point defects or anything else that disrupts the periodicity of the crystal lattice, electrons are scattered and produce oscillating patterns on the surface [7]. Sometimes, as for instance in between well defined steps, these patterns resemble one dimensional standing waves on water [Crommie, Lutz, and Eigler, 1993; Hasegawa and Avouris, 1993]. Detail theoretical calculation of this effect was done by Capriotti, Scalapino, and Sedgewick [2003], for the present explanation I will stick to the more qualitative treatment given by Hoffman [2011].

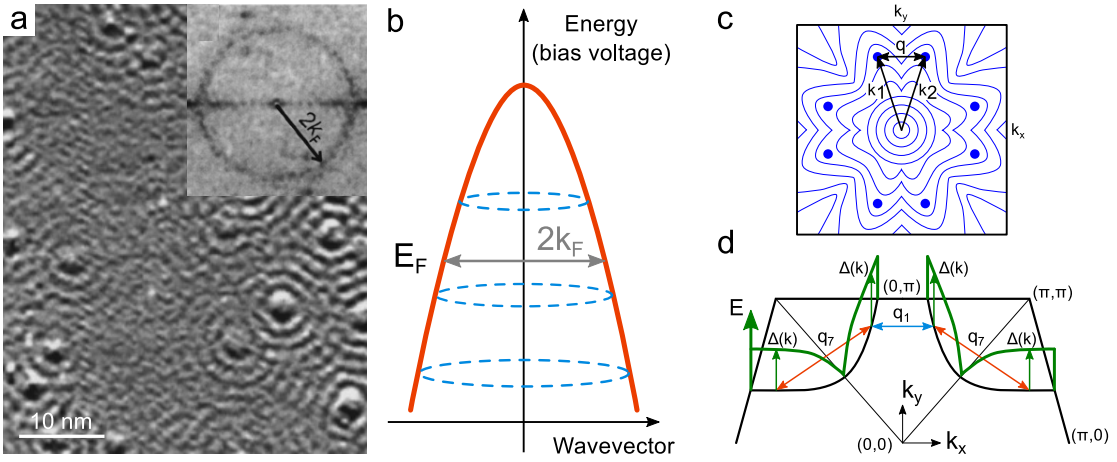

Figure 2.8: a) Adapted from Petersen *et al.* [1998]. Constant current STM image taken in Cu(111) at $150\,mK$ with $V = -5\,mV$. A complex patter of standing waves emerging from point defects. Inset: 2D-FFT indicating the main scattering vector extracted form the oscillation in real space. b) Schematics of how the dispersion relation of Cu(111) can be reconstructed form the scattering vectors found in STM images at different bias voltages. c) Adapted from Hoffman [2011]. Schematic Brillouin zone indicating the scattering between parts of the Fermi surface with large JDOS, the so called *hotspots*. d) Adapted from Hoffman [2003]. Schematic draw of the variation of the order parameter in the reciprocal space highlighting scattering vectors between hotspots.

When scattering between electronic states with the same energy is produced in such a way that it mixes states with $\vec{k_1}$ and $\vec{k_2}$, the result is a standing wave with a wavevector $\vec{q} = (\vec{k_2} - \vec{k_1})$. Having into account Eq.2.8, this wavevector will produce a modulation with $\vec{q}$ in the $LDOS$ that can be observed in the differential tunneling conductance (dI/dV). This can be understood through the Fermi golden rule,

$$w(i \to f) \propto \frac{2\pi}{\hbar} |V(\vec{q})|^2 \, N_i(E_i, \vec{k_i}) \, N_f(E_f, \vec{k_f}), \tag{2.9}$$

where for elastic scattering, $E_i = E_f$. $\vec{q} = \vec{k_f} - \vec{k_i}$ is the scattering vector, $V(\vec{q})$ the scattering potential and N_i and N_f the initial and final densities of states. From Eq.2.9 one imagines that a high signal will appear for scattering vectors connecting states with large joint DOS ($JDOS$). Large $JDOS$ will be found for $\vec{q}$ connecting parallel regions

[7] for the particular case of standing waves at the Fermi level they are called Friedel oscillations

of the bandstructure (see Fig.2.8.b) or from large flat regions in the k-space that have a large DOS – given that $DOS(E) \propto 1/|\nabla_k(E))|$. These points of flat k-space areas are commonly called *hotspots* (see Fig.2.8.b-c). Finally, $V(\vec{q})$ would account for any contribution coming from the scattering process itself like, for instance, spatial anisotropies of defects [Hirschfeld *et al.*, 2015].

In superconductors, states above the gap are Bogoliubov quasiparticles with a dispersion relation:

$$E_{\pm}(\vec{k}) = \pm\sqrt{\epsilon(\vec{k})^2 + \Delta_{\vec{k}}^2}, \tag{2.10}$$

where Δ is the superconducting gap measured from the normal state Fermi level. The scattering of quasiparticles also result in modulations in the differential conductance. The same Fermi golden rule explanation is valid for superconductors introducing the effect of coherence factors,

$$w(i \to f) \propto \frac{2\pi}{\hbar} |u_{k_i} u^*_{k_i} \pm v_{k_f} v^*_{k_f}|^2 \, |V(\vec{q})|^2 \, N_i(E_i, \vec{k_i}) \, N_f(E_f, \vec{k_f}). \tag{2.11}$$

where the plus sign is for magnetic scatterers, the minus sign is for non-magnetic scatterers, and $|u_k|^2$ and $|v_k|^2$ are the probabilities that a pair of states with wavevectors $\pm\vec{k}$ is empty or filled, respectively [Tinkham, 1996]. Therefore, in a superconductor, a large $JDOS$ will result in large quasi-particle interference (QPI) signal only when the additional constraint is satisfied that the coherence factor is non-zero. However, we should bear in mind that there is no simple separation between effect related to coherence factors and to the joint density of states.

A periodic modulation in real space will result in an enhancement of the spectral weight for the corresponding $\vec{k}$ in the reciprocal space. Thus, having a set of conductance maps at different energies makes possible to track these scattering vectors as a function of energy. Identifying the different parts of the Fermi surface involved in the scattering process will allow to extract a dispersion relation using STM as shown in the schematic draw in Fig.2.8.b. The only requirement is the existence of a certain number of scattering centers in our material.

The quasi-particle interference signal has a complex dependence on the sources of disorder, impurity potentials, and $\vec{k}$ dependence of the tunneling matrix elements which are unknown. All this makes difficult to came with a reliable quantitative theory. However, positions of the scattering vectors $\vec{q}$ do not depend on these effects and are related only to the electronic structure, including the superconducting gap function. It is therefore possible to explore the bandstructure through the energy dependence of the scattering vectors through STM measurements. Furthermore, STM is capable to scan on both filled and empty electronic states in the material in a wide energy range which gives it advantage over other techniques that, like ARPES, can only access filled states.

STM resolution of the reciprocal space image $\Delta(q)$ is given by the size of the real

space image L and its size q is given by the real space resolution $\Delta(L)$:

$$\Delta(q) = \frac{1}{L} \quad , \quad q = \frac{1}{\Delta(L)}. \tag{2.12}$$

In order to be able to see all possible scattering vectors the size of the Fourier transform should be at least twice that of the 1^{st} Brillouin zone. This implies, in la square lattice, $q \approx 2/a \Rightarrow \Delta(L) < a/2$, with a the lattice parameter. On the other hand we need a suitable k-space resolution. To distinguish a $1\,\%$ of the Brillouin zone the size of the real space image should be $\Delta(q) = 0.01/a \Rightarrow L = 100\,a$.

In FeBSC the lattice parameter is typically $a \approx 0.4\,nm$ which implies a first Brillouin zone of $2.5\,nm^{-1}$. Our QPI measurements should therefore have a resolution higher than $2\,\text{Å}/pixel$ in the real space with a lateral size larger than $40\,nm$ in order to be able to see all scattering vectors in the first Brillouin zone with a resolution of a $1\,\%$ of the Brilloun zone.

Real experiments are time limited and care should be taken to find a suitable scanning window and set the adequate measurement parameters for topographic and energy resolution. In our case, we are limited by the time between helium transfers which is typically of 2 or 3 days for this system. Our QPI measurements last usually between 30 and 50 hours.

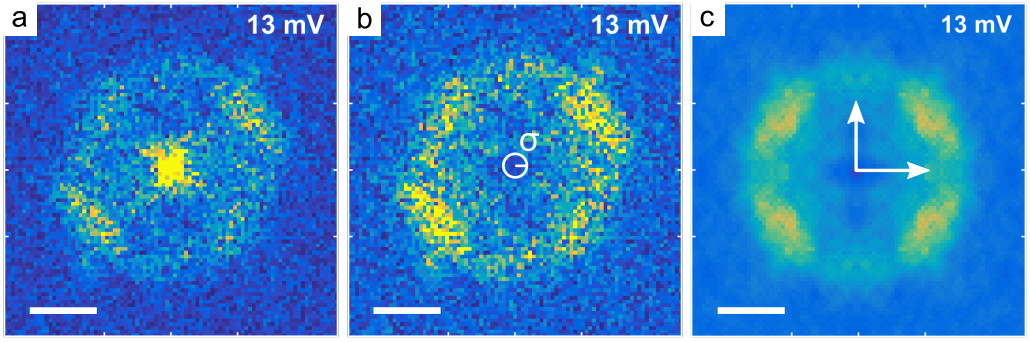

Figure 2.9: a) Example of a 2D-FFT from a conductance map taken with STM. b) Conductance map in (a) after removing the central part of the image multiplying by a Gaussian of width σ. c) Same conductance map after symmetrizing the data with respect to the high symmetry axis of the Fermi surface and applying a standard Gaussian filter.

With the aim of reduce the noise and enhance the QPI signal in the 2D-FFT, we perform some treatment to the data. We first remove the central part of the 2D-FFT, corresponding to the larger wavelength vectors, using a normalized Gaussian with a σ a few pixels (Fig.2.9.a). The central point corresponds to the average value of the conductance and it is of no use for the analysis of the scattering vectors. Any possible information regarding the bandstructure hidden in the large wavelength vectors will be very difficult to extract due to the influence of the central peak. We then symmetrize our data following the symmetry axis of the Fermi surface (Fig.2.9.b). By doing so we enhance the actual scattering signal over the background noise in the 2D-FFT. Finally

we apply a standard Gaussian filter to the image before we extract the values of the scattering vectors (Fig.2.9.c).

To perform data treatment and analysis we have implemented a series of functions and a graphical user interface (GUI) in Matlab that allows for simultaneous visualization of the spectroscopic maps and their 2D-FFT. All post acquisition processes are done using this program. Details of the code will be given elsewhere.

2.3 STM in dilution refrigerator and with high magnetic fields

2.3.1 Setup and modifications in the dilution refrigerator

For this thesis the equipment used was a MX400 dilution refrigerator from Oxford Instruments with a $10\,T$ superconducting magnet. The gas handling system is also from the same company.

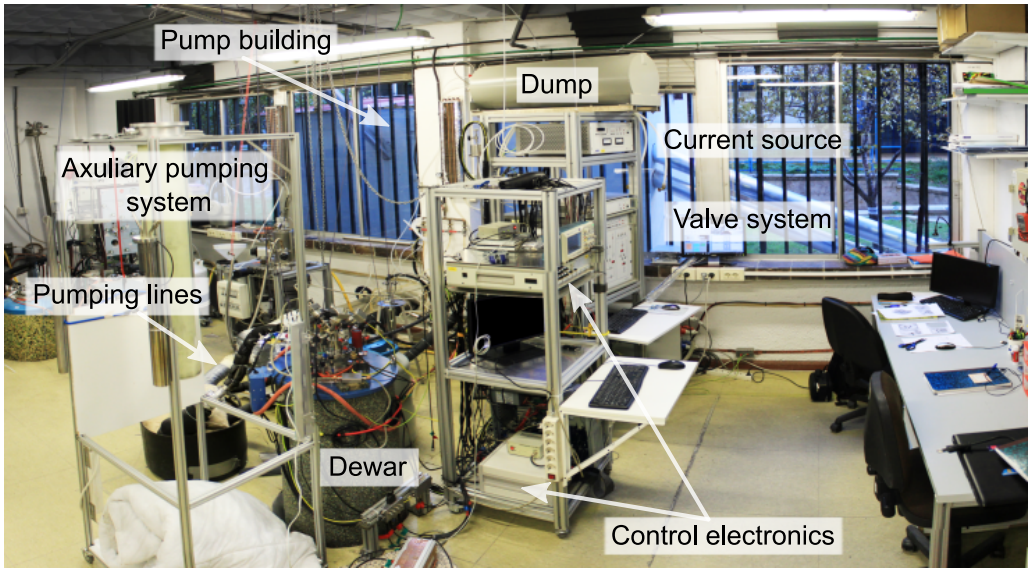

Figure 2.10: Photograph of the experimental system in the laboratory. Different parts are indicated in the figure

Mechanical isolation is a fundamental issue in all microscopy facilities. At the beginning of this project we decided to address this problem trying to reduce vibrations. The previous isolation system was removed and to avoid vibrations as much as possible we suspend the cryostat from a beam in the ceiling of the laboratory using climbing ropes and shock absorbers as can be seen in the photograph of Fig.2.10. The shock absorbers work for frequencies above 8 and $10\,Hz$. The performance of this system is remarkably efficient and can be compared to other more sophisticated methods.

All pumps used during the operation of the system are located in a separate building outside the lab (check Fig.2.10) in order to reduce mechanical noise sources and the incoming tubes have been covered with isolating material and introduced into a sand box in order to damp vibrations. We have also modified some of the pumping lines adding more flexible pipes that reduce induced vibrations in the Dewar and have less effect in the performance of the isolation system.

Also, in order to improve the performance of the isolation system the Dewar was replaced for a new one which is lighter and has the center of mass in a lower position, making more efficient the damping produced by the ropes. This also has reduced the Helium consumption (see figure 2.11) which dropped a around a 9% (from 0.47 m^3/h to 0.42 m^3/h), increasing the work time between transfers. In a practical sense it meant to transfer every three days instead of every two.

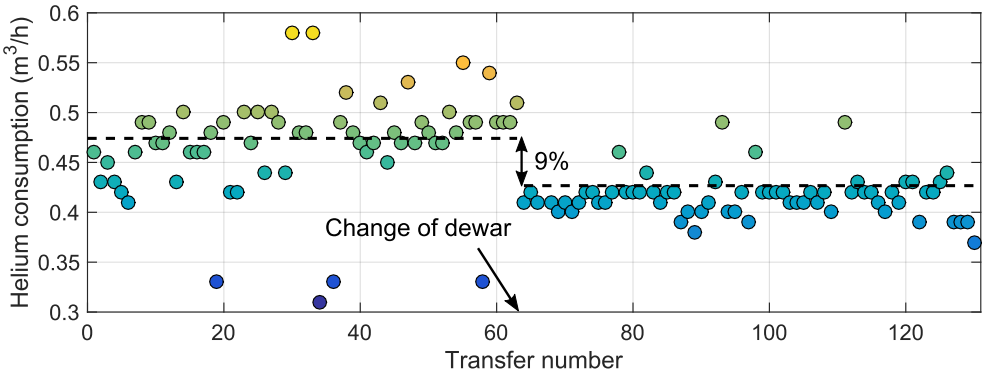

Figure 2.11: Helium consumption in operation as a function of the transfer number. Black lines represent the mean consumption. Cooling down points were removed from the plot. Note how average consumption drops around a 9% after the change of Dewar.

Finally, I would like to mention that we have considerably modified the gas handling system of the dilution unit. Due to a leak, we dismounted the whole system and substituted a few valves inside. The construction of the gas handling system, based on a set of valves mounted on a single aluminum block, is not adequate for leak testing and can provide considerable problems when a joint leaks. Present gas handling systems of the company are made using a different technology. I worked to repair the leak by adding one valve outside the gas handling system. Furthermore, I found and repaired a leak in the ^{3}He pump.

2.3.2 Setup and modifications in the microscope

The STM used during this thesis, as all the microscopes used in the low temperature laboratory of the *Univerisdad Autónoma de Madrid*, is a home-made design and was built in the university workshop (SEGAINVEX). Details of the design can be found in Suderow, Guillamón, and Vieira [2011]. Fig.2.12 shows a schematic picture of the microscope where the main parts are indicated: the main body (1), the a slider (2) to

which the piezotube (3) is attached and the base (4) of the structure with a track where the sample-holder (5) can slide.

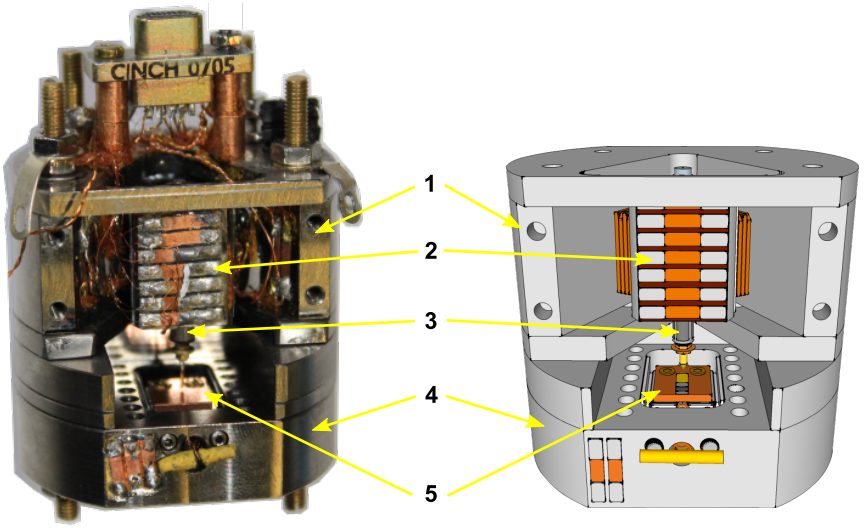

Figure 2.12: Photograph of the microscope together with a schematic draw indicating its main parts. 1. Main body, 2. vertical slider, 3. piezotube, 4. base and 5. sampleholder.

This design allows three different movements; the vertical displacement of the slider, the 3D movement of the piezotube and the horizontal movement of the sample-holder, each of them controlled in a different way.

For the vertical displacement we use stacks of piezo shears. The slider is held horizontally to the stacks thanks to a Copper-Berilium spring and it is moved using a fast sawtooth signal applied to the stacks. In between the slider and the stacks we place alumina pieces in order to allow sliding (Fig. 2.13). With this system displacements of several mm are possible overcoming the height differences between different samples. I will refer to this movement as Z'. The piezotube, as mentioned above, has six electrodes, two for each of the Cartesian axes. In this configuration we can scan windows of up to $1.8\,\mu m \times 1.8\,\mu m$ with height differences of around $150\,nm$. Finally the sample holder can move along the track in the microscope base. This motion, as illustrated in the scheme of Fig.2.13, is mechanically controlled from outside thanks to a piano cord that is attached to it with a small rope and goes all the way up to a micro-metric screw set in the top of the cryostat. Thus, we can move the sample holder with no noticeable change in the temperature of the experiment.

The horizontal displacement of the sample-holder allows us to change the scanning window in the same sample or even change between different samples in a controlled way. If a sample made of the tip material is placed in the sample-holder, there is also the possibility to clean the tip through a controlled nanoindentation process described by Rodrigo *et al.* [2004] that leads to atomically sharp tips (see right panel in Fig.2.14). The method is based on the controlled achieving of single atom point contacts, whose conductance is given by the quantum of conductance G_0 in Au. In the tunneling limit,

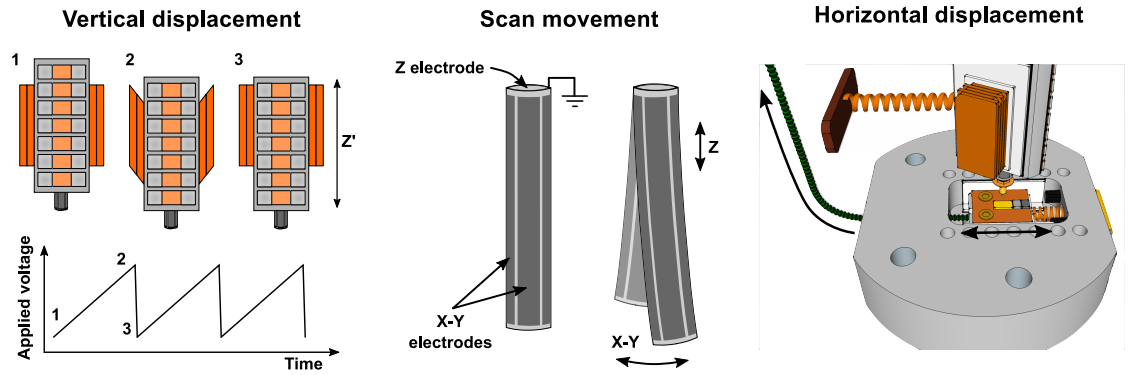

Figure 2.13: Cartoon pictures of the three types of movements in the microscope. Vertical displacement of the slider (Z') showing the corresponding saw-like voltage signal applied to the piezo stacks. 3D Movement of the piezotube which works during the scanning processes and horizontal displacement of the sample-holder with the piano cord.

we can extract the workfunction of Au. This method can be also used to extract the workfunction of the material we are tunneling into. Inset in the left panel of Fig.2.14 shows the fit to the gold workfunction for the gold-gold junction. Same figure also shows a scheme of the different steps in the indentation process.

The versatile design of the STM let us include different modifications required by some particular experiment. For example, if you want to cleave your sample *in situ* there are different options that can be used, and depending on the particular characteristics of the sample some might be more adequate than others. At the beginning of my thesis I set up the cleaving method shown in Fig.2.15 that I used repeatedly to get large and flat surfaces in cryogenic ultra high vacuum conditions.

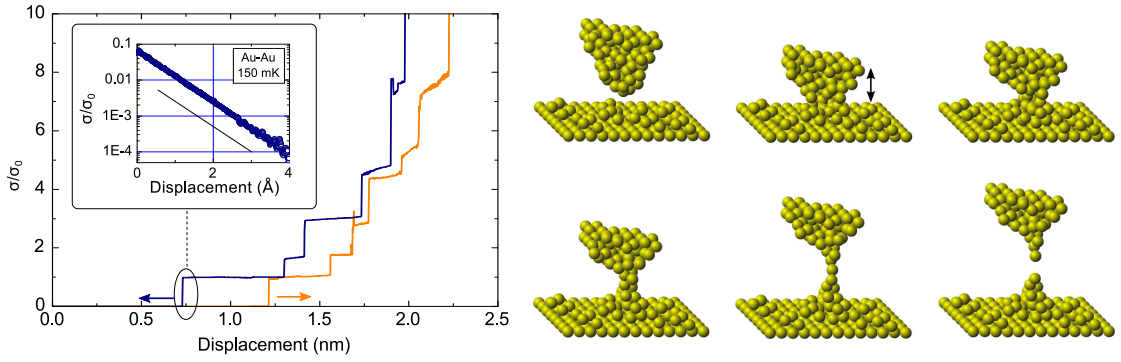

Figure 2.14: From Guillamón [2009]. Left panel: Current as a function of the distance between tip and sample. Inset: exponential fit to the last current step showing the gold workfunction. Right panel: Cartoon of the nanoindentation process.

This method, described in Fente *et al.* [2014], is suitable for crystalline samples that cleave easily, in particular samples that can be peeled out. It works as follows: sample (1) is mounted in the sample-holder with a brass piece (2) stacked at the top of it and a

copper beam (3) is placed across the sample-holder track in such a way that everything but the brass piece can slide below the beam. Once at low temperature, where cryogenic ultra high vacuum conditions are reached, the sample-holder is moved backwards using the piano cord (horizontal movement in Fig.2.13) and the sample breaks. The result is a clean and fresh surface that remains in the sampleholder while some part, that is still stuck to the brass piece that goes to the bottom of the vacuum chamber.

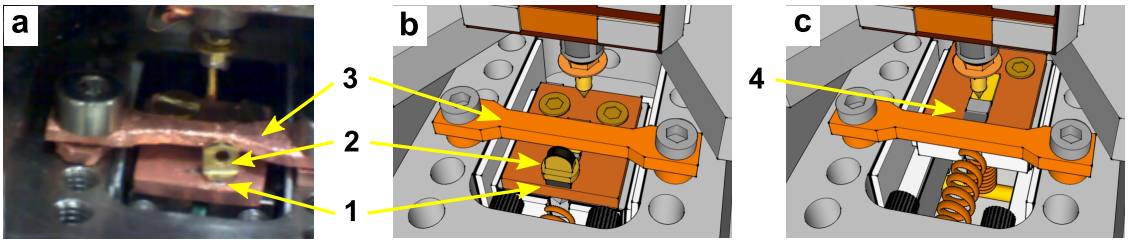

Figure 2.15: Representation of the cleaving system used during this work. (a) Photograph of the microscope with the cleaving setup before the cleaving takes place. (b) Schematic representation of the system indicating the different parts (see text for the identification). (c) Schematic view of the system after the cleaving.

As said, this method was developed during this thesis and used repeatedly with remarkably good results. It might happen that the loose part stays in the sampleholder track blocking its movement. In order to rule this out some weight can be attached to the brass piece using a cord, making it fall to the lower part of the vacuum chamber.

2.4 Growth of high quality single crystalline samples

Single crystals provide a unique opportunity to study the properties of a particular material. In polycrystalline samples, properties like anisotropy can be hidden by the effect of the different crystal domains. In single crystalline samples do not have such a problem.

Solution growth is a very powerful method to grow single crystals that allows for the synthesis of both congruently and not congruently melted materials [Fisk and Remeika, 1989; Canfield and Fisk, 1992; Canfield and Fisher, 2001; Canfield, 2010]. Elements participating in the growth are placed together with an adequate solvent into an alumina crucible and sealed in an inert atmosphere, often Ar of He gas. Temperature is increased and kept at a high value until all elements are melted into a uniform liquid. Then the mixture is slowly cooled and as the temperature reaches the liquid line, crystals of the desired composition start to nucleate. As the temperature is further decreased, crystals grow bigger and composition of the liquid changes accordingly. Crystals can be separated from the remaining liquid by a centrifuge process at the decanting temperature. The solvent used can be either an element not present in the desired compound (non-self-flux) or an element of the compound (self-flux). It is usually preferable to use self-flux if possible, in order to avoid possible external elements in

the crystal. However, this is not always possible due to the technical requirements of the process.

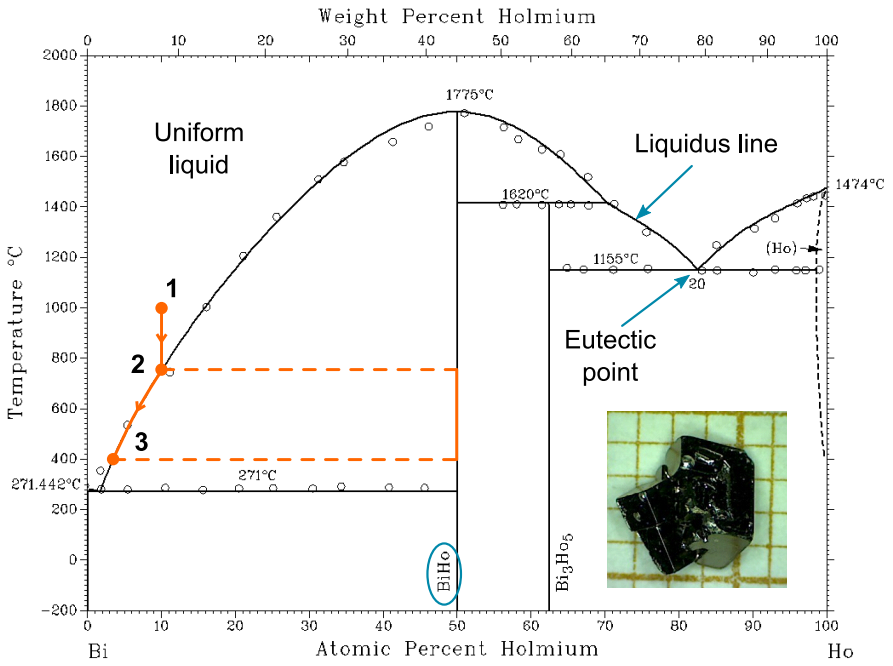

Figure 2.16: Bi-Ho phase diagram adapted from Okamoto [1994] indicating the growth made in Fente *et al.* [2013] as an example of binary solution growth. Inset: picture of one of the grown crystals over a *mm* scale.

Fig.2.16 shows an example of a binary phase diagram to exemplify solution growth method. BiHo is a congruently melted compound with a high melting temperature – in terms of the typical temperatures reached by furnaces at the laboratory. Solution method allows to grow it at a 10 % Ho concentration since at this concentration the mixture of Bi and Ho remains liquid for much lower temperatures. Following the procedure described above, components are mixed in the mentioned proportions, sealed inside a silica ampoule and heated using a resistive furnace up to 1000°C where they form an homogeneous liquid (1). The mixture is then slowly cooled and as it touches the liquid line, crystals of BiHo start to nucleate (2). Further cooling increase the size of the nucleated crystals and changes the remaining liquid concentration accordingly. Before all the mixture solidifies the single crystals are separated from the remaining liquid using a centrifuge (3). Inset of Fig.2.16 shows one of the obtained crystals from this growth.

2.4.1 Growth of 122 pnictides in Ames laboratory

All iron pnictides measured here were grown using solution growth method. During my master and the first years of my thesis I have participated in a number of growths

using solution method, mostly binary or ternary magnetic and superconducting compounds [see Pérez-Castañeda *et al.*, 2013; Fente *et al.*, 2013; Luccas *et al.*, 2015; Herrera *et al.*, 2015; Barrena, 2016], that were grown in our laboratory in Madrid. For the materials I present results here, some more sophisticated equipment is needed in order to perform intermediate growth steps and deal with the toxicity of As, so all of them were grown at the Ames laboratory (IA, USA) in the group of Prof. Canfield. I was involved in the growth of $Ca(Fe_{1-x}Co_x)_2As_2$ which was done during my three-month stay in Prof. Canfield laboratory in the summer of 2012.

First samples $CaFe_2As_2$ were grow using Sn as flux [Ni *et al.*, 2008b; Ronning *et al.*, 2008] as used for $BaFe_2As_2$ crystals. In those those growths, transition metal substituted samples showed little reproducibility in the physical properties due to issues of solubility of cobalt in tin. Soon, an alternative growth method using self-FeAs flux was developed [Sefat *et al.*, 2008; Wu *et al.*, 2008], resulting in larger size crystals and reproducible results in the phase diagram since this method allows for homogeneous substitution onto the Fe site for transition metals. The samples used in this work were grown from excess FeAs.

The use of FeAs as a flux requires a two step process. First FeAs and CoAs (or the equivalent using another transition metal) are synthesized by a hybrid vapor phase / solid state reaction method. Then, $Ca(Fe_{1-x}Co_x)_2As_2$ is synthesized by solution growth mixing Ca, FeAs powder and CoAs powder in the ratio Ca:FeAs:CoAs = $1 : 4(1-x) : 4x$, where x is the nominal concentration of Co. All mixing processes should be carried out in a glove box filled with a non reacting gas, in order to avoid oxidation and problems due to the toxicity of As. In contrast to what is found in Sn grown samples, using self flux there is little variation between nominal and real concentrations in the case of Co doping, as shown by wavelength-dispersive x-ray spectroscopy (WSD) analysis [see Ran, 2014, chapter 6]. This demonstrates the relative homogeneity of the samples grown from self flux.

Materials are sealed into a quartz ampoule under 1/3 atmosphere of argon gas and then heated up to 600°C in 3 hours. In order to allow remaining As to react, temperature is kept at 600°C for an hour. Temperature is then raised to 1180°C at 100°C/hour and kept at 1180°C for 3 hours in order to get a homogeneous liquid. The melt is then cooled from 1180°C to 1020°C in 3 h and slowly cooled from 1020°C to 960°C over 40 h to allow nucleation. After this time the growth is decanted using a centrifuge. For more detailed explanation of the growth and the intermediate step see Ran *et al.* [2011]; Ran [2014].

2.4.2 Growth of $LaRu_2P_2$ at the LBTUAM

As said, the growth facilities we have in the low temperature laboratory in Madrid are not suitable for growths containing As. There are, however, interesting compounds that can be grown like ruthenium phosphides. Known for a long time already, those materials regain some interest lately due to their similarities in crystalline structure with FeBSC [Mizusaki *et al.*, 2009]. $LaRu_2P_2$ has the same crystal structure as the AFe_2As_2

family and it has been known to be superconductor with a $T_c \approx 4\,K$ for almost 30 years [Jeitschko, Glaum, and Boonk, 1987]. Recent transport and magnetization experiments in this compound show isotropic superconductivity and low vortex pining [Ying *et al.*, 2010] and enhancement of T_c under pressure [Li *et al.*, 2016]. Studying this compound in comparison with iron based materials may reveal insight in the intrinsic high critical temperature of iron-based superconductors. We planned to investigate this sample through scanning tunneling microscopy during this thesis but in the end it was not possible to do so. This is now part of the new student's project and measurements are in process.

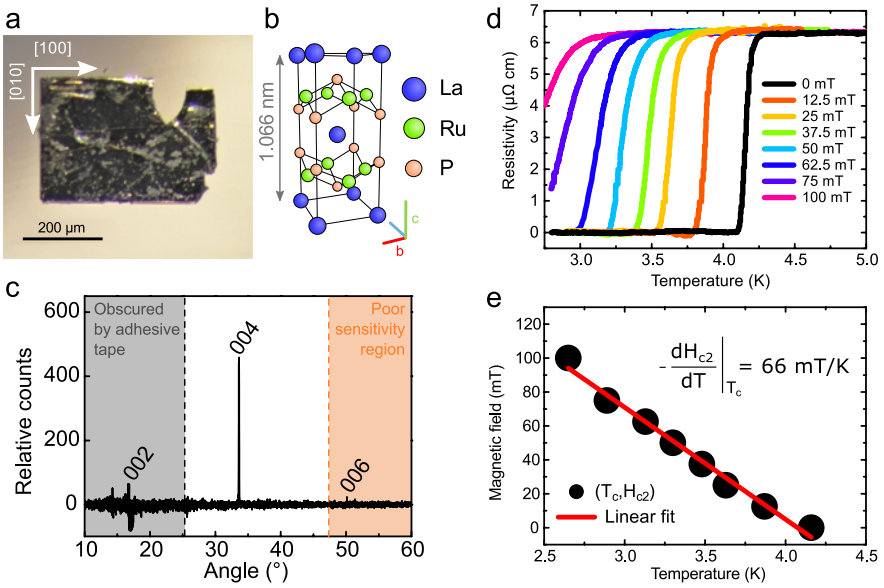

Figure 2.17: Adapted from Barrena [2016]. a) Picture of the crystals obtained from the growth described in the text. b) Scheme of the tetragonal $ThCr_2Si_2$-type (I4/mmm space group) crystalline structure. c) X-ray diffraction pattern showing a clear (004) peak. d) Transport measurements as a function of the field showing results consistent with those found in Ying *et al.* [2010]. e) Plot of the critical field H_{c2} as a function of temperature.

We have synthesized $LaRu_2P_2$ using Sn flux. La, Ru, P and Sn were mixed an put into an alumina crucible with the ratio La:Ru:P:Sn = 1 : 2 : 2 : 15, sealed into a silica ampoule under $1\,mbar$ of He gas. Components were then heated up to 1200°C and kept there for 24 h in order to get a uniform liquid. Temperature was then slowly decreased to 750°C in 12 days and decanted and centrifuged at this temperature. In order to remove the excess Sn flux a HCl solution (HCl Sigma-Aldrich, 37 %) was used.

Single crystals with sizes of $0.5\,nm \times 0.1\,nm \times 0.02\,nm$ with metallic-like surfaces were obtained (see Fig.2.17.a). In order to check the crystal structure and macroscopic properties of the samples we performed x-ray analysis, magnetization and transport measurements. Results of this study are summarized in Fig.2.17. X-ray pattern is similar to the one seen in previous reports by Jeitschko, Glaum, and Boonk [1987]; Li *et al.* [2016] with a pronounced (004) peak giving a unit cell height of $c \approx 1.066\,nm$. Resistivity measurements in Fig.2.17.d show a Residual Resistance Ratio (RRR) of ≈ 20 with

a clear superconducting transition at $4.16\,K$ for zero field. Applying field perpendicular to the basal plane results in a gradual reduction of T_c. From the measurements the critical field extracted is $H_{c2} \approx 190\,mT$, consistent with the values found in [Ying *et al.*, 2010].

2.5 Cleaving and reconstruction of FeBSC

Within the materials known as iron pnictides, there is a number of different families depending on the crystallographic structure. Most studied materials are the ones displayed in figure 1.16. All are formed by characteristic Fe-As planes in tetrahedral coordination with intecalation of different layers of other species, depending on the particular family. In all cases they have layered structure which allows to get atomically flat surfaces with mechanical cleaving processes such as the one described above. This makes iron pnictides suitable materials for the surface sensitive probes like STM.

Cleaving planes and surfaces are of relevance for this kind of experiments and identification of such surfaces is no trivial task. A large effort has been concentrated in trying to understand the patterns observed by STM at the surface of pnictides [see Hoffman, 2011, and references therein]. Here I will recall some of the characteristic surfaces seen in the $A\mathrm{Fe_2As_2}$ compounds using STM.

Given the structure of these materials it is highly unlikely that cleaving will occur breaking the bonds between Fe and As atoms. Furthermore, to the best of our knowledge, no experimental evidence was found suggesting exposed Fe-Fe surfaces. There is, however, no agreement in the cleaving plane. Some STM groups interpret their data to be the A layer, while others believe their are imaging As planes. A careful review of this controversy was done by Hoffman [2011].

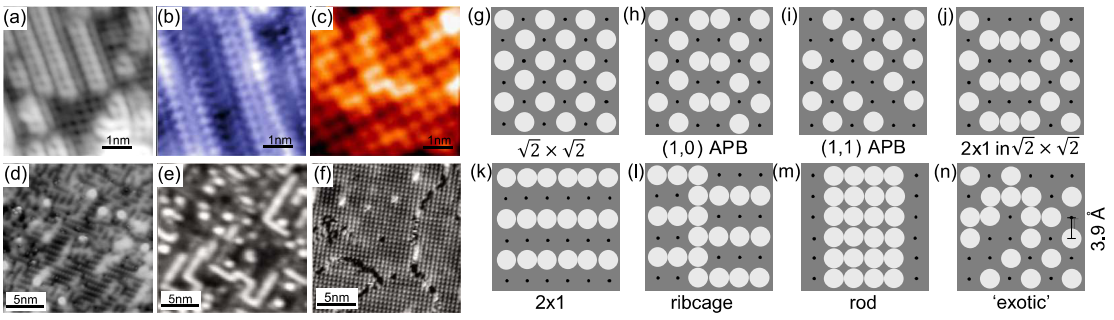

Figure 2.18: Adapted from Hoffman [2011]. (a-f) Various topographic images of cleaved 122 surfaces, presumed to be Ba/Sr-terminated from Boyer *et al.* [2008] (a), Yin *et al.* [2009] (b), Zhang *et al.* [2010] (c), Hsieh *et al.* [2008] (d) and Massee *et al.* [2009b] (g-n). Schematic representation of possible Ba surface reconstructions. Large (small) circles indicate the presence (absence) of a Ba atom [Massee *et al.*, 2009b].

First principle calculations made by Gao *et al.* [2010] on $A122$ (being A = Ba, Sr,

Ca) systems reported energetically favorable surfaces cleaving within the A plane or in between A and As planes due to the strong bonds existing between Fe and As. Same work provides calculation of the energies associated with the $\sqrt{2} \times \sqrt{2}$ and 2×1 reconstructions in both Ca122 and Ba122 finding the $\sqrt{2} \times \sqrt{2}$ to have less energy in the case of Ba122 and 2×1 being more likely in the case of the Ca122. Same surface reconstruction is found for the two compounds to be favorable in the orthorhombic and the tetragonal structure. Experiments done by Boyer *et al.* [2008]; Yin *et al.* [2009]; Hsieh *et al.* [2008]; Massee *et al.* [2009b]; Zhang *et al.* [2010] on $A122$ materials with different doping support this hypothesis. Boyer *et al.* [2008] even report for $SrFe_2As_2$ images of 2×1 reconstruction coexisting with an atomic lattice with $a \approx 0.4\,nm$ lying $0.2\,nm$ below with a lateral shift of half a unit cell with the reconstruction (Fig.2.18.a), which would be expected from a As lattice below a Sr reconstruction. Massee and coworkers performed an extensive study combining LEED and STM measurements on $Ba(Fe_{1-x}Co_x)_2As_2$, $BaFe_2(As_{1-x}P_x)_2$ and $Ca(Fe_{1-x}Co_x)_2As_2$ [Massee, 2011; Massee *et al.*, 2009b]. They characterize a number of surface reconstructions for the doped Ba compounds that vary with cleaving temperature and thermal cycling confirming the cleaving plane to be the A plane (see Fig.2.18.g-n). Surfaces of Ca122, however, display only 2×1 reconstruction. Evidence for the metastable character of the reconstruction suggested by Gao *et al.* [2010] also agrees with the results of Boyer *et al.* [2008]; Yin *et al.* [2009]; Hsieh *et al.* [2008]; Massee *et al.* [2009b]; Zhang *et al.* [2010] regarding cleaving temperatures, thermal cycling and coverage percentage. Other experimental evidence suggesting A terminated surfaces coming from results in ARPES [Hsieh *et al.*, 2008; van Heumen *et al.*, 2011], photoemission [de Jong *et al.*, 2009] and LEED [van Heumen *et al.*, 2011] reinforce the hypothesis of Gao *et al.* [2010]

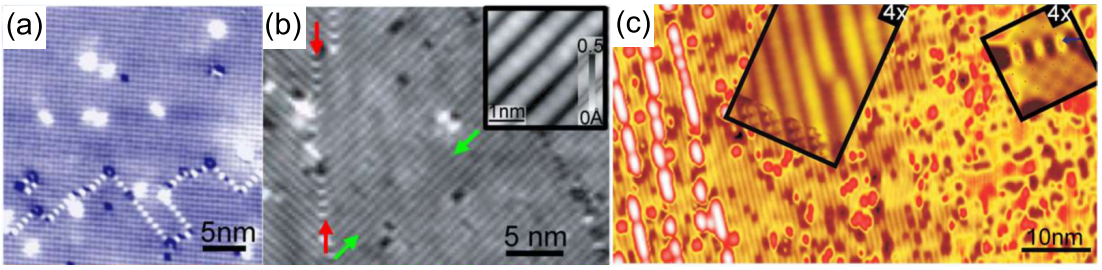

Figure 2.19: Adapted from Hoffman [2011]. Topographic images of cleaved 122 surfaces, presumed to be As-terminated from Li *et al.* [2012] (a), Chuang *et al.* [2010] (b) and Niestemski *et al.* [2009] (c).

On the other side, some groups claim to have As terminated surfaces. They have also found $\sqrt{2} \times \sqrt{2}$ and 2×1 structures, which are unlikely in an As surface but were explained arguing that half of the atoms were invisible due to the structural reconstruction [Nascimento *et al.*, 2009] or to different spin environments [Li *et al.*, 2012]. Niestemski *et al.* [2009] showed a reconstructed surface where the expected amount of atoms for a full lattice are seen (Fig.2.19.c), what together with the lack of steps to an underlying lattice (like the one found by Boyer) lead them to conclude they were imaging the As lattice [Niestemski *et al.*, 2009] with half of the atoms not visible due to the imaging conditions. LEED experiments by Nascimento *et al.* [2009] and calculation of

the Pendry factors (which gives a measurement or reliability of structural fits) conclude also in favor to the As layer.

At this point, considering all the experimental results we believe more likely that A122 materials cleave on the A plane leaving half of the atoms in each plane. All experiments in favor of As cleaving have shown surface reconstructions that can be easily explained in a 1/2 A cleaving. This argument is reinforced by the fact that full atomic As lattice with no missing atoms is imaged in compounds like $LaFeAsO_{1-x}F_x$ where it is unambiguously identified [Zhou *et al.*, 2011].

In summary, all suggest that the 2×1 reconstruction showing rows of Ca atoms is the most likely to appear in Ca122, which is the material we are interested in. The difference in free energy for other possibilities is, in any case, small. As long as the sample is cleaved at low temperatures and the temperature is kept below $4\,K$, the most likely situation is the appearance of stripes due to the Ca atoms. However, as these stripes can be along two degenerate orientations of the crystalline lattice, their orientation is random and contains domains. These domains appear during the cleaving process and remain quenched at low temperatures.

CHAPTER 3

Determining the size of the vortex core with STM

3.1 The problem of the vortex core

The spatial distribution of the quasiparticles density of states (DOS) within the vortex lattice (VL) is intimately related to the spatial distribution of the order parameter. The latter is governed by the coherence length ξ which provides the smallest length scale over which we can find spatial variations in the order parameter.

As seen in chapter 1, coherence length was first introduced as a parameter in the Ginzburg - Landau (GL) theory where it sets the characteristic distance in which superconducting properties vary in the superconducting state. This means that, among other things, coherence length governs the changes in the order parameter present in superconducting vortices. In the literature, there is however no commonly accepted definition for the size of the vortex core. The problem of determining the vortex core is important due to its intimate relation with the spatial variation of the superconducting properties. A recent example where the vortex core size is of relevance are studies made by Putzke *et al.* [2014] in FeBSC which suggest that, near the quantum critical point where magnetic order disappears, there might be strong changes in the superconducting condensation energy. They propose that these changes might show up in an enhancement of the vortex core size. The vortex core size is also relevant, for instance, to understand vortex pinning and multiband superconductivity.

Scanning tunneling microscopy (STM) has the advantage of directly probing the spatial distribution of the quasiparticles DOS within the vortex lattice (VL) (see chapter 2 for further details). The DOS depends on the value of the order parameter $|\Delta(r)|$ and can be used to map $|\Delta(r)|$ within VL. This would, in principle, make STM an ideal tool to measure the vortex core size.

Hess *et al.* [1989] first studied the spatial extension of a vortex by measuring the zero bias tunneling conductance $\sigma(r)$ along a line from the vortex center (Fig.3.1.a). They found the width of the vortex at half the height of the profile is of two times the the value of the coherence length, as extracted from H_{c2} ($\xi_{H_{c2}} = \sqrt{\phi_0/2\pi H_{c2}}$). Hartmann

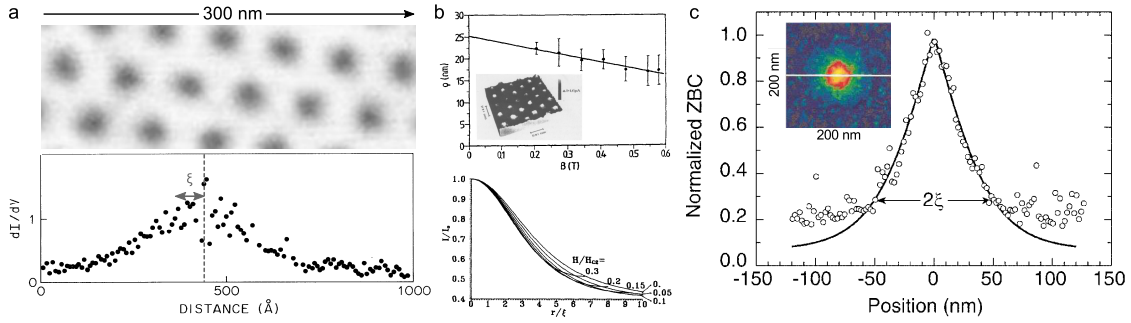

Figure 3.1: a) Adapterd from Hess *et al.* [1989]. Top panel shows the vortex lattice in $NbSe_2$ for a $1\,T$ applied field in the $c-axis$. Lower panel shows zero bias normalized conductance values along a vortex at $0.03\,T$ and $1.8\,K$. They investigate the spatial extent of the vortex finding that for half width it is of the order of $15\,nm$, almost two times the in plane coherence length ($\approx 7.7\,nm$). b) Adapted from Hartmann *et al.* [1994]. Top panel: measurement of the vortex radii in $NbSe_2$ defined as the distance from the vortex center at which $I = 0.36\,(I_{max} - I_{min})$ as a function of the applied magnetic field. Data were taken at a voltage of $0.64\,\Delta$. Inset: image of the vortex lattice taken at $H/H_{c2} = 0.14$ with $V_{bias} = 0.88\,\Delta$. Lower panel: calculation of the vortex profile using a self-consistent solutions of the Usadel equations for the same bias voltage as in the top panel. Their theoretical calculations agree qualitatively with the behavior found in the data, showing a decrease in the vortex size as the field is increased. However, both experimental and theoretical values are much larger than the coherence length. c) Adapted from Eskildsen *et al.* [2002]. Inset: isolated superconducting vortex in MgB_2 measured with an applied field of $0.05\,T$ at $2\,K$. Profile along the white line in the inset showing the spatial dependance of the vortex shape. They experimentally observe a larger vortex size than the expected from the $\xi \approx 10\,nm$ found from H_{c2}. Fitting their data to $\sigma'(x,0) = \sigma'_0 + (1-\sigma'_0) \times (1 - \tanh x/\xi)$ they get a value of $\xi \approx 50\,nm$.

et al. [1994] defined the vortex size to be the radius at which the tunneling current was $I = 0.36\,(I_{max} - I_{min})$. Using this definition, the plotted the vortex size for different fields in $NbSe_2$ finding a reduction of the vortex size for increasing field. They compare with theoretical calculations finding qualitative agreement but the values extracted from both experiment and calculations were well above ξ extracted from H_{c2}, $\xi_{H_{c2}}$ (Fig.3.1.b). Fig.3.1.c shows the measurements of Eskildsen *et al.* [2002] for the vortex core in MgB_2. Fitting their data to the phenomenological $\sigma'(x,0) = \sigma'_0 + (1-\sigma'_0) \times (1 - \tanh x/\xi)$, with σ' the measured tunneling conductance and $\sigma'_0 = 0.068$ the normlalized zero bias conductance at zero field, they extract a coherence length of five times the expected value for H_{c2}. They explain the high value found by assuming that it is due to the presence of two length scales. The one which they are observing is due to the π band, whereas the value obtained from the upper critical field would be different.

Thus, there is a serious contradiction between the length scale extracted from STM measurements and the coherence length. In addition, some experiments propose, on the basis of muon scattering measurements (which provide an indirect path to determining a length scale associated to the order parameter), that the vortex core shrinks with increasing magnetic field. This has not been clearly demonstrated using STM. Although some hints have been published [Hartmann *et al.*, 1994], these were obtained

using the current at a single bias voltage, which can hardly be associated to the DOS nor the order parameter. Thus, we need to understand how to read and interpret STM images if we want to obtain from them the spatial dependence of Δ.

In this chapter we apply a simple phenomenological model for the spatial distribution of the DOS within vortex lattices. The model was elaborated by Dr. Vladimir Kogan from Iowa State University and Ames Laboratory (Ames, IA, USA). For the analysis of the vortex core we have chosen β-Bi_2Pd for a single gap superconductor, and 2H-$NbSe_{1.8}S_{0.2}$, 2H-NbS_2 and $CaKFe_4As_4$ which are multigap superconductors with no in-plane anisotropy. We also analyze the canonical multiband superconductor MgB_2. Data from β-Bi_2Pd and 2H-NbS_2 were measured by Herrera *et al.* [2015] and Guillamón *et al.* [2008b] respectively, Data for 2H-$NbSe_{1.8}S_{0.2}$ and CaF_4As_4 was taken on the samples described in chapter 6.2 and 5 respectively, and data on MgB_2 was provided by Prof. Morten Eskildsen from the University of Notre Dame (Notre Dame, IN, USA).

3.2 Model for the vortex core

Within the model, we define the vortex core size C through the slope of the order parameter at the vortex core center. In that way, the vortex core size C is related to the coherence length ξ and the order parameter Δ through $d\Delta/dr|_{r\to 0} \propto 1/\xi \propto 1/C$.

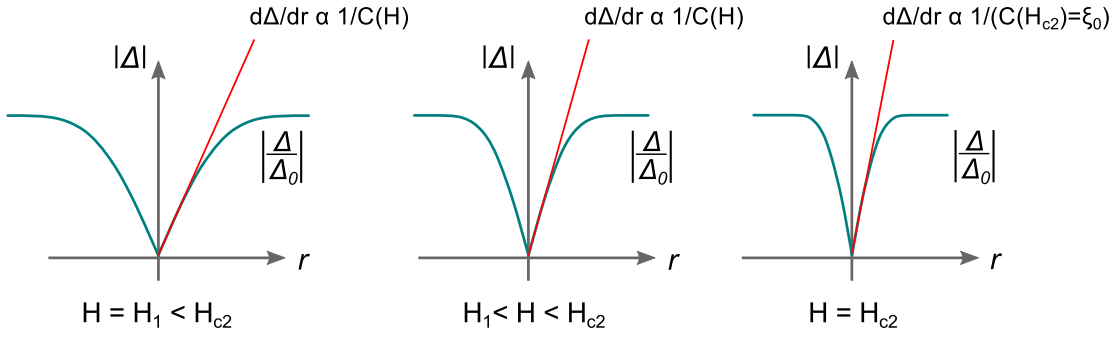

Figure 3.2: Schematic draw of the variation of the order parameter in the vortex core as a function of field. The derivative of the order parameter at the core center (red line) is related to the coherence length and the vortex core size. When increasing the magnetic field, vortices approach each other, but the order parameter close to the vortex center remains zero. The slope of Δ increases when increasing the magnetic field and the intervortex distance decreases.

Having this definition in mind we can visualize the variation of the order parameter with the field as the scheme in Fig.3.2. For low fields, when the intervortex spacing is large, the order parameter varies over larger distances (left panel). When we increase the magnetic field, we reduce the intervortex distance and, therefore, increase the slope of the order parameter. Thus, for larger fields the slope will increase and, since $d\Delta/dr|_{r\to 0} \propto 1/C$, the core size will be reduced. The corresponding length scale

varies with the field, decreasing until H_{c2} when it reaches the commonly used value of $\xi_{c2} = \sqrt{\phi_0/2\pi H_{c2}}$.

The model, developed by V. Kogan, is based on P.G. de Gennes equation for the zero bias DOS [deGennes, 1964; Saint-James, Sarma, and Thomas, 1969]:

$$\frac{N(\mathbf{r})}{N_n} = 1 - \frac{|\Delta(\mathbf{r})|^2}{\Delta_0^2}, \tag{3.1}$$

where $N(r)$ is the zero bias DOS and N_n is the DOS in the normal phase. Eq.3.1 gives the value of the LDOS in terms of the order parameter at the same point, directly relating both quantities. Regarding the spatial variation of the order parameter, the model follows the dependence given by Schmid [1966] and Clem [1975].

All samples studied here have triangular vortex lattices where the unit cell can be taken as a hexagon centered at the position of a vortex. As the model does not take into account in-plane anisotropic properties, nor vortex bound states, we discuss systems where the vortex core is isotropic and the bound states are not very pronounced. As we show below, there is just one case where the bound states are of relevance, the case of NbS_2. There, we have verified that changing normalization conditions discussed in the following does not change the obtained result.

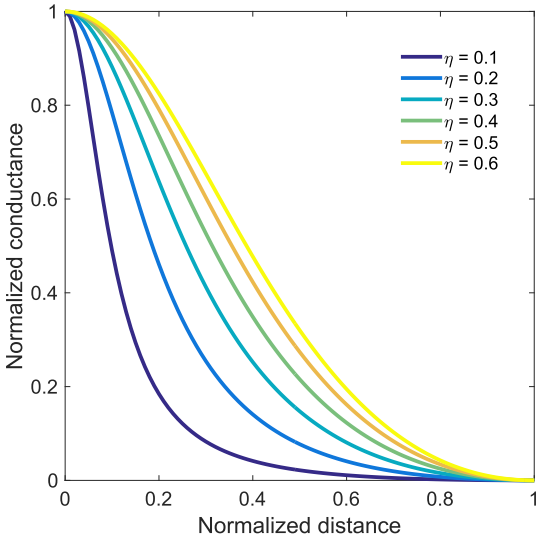

Figure 3.3: Zero bias normalized conductance of the vortex core given by our model for one band as a function of the normalized distance. Normalization procedures are given in the text. Conductance is plotted for different values of the fitting parameter η. Larger η implies a larger core size.

To simplify the spatial dependance we use the Wigner-Seitz approximation and consider the unit cell as a circle of radius a such that $\pi a^2 = \phi_0/B$, where ϕ_0 is the magnetic flux quantum, and B is the magnetic induction. The cell radius a is close to half of the

intervortex distance L: $2a/L = (2\sqrt{3}/\pi)^{1/2} \approx 1.05$.

The proposed model considers the normalized conductance σ to vary as

$$\sigma = 1 - \frac{\rho^2(1+\eta^2)}{\rho^2+\eta^2}\exp\left[\frac{\eta^2(1-\rho^2)}{1+\eta^2}\right], \qquad \rho = r/a, \qquad \eta = C/a, \tag{3.2}$$

where all distances have been normalized to the radius a of the Wigner-Seitz approximation. So, within the model, for $r < C$ the slope $d\Delta/dr|_{r\to 0} = \Delta_0/C$ and C can still be taken as the core size. The formula allows to take into account the lattice periodicity as $d\Delta/dr = 0$ at $r = a$.

In order to illustrate how the model works, figure 3.3 includes the results from evaluating Eq.3.2 for different values of the parameter η. η is like the width of a Gaussian curve. When we increase η, the conductance profile expands. While changes for low values of η (below 0.5) produce easily noticeable changes in the curve shape, changes in parameter above those values have a smaller effect on the curve.

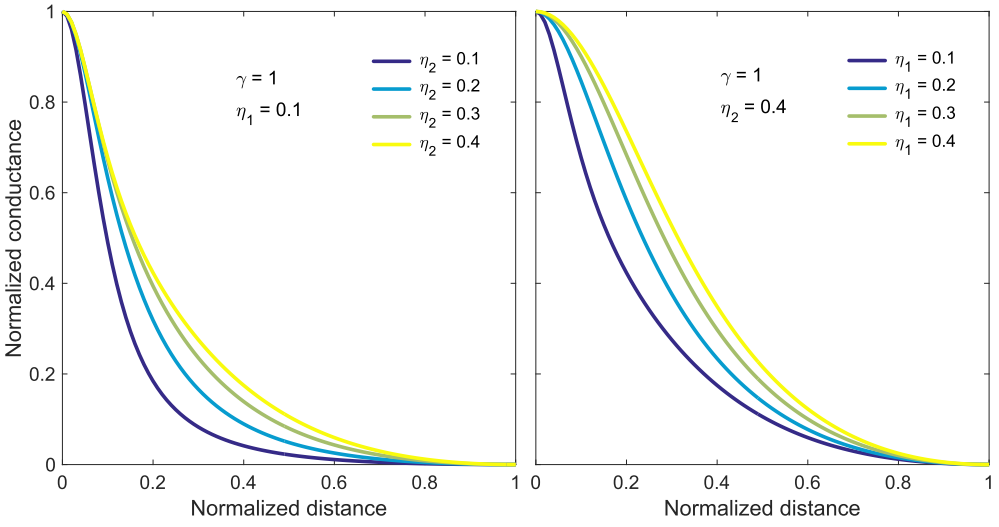

Figure 3.4: Zero bias normalized conductance of the vortex core given by our model for two band version as a function of the normalized distance. Left panel shows the changes in the conductance produced by varying η_2 from 0.1 to 0.4 while keeping η_1 constant at 0.1. Right panel contains the opposite situation, keeping η_2 constant at 0.4 and changing η_1 from 0.1 to 0.4. η_1 and η_2 are associated, respectively, to bands with smaller and larger values of the core size C.

So far we have only used one order parameter in the model, however, as shown by V. Kogan, the model can be generalized for two gap superconductors [Fente *et al.*, 2016]. Assuming the order parameter takes values Δ_1 and Δ_2 on two different bands one can write the spatial dependence of the density of states as

$$\frac{N(r)}{N_n} = 1 - n_1\frac{\Delta_1^2(r)}{\Delta_{1,0}^2} - n_2\frac{\Delta_2^2(r)}{\Delta_{2,0}^2}, \tag{3.3}$$

being $n_{1,2}$ the partial densities of states ($n_1 + n_2 = 1$). Because both bands should be periodic in the vortex lattice, each Δ_ν ($\nu = 1, 2$) satisfies the boundary condition $d\Delta_\nu/dr = 0$ at the cell boundary $r = a$. The normalized order parameter for each band can be written as:

$$\frac{\Delta_\nu(r)}{\Delta_{0,\nu}} = \delta_\nu = \frac{\rho^2}{\sqrt{\rho^2 + \eta_\nu^2}} \exp\left[-\frac{\rho^2 \eta_\nu^2}{2(\eta_\nu^2 + 1)}\right], \tag{3.4}$$

where $\eta_\nu = C_\nu/a$ and $\nu = 1, 2$. In expression 3.4 each δ_ν is normalized to its corresponding $\Delta_{0,\nu}$. Going back to Eq.3.3 and substituting

$$\sigma = 1 - \frac{\delta_1^2(\rho) + \gamma\delta_2^2(\rho)}{\delta_1^2(1) + \gamma\delta_2^2(1)}, \qquad \gamma = \frac{n_2}{n_1}, \tag{3.5}$$

Being γ the ratio between the partial density of states in each band. In Fig.3.4 we consider results using this two band model. Note that the effect is to introduce two length scales in the decay.

Keeping one of the parameters at a low value and increasing the other results in a widening of the lower part of the curve. This effect can be seen in the left panel of Fig.3.4 where $\eta_1 = 0.1$ and η_2 changes. The opposite happens when one of the parameters is kept in a high value and the other is reduced: the upper part of the curve is narrowed. Right panel of Fig.3.4 shows this effect for $\eta_1 = 0.4$ and different values of η_2. For the sake of simplicity in these examples we use $\gamma = 1$, giving equal weight to both bands. However, this result does not change when changing γ.

3.2.1 Normalization procedure

To obtain the plot of the tunneling conductance as a function of the distance from the vortex center, we select single vortices out of zero-bias conductance images and evaluate angular averages of the normalized conductance σ_0 for each r. Whenever possible we try to use images of isolated vortices with the highest available spatial resolution. We define the renormalized tunneling conductance σ as:

$$\sigma = \frac{\sigma_0(r) - \sigma_0(r^*)}{\sigma_0(0) - \sigma_0(r^*)} \tag{3.6}$$

where r^* is the distance from the vortex center to the point where the tunneling conductance is minimum (in the triangular lattice, the center of an equilateral vortex triangle). We present in figure 3.5 a detail of one of the fits in 2H-$NbSe_{1.8}S_{0.2}$. Fig.3.5.a shows the radial average of the profile of the vortex presented in the inset. In this plot the tunneling conductance is normalized to its value outside the superconducting gap following the procedure described in chapter 2. In the vortex core center ($r = 0$) conductance rises slightly above one. As we move away from the vortex center, conductance drops approaching zero. Fig.3.5.b shows the same data in a but renormalized following Eq.3.6.

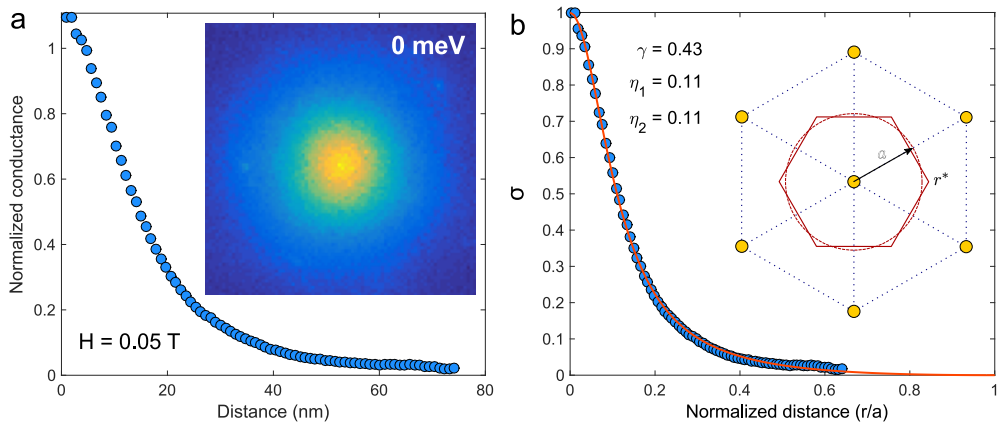

Figure 3.5: Detail of one of the fits performed in 2H-$NbSe_{1.8}S_{0.2}$. The applied field is $0.05\,T$ along the c axis. a) Radial average for the vortex shown in the inset. Conductance is normalized to its value outside the gap, far from the quasiparticle peaks (usual normalization procedure described in chapter 2). b) Blue circles represent the data in (a) normalized following Eq.3.6. Red line represents the fit to the two band model using $\gamma = 0.43$, $\eta_1 = \eta_2 = 0.11$. Inset: cartoon of the Wigner-Seitz approximation highlighting the distance a we use to normalize our data and the point r^* where we take the value of the conductance in between three vortices. Yellow circles represent the vortex positions on a triangular lattice.

The renormalized conductance ranks from 1 at the vortex core center to 0 at $r = a$. Red line in the plot corresponds to the fit of the experimental data to the two band model in Eq.3.5. Inset of Fig.3.5.b shows a scheme of the Wigner-Seitz approximation and how where the distances a and r^* are taken. The remarkable quality of the fits points towards the validity of the model for STM data.

3.3 Results on different superconducting systems

3.3.1 Vortex core size in β-Bi_2Pd

β-Bi_2Pd is a single gap superconductor ($\Delta = 0.76\,meV$) with a zero field conductance that follows s-wave BCS theory and shows a hexagonal VL [Herrera *et al.*, 2015]. We have chosen to analyze this material as an example of an isotropic single gap superconductor. Measurements and data analysis for this compound have been carried out by E. Herrera.

Fitting the data to Eq.3.2 and using η as a fit parameter we can extract the core size C. The fits yield to values of $\eta \approx 0.50 \pm 0.08$ in a field range where H changes by a factor of 4. Since $\eta \approx const$, we can write

$$C = \eta a = \eta \sqrt{\frac{\phi_0}{\pi H}} \tag{3.7}$$

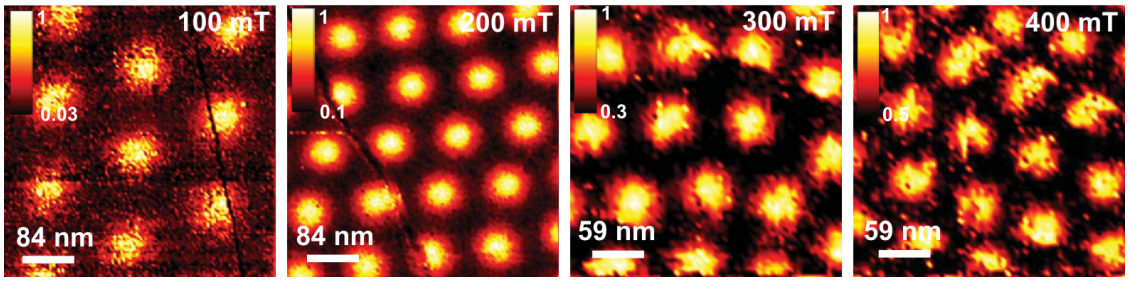

Figure 3.6: Vortex lattice in β-Bi_2Pd for different fields [adapted from Herrera *et al.*, 2015]. Comparing scalebars with the size of the areas corresponding to the vortices, we see that the general behavior of the vortex core observed with STM is that the core shrinks as the applied magnetic field is risen.

Hence, the core size C varies with applied field as $1/\sqrt{H}$. Blue points in the right panel of figure 3.7 provide the variation of C with the magnetic field showing this dependence. Kogan and Zhelezina [2005] suggest that, in large fields, the coherence length as a function of field should behave as $\xi \approx a/\sqrt{H}$. As mentioned, this relation should hold at the upper critical field H_{c2}, which gives a value for the constant a of $a = \sqrt{\phi_0/2\pi}$ so that the coherence length has a dependence:

$$\xi = \sqrt{\frac{\phi_0}{2\pi H}} \equiv \xi_H. \tag{3.8}$$

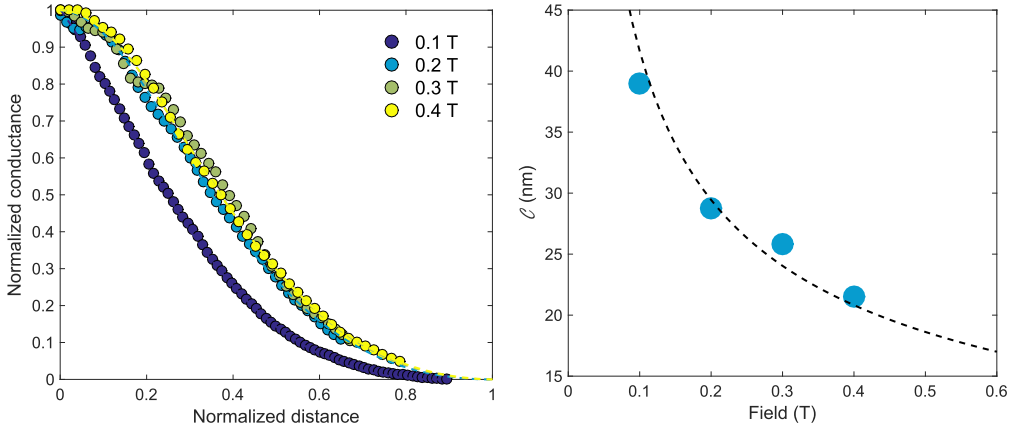

Figure 3.7: The left panel: the normalized tunneling conductance σ of Eq.3.2 vs. distance r from the vortex center, normalized to the cell radius a, for β-Bi_2Pd and in fields indicated. Data are taken at $0.15\,K$ and have been obtained from images of vortices radially averaged and normalized as described in the text. The right panel: the core size C of Eq.3.7 vs H. Dots are the values of $C = \eta a$ obtained from the fits of the left panel with a being the Wigner-Seitz cell size. The line is C calculated with $\eta \approx 0.5$ found in the fits.

Having this in mind, the variation of the core size C with the magnetic field would

be

$$C = \eta a = \eta\sqrt{\frac{\phi}{\pi H}} = \eta\sqrt{2}\xi_H. \tag{3.9}$$

Using the value $\eta \approx 0.5$ obtained by the fits in β-Bi_2Pd, we find $C \approx 0.7\xi_H$. This equation implies that the order parameter and DOS distributions within the vortex lattice in large fields of one-band isotropic materials are governed by a universal length ξ_H (Eq.3.8). It is also patent from Eq.3.9 that when $H \to H_{c2}$, ξ_H reaches the value of the standard coherence length $\xi_{c2} = \sqrt{\phi_0/2\pi H_{c2}}$.

3.3.2 Vortex core size in 2H-$NbSe_{1.8}S_{0.2}$

In the case of 2H-$NbSe_{1.8}S_{0.2}$ all experiments were performed during this thesis with the system described in chapter 2. Details on the material and the experiment will be presented in chapter 6. Here we focus on conductance changes much larger than those ones produced by Shiba states studied in the same chapter performing radial averages centered at the superconducting vortices. The effect of the impurity states can be safely neglected.

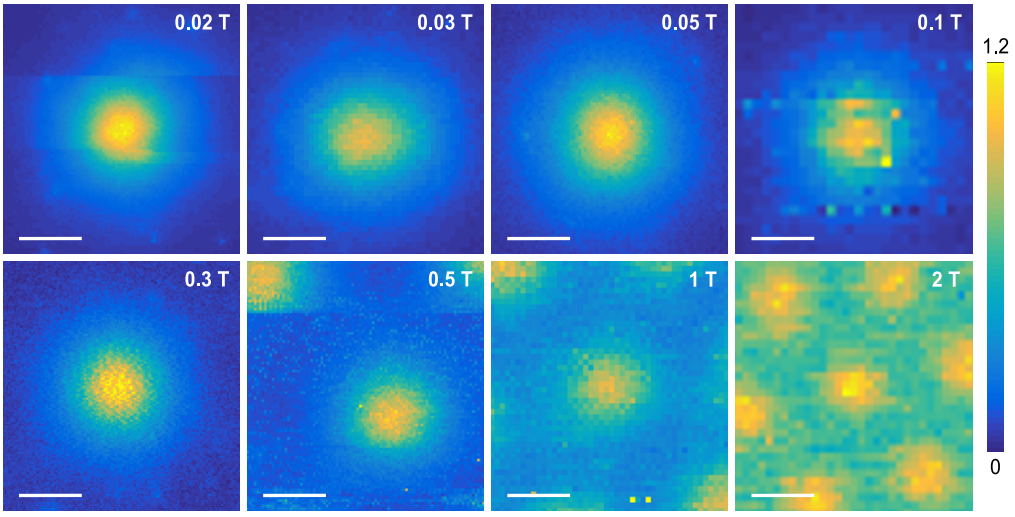

Figure 3.8: Detail of vortices in 2H-$NbSe_{1.8}S_{0.2}$ at different fields between $0.02\,T$ and $2\,T$. All images are of the same size and all scale bars are of $20\,nm$. The field is increased by two orders of magnitude but the size of the vortex core remains essentially the same size at all fields.

2H-$NbSe_{1.8}S_{0.2}$ has been chosen as a multiband isotropic superconductor. As will be shown in detail in chapter 6, the effect of doping 2H-$NbSe_2$ with sulfur suppresses the strong in-plane gap anisotropy present in 2H-$NbSe_2$. Vortex cores in this material are round an no trace of the star shaped form seen in the pure material remains (see Fig.3.8). However, the zero field tunneling conductance cannot be fitted using a single gap model. Instead, we have to use two values of the superconducting gap. These are

relatively close to each other ($\Delta_1 = 0.78\,meV$, $\Delta_2 = 1\,meV$) but are still needed to describe the findings in this compound.

All images in Fig.3.8 show the zero bias tunneling conductance normalized to its value outside the gap. Color maps and lateral sizes are the same in all images.

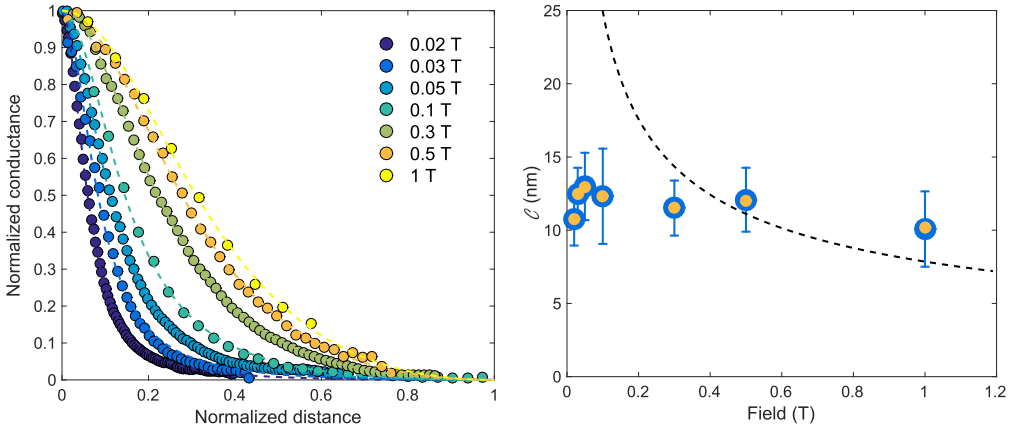

Figure 3.9: Left panel contains the fits performed using the two band model for different fields for 2H-$NbSe_{1.8}S_{0.2}$. Dots represent the radial averages of the vortex and dashed lines the different fits. Circles in the right panel represent the different sizes of the vortex core calculated using Eq.3.7 with η_1 (blue) and η_2 (orange) for each field. Line is C calculated with $\eta \approx 0.3$ for comparison.

As was done for β-Bi_2Pd we renormalized the conductance $\sigma(r)$ for 2H-$NbSe_{1.8}S_{0.2}$ following Eq.3.6 and plot it as a function of the normalized distance r/a. Fig.3.9.a show these normalized conductance curves for fields from $0.02\,T$ to $1\,T$ together with the fits to the two band model. The good quality of the fits is remarkable, an indication that Eq.3.5, derived from the proposed model, describes well the spatial distribution of the LDOS in two-gap systems. The density of states spreads considerably when applying magnetic field meaning that the parameters η_ν obtained from the model increase with magnetic field. This variation implies that the core size calculated as $C = \eta a$ does not shrink with increasing magnetic field. Fig.3.9.b contains calculated core sizes C_ν for each band calculated using the η_ν obtained from the fits. From them we can see that not only C is field independent but it is the same in each of the two bands. This means that there is a single length scale for spatial variations in the order parameter, a result that has important implications to understand two-band superconducting materials.

According to Kogan and Zhelezina [2005], magnetic field independence of C is expected for one-band superconductors in the dirty limit. In the case of 2H-$NbSe_{1.8}S_{0.2}$ there is a remarkable increase of H_{c2} of a factor of two with respect to pure 2H-$NbSe_2$ and the zero bias peak at the vortex core is considerably suppressed (see section 6.2). These facts point to scattering induced by the sulfur dopants as the reason for the observed behavior of the vortex core size with the magnetic field.

3.3.3 Vortex core size in 2H-NbS_2

2H-NbS_2 is, as 2H-$NbSe_{1.8}S_{0.2}$, a multiband superconductor with no in-plane anisotropy. Data presented here for this material are from Guillamón *et al.* [2008a].

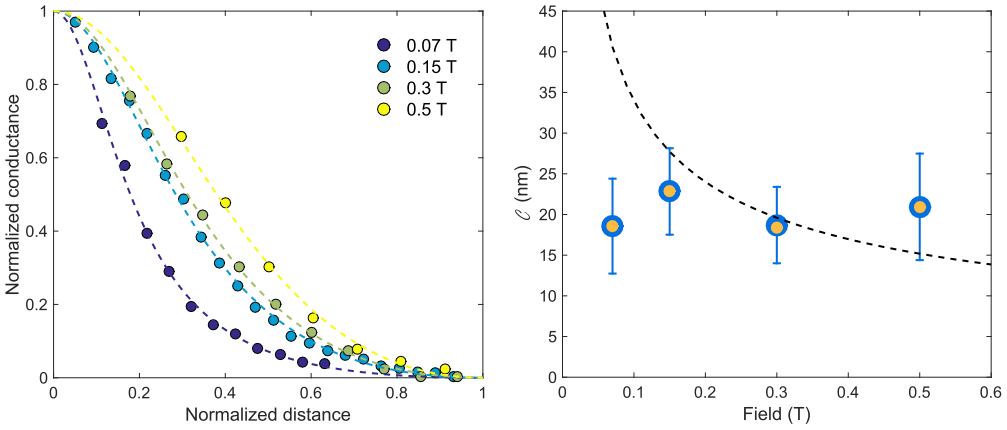

Figure 3.10: Left panel contains the fits performed using the two band model for different fields for 2H-NbS_2. Dots represent the radial averages of the vortex and dashed lines the different fits. Circles in the right panel represent the different sizes of the vortex core calculated using Eq.3.7 with η_1 (blue) and η_2 (orange) for each field. Line is C calculated from Eq.3.7 using $\eta \approx 0.3$ for comparison.

Left panel in Fig.3.10 contains the fits to our model for vortices in 2H-NbS_2 at different fields in the range of $0.07\,T$ to $0.5\,T$. Right panel displays the evolution of the calculated core size using the parameters from the fit as the field is increased. We find for this material the same dependence seen for 2H-$NbSe_{1.8}S_{0.2}$; tunneling conductance is spread for increasing fields and therefore the vortex core size remains constant ($\approx 20\,nm$) for all the measured fields.

In 2H-NbS_2, the residual resistivity is the lowest among the compounds discussed here [see Fente *et al.*, 2016], and there is a clear zero-bias peak at the vortex core, comparable to the peak observed in pure 2H-$NbSe_2$ as shown by Guillamón *et al.* [2008a]. The observed magnetic field independence of C is, in the case of this material, unexpected and requires more careful band dependent calculations. One possible explanation is that scattering is band dependent, which gives different sensitivities to scattering on the zero-bias peak and the spatial dependence of the order parameter in vortex cores.

3.3.4 Vortex core size in $CaKFe_4As_4$

Measurements in this compound were also performed, as the ones in 2H-$NbSe_{1.8}S_{0.2}$, during this thesis in the system described in chapter 2. Details on the material and the particular experiment are given in the previous chapter (see chapter 5).

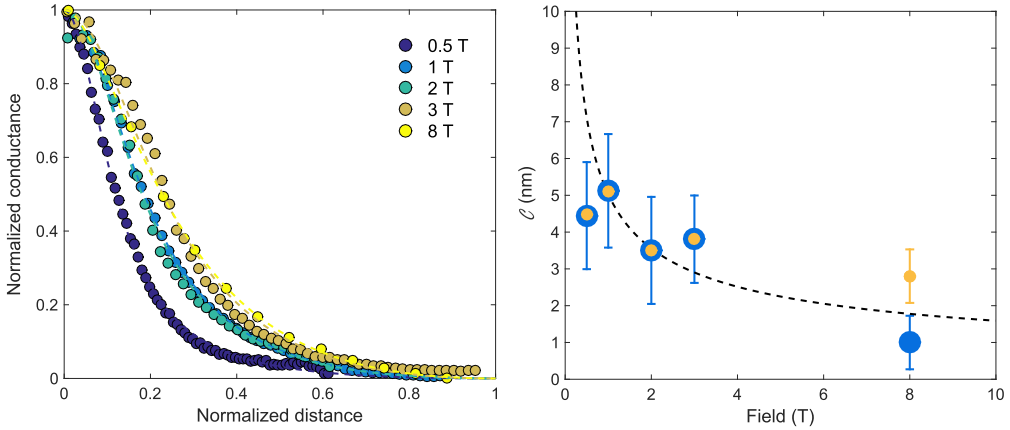

Figure 3.11: Left panel contains the fits performed using the two band model for different fields for $CaKFe_4As_4$. Dots represent the radial averages of the vortex and dashed lines the different fits. Circles in the right panel represent the different sizes of the vortex core calculated using Eq.3.7 with η_1 (blue) and η_2 (orange) for each field. The line is C calculated from Eq.3.7 using $\eta \approx 0.2$ found in the fits.

From the data fits, we find again the same values of C_i for each band, except at $8\,T$, where we obtain a small difference (see Fig.3.11). We compare the measured C_i with the behavior expected for a superconductor in the clean limit (Eq.3.9). Although at low fields the data are somewhat below the proposed behavior, given the crude approximations involved in the formalism, we consider this to be a good agreement. When we extrapolate C_i up to H_{c2} ($\approx 70\,T$ according to Meier *et al.* [2016]), we find a value for the coherence length ξ of $1.8\,nm$, which is close to the value obtained previously from H_{c2} in the same reference ($2\,nm$, using $\xi \approx \sqrt{\phi_0/2\pi H_{c2}}$). Using $\eta \approx 0.2$ obtained by the fits, we find $C \approx 0.28\,\xi_H$. Thus, as in β-Bi_2Pd, in $CaKFe_4As_4$ the core shrinks with magnetic field, as expected for clean superconducting materials.

3.3.5 Vortex core size in MgB_2

We have also applied our model to MgB_2 in order to analyze a reference example for multiband superconductivity. Data used in the analysis were provided by Prof. Morten Eskildsen from the University of Notre Dame (Notre Dame, IN, USA) and have been published in Eskildsen *et al.* [2002, 2003b,a].

Left panel of Fig.3.12 contains the radial average of the normalized conductance for individual vortices at different fields in MgB_2 together with the fits to the two band model. Using the parameters extracted from those fits we can calculate from each band the corresponding core size using Eq.3.7. These values are plotted in the right panel of Fig.3.12. As shown in the figure, C_i are found to be the same for each band. We add to the plot the $\xi(H)$ calculated using $\eta \approx 0.36$.

It is difficult to unambiguously determine the behavior of $\xi(H)$ in MgB_2 from Fig.3.12. Considering the tendency found for β-Bi_2Pd and $CaKFe_4As_4$ with $\xi(H) \propto 1/\sqrt{H}$, we

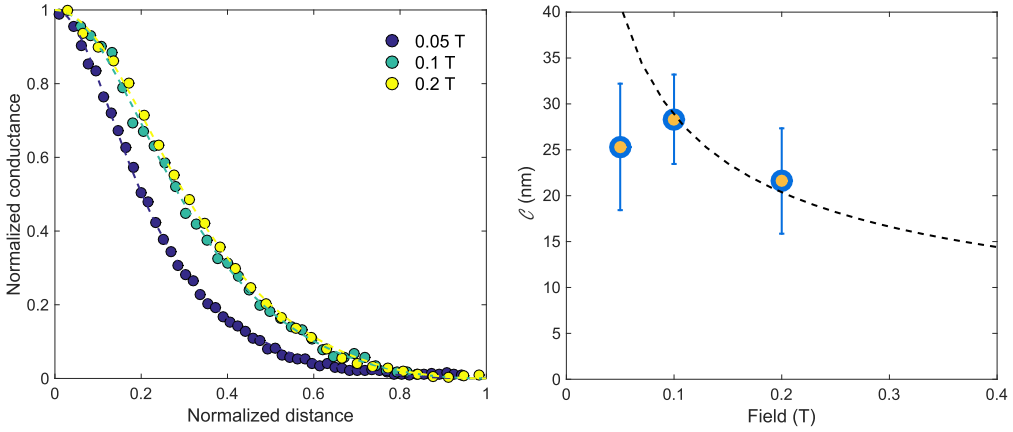

Figure 3.12: Left panel contains the fits performed using the two band model for different fields for MgB_2. Dots represent the radial averages of the vortex and dashed lines the different fits. Circles in the right panel represent the different sizes of the vortex core calculated using Eq.3.7 with η_1 (blue) and η_2 (orange) for each field. The line is C calculated from Eq.3.7 using $\eta \approx 0.36$ found in the fits and ξ_{c2} extracted from the value $H_{c2} \approx 3\,T$ [Angst *et al.*, 2002].

extrapolate the coherence length to be of $\approx 10\,nm$ at H_{c2}. However, dispersion of the data points show that more experimental data are needed to clarify this point. Nevertheless, we would like to remark that the model gives the same characteristic length scale for both bands which is a factor of two smaller than those previously reported [Eskildsen *et al.*, 2002].

In the case of MgB_2, the size of the vortex core has been associated with the large coherence length of the π-band which was found to be $\xi_\pi \approx 50\,nm$ [Eskildsen *et al.*, 2002]. Using our model we can extrapolate the coherence length $\xi(H)$ to be of $\approx 10\,nm$ at H_{c2}, as seen in bulk measurements [Angst *et al.*, 2002].

3.3.6 Distance dependence of the tunneling conductance for finite bias voltages

In Fig.3.13 we plot the spatial distribution $N(r,\epsilon)$ at finite bias voltages for β-Bi_2Pd, $CaKFe_4As_4$, $NbSe_{1.8}S_{0.2}$ and NbS_2. In Fig.3.13 we show the angular averaged $N(r,\epsilon)$ for all four compounds normalized to the parameters extracted from the zero bias conductance fits. The shape of the conductance vs bias voltage remains roughly the same in increasing fields in β-Bi_2Pd and in $CaKFe_4As_4$. Rising the magnetic field does not introduce big differences in the distance from the vortex center at which the superconducting gap starts to open or its size at $0.45\,a$. For the other two compounds the conductance tends to increase away from the core with increasing H. This same tendency is seen by comparing the curves obtained from the zero bias data in Figs.3.7, 3.9, 3.10 and 3.11.

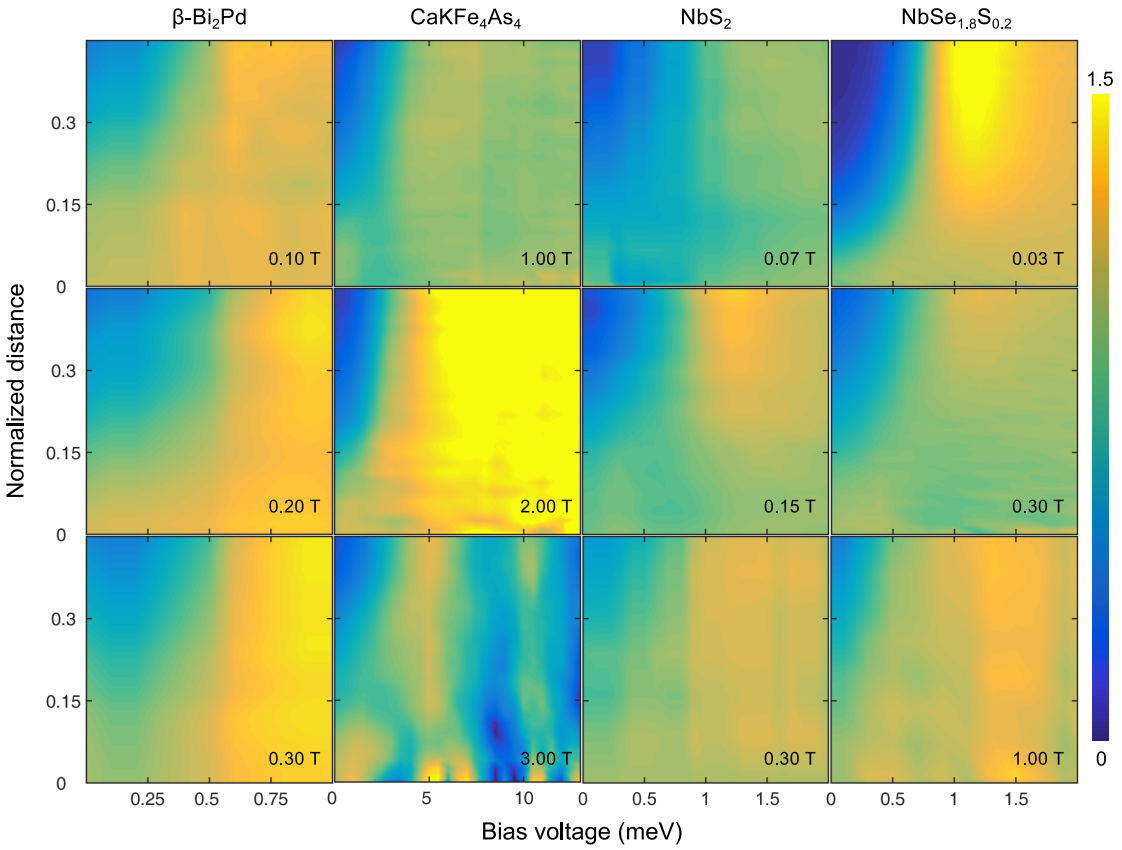

Figure 3.13: The angular averaged conductance normalized to the zero bias curve plotted as a function of distance r/a (with a being the $1.05\times$ half the intervortex distance) and the bias voltage at magnetic fields marked in the figure.

3.4 Discussion and conclusions

In this chapter we have studied multiband superconductors with very different characteristics: NbS_2 and $NbSe_{1.8}S_{0.2}$ are isotropic with Δ on the order of the meV, $CaKFe_4As_4$ has a $T_c = 35\,K$, and the canonical MgB_2.

We have provided a method with which we can find a length scale for the variation of the superconducting order parameter from STM images. The method yields values that can be compared to the coherence length obtained from H_{c2}. This shows that previous reports of an increased length scale due to two-gap behavior are not consistent with available STM data.

In future, it will be interesting to consider how the overall DOS varies with the magnetic field, as found in macroscopic experiments. Here, we simply leave the magnetic field behavior of the DOS in between vortices out of the discussion, because we normalize the tunneling conductance to its value in between vortices.

In the case of MgB_2 we find that using our model we can extrapolate the coherence length $\xi(H)$ to be of $\approx 10\,nm$ at H_{c2}, as seen in bulk measurements [Angst *et al.*, 2002].

This observation is in contrast with the previously reported values from STM experiments [Eskildsen *et al.*, 2002]. This discrepancy can be understood in terms of the field dependence of the density of states, as obtained from thermal conductivity and specific heat [Sologubenko *et al.*, 2002; Nakai, Ichioka, and Machida, 2002]. Similar results are obtained in a variety of materials where it is thought that multiple gaps open on the Fermi surface [see Fig.7 of Sologubenko *et al.*, 2002; Herrera *et al.*, 2015; Seyfarth *et al.*, 2006]. To explain these results, the widely used proposal is that the density of states of the part of the Fermi surface with the smaller sized gap is easily affected by the magnetic field [Nakai, Ichioka, and Machida, 2002]. This dependence will strongly affect the apparent size of the core measured by STM leading, without the proper renormalization, to larger values.

There are, however, reports about a DOS that is enhanced when applying a magnetic field in two-gap and in multiband superconductors. These reports have been taken as a support to the presence of two or multiple length scales [Boaknin *et al.*, 2003]. Here we have shown that there is no reason for this. The magnetic field dependence of the DOS in between vortices is responsible for the observed behavior in those measurements, but not different length scales.

We summarize now our conclusions for this chapter:

- We have analyzed carefully the problem of the vortex core size using STM images of the vortex lattice in single gap and in multigap superconductors. We find that a phenomenological model proposed by Dr. Kogan fits very well the radial dependence of the superconducting density of states in all analyzed compounds.
- In two materials, β-Bi_2Pd and $CaKFe_4As_4$, we find that the size of the vortex core shrinks with increasing magnetic field as $1/\sqrt{H}$, giving a measurement of the characteristic length scale dependence with the magnetic field. Furthermore, when extrapolated to H_{c2} it gives the value expected form $\xi_{c2} = \sqrt{\phi_0/2\pi H_{c2}}$.
- In other two systems, 2H-$NbSe_{1.8}S_{0.2}$ and 2H-NbS_2, we find a magnetic field independent vortex core size. Most likely due to the existence of interband scattering.
- Finally, we find that in all the analyzed multiband superconductors, the characteristic length scales for the variation of the superconducting density of states remain band independent.

CHAPTER 4

Strain induced coexistence of superconductivity and nematicity in Co-doped $CaFe_2As_2$

4.1 Previous studies in Co-doped $CaFe_2As_2$

As discussed in the introduction, the nematic properties of some pnictide superconductors provide evidence for a peculiar electronic anisotropy that is not easy to grasp. The anisotropy is linked to an extend that has been intensively studied to structural and/or magnetic transitions. Nematicity was first shown in the pnictides in the $CaFe_2As_2$ system. Chuang *et al.* [2010] imaged a nematic hole-like band in the non-superconducting cobalt doped compound grown out of Sn flux using quasi-particle interference techniques. After this, nematicity has been reported in many studies in different FeBSC and using different techniques [Chu *et al.*, 2010].

From the point of view of sample growth, it has been quite difficult to dope $CaFe_2As_2$ and obtain reproducible and precise phase diagrams. First samples were grown from Sn flux [Ni *et al.*, 2008b; Ronning *et al.*, 2008], but the resulting compounds showed different nominal and experimentally determined concentrations of cobalt [Harnagea *et al.*, 2011; Hu *et al.*, 2012]. In addition, evidences for inhomogeneous distribution of dopants have been discussed. It was suggested that these differences were due to the solubility of Co in Sn [Ran, 2014].

Chuang *et al.* [2010] made experiments on a sample with Co concentration that was in the antiferromagnetic/orthorhombic phase, and no attempts were made to study superconducting samples. They found through quasiparticle interference analysis that the main scattering vectors of the hole band around the Brillouin zone center had a preferred direction. This results in breaking of the C_4 symmetry of the tetragonal crystal lattice and was called *nematic* in reference to liquid crystals. Soon after those experiments, Chu *et al.* [2010] designed an experiment to detwin samples by applying uniaxial pressure. Using this technique they prevent the formation of structural domains below the AF/ORTH transition being able to distinguish between long and short axes of the orthorhombic structure. They compared the resistivity along both

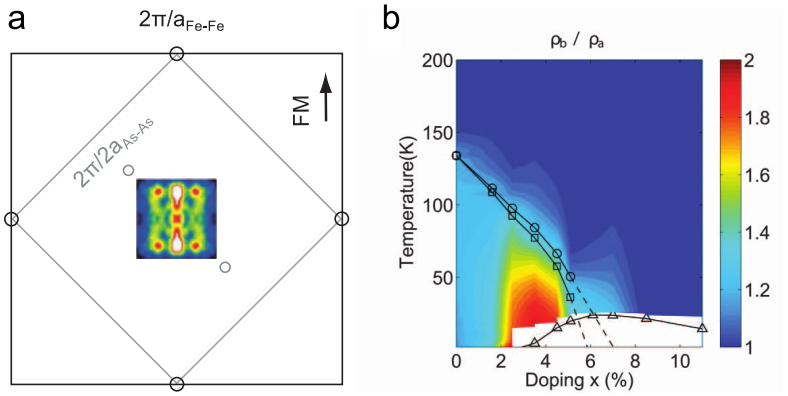

Figure 4.1: a) Adapted from Chuang *et al.* [2010]. Schematic draw of the Fermi surface together with the QPI signature found in STM experiments on Sn-grown $Ca(Fe_{1-x}Co_x)_2As_2$. Measurements were done in the AF/ORTH ground state. Scattering vectors coming from the QPI analysis of the hole band (central part of the image) are oriented with the FM axis of the crystal structure breaking the C_4 symmetry of the crystal structure. b) Adapted from Chu *et al.* [2010]. Phase diagram of $Ba(Fe_{1-x}Co_x)_2As_2$ as a function of cobalt content (x) assembled through resistivity measurements on detwinned single crystals. Background color scale indicates the resistivity anisotropy between each of the orthorhombic axes as ρ_b/ρ_a. The higher electronic distortion is not found for the higher structural transition temperatures but for finite concentrations near the point where superconductivity emerges. This is consistent with the electronic origin of the distortion.

axes in $Ba(Fe_{1-x}Co_x)_2As_2$ finding an anisotropy between symmetry directions that changes with doping in a non trivial way (see phase diagram on Fig.4.1.b). The resistivity anisotropy was found to be higher for finite doping ($\approx 3\%$), before the structural transition disappears where its transition temperature is reduced. The observed anisotropy was too strong to be explained as a mere consequence of the structural distortion, suggesting electronic origin. A later work by Allan *et al.* [2013] associated the directionality of the electronic scattering in $CaFe_2As_2$ to the internal structure of the Co dopants that formed dimers along one of the crystallographic directions. This also explains that the nematic signal observed in resistivity is higher for a higher Co concentration. However, it is still unclear if this electronic nematic phase has some relation with the emergence of superconductivity. Nematicity has been previously seen to coexist with the superconducting state for some compounds like FeSe films by Song *et al.* [2011], $NaFe_{1-x}Co_xAs$ by Cai *et al.* [2014], or in $FeSe_{0.4}Te_{0.6}$ by Singh *et al.* [2015]. In the case of NaFeAs, Rosenthal *et al.* [2014] observe the nematic signal in a superconducting compound but above T_c.

The effort of the growth community to overcome the issues of Sn-grown samples soon crystallized in the development of a new self flux method using an excess of FeAs (see chapter 2.4.1 for detailed references). Samples grown using this method provide reproducible phase diagrams and allow for detailed studies as a function of doping.

Among $A122$ compounds $CaFe_2As_2$ shows an extremely high sensitivity to pressure. For instance, the collapsed tetragonal (CT) phase that appears in other compounds like

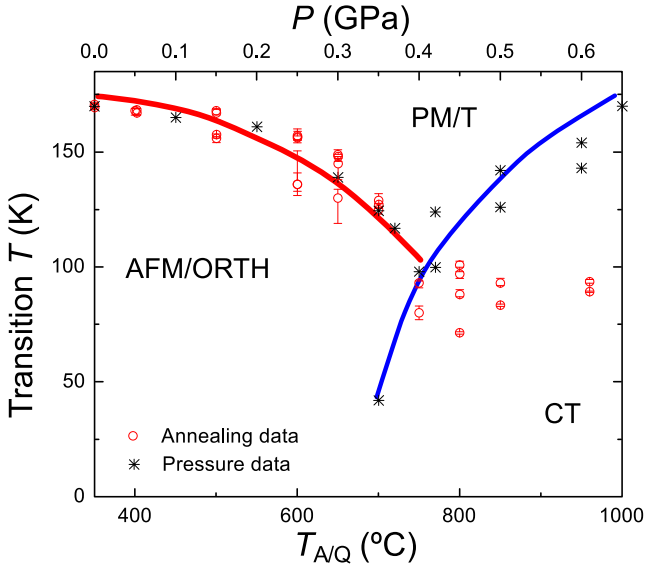

Figure 4.2: Phase diagram of the parent compound $CaFe_2As_2$ comparing post-growth annealing temperature and pressure as tuning parameters [Ran *et al.*, 2011]. Black asterisks stand for pressure data in Sn-grown sample measured by Yu *et al.* [2009] while red circles indicate the annealing data. Ground state evolves from a low pressure (low annealing temperature) AF/ORTH to the high pressure (high annealing temperature) CT. Adapted from Ran [2014].

$BaFe_2As_2$ at pressures of the order of $29\,GPa$ at $33\,K$ [Mittal *et al.*, 2011] is accessible at a much more moderated value ($0.35\,GPa$) in $CaFe_2As_2$ [Yu *et al.*, 2009]. Ran *et al.* [2011]; Ran [2014] showed that this ground state can also be stabilized at ambient pressure using a post growth annealing treatment (see phase diagram in Fig.4.2). They associate these changes in the ground state to the a change in the internal strain of the produced by an excess of FeAs that forms nanoprecipitates in the sample. Changing the temperature of annealing, the size and distribution of those nanoprecipitates can be controlled, tuning the sample into a different ground state through internal strain.

Annealing and Co-doping phase diagram

Ran *et al.* [2012] combined cobalt substitution with post-growth anneal to assemble a 3D-phase diagram. By using these tuning parameters the system can be driven into new ground states: superconducting/paramagnetic/tetragonal (SC/PM/T) and normal/paramagnetic/tetragonal (N/PM/T). Phase diagram of Fig.4.3.a, assembled from resistivity, specific heat and susceptibility measurements [see Ran *et al.*, 2012; Ran, 2014, for experimental details], shows the different ground states as function of the two tuning parameters. Hydrostatic pressure studies performed by Gati *et al.* [2012] show consistence with the phase diagram assembled by Ran *et al.* [2012]. In their study, Gati and coworkers found the pressure coefficients to be $dT_{s,N}/dP = -(1100 \pm 50)\,K/GPa$ for the structural and magnetic transition and $dT_c/dP = -(60 \pm 3)\,K/GPa$ for the superconducting transition. A further sign of the extreme sensitivity of $CaFe_2As_2$ to pressure.

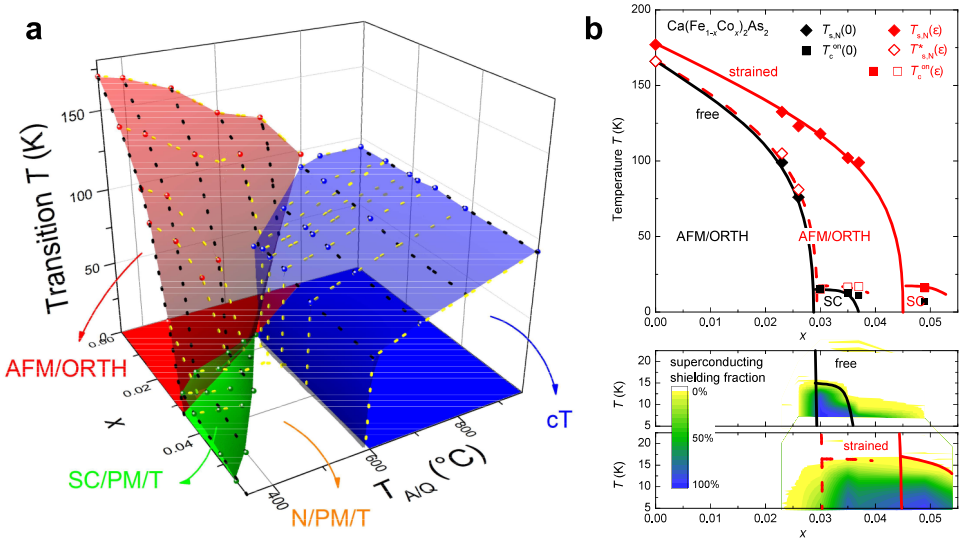

Figure 4.3: a) Adapted from Ran [2014]. 3D phase diagram of $Ca(Fe_{1-x}Co_x)_2As_2$ for free standing samples as a function of the Cobalt concentration (x) and the annealing/quenching temperature ($T_{A/Q}$). Four different ground states can be stabilized using these tuning parameters: antiferromagnetic/orthorhombic (red), collapsed tetragonal (blue), superconducting/paramagnetic/tetragonal (green) and normal paramagnetic (white). b) From Böhmer *et al.* [2016]. Top panel: comparison of phase diagrams for free and strained samples. Transitions in strained samples are shifted to higher temperatures. Lower panel: zoom on the low temperature part of the phase diagram showing the superconducting shielding fraction in a color scale.

The studies from Ran *et al.* [2012] were performed using free standing samples, meaning that samples were simply fixed using grease or other soft glues that did not produce appreciable strain. However, many experimental techniques, such as STM, require samples to be firmly bond to a substrate. Böhmer *et al.* [2016] studied the effect of the strain induced by substrates in $Ca(Fe_{1-x}Co_x)_2As_2$. For that, they measured a series of samples with different concentrations first in free-standing conditions and afterward glued to a substrate. Using high energy x-ray diffraction (XRD) and capacitance dilatometry they characterize the changes in the in-plane and c-axis lattice parameters of the strained sample. Their results indicate that the constant strain induced by the difference between sample and substrate thermal expansion coefficients, totally modifies the sample state. In particular, superconducting samples showing no AF/ORTH transition when free standing, do show an structural transition when glued to a substrate.

Fig.4.3.b. shows the effect of strain on the phase diagram of $Ca(Fe_{1-x}Co_x)_2As_2$. As the temperature of the strained sample is lowered the basal plane is compressed, favoring the nucleation of orthorhombic domains in certain parts of the sample while others remain tetragonal. In the case of uderdoped samples ($x < 0.028$) the system undergoes the strain induced structural transition (red line in the phase diagram) at a temperature higher than that of the AF/ORTH of free standing samples. Below this temperature the sample has both tetragonal and orthorhombic domains. Then, at a temperature near the AF/ORTH transition of free standing samples, the remaining tetragonal parts nat-

urally undergo the ORTH transition. For cobalt concentrations $0.28 < x < 0.49$ strain induces the formation of tetragonal and orthorhombic domains that coexist down to lower temperatures. For those concentrations, when the temperature is reduced below the T_c of free-standing samples, strained samples develop superconductivity associated to the remaining tetragonal parts of the sample. For concentrations above $x > 0.049$ no structural transition is seen and at lower temperature, superconductivity appears with values of T_c slightly higher than in free standing samples.

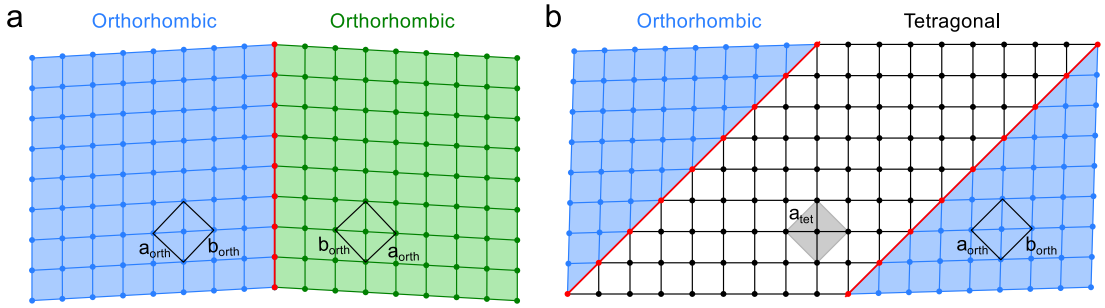

Figure 4.4: Crystallographic domain boundaries found in strained samples. a) Boundary between the two possible orthorhombic domains. b) Twin boundary between orthorhombic and tetragonal domains. Different background colors are used for each crystallographic domain and red lines represent the boundary between them. Adapted from Tanatar *et al.* [2009] and Böhmer and Kreyssig [2017].

Samples presenting both orthorhombic and tetragonal fractions have domain boundaries between the different crystallographic orientations. Fig.4.4 presents the possible domain boundaries in these samples. Boundaries between orthorhombic domains (Fig.4.4.a) are oriented at $45°$ with respect to the crystallographic axes. Boundaries between orthorhombic and tetragonal domains are oriented in the direction of the crystallographic axes (Fig.4.4.b).

Substrates and glues produce strain due to differences in thermal expansion for all materials. Effects of this strain, however, are small and cannot be seen in most materials. The extreme sensitivity of $CaFe_2As_2$ to pressure, reflected in its pressure coefficients, is what makes this strain to have such dramatic effects in the phase diagram.

4.2 Complementary studies in our samples

4.2.1 Magnetization measurements

In order to explore the superconducting ground state of $Ca(Fe_{1-x}Co_x)_2As_2$ below the strain induced structural transition we have chosen to study a sample doped with a $3.5\,\%$ of cobalt and annealed at $350°$C. Strain in the sample is produced by differences in thermal expansion coefficients of the silver epoxy used as glue and our copper sample-holder and the sample.

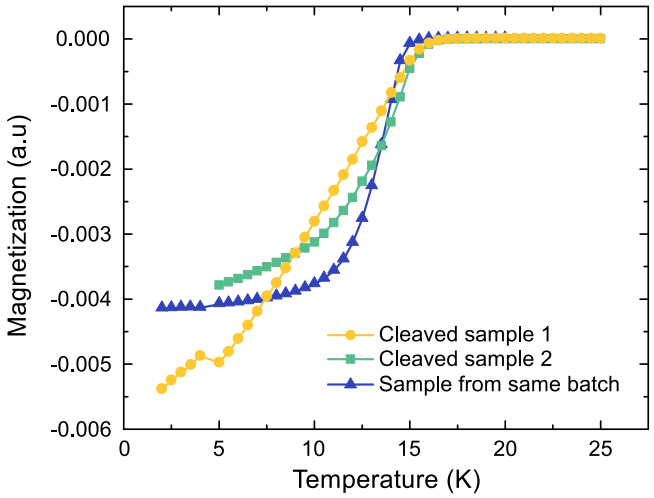

Figure 4.5: $M(T)$ measured at constant field in a Quantum Design MPMS comparing two samples glued into our copper sample-holder and cleaved to a free standing sample from the same batch.

To characterize the sample, we measured its properties at Ames after we finished the STM experiments. T_c was checked measuring temperature dependence of the magnetization at constant – low – applied field ($M(T)/H$) with a Quantum Design Magnetic Properties Measurement System (MPMS). Result is shown in Fig.4.5. The glued sample showed the same superconducting critical temperature as the free standing one ($T_c \approx 15\,K$) in agreement with the shifted phase diagram of Fig.4.3.b. We also note that the transition width is slightly larger in the glued samples than in the free standing one, suggesting that superconductivity is less homogeneous when the sample is attached.

4.2.2 AFM and MFM measurements

We have also studied the same samples through combined Atomic Force and Magnetic Force Microscope (AFM/MFM) measurements, to observe simultaneously magnetic and structural transitions at or close to zero field. Characterization of the samples with AFM and MFM in the range of $4\,K$ - $80\,K$ was done in the group of Mar García-Hernández at the *Instituto de Ciencia de Materiales de Madrid, Consejo Superior de Investigaciones Científicas* (ICMM/CSIC). I present here some measurements made by Alex Correa-Orellana on one of the samples previously measured with STM using the same sample-holder in order to keep it in the very same part of the phase diagram.

Temperature evolution of AFM and MFM signals is shown in Fig.4.6. Details of the experiment are beyond the scope of this thesis so they will not be given here. At high temperature (above $70\,K$) AFM topographies show flat surfaces like first one in the top panel of Fig.4.6, with steps of some unit cells similar to those discussed below from STM measurements. For lower temperatures, we find three clear stripe-like features

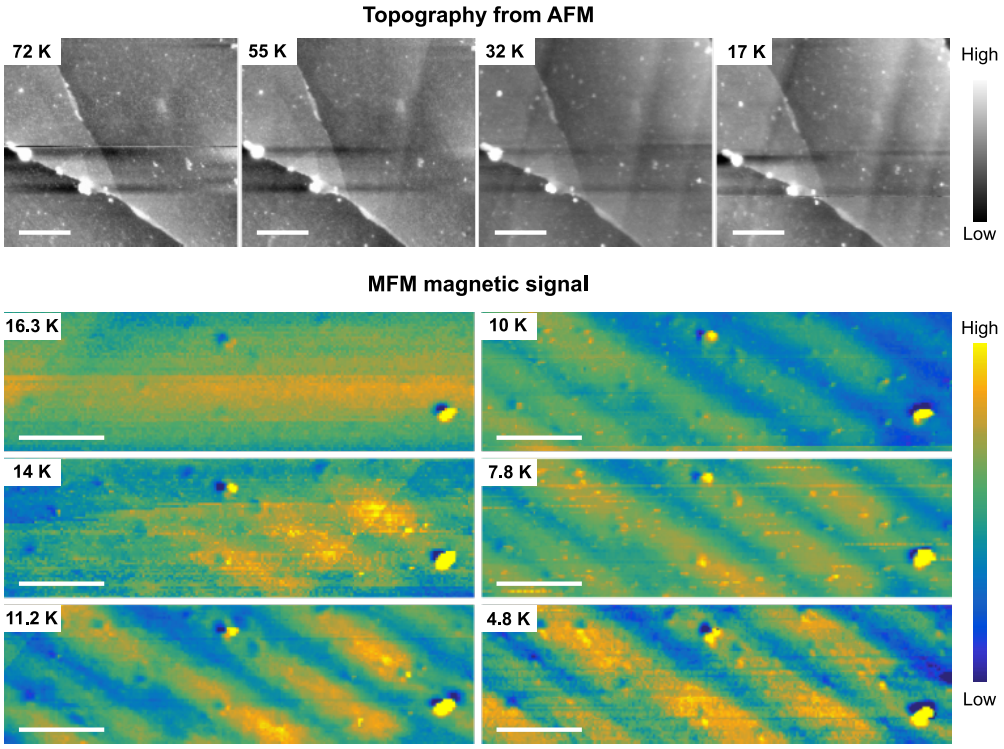

Figure 4.6: Upper panels: evolution of the AFM topographic images as the temperature is lowered. At temperatures above $72\,K$, topography is flat with steps of several unit cells created during the cleaving process. As the temperature is lowered, stripe-like features start to appear suggesting we cross a structural transition temperature. At these temperatures no magnetic signal is observed with the MFM. White bar scale is of $2\,\mu m$. Lower panels: evolution with temperature of the magnetic signal for a different scanning window from that in the top panel. At $16\,K$ the MFM signal still shows no magnetic contrast. As the temperature is further lowered and the superconducting transition ($15\,K$) is crossed a striped pattern starts to appear also in the magnetic signal. This contrast can be associated to an enhancement of superfluid density at certain areas of the sample. White bar scale is of $1.5\,\mu m$. All measurements are done with an applied field of $2.3\,mT$

crossing the surface. They have more or less the same orientation, which roughly coincides with that of the crystallographic axes, and similar, but not identical, size. As the temperature is further lowered, some more stripes appear while the previously present ones remain in the same positions. Spacing between them is not regular along the sample. Those features are only seen in AFM images (MFM gives at these temperatures a flat signal as the one in the $16.3\,K$ image in the lower panel of the figure).

Lower panel of Fig.4.6 shows the evolution of the magnetic signal as the temperature is lowered below the superconducting transition ($15\,K$). As the sample enters the superconducting state a stripe-like pattern appears with the same orientation of that in topographic images (or orthogonal to it). When temperature is further lowered, the stripes remain at the same positions. The striped pattern in the magnetic signal is only observed below the superconducting critical temperature indicating that it is associated to superconductivity.

To explore the relationship between structural and magnetic features we made simultaneous AFM and MFM measurements on the same area. Left panel in figure 4.7 shows an AFM topography of the sample in the superconducting state ($4\,K$, T_c = $15\,K$). A clear stripe-like signature is seen in the image. Right panel of Fig.4.7 shows MFM image for a field of $6.9\,mT$ in the same area as the topographic image (left panel). Blue features observed in the magnetic contrast are found at the same positions of those in the topography, establishing a clear relation between them.

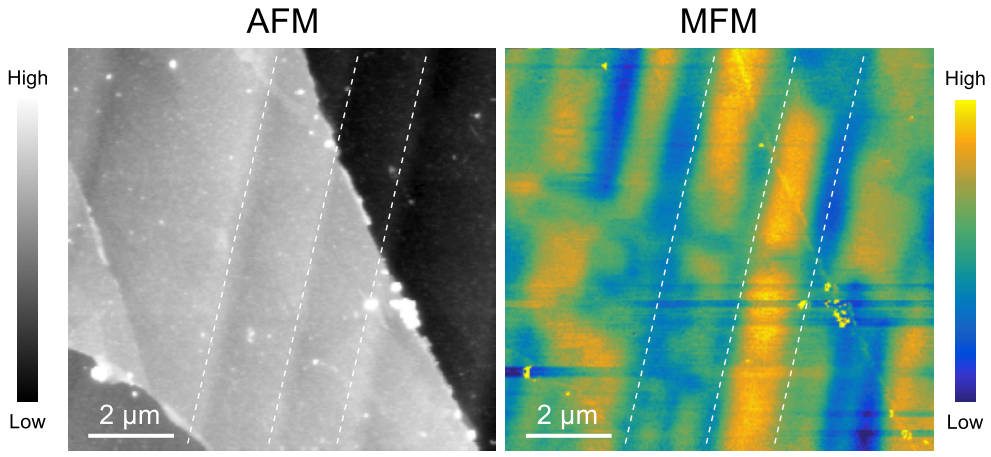

Figure 4.7: Topographic AFM image and the corresponding MFM measurement in a sample of $Ca(Fe_{0.968}Co_{0.032})_2As_2$ glued to a copper sample-holder with silver epoxy. Measurement taken at $4.2\,K$ with an applied field of $6.9\,mT$. Stripe features in topography are directly related with the magnetic signal as indicated by white dotted lines in both figures.

As shown in the lower panel Fig.4.6 this magnetic response appears simultaneously in all the surface below the superconducting critical temperature indicating its relation to bulk superconductivity. Furthermore, the pattern is directly related to the stripe features observed in the topography (Fig.4.7).

These results can be compared to the phase diagram found in Fig.4.3.b for the same concentration. Stripes found in AFM topographies are oriented with the crystallographic axis and appear below the structural transition temperature, indicating that they are produced by structural domains. These experiments are consistent with the superconducting and structural transition temperatures found by Böhmer *et al.* [2016].

4.3 STM studies

4.3.1 Topographic STM images

All STM measurements were performed in the system described in chapter 2 cleaving the samples *in situ* at cryogenic temperatures with the method described in the same

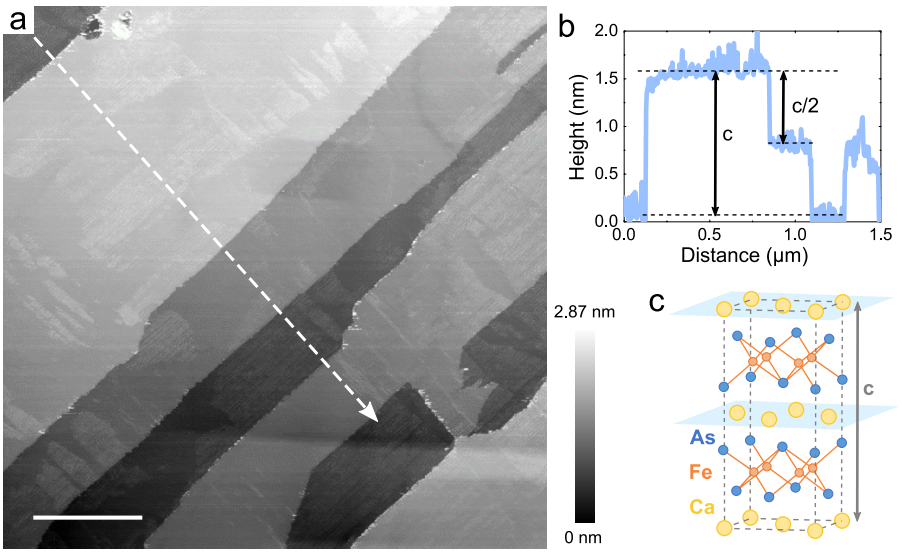

Figure 4.8: a) Large topographic image of the surface of $Ca(Fe_{0.968}Co_{0.032})_2As_2$ taken at $100\,mK$ with $10\,mV$ of bias voltage and $5\,nA$ of tunneling current. White scale bar is of $300\,nm$. The size of the image is almost our whole scanning window (see details of the microscope in chapter 2, Fig.2.13). The difference in height of the terraces seen in the image is of one or half unit cell as shown in the profile in the (b). This is an indication of both the quality of the sample and the performance of the cleaving method. c) Cartoon of the schematic crystal structure indicating the cleaving planes (light blue).

chapter. Very large and atomically flat surfaces can be found in this sample allowing us to take images as big as the whole scanning window of the microscope ($1.8\,\mu m \times 1.8\,\mu m$) with height differences of a few nanometers. One of those surfaces is shown in figure 4.8.a. Different terraces of several hundreds of nm wide can be seen, all of them with differences in height of one or half unit cell as shown in the profile in Fig.4.8.b. Surfaces like the one shown are common in the sample and are a proof of the quality of the same and the performance of our cleaving method.

$CaFe_2As_2$, as a member of the 122 family, is expected to cleave in the Ca plane creating surface reconstructions as explained in chapter 2.5. Cleaving planes are indicated with light blue shades in the schematic cartoon of the crystal structure in figure 4.8.c. The distance between Ca planes is of approximately $0.6\,nm$ (half a unit cell). This distance matches the jumps seen in the profile shown in Fig.4.8.

We ubiquitously find the 2×1 reconstruction over the surface in all measured samples. The two orientations of the reconstruction – corresponding to the two main axes of the Ca sublattice – are found with no noticeable difference in the coverage percents. In Fig.4.9.a reconstruction is oriented only in one of the preference directions. Some defects corresponding to missing rows or extra atoms can be seen randomly distributed over the surface. The profile taken perpendicular to the reconstruction at, top right part of the image, shows the $\approx 0.8\,nm$ spacing between the reconstructed lines, which is the expected value having into account the $\approx 0.4\,nm$ distance between Ca atoms. Fig.4.9.b shows in an schematic way how reconstruction is formed by removing ever

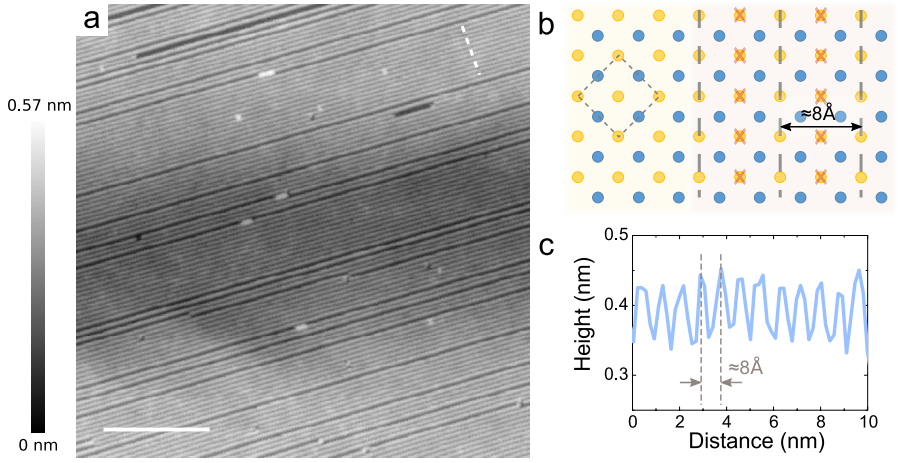

Figure 4.9: a) Topographic image taken at $100\,mK$ with $10\,mV$ of bias voltage and $5\,nA$ of tunneling current. The 2×1 reconstruction is shown here in detail. Scale bar is of $20\,nm$. b) Schematic top view of the crystalline structure showing how the reconstruction is formed along the axis of the Ca-Ca lattice by removing every other row of Ca atoms in the surface. c) Profile over the white dashed line highlighted in (a) showing the spacing between reconstruction rows.

other row of atoms in the calcium lattice.

Apart from surface reconstruction, we have found other topographic features that can be directly associated to crystalline boundaries between twin orthorhombic domains and between tetragonal-orthorhombic domains. In the next section, I will describe the topographic and spectroscopic characterization of these features.

4.3.2 Domain boundaries with STM/S

Orthorhombic-orthorhombic boundaries

In a tetragonal structure (as sketched in Fig.4.9.b), the Ca unit cell is a square and the two directions of the reconstruction are perpendicular to each other. When the orthorhombic distortion is included, the angle between the two orientations is now different from $90°$. This is schematically shown in Fig.4.10.a. The angle between these two directions is directly related to the orthorhombic distortion. Considering a and b respectively the long and short axes of the orthorhombic unit cell, the angle 2α between the two reconstruction orientations is given by $\sin(\alpha) = a/\sqrt{a^2 + b^2}$. The supplementary angle is then described by $\sin(\beta) = b/\sqrt{a^2 + b^2}$. We can therefore obtain an idea of the orthorhombic distortion by measuring the angle between the two main directions of the reconstruction.

To identify orthorhombic domains we make use of high resolution STM topographic images and follow the procedure described by Chuang *et al.* [2010]. In order to do so, we look for areas like the one in Fig.4.10.b, where the two main directions of the reconstruction can be identified. We recalibrate the image by means of the spacing between

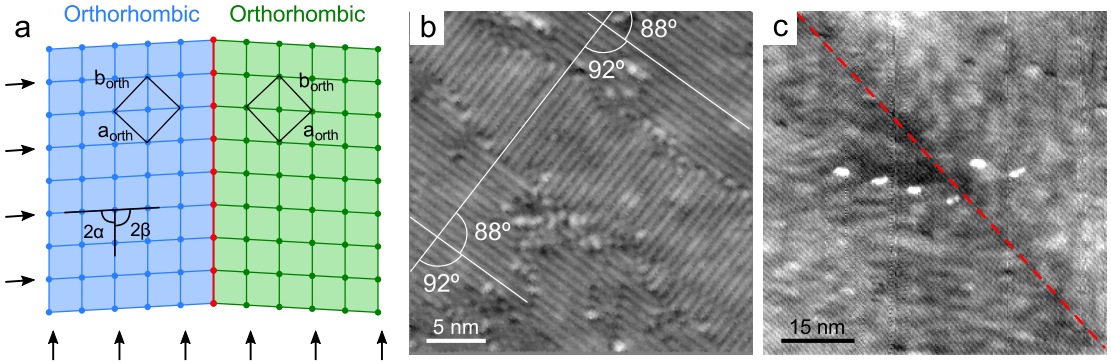

Figure 4.10: a) Schematic representation of the orthorhombic-orthorhombic boundary as depicted in Fig.4.4. Black arrows indicate the possible directions of the reconstruction. Inside an orthorhombic domain the two main directions of the reconstruction are oriented forming an angle $\neq 90°$ as shown in the scheme. b) STM topography showing the two main directions of the reconstruction. The two direction are not orthogonal, indicating that we are imaging an orthorhombic domain. c) STM topography of an orthorhombic-orthorhombic twin boundary. As indicating with the red line in (a), the direction of the boundary is parallel to the reconstruction. The two orthorhombic domains are characterized by the electronic nematic signal of the image which shows a different orientation at each side of the boundary.

lines of the reconstruction, that is the same for both directions. We then measure the angle between these two domains finding a difference of $\approx 2°$ with the orthogonal direction. Using these values we obtain a value of the orthorhombic distortion of $\approx 3\,\%$ finding a clear indication of orthorhombicity. This value is within the order of magnitude of that observed by Böhmer *et al.* [2016] with x-ray diffraction.

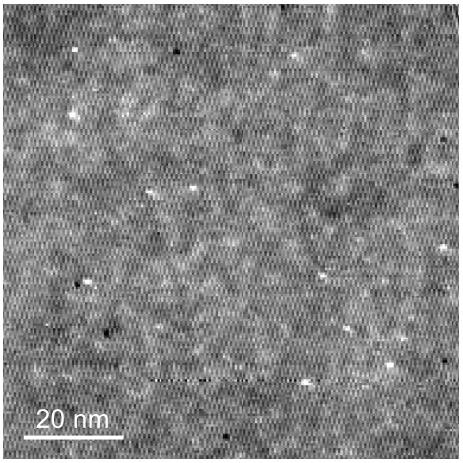

Figure 4.11: Topographic STM image of an area inside an orthorhombic domain where we have performed QPI measurements. It is located far away from the twin boundaries and showing only one direction of the surface reconstruction. Corrugation of the area its around 1 Å.

Fig.4.10.c gives further evidence of orthorhombicity. Fig.4.10 shows a high resolution topography of a twin boundary in our sample. Two orthogonal domains for the nematic order can be distinguished in the top right and bottom left areas of the fig-

ure. The scheme of the twin boundary between orthorhombic domains in Fig.4.10.a includes the possible orientations of the surface reconstruction marked as black arrows. "Horizontal" orientation in Fig.4.10.a will show an angle related to the orthorhombic distortion precisely at the boundary. The "vertical" direction will be parallel to the boundary as in the case of Fig.4.10.c.

With the aim of studying nematicity in this compound we have performed quasiparticle interference measurements. Fig.4.11 presents an area inside an orthorhombic domain far from a twin boundary. We have looked for an area where the reconstruction is as homogeneous as possible to avoid signals that might obscure the interference pattern. The selected window has $100\,nm$ of lateral size and a small corrugation of around 1 Å.

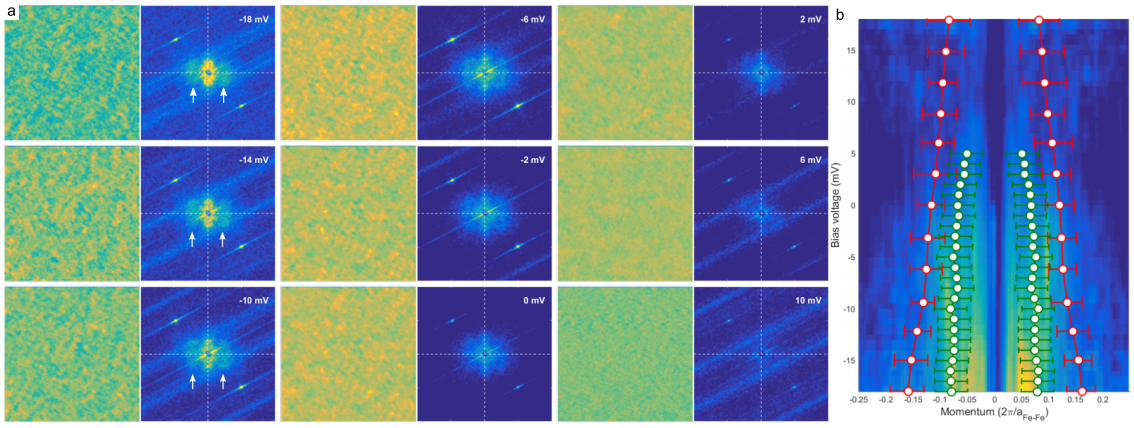

Figure 4.12: a) Zoom of conductance maps at different voltages taken at 100 mK in an area completely covered by the same direction of the 2×1 reconstruction and with very low concentration of reconstruction defects to highlight the real space oscillations created by the QPI pattern. Each map is presented with its 2D-FFT. Fourier transforms show a clear nematic signal of a hole-like band as the one seen in Chuang *et al.* [2010]. Scattering vectors are reduced as the voltage is increased, disappearing completely a few mV over the Fermi level. b) Dispersion relation along the $(0,\pi)$ direction of the FFT. Red circles indicate the result found in Chuang *et al.* [2010].

Spectroscopy for in this area as a function of the bias voltage is presented in Fig.4.12.a. The 2×1 reconstruction present in the topography can be identified as well in the spectroscopic maps, suggesting it has some effect in the conductance. Each map is presented near to the 2D-FFT at the corresponding energy. The Fourier transforms show signatures of the nematic order similar to those reported by Chuang *et al.* [2010]. We clearly identify the reflections or *satellites* of the hole band scattering located at $\approx 8\,a_{Fe-Fe}$ (white arrows in Fig.4.12.a). We can see from the set of 2D-FFT that the intensity of the QPI signal is stronger for the lowest voltages. As the energy is risen scattering vectors move closer to the center of the 2D-FFT and the pattern loses intensity. For voltages above $6\,mV$ is not possible to distinguish scattering vectors anymore. The position of the scattering vectors for different energies is plotted as green circles in Fig.4.12.b. Red circles correspond with the data obtained by Chuang *et al.* [2010] for the non-

superconducting sample. Our results show that the hole band has been moved to lower energies, making the hole pocket at the Fermi level smaller and giving a slightly higher effective mass for the superconducting compound.

Dispersion relation given in Fig.4.12.b shows no signature of the superconducting gap. This is in agreement with the picture proposed by Böhmer *et al.* [2016] where superconductivity has been associated with the tetragonal phase of the sample.

Orthorhombic-tetragonal boundaries

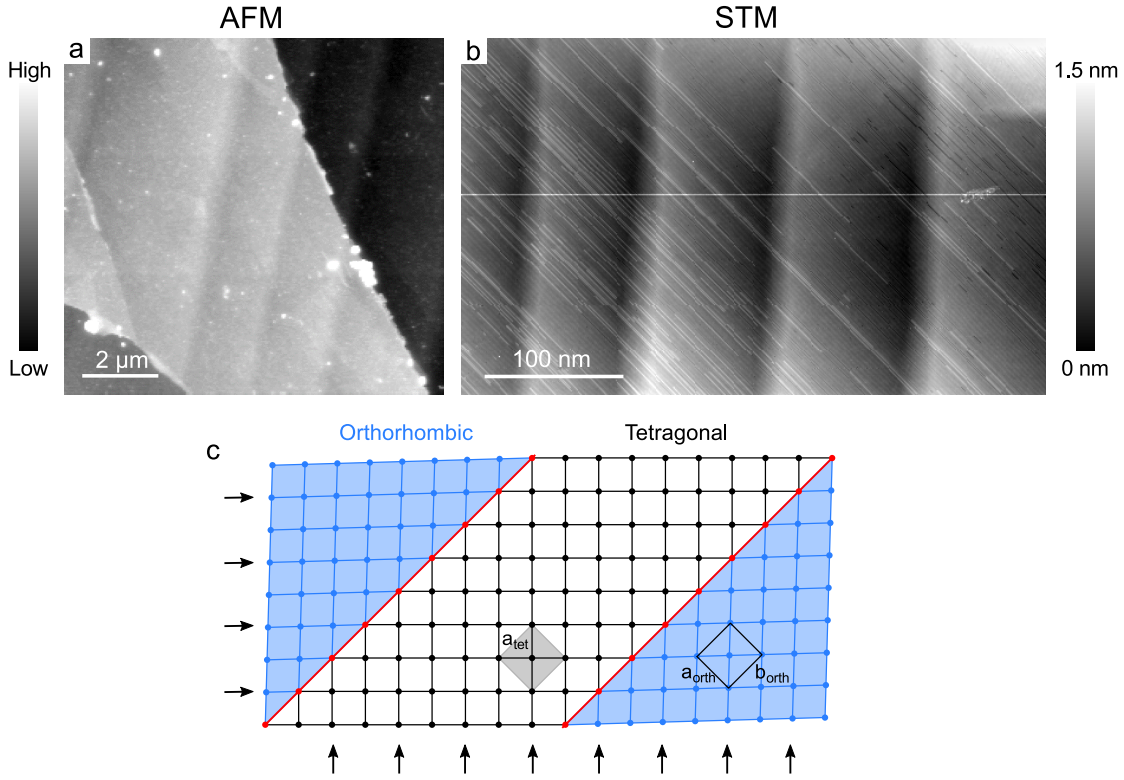

Figure 4.13: AFM image (a) and STM topography (b) of the surface of strained $Ca(Fe_{0.965}Co_{0.035})_2As_2$ annealed at 350°C taken at $T < 4.2\,K$. Both images display roughly parallel elongated features of structural origin. c) Schematic representation of the orthorhombic-tetragonal twin boundaries as depicted in Fig.4.4.b. Black arrows indicate the possible directions of the surface reconstruction, always forming a $45°$ degree angle with the orthorhombic-tetragonal boundaries (red lines).

In large scale topographic images, we often observe striped features aligned with the crystallographic axis, as the one shown in Fig.4.13 b. These features resemble those observed in AFM images at temperatures below the structural transition. Fig.4.13 compares an AFM image taken at $4.2\,K$ (a) with the STM topography acquired at $2\,K$ (b). By looking at the two images we see the same kind of features in both of them. The topographic landmark of this features in STM topography is a small bump of a few angstroms high. Thanks to the STM resolution we can compare the orientation of the

features with the 2×1 reconstruction seen all over the image. Features are oriented at $45°$ with the reconstruction, meaning oriented with the crystallographic axes of the sample. This gives two different orthogonal orientations for the stripe-like features. For instance, a closer look in the top right part of the STM image, reveals a small feature oriented perpendicular to the others, in the direction of the perpendicular crystallographic axis.

Studying STM images we can say that those features are variable in size (from some tens to almost $100\,nm$ wide and several hundred nm length) and that the spacing between them and their distribution over the sample are irregular with no pattern but the alignment with the crystallographic axes. As mentioned, despite they are clearly visible, the difference in height is small and no noticeable change is seen in the surface reconstruction or terraces as those features cross them (see, for instance, Fig.4.15.a).

Fig.4.13.c shows the boundary between orthorhombic and tetragonal domains as shown in Fig.4.4.b. Black arrows indicate the possible orientations of the reconstruction with respect to the boundary. We see that they form an angle of $45°$ just like the elongated features observed in AFM and STM topographies in Fig.4.13. We have seen in temperature dependence AFM (Fig.4.6) that these features correspond to a structural transition. It seems therefore clear that those features are the landmark of the orthorhombic-tetragonal (ORTH/T) boundaries.

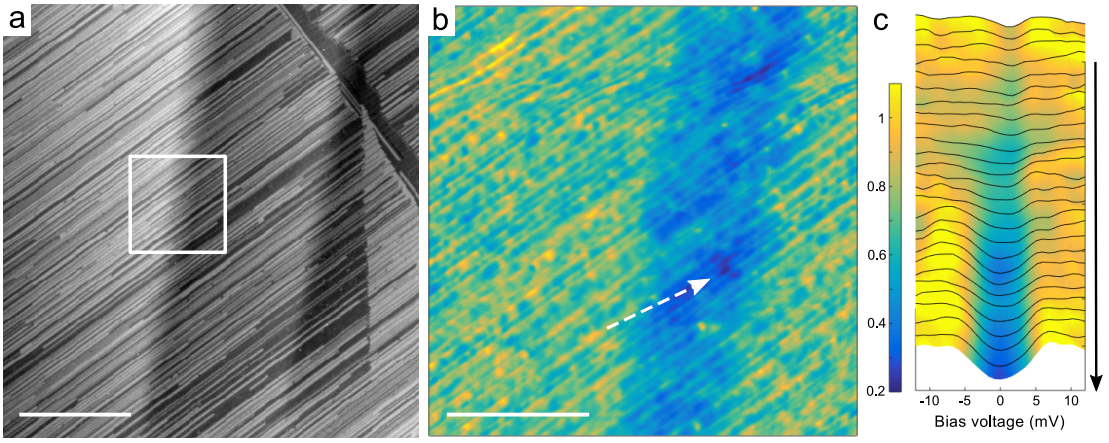

Figure 4.14: a) Topographic image taken at $2\,K$ with $20\,mV$ bias voltage and $5\,nA$ of tunneling current. Surface shows a bump feature similar to those found in AMF measurements indicating the presence of a boundary. Scale bar is of $70\,nm$. b) Zero bias normalized conductance map of the area in the white square of (a) at zero magnetic field. Scale bar is of $20\,nm$. c) Normalized conductance curves along the line in (b) showing a superconducting gap in the expected energy range opening near the twin boundary. Color scales are the same in (b) and (c).

We now analyze spectroscopic measurements in these boundaries. Fig.4.14 shows a detailed spectroscopy over a fully reconstructed area including a ORTH/T boundary. Spectroscopy is taken over the area highlighted with a white square in (a). Fig.4.14.b shows the corresponding zero bias normalized conductance map at zero magnetic field. A strong change in conductance curves related with the topography is seen. Fig.4.14.c

shows the evolution of conductance curves over the white arrow in (b). Outside the blue area, conductance curves are basically flat while a superconducting gap develops as we enter the blue area. The tunneling conductance in the gapped region is not zero at low energies and does not show well defined quasi-particles peaks. Nevertheless, the gap size matches the expected energy value for the T_c ($\Delta = 1.76\, k_B T_C \approx 2.3\, mV$).

Given the previous results, one might expect superconductivity to appear all over the tetragonal domains. Spectroscopic results, however, show that the superconducting gap appears only in small regions that seem associated not to a crystallographic domain but to the boundary between an orthorhombic and a tetragonal domain. We have reproducibly observed these modifications in the superconducting DOS along or close to the the ORTH/T boundaries found in different areas and in several samples but no clear sign of it far from these boundaries.

To further characterize superconducting properties of the sample, we have performed spectroscopic measurements under a magnetic field of $6\, T$ applied perpendicular to the basal plane. Figure 4.15 shows a topographic image taken over a large area where two ORTH/T boundaries are clearly seen in the center of the image at the lower part. (b-c) show a detailed topography of the area highlighted in (a) and the zero bias normalized conductance map of the simultaneously acquired spectroscopy. Spectroscopy is taken over one of the ORTH/T boundaries to image the effect of the magnetic field on the superconducting properties of the sample.

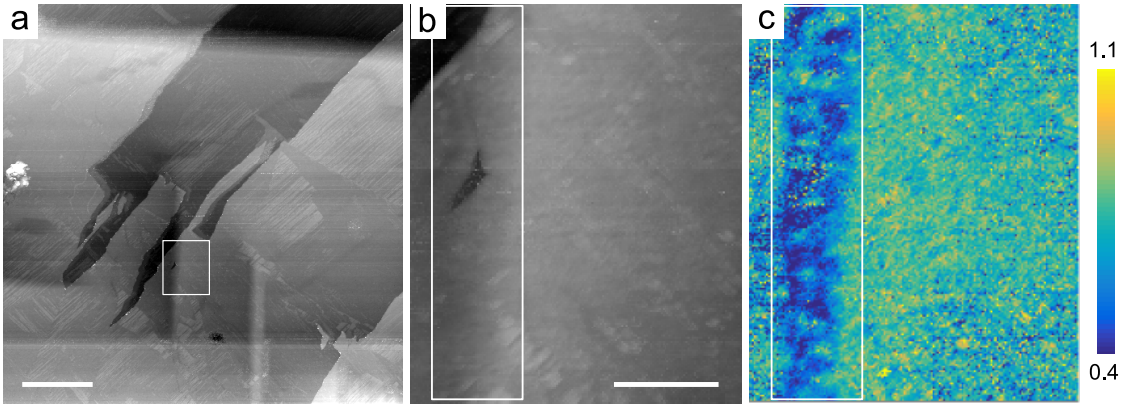

Figure 4.15: a) Large topographic image taken at $2\, K$ with $10\, mV$ bias voltage and $5\, nA$ of tunneling current and $6\, T$ of applied field in the c axis. Scale bar is of $300\, nm$. Two ORTH/T boundaries can be seen in the center-lower part of the image. b) Detailed topography of the square highlighted in (a) taken in the same tunneling conditions. Scale bar is of $50\, nm$. c) Zero bias normalized conductance map taken simultaneously as (b). White rectangles in (b) and (c) indicate the area where superconducting vortices are observed in the sample.

The better visualization of the superconducting gap observed near the ORTH/T boundaries, allows for the observation of superconducting vortices over these areas as shown in the conductance map in Fig.4.15.c. Vortices show the expected intervortex distance for bulk superconductivity at $6\, T$ indicating we are imaging a bulk vortex

lattice. Due to the size of this area, it is not possible to see any order in the vortex positions. Conductance in between vortices does not go to zero and it is very similar to the gap found at zero field.

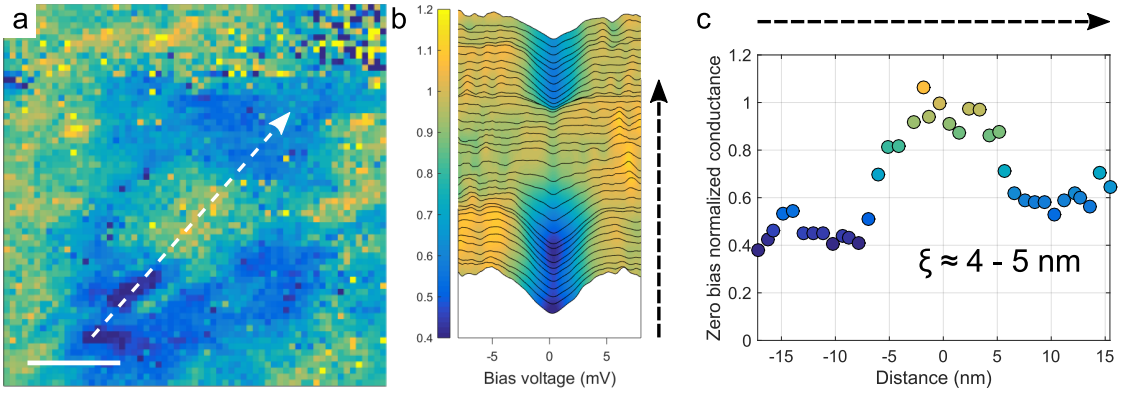

Figure 4.16: a) Zero bias normalized conductance of a detailed spectroscopy on one of the vortices in Fig.4.15.c. Scale bar in the figure is $10\,nm$. b) Normalized conductance curves along the white dashed line in (a). A superconducting gap within the expected energy range opens as one moves away from the center of the vortex. The superconducting gap is not fully opened probably due to pair breaking effects of the surface reconstruction. No sign of core states is seen. c) Zero bias profile of the vortex. We find a value for the the coherence length of $4-5\,nm$ from the profile.

Zero bias normalized conductance map from a detailed spectroscopy on one of the vortices in figure 4.15 is presented in figure 4.16.a. Vortex cores seem to be round and they show no identifiable core states. Fig.4.16.b shows the conductance curves taken along the arrow in (a). Conductance curves outside the vortex are similar to those seen at zero field while inside the vortex they are flat. Normalized zero bias conductance along the arrow in (a) is plotted in (c). From the profile of the vortex we can estimate the core size to be of $\approx 5-6\,nm$. Based on the one band model explained in chapter 3 and assuming the behavior of the core size in the 122 material is similar to that found for other FeBSC, we can extrapolate the behavior of the vortex core to high fields and extract a correlation length of $\xi \approx 3-4\,nm$ using $H_{c2} \approx 20\,T$ found by Ran *et al.* [2012] for the free standing samples.

Fig.4.17 represents an area where several ORTH/T boundaries are close in comparison with other places in the sample (central part of the image marked by a white rectangle in Fig.4.17a). This allows us to observe the superconducting gap in a bigger area and therefore to visualize a larger number of vortices. Intervortex distance is, once again, consistent with the applied field as shown in the lower panel of Fig.4.17.b. 2D-FFT (inset in Fig.4.17.b) shows a blurry hexagon indicating that the lattice is disordered but suggesting that the vortices tend to arrange in a triangular lattice.

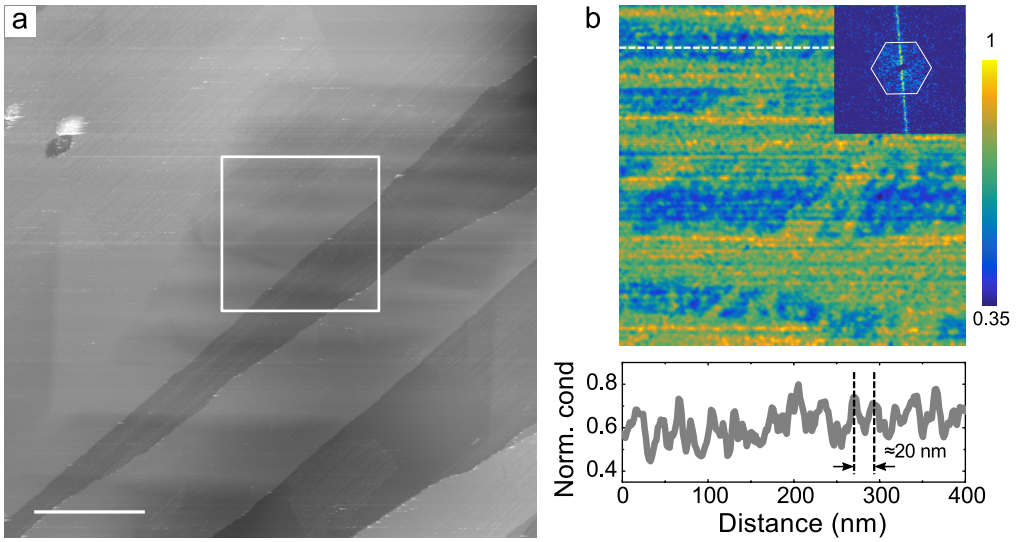

Figure 4.17: a) Topographic image taken in the same tunneling conditions as Fig.4.15. Scale bar is of $300\,nm$. The image shows ORTH/T boundaries in the horizontal direction. b) Zero bias normalized conductance from an spectroscopic measurement acquired in the area highlighted with a white rectangle in (a). Inset contains the 2D-FFT where a blurry hexagon appears as indication of a very disordered triangular lattice. Lower panel profile shows the normalized conductance along the dashed line in the conductance map. In the areas affected by the ORTH/T boundaries superconducting vortices appear with the expected intervortex distance for the $6\,T$ field.

4.3.3 Unreconstructed surfaces

Spectroscopic maps in Figs.4.12 and 4.14 show clear modulations corresponding to the surface reconstruction. This suggests that the reconstruction might have some influence in the observed DOS in STM measurements. In order to investigate this effect we have looked for unreconstructed areas.

As mentioned, reconstruction has two main orientations corresponding to the Ca-lattice axes. Areas where the two orientations are found usually show a more disordered reconstruction pattern. After thorough search following the boundaries between the two domains of the reconstruction we have been able to find unreconstructed areas where the underlying As atomic lattice is exposed. Fig.4.18 shows one of those small areas. Difference in height between the reconstruction and the atomic lattice is seen in the profile in Fig.4.18.b. The $0.2\,nm$ height matches the difference between the Ca plane and the As plane just below it (see schematic cartoon in Fig.4.18.c). A schematic top view of the surface imaged together with a detailed topography of the lattice are shown in 4.18.d, e.

There is extensive literature on the surface reconstruction found in FeBSC (see chapter 2.5). However, to the best of my knowledge, unreconstructed surfaces in the AFe_2As_2 materials have only been reported by Boyer *et al.* [2008]; Song *et al.* [2013] and only for a few lattice constants. I believe our data show for the first time images where a non reconstructed area is unambiguously observed in a compound of the 122

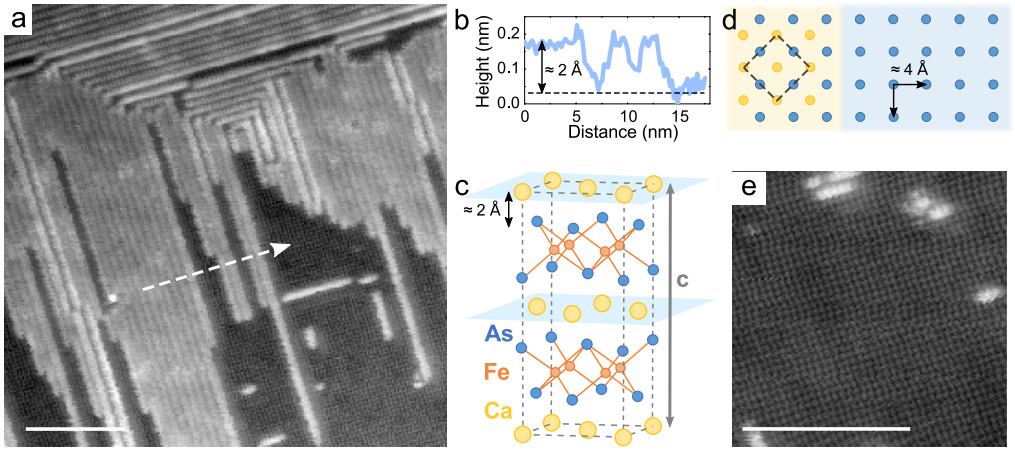

Figure 4.18: a) Topographic image of a reconstruction domain boundary. These areas show a more disordered pattern in the reconstruction leading to unreconstructed surfaces like the one shown in the lower right part of the image. b) Profile along the white dashed line in (a) indicating a height difference of $0.2\,nm$ between the reconstruction and the sublying exposed atomic lattice. c) Schematic cartoon of the crystal structure indicating the $0.2\,nm$ jump between the Ca and the As plane. d) Cartoon top view of the exposed As atomic lattice. e) Detailed topography of the As atomic lattice with some Ca atoms remaining in the surface. Both (a) and (e) were taken at $100\,mK$ with $10\,mV$ bias voltage and $5\,nA$ of tunneling current. Scale bars are of $10\,nm$.

family. The small size and number of these areas suggest that they are metastable and that they can only be imaged if cleaving and subsequent measurements take place at low enough temperatures. In the case of this experiment the cleaving temperature was $4.2\,K$ in order to expose the surface in cryogenic ultra high vacuum conditions. The idea of metastable surface reconstruction is reinforced by the reconstruction disorder observed in those areas where the atomic lattice is seen.

Pair breaking

We have studied the effect of the reconstruction on the tunneling conductance over an area near an ORTH/T boundary where the atomic lattice is exposed. Such area is shown in Fig.4.19.

The large topography in Fig.4.19.a shows several ORTH/T boundaries over a flat surface. The top part of the image shows disorder in the reconstruction and a closer look (Fig.4.19.b) reveals unreconstructed surfaces. Fig.4.19.c shows an unreconstructed area together with some remaining reconstruction rows. Zero bias normalized conductance map of the same area is presented in Fig.4.19.d. Conductance at the center of the area –where we are tunneling directly into the As-As lattice – shows clear superconducting features. The tunneling conductance is not zero at low energies and does not show well defined quasi-particles peaks. Nevertheless, as we mentioned before the gap size matches the expected energy value for the T_c ($\Delta = 1.76\,k_BT_C \approx 2.3\,mV$). Curves in Fig.4.19 show the difference between conductance over the reconstruction (yellow)

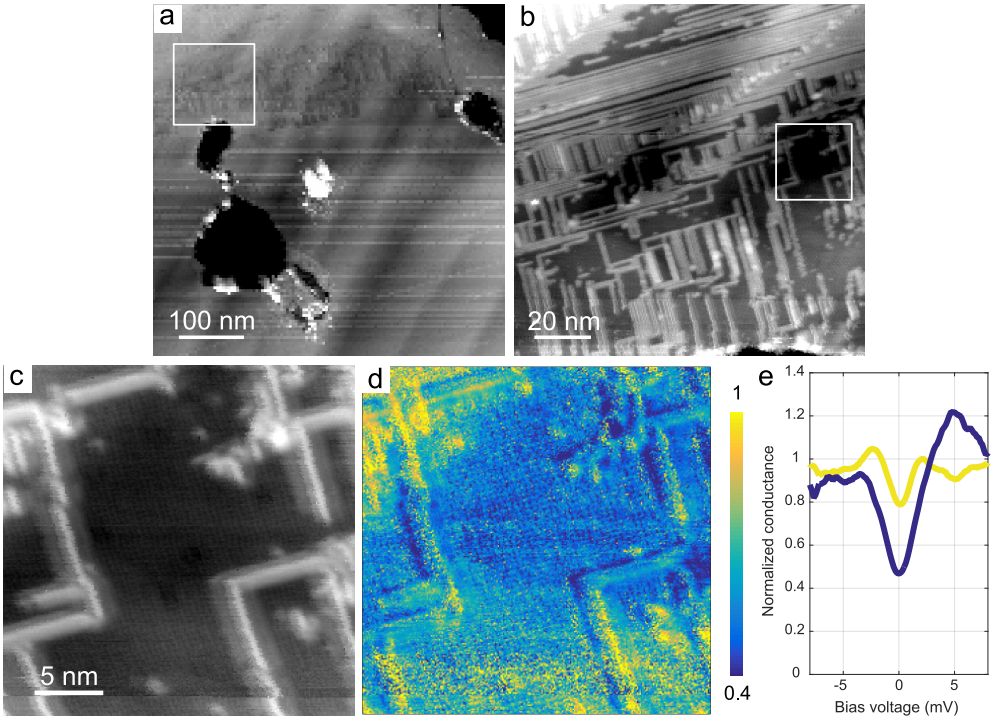

Figure 4.19: a) Topographic image taken at 100 mK with 10 mV bias voltage and 5 nA of tunneling current showing a large area with multiple ORTH/T boundaries. b) Topographic image taken in similar conditions as (a) inside the white square. The modulation corresponding to the ORTH/T boundary is clearly seen going from the top right part of the image to the center. c) Detailed topography of the exposed atomic lattice taken in similar conditions as (a) and (b) in the small area highlighted in (b) with a white square. The area contains an unreconstructed surface near to a ORTH/T boundary. d) Zero bias normalized conductance map taken simultaneously in the same region as (c). It can be seen how the areas where the reconstruction is present show pair breaking effects while in the center of the image where there is no reconstruction, the superconducting gap is seen more clearly. e) Comparison of curves taken at the reconstruction (yellow) and the atomic lattice (blue). Curves are made averaging several curves. The gap shows increased zero bias conductance at the reconstruction.

and the atomic lattice (blue). It is clear that over the reconstruction in-gap tunneling conductance is increased with respect to that directly measured over the atomic lattice.

These observations strongly suggest that the reconstruction induces pair breaking, increasing the in-gap density of states. The finite zero bias conductance observed in the unreconstructed areas can be either due to non fully open gap or other sources of pair breaking effects in these areas.

In Fig.4.20 we plot a conductance curve measured over the exposed As atomic lattice and one taken by an ORTH/T boundary. Curves show comparable features with the same zero bias conductance and gap values. This is consistent with the single T_c value observed by macroscopic measurements and confirmed in MFM measurements (Figs.4.5 and 4.6)

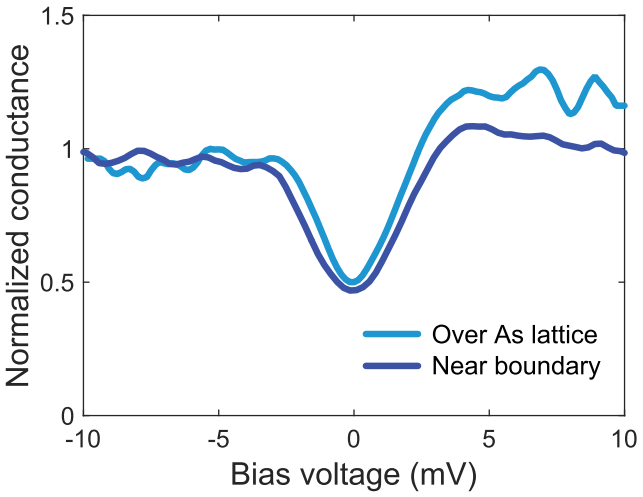

Figure 4.20: Conductance curves one measured over the exposed atomic As lattice and the other near to an ORTH/T boundary. Comparable superconducting gap features are seen in both cases.

4.4 Discussion and conclusions

First phase diagram made for FeAs-grown $Ca(Fe_{1-x}Co_x)_2As_2$ showed that for free standing samples the magnetic and structural transition happen at the same temperature and remain first order down to the lower temperature. Superconductivity develops only for concentrations where the magnetic/structural transition disappears. Therefore superconductivity is always found for a tetragonal structure with no magnetic order [Ran *et al.*, 2012]. In glued samples, strain induces the formation orthorhombic and tetragonal domains for concentrations where the free standing samples remain tetragonal. Those samples show superconductivity that has been associated to the parts of the sample that remain tetragonal (Fig.4.3.b).

Magnetic contrast found in MFM is consistent with this picture. Superconducting tetragonal domains screen the magnetic field creating the patterns seeing in Figs.4.6 and 4.7.

However, the most intriguing result in our measurements is the observation of enhanced superconductivity not over a whole tetragonal domain but at the ORTH/T twin boundaries. Our study demonstrates the presence of these crystalline boundaries and combines structural evidence (from AFM and STM), magnetic signal (from MFM) and superconducting density of states. From the DOS and the observation of the vortex lattice, we conclude that the gap value is the one expected from macroscopic measurements of T_c (see Fig.4.20), suggesting that the order parameter remains of roughly the same size for the whole sample.

We have seen an enhancement of the superconducting signal at the ORTH/T boundaries in $Ca(Fe_{1-x}Co_x)_2As_2$. Along boundaries involving stripe magnetic order in the orthorhombic domains we expect spin to be ill defined. This situation would favor

spin-fluctuation-mediated pairing along the boundary, explanation that agrees with the $s_{\pm}$ scenario proposed for FeBSC (see chapter 1). This scenario is consistent with our observations. A similar proposal has been used to explain results obtained in cobalt doped $BaFe_2As_2$ using scanning squid microscopy [Kalisky *et al.*, 2010, 2011; Kirtley *et al.*, 2010]. They reported an enhancement of the magnetic susceptibility along twin boundaries between orthorhombic domains.

The pair breaking effect of the Ca reconstruction seen in Fig.4.19 can be understood in the frame of an $s_{\pm}$ symmetry of the order parameter where the reconstruction is acting as a non magnetic defect that causes scattering between parts of the Fermi surface with opposite sign. Pair breaking effect of the reconstruction explains why the gap is not fully open, why the density of states does not develop quasi-particle peaks despite being at a temperature much lower than T_c and why superconducting features are not seen over the whole tetragonal domains but only at the boundary whore the superfluid density is enhanced.

Our observations in quasi-particle interference measurements in the orthorhombic phase are consistent with a nematic hole-like band closing above the Fermi level (Fig.4.12.b). We find that the band has a higher effective mass than that found by Chuang *et al.* [2010] in the AF/ORTH phase in the Sn grown samples.

We summarize now the main conclusions of this chapter.

- We study strained samples of $Ca(Fe_{1-x}Co_x)_2As_2$ using low temperature STM. Large scale imaging shows topographic features consistent with ORTH/T boundaries below the strain-induced structural transition. The superconducting gap and a disorder triangular vortex lattice is always much better observed along or close these features. This shows that superconductivity is in some way enhanced at those boundaries.

- We have reported first STM measurements of superconducting gap and disorder triangular vortex lattice in $Ca(Fe_{1-x}Co_x)_2As_2$ that shows bulk superconductivity below $16\,K$.

- A detailed spectroscopic study at atomic scales shows that the surface reconstruction provides pair breaking probably associated to the $s_{\pm}$ order parameter.

- Using QPI, we find electron nematicity in the orthorhombic phase, reinforcing the idea that the two-fold anisotropic electronic properties are quite generic within the Fe based materials.

- We measure the electronic dispersion of a hole band with a slightly higher effective mass than in the non-superconducting sample, suggesting an electronic mediated mechanism behind mass enhancement is also responsible for superconductivity.

CHAPTER 5

Vortex pinning by pair breaking centers in 1144 FeBSC

5.1 Stoichiometric 1144 FeBSC

We have mentioned in the introduction that in the generic phase diagram of FeBSC superconductivity appears upon doping with either holes or electrons (see chapter 1). Only a few stoichiometric compounds are superconductors and all of them with relatively low critical temperatures (see table 5.1). So, in most cases, the highest T_c's among Fe based materials appear in doped systems which present substitutional disorder [see the reviews from Canfield and Bud'ko, 2010; Paglione and Greene, 2010; Hirschfeld, Korshunov, and Mazin, 2011; Efremov *et al.*, 2011; Hosono and Kuroki, 2015; Bascones, Valenzuela, and Calderón, 2016].

Compound	$T_c(K)$	Reference
KFe_2As_2	$3.8\,K$	[Rotter *et al.*, 2008]
FeS	$5\,K$	[Lai *et al.*, 2015]
LiFeP	$6\,K$	[Deng *et al.*, 2009]
LaFePO	$6\,K$	[Hamlin *et al.*, 2008]
FeSe bulk	$\approx 9\,K$	[Hsu *et al.*, 2008; Xia *et al.*, 2009]
LiFeAs	$18\,K$	[Wang *et al.*, 2008]

Table 5.1: FeBSC which are superconductors in their parent compound together with their corresponding critical temperatures and references.

The effect of doping, makes difficult to study certain properties of the material because they also introduce disorder. In the case of FeBSC, most doped compounds (as well as many undoped ones) show structural transitions. Those transitions are also a source of disorder since can produce domains with different orientations, for example orthorhombic domains. In chapter 4 we have shown the effect that structural transitions might have on the LDOS, strongly affecting STM measurements. It is therefore important to study materials without structural transition or substitutional disorder in order to separate their effects on superconductivity and try to understand the mechanism of pairing in these compounds.

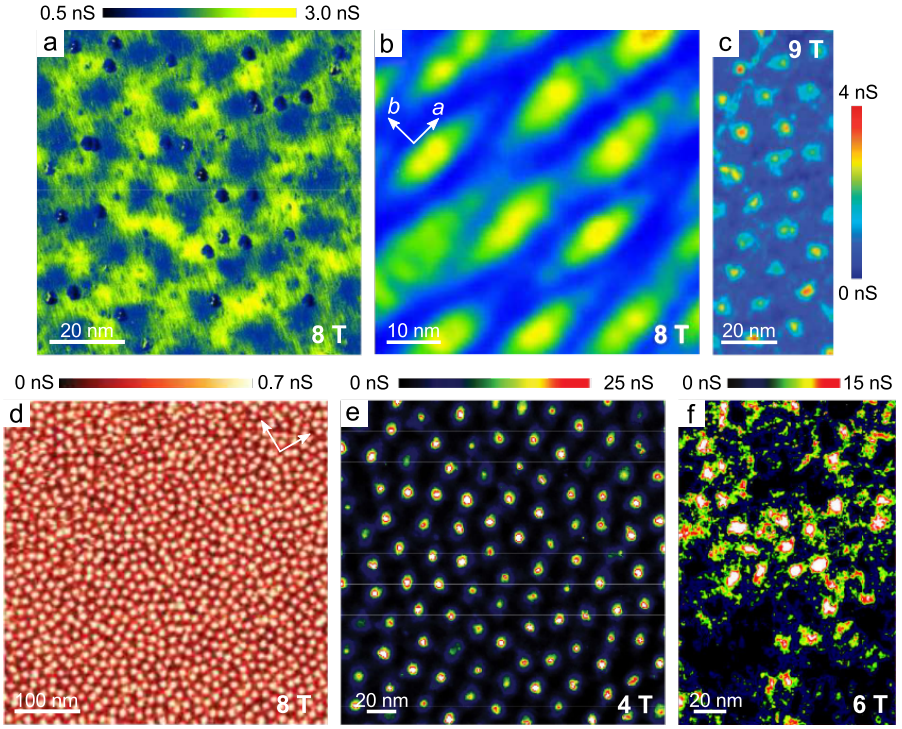

Figure 5.1: STM images of the vortex lattice for different FeBSC: a) $BaFe_{1.8}Co_{0.2}As_2$ at $8T$ from Yin *et al.* [2009], b) FeSe at $8T$ from Song *et al.* [2011], c) $Ba_{0.6}K_{0.4}Fe_2As_2$ at $9T$ from Shan *et al.* [2011], d) LiFeAs $8T$ from Hanaguri *et al.* [2012] and e-f) pristine and ion-irradiated $FeSe_{0.45}Te_{0.55}$ at $4T$ and $6T$ respectively from Massee *et al.* [2015]. All figures have been adapted form the corresponding references.

The relevance of doping is particularly visible when discussing the symmetry of the vortex lattice imaged by STM in several Fe based superconducting systems. Fig.5.1 contains images of the vortex lattice from different STM groups. Experiments done by Yin *et al.* [2009] in $BaFe_{1.8}Co_{0.2}As_2$ (Fig.5.1.a) show isotropic vortices arranging themselves into a disordered lattice. They found no correlation between topographic defects and vortex positions and associate this to a major contribution of bulk pinning. Fig.5.1.b shows the distorted hexagonal Abrikosov lattice found FeSe thin films by Song *et al.* [2011]. The work of Shan *et al.* [2011] in $Ba_{0.6}K_{0.4}Fe_2As_2$ shows again round vortices (Fig.5.1.c). A distorted hexagonal lattice is seen in small areas consistent with the lack of long range order in the lattice. They associate the distortion in the vortex lattice with the tendency of the vortices to pin along lines created by the structural distortion present in this material. In the stoichiometric system LiFeAs Hanaguri *et al.* [2012] reported very disordered vortex lattice (Fig.5.1.d). They proposed that vortex disorder is caused in this compound by the softening of the lattice when increasing the magnetic field. Massee *et al.* [2015] studied the effects of high energy ion irradiation in bulk $FeSe_{0.45}Te_{0.55}$ finding a disordered hexagonal lattice for pristine samples (Fig.5.1.e) that is strongly affected by the defects created by the ions (Fig.5.1.f).

Thus, it is quite a generic observation that vortex lattices in the FeBSC are disordered.

Strong modifications by irradiation [Massee *et al.*, 2015] increase the degree of disorder and there seems to be some correlation of vortex positions with structural domains. However, the origin of the disorder mechanism in the vortex lattice remains unclear. This is puzzling, since the vortex lattices in other family of materials like, for instance, the doped $NbSe_2$, discussed later on in this thesis, but also the nickel borocarbides or bismuth based superconductors, are well ordered, even when the mean free path is low. Therefore, disordered vortex lattices might be a generic and intrinsic feature of the FeBSC. The question is then which of the features of the FeBSC is generating the disordered vortex lattices.

Investigation of this question in the 1144 is not just favored because of the absence of disorder in a high T_c compound. Absence of magnetic or structural transition considerably helps.

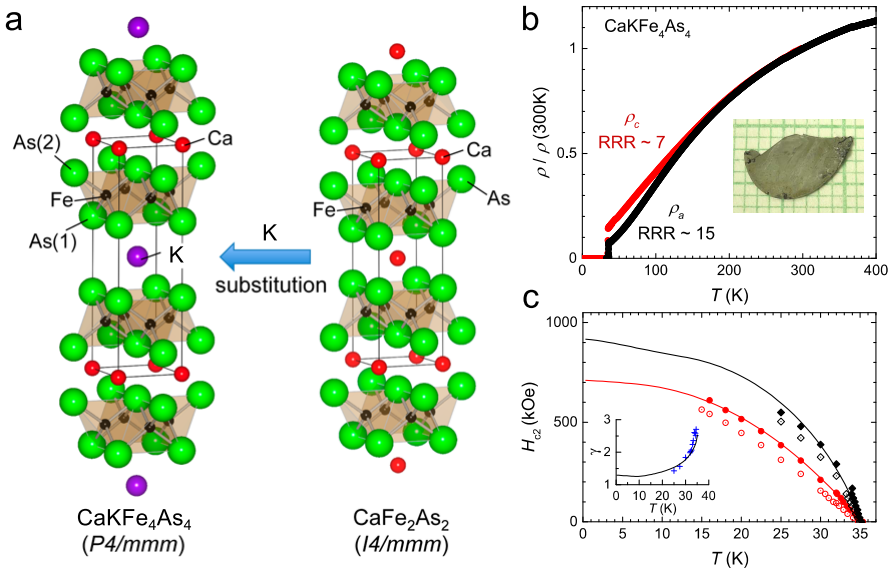

Figure 5.2: a) Adapted from Iyo *et al.* [2016]. Crystal structure of the 1144 family (left) compared to the one of the 122 family. One every other Ca plane in the Ca122 structure has been substituted by a K plane going from a *I4/mmm* structure to a *P4/mmm*. b-c) From Meier *et al.* [2016]. b) Electrical resistivity of $CaKFe_4As_4$ normalized to its room temperature value plotted versus temperature for the in plane and out of plane directions. No sign of structural transition is found down to the superconducting transition temperature at $35\,K$. Inset: picture of a $CaKFe_4As_4$ single crystal grown by solution methods. Background in mm scale. c) Critical field H_{c2} of $CaKFe_4As_4$ as a function of temperature for the in plane and out of plane directions. Extrapolated fields at low temperatures give values above $70\,T$. Inset shows the anisotropic parameter $\gamma(T) = H_{c2}^{\perp}/H_{c2}^{\parallel}$.

In March last year Iyo *et al.* [2016] reported superconductivity in polycrystalline of $CaKFe_4As_4$. As shown in Fig.5.2.a the crystal structure is similar to that of Ca122 but changing every other plane of Ca for a K plane and going from a *I4/mmm* structure to a *P4/mmm*, which has two different As sites. Within a few months our collaborators in the group of Prof. Paul Canfield had grown and characterized pure single crystals

of this material. Meier *et al.* [2016] found for this material low residual resistivity with $T_c = 35\,K$, no sign of a structural phase transition below room temperature and the upper critical field H_{C2} above $70\,T$ (see Fig.5.2.b-c). $CaKFe_4As_4$ gives, therefore a extraordinary opportunity to study superconductivity in a stoichiometric iron pnictide with a remarkably high critical temperature compared to other stoichiometric FeBSC. High quality and large single crystals can be grown out of self flux providing suitable samples for almost any kind of experiment.

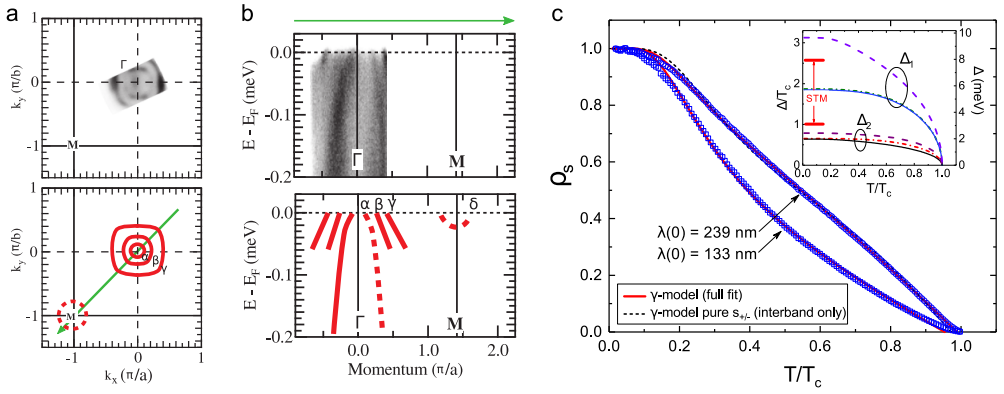

Figure 5.3: a-b) Adapted from Mou *et al.* [2016]. a) Fermi surface (FS) intensity acquired using photon energy of $6.7\,eV$ at $T = 40\,K$ (Top panel). Lower panel: sketch of the FS based on data in the top panel. b) Top panel: measured ARPES intensity along a cut through the Γ point. Cut position is indicated in panel (a) with a green arrow. Lower panel contains a sketch of the band structure based on data in the top panel. c) From Cho *et al.* [2017]. Superfluid density, ρ_s, calculated with $\lambda(0) = 133\,nm$ (open squares) and $\lambda(0) = 239\,nm$ (open circles). Self-consistent γ-mode fits with all coupling parameters is shown using solid lines and interband-only coupling fits shown by the dashed line (for $\lambda(0) = 239\,nm$ case). Inset shows the temperature dependence of the two order parameters obtained from the fits in the main figure. Solid and dash-dotted lines are for the all-parameters fits for the two values of $\lambda(0)$, respectively. The dashed lines are for the interband only fit. The thick red lines mark the spread of the order parameter values determined from the STM measurements as discussed in the text.

ARPES experiments in this compound found that the band-structure is similar to that of $(Ba_{1-x}K_x)Fe_2As_2$. Mou *et al.* [2016] observed in the Fermi surface three hole pockets at the Γ point and one electron pocket at the zone corner (M point), as shown in Fig.5.3.a. While the smallest hole pocket (α) is completely round, the other two (β and γ) are slightly squarish and cross the Fermi level. In all pockets they found the superconducting gap to be nearly isotropic with extrapolated values between $8-13\,meV$. Nevertheless, we should insist that the energy resolution of the ARPES experiments is limited to several meV ($\Delta E = 4\,mV$ in the case of the experiment of Mou *et al.* [2016]). This means that statements of gap size and anisotropy are necessarily limited. β shows the largest superconducting gap among the hole pockets and it is of similar size of that of the electron pocket (δ). Since both bands have similar diameters, they conclude that the nesting between these two bands enhances superconductivity, which is consistent with $s_\pm$ symmetry. They also performed a study with DFT (Density Functional Theory) combined with LDA (Low Density Appoximation) revealing that in addition to

the yz/xz and $x^2 - y^2$ orbital contributions to the FS pockets, there is a strong admixture of $3z^2 - r^2$ states to the α and γ bands.

We have performed the first tunneling experiments on $CaKFe_4As_4$. In a collaboration with the group of Dr. Ruslan Prozorov (Ames Laboratory, Ames Ia, USA) we showed in a combined study of penetration depth (performed in Ames) and STM (carried out in Madrid) evidence for two well defined superconducting gaps and sign changing behavior in agreement with $s_\pm$ superconductivity [Cho *et al.*, 2017]. Superfluid density obtained from penetration depth measurements is shown in Fig.5.3.b. This data is well described using a pure $s_\pm$ model obtaining gap values consistent with those obtained from STM that will be presented in the following sections. London penetration depth results also suggest that superconductivity in $CaKFe_4As_4$ is comparable to that in optimally doped $(Ba_{1-x}K_x)Fe_2As_2$ [see Cho *et al.*, 2016], a system where the symmetry of the order parameter is known to be $s_\pm$. Superconducting gap values found in both London penetration depth and STM in $CaKFe_4As_4$ in this study are also consistent with the observations of Mou *et al.* [2016] in ARPES.

We present in this chapter detailed tunneling experiments on this material, investigating the local variations of the superconducting density of states, viewing the vortex lattice and performing quasi-particle interference experiments.

5.2 Topography and superconducting properties

We use single crystals of $CaKFe_4As_4$ grown from FeAs flux as described by Meier *et al.* [2016]. In order to make sure they are single phase, they were screened as in Meier *et al.* [2016]; Cho *et al.* [2017]; Mou *et al.* [2016]. Crystals are plate like of several millimeters size and several hundreds of microns thick, with the c-axis perpendicular to the surface, being suitable for the *in-situ* cleaving system described in chapter 2. After doing experiment and heating, we verified that the remaining surface is optically shiny and flat.

In Fig.5.4 we show an STM topography of the surface of $CaKFe_4As_4$. The zooms in the upper left and right panels provide the typical images found at the surface of $CaKFe_4As_4$. These surfaces are flat down to fractions of a nm and are found to be large, of the order of the size of our scanning window ($\approx 2\,\mu m$). Within the same image we also show an area with ordered linear arrangements of atomic size (bottom right panel of Fig.5.4). These areas are rare in $CaKFe_4As_4$, covering less than $10\,\%$ of the surface, and are very similar to most surfaces found by STM for the Ca122 Fe-based materials (see chapter 2.5).

Calcium is known to have a large steric pressure which is responsible for the dramatic effects caused by pressure and strain in Ca-based pnictides. This is the case of $Ca(Fe_{1-x}Co_x)_2As_2$, discussed in chapter 4. The $CaKFe_4As_4$ system takes advantage of the regular spacing between Ca and K atoms and their different atomic radii to release

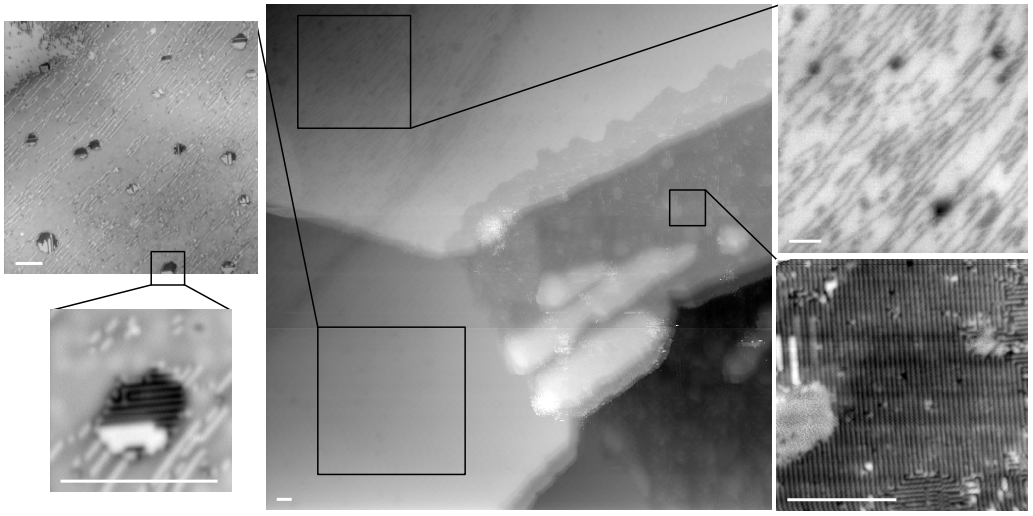

Figure 5.4: Typical features in the topography as measured by STM of $CaKFe_4As_4$. Scale is given by the white bars in every panel, of $20\,nm$ size. In the main panel ($5.6\,nm$ increase in height from black to white) different areas are seen. We have chosen the contrast to highlight three different areas, leaving the black triangle on the bottom right out of the discussion. The upper right and upper left panels provide a zoom on two of these areas. These are most frequently observed on the surface of the sample. The top left image shows a height increase from black to white of $0.85\,nm$. The top right image of $0.3\,nm$. In the top left image, we make an additional zoom into a small hole like defect and show the zoom in the bottom left image. The height difference in this image (from white to black) is of $0.5\,nm$, that is, of just two atoms. The bottom right image is a zoom on an area where we observe a surface reconstruction. This is rarely observed on the surface of the sample.

steric pressure of the Ca ions [Meier *et al.*, 2016]. Given the characteristics of the bonding in these materials and its structural similarities to AFe_2As_2 systems, we believe that the cleaving in $CaKFe_4As_4$ occurs also in between Fe-As blocks. However, the absence of surface reconstruction is remarkable. The release of steric pressure in the crystalline structure might also release tensions at the surface, influencing also the formation of a surface reconstruction.

The large unreconstructed and atomically flat areas of the surface are most likely made of Ca or K atoms, interspersed with small stripes and holes. The stripes, which appear in our images as white lines in upper right panel of Fig.5.4 and black lines in upper right panel of figure 5.4, are just a few atoms wide and point to remanent or missing rows of Ca or K. Within the holes we often observe the lines characteristic of the reconstructed Ca or K surfaces seen in the bottom left panel of Fig.5.4. These are, probably, small areas where the sample cleaved leaving half of the Ca or K atoms behind as happens in Ca122 (see Fig.4.9).

Tunneling conductance shows superconducting features with zero conductance at zero bias over the unreconstructed surface (upper left and right panels of Fig.5.4). In Fig.5.5 we show tunneling spectroscopy in a small window in a non reconstructed area having small topographic modulations shown in the upper left panel of Fig.5.4. These small topographic modulations are several nanometers long and correspond to a step

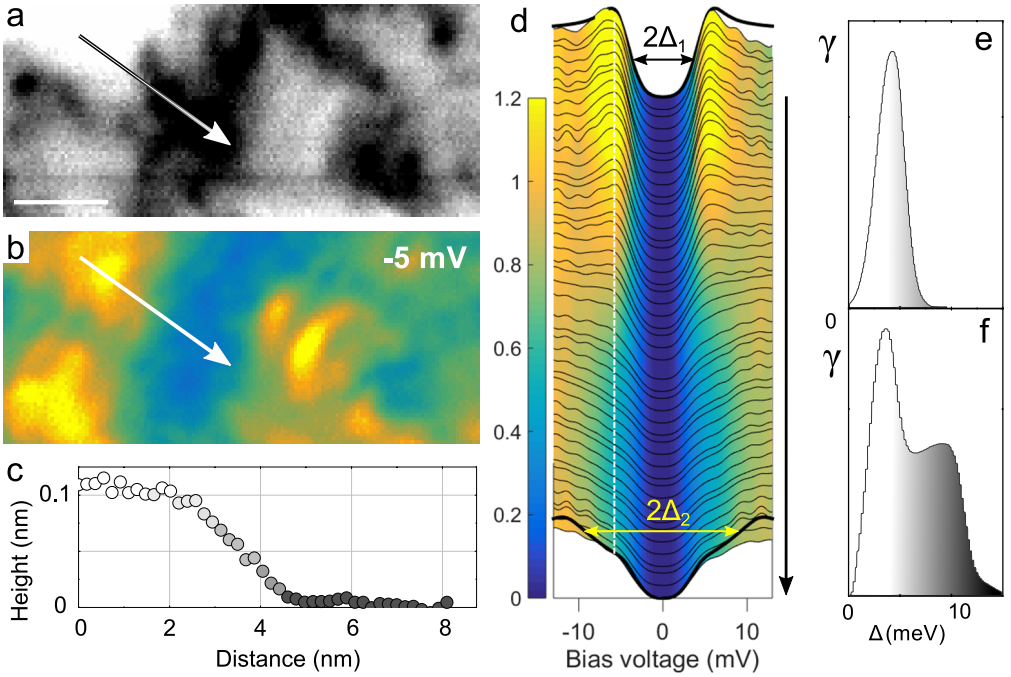

Figure 5.5: (a) Topographic image over an atomically flat area in the surface of $CaKFe_4As_4$. Height profile over the arrow is given in (c). The white scale bar is of $4\,nm$. b) Normalized conductance map over the scanning window in (a) taken at $-5\,mV$. Color scale is given by the white line over the profile in (d). d) Conductance curves taken along the arrows in (a) and (b) showing a spatial variation of the gap structure that is correlated with the topographic image. e-f) Distribution of gap values Δ being the gap values and the relative weight of the corresponding gap values γ. Using the distributions shown in the figure, we generate a superconducting density of states summing over all gaps with the corresponding weights (see text). We convolute the resulting density of states with the derivative of the Fermi function to find the tunneling conductance given by the black lines at the top and bottom of the panel in (d).

height of about an Å. Similar features were previously observed by Shan *et al.* [2011] in unreconstructed surfaces of $Ba_{0.6}K_{0.4}Fe_2As_2$.

The tunneling conductance shows two characteristic gap features as shown in Fig.5.5.d. The LDOS changes with small variations of the topography similar to those along the stripes in the top right panel of Fig.5.4. This effect is clear in the curves taken along the profile in Fig.5.5.a-b and shown in Fig.5.5.d. We observe everywhere two-gap features, but the height of the quasi-particle peaks corresponding to each feature depends on the tunneling plane. In the black regions of the topography, we observe a smeared quasi-particle peak for the smaller gap and a small quasi-particle peak at the larger gap. In the white regions, we observe a high quasi-particle peak for the smaller sized gap and a barely visible shoulder for the larger sized gap. To make this more quantitative, we calculate the tunneling conductance assuming a density of states of the form

$$LDOS \propto \sum_{\Delta_i} \gamma_i \,\mathrm{Re}\left(\frac{E}{\sqrt{E^2-\Delta_i^2}}\right) \tag{5.1}$$

and convolute the result with the derivative of the Fermi function. We have previously used this approach to discuss gap distributions in other systems (see section 1.2.2 in the introduction chapter). Using the distributions γ_i shown in Fig.5.5.e-f, we can reproduce the main features of the conductance curves in the white and black areas of the topography as can be seen from the top and bottom black curves in Fig.5.5.d. It is clear from the distribution that at the white areas there is mostly a contribution from only one gap while for the dark areas the distribution has two clear peaks with larger weight of the small one. The values obtained are of $\Delta_1 \approx 3\,meV = 0.6\,\Delta_0$ and $\Delta_2 \approx 8\,meV = 1.5\,\Delta_0$ (with $\Delta_0 = 1.76\,k_B T_c$).

The LDOS observed by STM is affected by the part of the Fermi surface into which we are tunneling through the tunneling matrix elements (see section 2.2.1). If this contribution changes as a function of the atomic plane it will lead to changes in the observed density of states and therefore variations in the observed weights γ_i of Δ_1 and Δ_2 in Eq.5.1 [Shan *et al.*, 2011; Hoffman, 2011; Suderow *et al.*, 2014], explaining the variations seen in Fig.5.5.

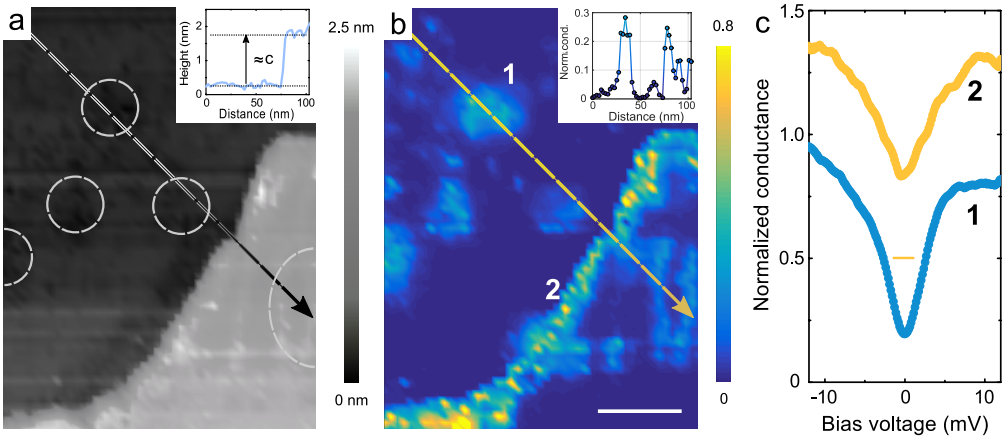

Figure 5.6: a) Topography with the height changes given by the bar on the right. Profile along the arrow in the image is shown in the inset. The step height is of order of the unit cell c-axis size, marked by a black arrow in the inset. b) Zero bias normalized conductance map in the same area, with the conductance given by the bar on the right. White bars are $20\,nm$ long. Tunneling conductance curves in the marked areas (1,2) are given in the left panels. These are shifted for clarity, providing the zero conductance position by horizontal bars of the same color.

This situation changes close to defects that imply steps of a sizable fraction of the lattice constant, as for example the holes discussed previously or large steps sometimes appearing on the surface. These defects influence the tunneling conductance, producing spectra with finite zero bias conductance as those shown in Fig.5.6.c. For example, in Fig.5.6.b we show a map that has, over most of the image, zero conductance at zero bias. However, close to steps or holes, we observe an increased zero bias conductance.

It is useful to review the influence of defects on the zero bias conductance in other FeBSC superconductors. In the Fe(Se,Te) materials, interstitial Fe impurities produce a

strong zero bias peak indicating strong pair breaking [Yin *et al.*, 2015]. In FeSe, superconductivity is modified at twin boundaries [Song *et al.*, 2012]. In both cases, it has been proposed that electronic modifications (either by magnetism or changes in the atomic arrangements) around these defects lead to modifications of the superconducting properties. In $(Ba_{1-x}K_x)Fe_2As_2$ and in similar doped compounds, the tunneling conductance varies strongly with position [Hoffman, 2011]. In the case of $BaFe_{1.86}Co_{0.14}As_2$, this effect has been associated to the distribution of dopants in the sample [Massee *et al.*, 2009a]. Finally, in LiFeAs, in-gap states are found at native defects on the surface, but the value of the zero bias conductance remains small in those defects [Grothe *et al.*, 2012].

In the framework of $s_{\pm}$ superconductivity, a material with different bands crossing the Fermi level can present scattering between bands having order parameter components of opposite sign [Suderow *et al.*, 1999; Kogan, 2009; Efremov *et al.*, 2011; Hirschfeld, 2016; Cho *et al.*, 2016]. This scattering leads to a finite density of states at the Fermi level around defects and pair breaking.

Stoichiometric $CaKFe_4As_4$, presents two Fe-As layers with interstitial atoms alternating between Ca and K (see Fig.5.2). The pair breaking we find is localized along defects that are identified in the surface topography and extend only a few nm along large step edges or holes. Our data strongly point out that large size defects produce scattering between parts of the Fermi surface with order parameter components of opposite sign.

5.3 Superconducting vortices

5.3.1 The vortex lattice

We focus now in the study of the individual vortices and the vortex lattice. When we apply a magnetic field to the sample, vortices appear over the whole surface. Fig.5.7 contains the vortex lattice imaged for fields between $1\,T$ and $8\,T$ in different scanning windows. For all magnetic fields where we have imaged the vortex lattice, we find that the lattice shows short range hexagonal order with defects appearing in the vortex lattice every few lattice spacings (see Fig.5.7). The evolution of the intervortex distance as a function of the applied magnetic is plotted in the lower right panel in Fig.5.7 and matches the expected distance for a hexagonal Abrikosov lattice (Eq.1.10).

From the autocorrelation functions, shown as insets in each image, we can see that the vortex lattice is hexagonal. We use here the autocorrelation function instead of the 2D-FFT because it mostly captures the nearest neighbor arrangements, whereas the full 2D-FFT provides the average behavior over the whole image (and is often just circular). Disorder of the lattice is clear from the blurry spots in the autocorrelation function. We will discuss the behavior of the lattice below and focus first on the shape of the vortex cores.

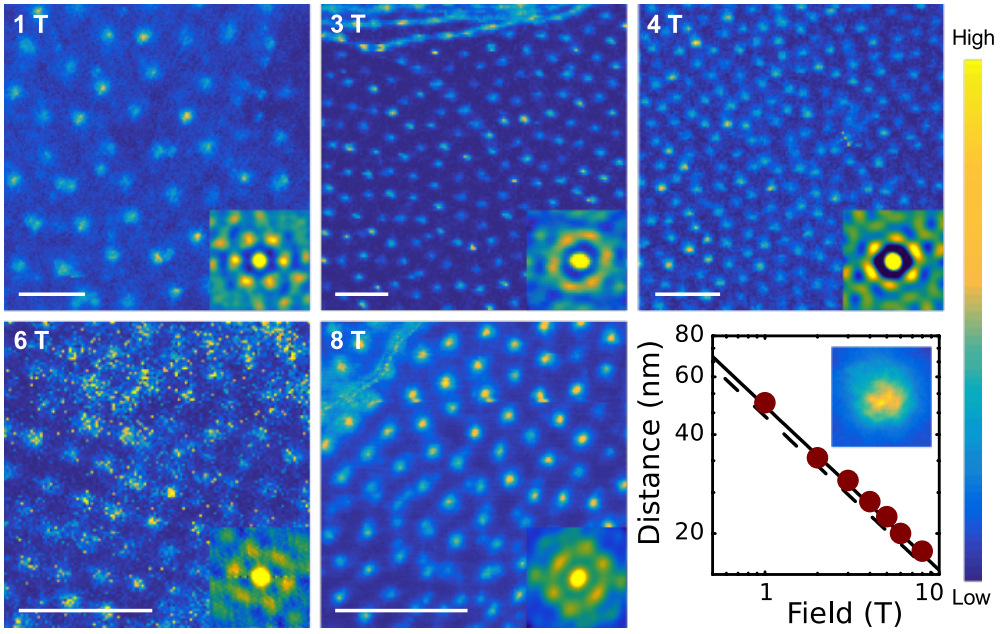

Figure 5.7: Zero bias conductance maps in fields between $1\,T$ and $8\,T$ taken at different positions. The color bar on the left provides the zero bias normalized tunneling conductance. The white bar in the images is of $82\,nm$ size. The insets in the images show the autocorrelation function of the images. Note that the lattice remains hexagonal, within first nearest neighbors, over the whole magnetic field range. The lower right panel shows the intervortex distance, obtained from the autocorrelation function, vs the magnetic field and the black lines are the expected intervortex distance for hexagonal (solid line) and square (dashed line) lattices; the inset shows the zero bias conductance map of an isolated vortex.

5.3.2 Vortex core states

In the case of $CaKFe_4As_4$ vortices are generally round (as seen in Fig.5.7), showing no sizeable in-plane anisotropy. In the doped Fe pnictides, vortex cores are often round, although it is not clear if this is due to defect scattering or if it is an intrinsic property of the material itself [Hoffman, 2011]. Some experiments, like the one done by Song *et al.* [2011] in FeSe showed a different behavior with elongated vortex cores produced by a strong in-plane electronic anisotropy (see for instance Fig.5.1). Hanaguri *et al.* [2012] also reported a four fold anisotropy in vortex cores of LiFeAs which they associate to the anisotropy of the Fermi surface found in ARPES. The result found here in stoichiometric $CaKFe_4As_4$ shows that anisotropies in the in-plane gap and Fermi surface of $CaKFe_4As_4$ are small.

When comparing tunneling conductance at zero field and at $8\,T$ in between vortices we found very similar curves, as can be seen in Fig.5.8.a. Features corresponding to both gaps are still clear and the enhancement of zero bias conductance is negligible.

This behavior of the zero bias conductance between vortices is different in $CaKFe_4As_4$ to that observed in other multiband materials like MgB_2 or $NbSe_2$ where it is strongly affected by the applied magnetic field. The superconducting density of states remains

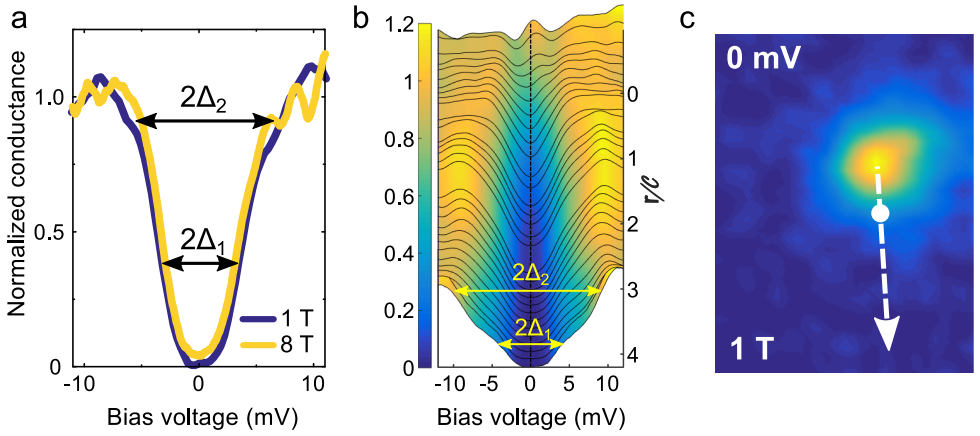

Figure 5.8: a) Normalized tunneling conductance in between vortices taken at $1\,T$ (dark blue curve) and at $8\,T$ (yellow curve). Both curves are very similar and there is almost no difference in the zero bias values. b) Normalized conductance curves taken along the profile indicated in (c). In the vortex core center there is a clear peak located at positive bias. As we move away from the core both gaps Δ_1 and Δ_2 start to be visible until they are fully opened at around $2.5\,C$, being C the vortex core size extracted with the model presented in chapter 3 for $1\,T$. Remarkably, and in agreement with our model, superconducting properties start to manifest at a distance C from the core center. c) Zero bias normalized conductance map of a vortex taken at $1\,T$.

largely unaffected by the magnetic field (see discussion in chapter 3). Although the range of magnetic fields studied here is small compared to H_{c2} (just $10\,\%$).

Nakai, Ichioka, and Machida [2002] analyze the DOS in between vortices for two-band superconductors and show that, if the pairing interaction in one band is nearly absent, small magnetic fields produce strong increases in the DOS. The observed absence of magnetic field dependence of the DOS in the 1144 compound indicates rather that the pairing interaction is strong in all bands.

If we now examine the evolution of the tunneling conductance from the vortex core to the gapped region in between vortices we find the curves shown in Fig.5.8.b with similar results in all magnetic fields. The upper curves in the figure show a a small peak for positive bias voltages at the vortex core center indicating electron-hole asymmetry. This peak at the vortex center gradually evolves from the asymmetric shape and increased conductance close to zero bias to the two-gap tunneling conductance in between vortices. It is worth pointing out that the superconducting features are established at a distance from vortex center of order of the vortex size C calculated for the corresponding field using the model described in chapter 3.

As explained in chapter 1.2.3 vortex core peak can be discussed in terms of quantized vortex core levels predicted by Caroli, deGennes, and Matricon [1964]. When the value of $\Delta^2/2E_F$ is not negligible [Hayashi *et al.*, 1998] the peak of the localized state can appear at a finite voltage, as has been reported in some compounds. For this to happen one needs to have values of $\Delta^2/2E_F$ in the mV range and $k_F\,\xi$ to be of the

order of one. This is the case of some FeBSC where a significant mass enhancements have been observed in a variety of measurements for x values close to optimal doping [see experiments on $BaFe_2(As_{1-x}P_x)_2$ done by Hashimoto *et al.*, 2012; Walmsley *et al.*, 2013]. Estimations of E_F from superfluid density measurements in this material lead to values in the range of a few hundred K [Hashimoto *et al.*, 2013]. All this suggests that $k_F\,\xi$ might be close to one in some of these systems.

In the particular case of $CaKFe_4As_4$, the conductance at the peak has a small value in comparison with that found in other materials (see Fig.5.8.b). Also, in $CaKFe_4As_4$ the peak is located at positive values of the bias voltage (tunneling into empty states of the sample), whereas it occurs at negative bias voltages in $(Ba_{0.6}K_{0.4})Fe_2As_2$ and in LiFeAs (tunneling into occupied states of the sample) as shown by Shan *et al.* [2011] and Hanaguri *et al.* [2012] respectively. It is not clear that in the case of $CaKFe_4As_4$ the shape of the bandstructure could explain the localized state in the vortex core. We will comment on this point when discussing the bandstructure below. We might advance that the top of the α hole band is close to the Fermi level in this compound, which might favor the observed peak at positive bias in 1144 (although calculations are needed to shed further light into this issue).

5.4 Pair breaking and vortex pinning

Let us focus again on the vortex lattice to discuss its behavior. As shown above, the autocorrelation functions have six-fold symmetric features, indicating that the underlying order is hexagonal over the whole magnetic field range studied. However, a look into the images in Fig.5.7 tells us that the vortex lattice is not well ordered. The effect of the topography is particularly clear in the alignment of the vortices at the top and center of the $3\,T$ image.

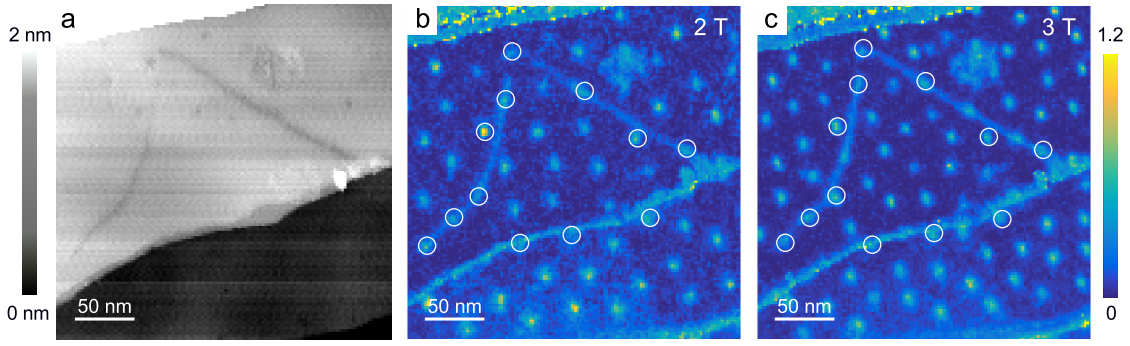

Figure 5.9: a) Topographic image of an area with two defects in the shape of lines near a step of half a unit cell. b-c) Zero bias normalized conductance maps of the area in (a) taken with applied fields of $2\,T$ and $3\,T$. From the conductance maps it can be seen that both lines and the step produce pair breaking. As the field is risen the vortex density in the image increases accordingly, however the vortices highlighted with white circles remain pinned to the pair breaking centers.

Consistently, autocorrelation functions show distortions from the hexagonal order for those images where the lattice is most affected by the topography ($3T$ and $8T$ images in Fig.5.7). The relatively blurry and large spots also point to disorder in the lattice.

Fig.5.9 shows zero bias conductance maps for the same area at $2T$ and $3T$, both of them with the expected density of vortices for each field. Left panel of the figure includes the topographic image taken at the same area where we find a particularly large amount of defects. In particular, the half unit cell step and the line defects seen in the topography produce a finite zero bias conductance shown in the Figs.5.9.a-b. The line defect produces a triangular form, that pins vortices to it. This finite zero bias conductance is a manifestation of the pair breaking caused by defects explained in Fig.5.6. We mark in the image taken at $2T$ some vortices marked with white circles that are joined by this finite zero bias conductance. As the field is increased to $3T$ the vortices remain at the same positions meaning that vortices are pinned to locations with finite zero bias conductance. This clearly shows that the pair breaking defects act as pinning centers for the vortex lattice. Here the effect is particularly strong due to the presence of extended defects where individual vortices are strongly pinned. This gives lines of pinned vortices that surround regions where vortices show a hexagonal symmetry that reminds a polycrystaline vortex lattice.

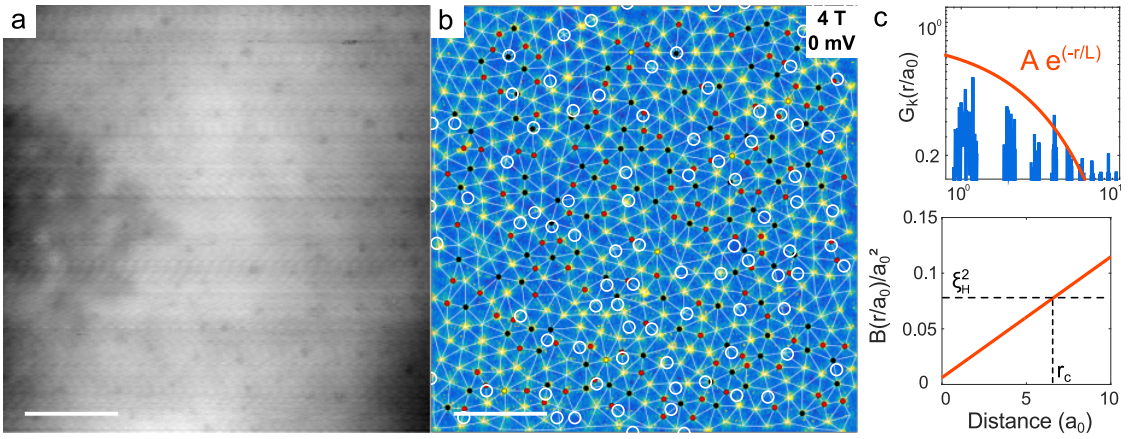

Figure 5.10: a) Topographic image taken at $4T$ with similar tunneling conditions as the ones in Fig.5.4. b) Zero bias normalized conductance map in the same area (same as the $4T$ image in Fig.5.7) showing the Delaunay triangulation. White circles highlight the position of hole-shaped defects in the topography. Scale bars are of $120\,nm$ c) Positional correlation function for the vortex positions (top) and displacement correlator calculated from the vortex positions in the triangulation.

Fig.5.10 shows a different situation. Here we found a region with many small holes randomly distributed (see topography of Fig.5.10.a). We should bear in mind that those small holes in the topography produce pair breaking as explained in Fig.5.6. Fig.5.10.b shows the vortex lattice measured in this region at $4T$. Here, we find an amorphous like vortex lattice indicating that the lattice is collectively pinned. Collective pinning takes place for weak pinning centers at large concentration so that each vortex is influenced by several pinning centers [Larkin and Ovchinnikov, 1979].

In order to quantify the disorder in the vortex lattice we have Delaunay triangulated the image. From the analysis, we obtain a hexagonal vortex lattice with a large amount of defects. Roughly the same number of five-fold and seven-fold vortices, that sums up to nearly the number of vortices with six nearest neighbors and we can even identify some four-fold and eight-fold defects.

To further characterize this disorder we have calculated the positional $G_k(r)$ correlation function of the lattice as explained by Guillamón *et al.* [2015]. Result is shown in the top panel 5.10.c. $G_k(r)$ decays as an exponential having a signal of the order of 0.1 after a few lattice spaces. From the exponential fit we can extract a correlation length $L \approx 3.5\,a_0$, being a_0 the expected intervortex distance for that field. The displacement correlator $B(r)$ quantifies the distance dependence of the deviations in the vortex positions with respect to a perfect hexagonal lattice. It can be calculated from $G_k(r)$ as $B(r) = -(k^2/2)\log[G_k(r)]$ with $k = 4\pi/\sqrt{3}\,a_0$ [see Giamarchi and Le Doussal, 1994]. We find that the displacement correlator increases linearly with distance, indicative of the collective pinning regime for small distances. Using Guillamón *et al.* [2015] and Giamarchi and Le Doussal [1994], we can measure the point where the displacement reaches, on average, the coherence length. According to Larkin (si no la encuentras, deja la referencia al paper de Isabel), this provides the size of the smallest bundles that move coherently on application of a current. We find $r_0 = 5 - 6\,a_0$.

The vortex lattice at $4\,T$ is completely disordered after a few $(5 - 6)$ lattice spacings. Thus, the pinning centers we have unveiled in this material influence the whole pinning landscape, from isolated vortex pinning when the density of defects is comparable to the intervortex spacing, up to collective pinning, where the vortex lattice is denser than the arrangement of pinning centers.

5.5 Quasi-particle interference

STM allows to explore the bandstructure of a material through quasi-particle interference analysis (see chapter 2.2.4). In $CaKFe_4As_4$ we have looked for a suitable area to perform this kind of measurements. Fig.5.11 presents a topographic image of the selected scanning window. It has a lateral size of $77\,nm$ which gives a reciprocal space resolution of $1/77\,nm^{-1} \approx 0.013\,nm^{-1}$ (that is $\approx 0.25\,\%$ of the first Brillouin zone). The spacing between voltage points in the tunneling conductance curves is of $0.625\,mV$.

Same figure presents a series of conductance maps taken at the same scanning window. Scattering of quasi-particles between different parts of the Fermi surface creates the oscillatory patterns seen in conductance maps. Analyzing these maps in the reciprocal space as a function of energy we obtain the energy dependence of the scattering vectors as explained in section 2.2.4.

Fig.5.12.a-i contains a series of 2D-FFT of the conductance maps at different bias

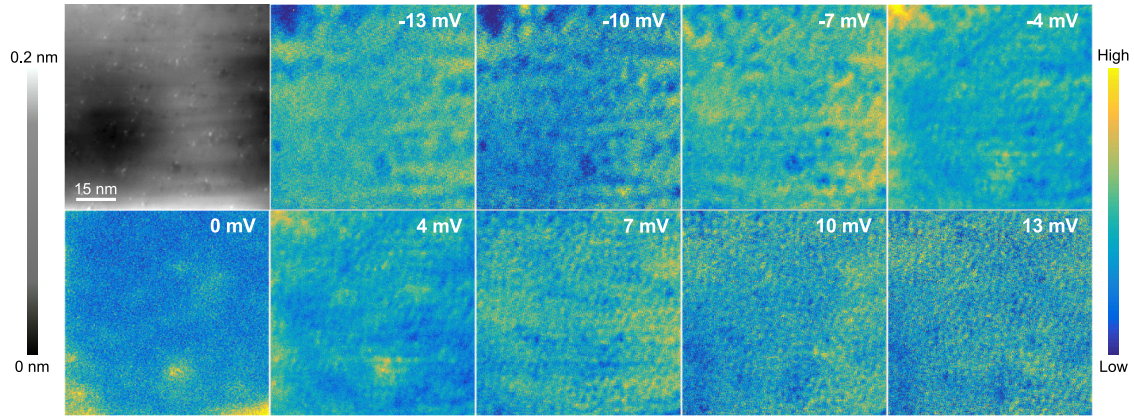

Figure 5.11: Topographic image taken at $800\,mK$ with a tunneling current of $2\,nA$ at a bias voltage of $30\,mV$ and conductance maps in the same scanning window taken at different bias voltages. Scattering between different parts of the Fermi surface creates the oscillatory pattern seen in conductance maps.

voltages where a clear evolution of the scattering vectors is seen. At each 2D-FFT we indicate with a white circle the value of the scattering vector for each energy. Tracking the energy dependence of the scattering vector we can obtain their dispersion relation $\vec{q}(E)$. In Fig.5.12.j we plot this variation and compare it with the results found in ARPES experiments on the same compound by Mou *et al.* [2016] included in Fig.5.3.a-b.

We show in this figure that scattering occurs preferentially between the two outer hole pockets found around the Γ point (Fig.5.12.j). We observe that below the Fermi level the scattering occurs between bands that follow parallel to each other when increasing the energy. This provides a scattering wave vector that is roughly constant with energy, having a small variation just below the superconducting gap where they start to deviate from this behavior. This is consistent with what ARPES observe for the γ and β pockets. Above the superconducting gap, where ARPES provide no data, we see that scattering vectors increase with increasing energy, which shows that one of the bands closes above the Fermi level. In the top and bottom insets we depict a schematic view of the scattering process we see and schematic draw of the three hole pockets seen in ARPES [Mou *et al.*, 2016].

In our measurements, close to the Fermi surface, we see no scattering corresponding to the α band but only between the β and the γ bands. Scattering amplitude seen in quasi-particle interference depends not only on the possible nesting but also on the shapes of the Fermi surface and the densities of states in each band (see 2.2.4).

QPI pattern in Fig.5.12 shows a slightly anisotropic signal with four slightly brighter spots. This is an effect enhanced through the symmetrization process (see section 2.2.4). Small topographic defects seen in the topography (see Fig.5.11), are oriented in a preferred direction producing wide spots in the FFT. These spots are responsible for the small anisotropy in the signal.

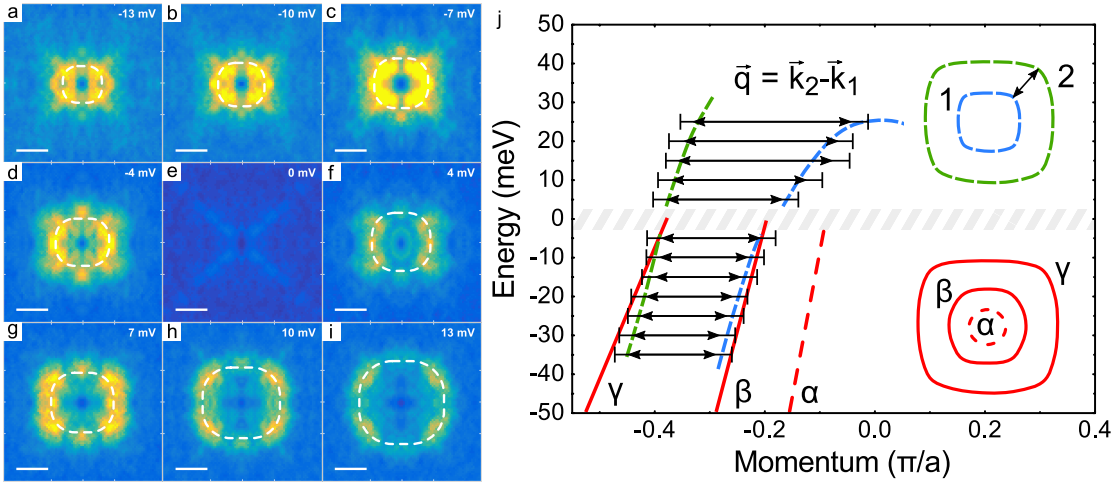

Figure 5.12: a-i) Symmetrized 2D-FFT of the conductance maps in an area of $77\,nm \times 77\,nm$ as a function of energy. There is a clear evolution of the scattering vectors as energy is risen. Dashed lines highlight the contour where the QPI signal is enhanced. In the lowest energy images we avoid yellow spots coming from the scanning lines. j) Scattering vectors plotted together with the ARPES bands from Mou *et al.* [2016]. The scattering vectors we see (black arrows represent experimental data) mach the ARPES data (red lines) within the error below the Fermi level. Above the superconducting gap there is an increase in the scattering vector size as the β band is closing. We add the hypothetical β and γ bands as guide to the eye as blue and green dashed lines respectively.

As we show in Fig.5.13, we can obtain the density of states versus energy by integrating the intensity of the scattering in k-space around the circle indicated in the right panel of Fig.5.13. We obtain broad quasi-particle peaks at sizes comparable to the ones shown in the tunneling conductance discussed earlier. This shows that we are imaging the opening of the gap. As we discuss above, the tunneling conductance at the surface is mostly dominated by a single gap feature (see Figs.5.5 and 5.8). Accordingly, here we mostly observed the same single gap feature. It is also clear from the curves that despite the intensity of the QPI pattern slightly changes with the angle, the position of the peaks does not, pointing towards an isotropic behavior of the superconducting gap.

5.6 Conclusions

- We have performed the first tunneling experiments in the recently discovered stoichiometric iron pnictide superconductor $CaKFe_4As_4$. In a combined study with the group of Dr. Prozorov, who performed London penetration depth measurements, we find a two gap structure consistent with $s_{\pm}$ pairing symmetry. This point is strengthened by our observation of pair breaking in topographic defects such as holes and unit cell height steps.

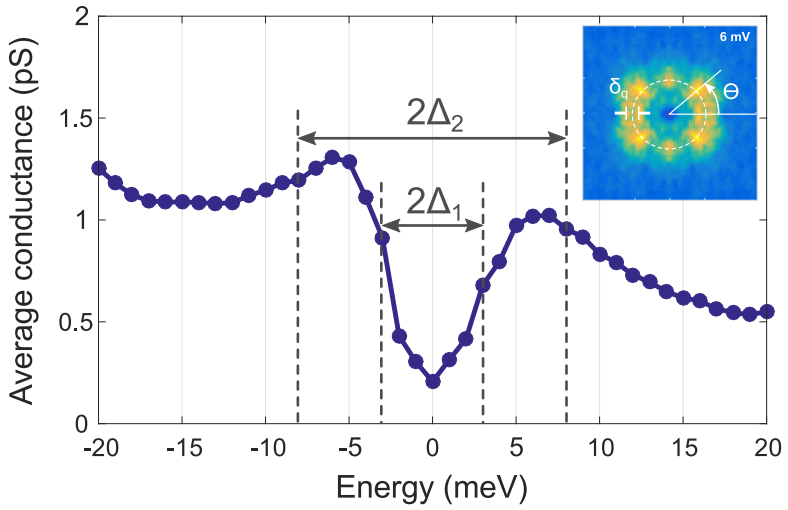

Figure 5.13: Left panel: conductance curves obtained from the reciprocal space data as a function of the angle (top). Bottom panel: mean conductance obtained from the curves in the top panel. Right panel: sketch indicating how curves on the right panel are obtained from the 2D-FFT.

- We characterized the vortex lattice in the same compound under magnetic fields between $1\,T$ and $8\,T$ finding a disordered triangular Abrikosov lattice at all studied fields. Study of individual vortices reveal that they are round, showing no sign of in-plane anisotropies and they have a localized state at finite positive bias.
- Furthermore, we have demonstrated that topographic defects producing a finite density of states at zero bias play a major role in the pinning of vortices. We find individual pining for densities of vortices smaller that that of the defects (usual situation at low fields) and collective pinnning behavior when the distance between vortices is smaller than that between defects (normally found at higher fields).
- Finally, we have performed QPI analysis finding scattering between the two outer hole pockets and imaging how the inner one closes above the Fermi level. Around the Fermi level we extract from reciprocal space data an isotropic behavior of the superconducting gap.

CHAPTER 6

Superconducting vortices and impurities in dichalcogenide systems

6.1 Shiba states in $NbSe_2$

6.1.1 Shiba states

Any impurity atom in a superconductor is a strange atom in the crystal structure that has a different electronic configuration and therefore a different Coulomb potential which interacts with the band electrons. This interaction has often local character since the Coulomb interaction is screened for length scales of the order of the lattice spacing. When the impurity atom has a magnetic moment, there is an additional exchange interaction between the magnetic moment and the electrons.

The presence of magnetic impurities in conventional superconductors introduces in-gap excitations that appear as a result of the pair breaking effects by the localized spins of the impurity. These states are known as Yu-Shiba-Rusinov (YSR or Shiba for brevity) and were theoretically predicted by Yu [1965]; Shiba [1968]; Rusinov [1968].

In the last few years the study of Shiba states has regained interest due to the physics of Majorana fermions. There have been a series of proposals for experiments to see Majoranas involving chains of magnetic atoms with helical magnetic order in conventional superconductors [Braunecker and Simon, 2013; Klinovaja *et al.*, 2013; Vazifeh and Franz, 2013]. These systems are supposed to tune themselves into a topological phase trapping Majorana modes at the ends of the chain.

The local nature of these phenomena implies that these exist only in small areas, usually involving a few atoms. That makes the STM an appropriate tool to study their properties.

6.1.2 STM studies on Shiba states

One of the first studies of magnetic impurities with STM was done by Yazdani *et al.* [1997] where they analyzed the effect of magnetic adatoms in the superconducting tun-

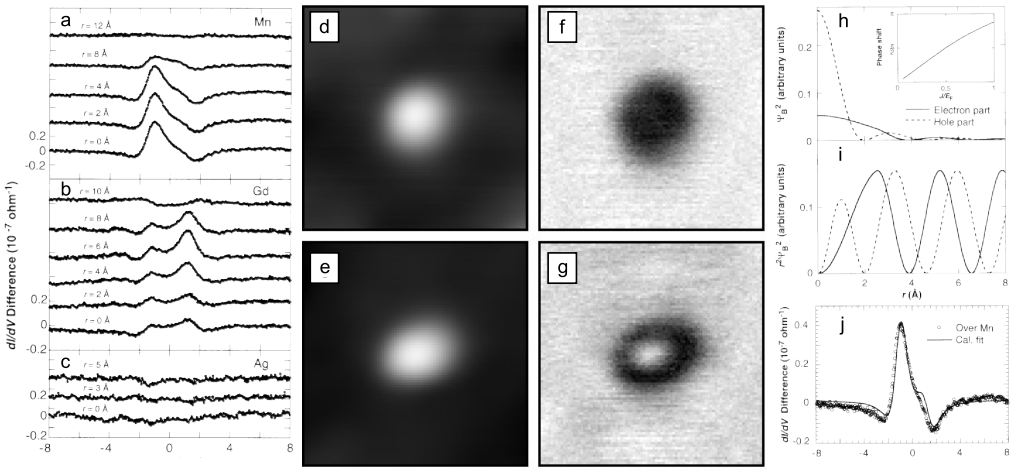

Figure 6.1: Adapted from Yazdani *et al.* [1997]. All experimental details are provided in the same reference. The substrate is superconducting Nb, and authors have evaporated single adatoms of different species on top of the Nb surface. In the left panels, we show the tunneling conductance around different kinds of impurities, two from magnetic adatoms Mn (a) and Gd (b) and one from a non-magnetic adatom Ag (c). Superconducting gap measured at an impurity free area was subtracted as a background. The non magnetic Ag impurity gives no sizable signal inside the gap. Mn and Gd impurities lead to a double peak structure. In the case of Mn the larger peak located at negative bias while for Gd impurites is located at positive bias. d-e) Contain constant current images for, respectively, impurities of Mn (taken at $-3\,mV$) and Gd (taken at $3\,mV$). Simultaneously acquired differential conductance (f-g) gives an idea of the extension of the localized states. h) Contains the Bogoliubov wave function for quasi-electrons and quasi-holes showing strong oscillatory antiphase spatial dependance. i) Presents the same function, multiplied by the superfluid density. Dephasing between both function is caused by the localized state being at finite voltage. j) Shows a fit to the experiment.

neling spectra. For this, they deposited coverages of 0.005 of a monolayer of magnetic atoms (Mn and Gd) over the surface of pure Nb ($T_C = 9.2\,K$). They compare conductance curves in the neighborhood of magnetic (Mn and Gd) and non magnetic adatoms (Ag) finding that magnetic elements introduce in-gap states with electron hole asymmetry over a few atomic distances around them (see central panels of Fig.6.1). As seen in left panel in Fig.6.1, intensity and asymmetry of the induced states was found to depend on the nature of the magnetic atom. Using a model based on Bogoliubov–de Gennes equations they find a bound excitation (mixture of both electron and hole excitations) at a finite energy $E_B < \Delta$. The spatial variation of these bound states is governed by a wavelength λ and decays with distance (r) as $(1/r^2)\,e^{-2r/\xi}$ with $\xi = \xi_0\,(\Delta/\sqrt{\Delta^2 - E_B^2})$. While the expected value for the coherence length in the measured Nb system is large, of about $40\,nm$, the signal corresponding to the Shiba states decays very rapidly and, already at $1\,nm$ apart from the impurity, it is no longer observed in the experiments. Clearly, the $1/r^2$ decay determines the amplitude of the density of states and a decay of the signal probed with an STM over short distances. This oscillation, in the presence of a magnetic potential also creates a phase shift between electron an hole components as can be seen in right panel of Fig.6.1. Using this model, they successfully fit their data for Mn adatoms.

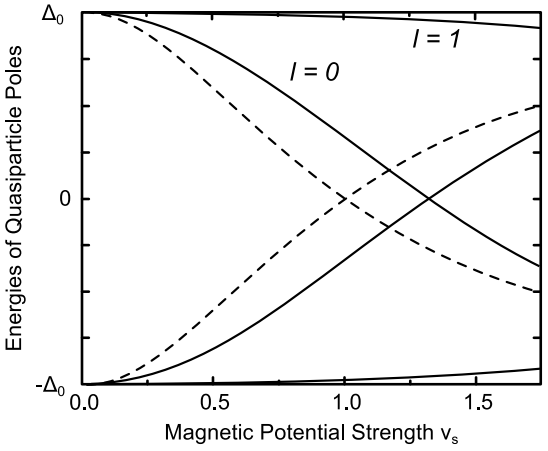

Figure 6.2: Adapted from Flatté and Byers [1997]. Localized excited state poles for angular momentum channels l = 0 and 1 (solid lines). Dashed lines show results of Shiba [1968]. At $v_s = v_{s0}^*$, the character of the l = 0 state is inverted.

The peaks can be understood using detailed calculations in the following way. In Fig.6.2 we reproduce the results of Flatté and Byers [1997]. For vanishing magnetic potential v_s, the energy of the bound state is close to the gap values and has two peaks for electron-like quasi-particles, who have spin up and hole-like quasi-particles with spin down. In that case, the impurity is provided by a classical spin down. The classical spin is down, so the electron like quasi-particle (with spin up) is attracted to it. When the interaction strength v_s increases, the spin up state becomes bound to the classical spin above a certain interaction strength. The overlap between the potential and the impurity state decreases the quasi-particle's energy by an amount that is of order of $v_s\Delta$. When this value exceeds the gap, it is favorable to have in the ground state a quasi-particle. This provides a quantum phase transition between a state that is spinless in the superconductor, to a state that has a spin-up quasi-particle that is bound to the spin-down state of the impurity.

The spatial decay of the quasi-particle states are given by $1/r^2$ in 3D, and by an exponential decay related to the superconducting coherence, as we discuss above.

The asymmetry in the spectral weights of electron and hole quasi-particles is related to v_s. For low values of v_s (states at the gap edge), the asymmetry is practically absent. When increasing v_s, the spectral weight is located at the band with opposite spin (spin-up here). The asymmetry increases when increasing v_s. Thus, in summary, the Shiba states around an impurity produce asymmetric in-gap peaks at fixed bias voltages whose height oscillates with the position. The height of the peaks depends on the actual coupling between the impurity spin and the superconductor. Its distance dependence is given by the spatial decay of the interaction potential and the superconducting coherence length. Due to the decay by $1/r^2$, the dependence of the decay on the interaction potential is barely observed in the experiment. The height of the peaks oscillates as a function of the position with a wavelength given by $\lambda_F/2$, giving a Friedel like behavior.

The oscillations between electron and hole quasi-particle bands are phase shifted by an amount that depends on the energy of the bound state. When the interaction energy is large and the impurity states crosses the Fermi level, the phase shift approaches unitary limit $\delta = \pi/2$.

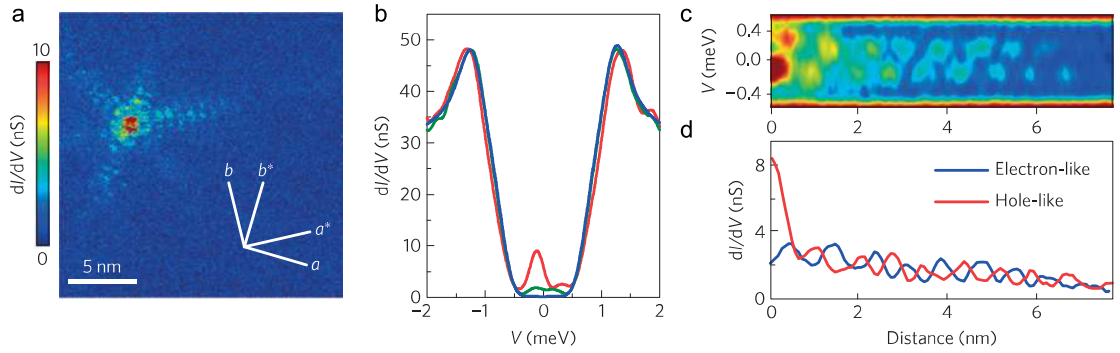

Figure 6.3: Adapted from Menard *et al.* [2015]. Experimental results of spectroscopic measurements on $NbSe_2$ with Fe impurities (a). Magnetic impurities produce in-gap states (b) that oscillate between positive and negative energies (c,d) as expected from theory.

A more recent study performed by Menard *et al.* [2015] focused in magnetic impurities embedded in 2H-$NbSe_2$. They found that impurity in-gap states arrange spatially in a star shaped form like that observed in superconducting vortices (see Fig.2.7 in chapter 2) and oriented in the same direction as shown in Fig.6.3.a and b. As shown in Fig.6.3.c-d, excited states decay along the arms of the star following an oscillating pattern that changes between electron-like and hole-like with a wave vector of the order of the Fermi wavelength. The spatial decay of the features at the impurity sites is rather extended, in particular as compared to Nb [Yazdani *et al.*, 1997]. They compare their results with calculations of the expected extent of Yu-Shiba-Rusinov states for an isotropic superconductor in 2D and 3D and associate the found behavior with the 2D character of superconductivity in $NbSe_2$ that changes the radial dependence from $1/r^2$ to $1/r$. (Fig.6.3).

YSR states near the Fermi energy ($E_{Shiba} \approx 0.2\,meV$) were found for all magnetic impurities. Depending on the behavior of the YSR states in each case they differentiate between two types of impurities. In most cases, the intensity of the hole-like peak was found to be much higher than that of the electron-like peak (Fig.6.3.b). They also see other types of impurities showing two peaks of almost the same intensity with slightly higher electron-like excitation. They associate those behaviors to the element making up the impurity. An analysis of the atomic contents in their samples shows an impurity content of 175 ppm of Fe, 54 ppm of Cr and 22 ppm Mn. They thus associate the observed behavior to different impurities, although they do not know the impurity where they are tunneling into in each case.

The case of interactions between impurities was analyzed in by Ji *et al.* [2008]. To this end, authors have mostly analyzed molecular structures with spins close-by, outside the superconductor, or magnetic dimers. When the impurities form a state with a finite

spin (triplet), the corresponding energy level is split, so that the two peaks transform into four. On the other hand, when the impurities form a zero spin state (singlet), they do not perturb the superconductor and, far away, their effect might vanish.

These works pose relevant new questions concerning our understanding of YSR states. First, the anisotropy of the superconducting gap clearly influences the spatial decay of the Shiba states. This was barely discussed in Menard *et al.* [2015], but it induces in-plane anisotropic length scale that seems related to the in-plane gap anisotropy. To this extend, it is interesting to see if we can create a situation with long range Shiba states, following the 2D behavior, and no superconducting gap anisotropy. Second, the influence of vortices and the associated supercurrents remains unaddressed. Third, it would be interesting to know if impurities located sufficiently close to each other can form a magnetic bound state and what would be the properties of such a bound state. Here we solve in particular the first question and provide first results that might help advancing in the other two issues.

6.2 The effect of S doping in 2H-$NbSe_2$

6.2.1 Sample growth and characterization

Sample growth, x-ray diffraction and resistivity measurements on this material were carried out by Samuel Mañas-Valero in the group of Prof. Eugenio Coronado at the *Instituto de Ciencia Molecular* (ICMol) (Valencia, Spain).

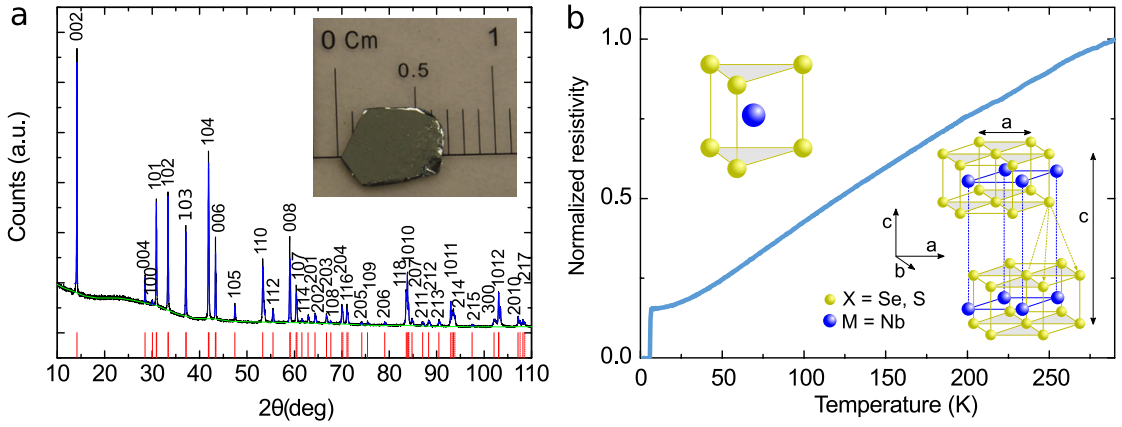

Figure 6.4: a) XRPD experimental pattern of 2H-$NbSe_{1.8}S_{0.2}$ single crystal (black) and corresponding fit (peaks in blue and background in green). The fit gives: $a = b = 3.4323(3)$ Å and $c = 12.513(1)$ Å, a hexagonal crystal system with $P63/mmc$ space group, $X^2 = 2.22 \times 10^{-5}$, and a Snyder's figure of merit of 44.3158. Inset: view of the grown single crystal. b) Temperature dependence of the resistivity normalized to its room temperature value. Inset: generic crystal structure of transition metal dichacogenides adapted from Meerschaut and Deudon [2001].

We have grown samples of 2H-$NbSe_2$ doped with S. Substituting Se by S usually

introduces a source of scattering which in this case is expected to reduce the intrinsic anisotropy of 2H-$NbSe_2$ [Anderson, 1959]. A small amount of Fe was then added to act as magnetic impurities. Inductively coupled plasma (ICP) analysis in our sample finds that Fe is present in a proportion of ≈ 150 parts per million (165 ± 34), producing no bulk magnetic order in the sample. The presence of other magnetic impurities in our sample is below the detection limit of the ICP analysis (below 25 ppm), so it is reasonable to assume that all impurities would be caused by localized magnetic moments of Fe.

For the sample synthesis, elements were mixed in a stoichiometric ratio, sealed inside the evacuated quartz ampoule and heated from room temperature up to $900\,°C$ at $1.5\,°C/min$. The sample was kept at constant temperature during 14 days and then was slowly cooled down ($0.07\,°C/min$). To obtain large single crystals, they mixed four $mmol$ with I_2 as a transport agent ($[I_2] \approx 5\,mg/cm^3$) in evacuated quartz tube, which was placed inside a three-zone furnace. They placed the material in the leftmost zone and heated the other two zones for three hours up to $700\,°C$ and kept them at this temperature for one day. After that, the leftmost zone was heated to $750\,°C$ within three hours and we established temperature gradients as $750\,°C$ / $700\,°C$ / $725\,°C$. These temperatures were kept for 22 days after which the oven was switched off for cooling.

The crystals so formed were analyzed by ICP spectrometry and by powder x-ray diffraction by the group in Valencia (Fig.6.4.a). The elements content given by the analysis is in good agreement with the expected values for 2H-$NbSe_{1.8}S_{0.2}$. Refinement of the x-ray pattern revealed a hexagonal lattice with a $P63/mmc$ space group (see inset in Fig.6.4.b) and a unit cell of $a = b = 3.4323(3)$ Å, $c = 12.513(1)$ Å, $\alpha = \beta = 90°$, and $\gamma = 120°$. These results are only slightly different from those for pure 2H-$NbSe_2$ [$a = b = 3.4425(5)$ Å, $c = 12.547(3)$ Å, $\alpha = \beta = 90°$, and $\gamma = 120°$ according to Meerschaut and Deudon, 2001]. In particular, note that the c-axis lattice parameter is only slightly larger than in the pure compound, indicating that S does not influence the spacing between 2H-$NbSe_{1.8}S_{0.2}$ layers. Fig.6.4.b shows the temperature dependence of the normalized resistance for 2H-$NbSe_{1.8}S_{0.2}$. It shows a metallic behavior for high temperatures and saturates below $25\,K$ with a RRR between 6 and 7 without showing any clear signature of CDW transition. Superconductivity appears at $6\,K$ with a sharp drop at the transition temperature.

6.2.2 Charge density wave

Pure 2H-$NbSe_2$ is known to have a CDW ordered phase below $33\,K$ [Harper, Geballe, and DiSalvo, 1977]. This ordered phase has a signature in resistivity and it is clearly visible with STM as an electronic modulation in topographic images. STM topographies are a measurement of the integrated LDOS from the Fermi level to the applied bias voltage. These measurements are therefore sensitive to local charge variations as the ones produced by the CDW.

STM topography in Fig.6.6 shows the Se atomic lattice in a window of $20\,nm$ of lateral size. The image also shows a supramodulation corresponding to the CDW. This

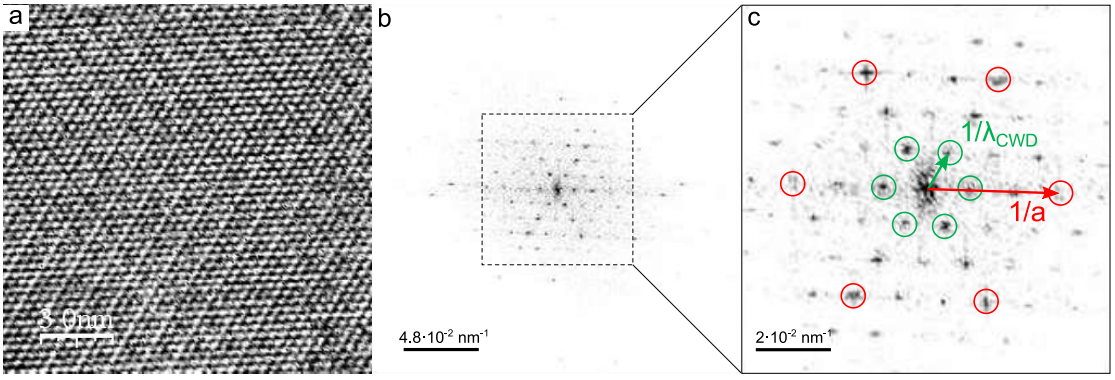

Figure 6.5: Adapted from Guillamón [2009]. a) Topographic STM image of the surface of 2H-$NbSe_2$ at $100\,mK$ showing a CDW order. b) 2D-FFT of (a). Bragg peaks of the atomic lattice, its harmonics and the CDW are well defined. c) Zoom of the central part of the 2D-FFT in (b) highlighting Bragg peaks associated to atomic and CDW modulations.

atomic plane corresponds to the Se plane, since cleaving in 2H-$NbSe_2$ exposes the Se lattice. We remind that S enters the compound substituting Se. We can, therefore, calculate the expected number of S atoms in the plane. Lateral size of the image is of $20\,nm$ and in plane lattice parameters give around 3 atoms per nm. Taking this into account we roughly expect $(20 \times 3)^2 = 1200$ atoms in the image. Since the concentration of S is of the $10\,\%$, one should expect approximately 120 S atoms in this scanning window. It is not possible to identify their position using STM, but we can assert that their presence disturbs considerably the CDW.

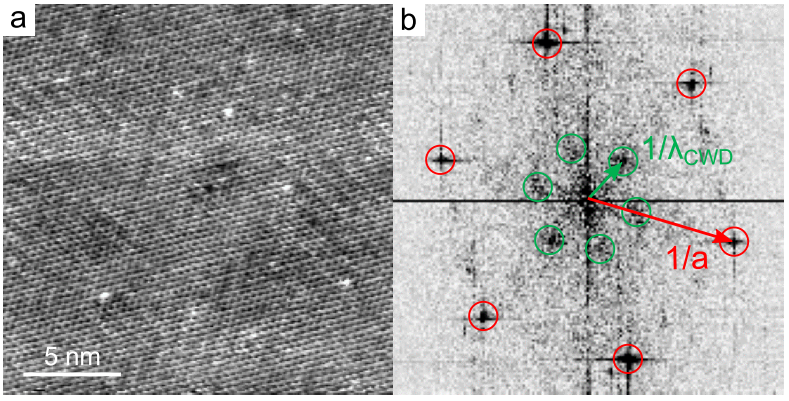

Figure 6.6: a) Topographic image of the surface of 2H-$NbSe_{1.8}S_{0.2}$ at $800\,mK$. Image was taken with $2\,nA$ of tunneling current and an applied bias voltage of $2\,mV$. Change between black and white is of $0.12\,nm$. CDW is still present but shows a large amount of disorder at this level of doping. b) 2D-FFT of (a) highlighting the relevant Bragg peaks as in Fig6.5.

CDW is, in this compound strongly suppressed with respect to pure 2H-$NbSe_2$. Substitutional disorder eliminates the kink feature in the resistivity (see Fig.6.4.b) and breaks up the CDW into small size domains, that give disordered CDW patches in the STM image and blurred Bragg peaks in its corresponding Fourier transform (Fig.6.6.b). Note that the CDW presents, at some positions, rather one-dimensional modulations.

Accordingly, there are Bragg peaks that are higher than others. This reminds the situation found in STM measurements above T_{CDW} by Soumyanarayanan *et al.* [2013], indicating that substitutional disorder is just disordering the CDW.

The anisotropy of the superconducting gap in $NbSe_2$ is, according to Guillamón *et al.* [2008a], directly related to the CDW. As we will see below, absence of the CDW leads to an in-plane behavior that is more isotropic in the compound with S.

6.2.3 Superconducting gap

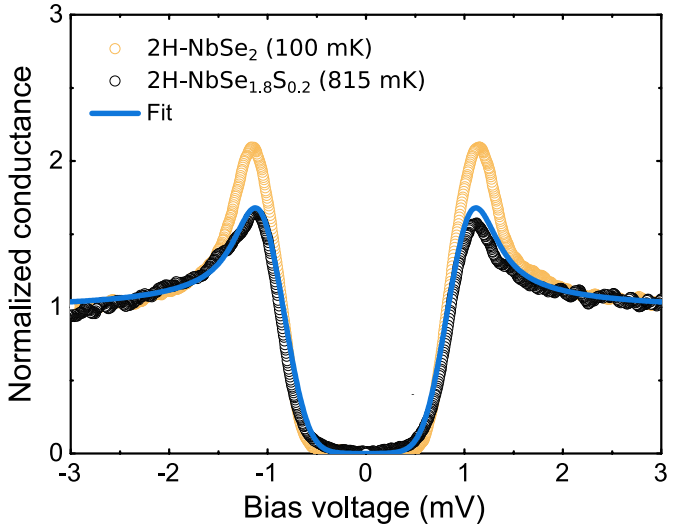

Figure 6.7: Comparison of the superconducting gap found in pure 2H-$NbSe_2$ [Guillamón, 2009] with the one found in 2H-$NbSe_{1.8}S_{0.2}$. The size of the superconducting gap is similar, however, quasi-particle peaks are reduced in the case of the doped compound.

Fig.6.7 shows two typical zero bias normalized conductance curves for 2H-$NbSe_{1.8}S_{0.2}$ and pure 2H-$NbSe_2$ for comparison. It can be seen that quasi-particle peaks are considerably reduced in the doped compound with respect to the pure one. As 2H-$NbSe_2$, low temperature normalized conductance of 2H-$NbSe_{1.8}S_{0.2}$ can be fitted using BCS theory with a two gap model introducing a Gaussian broadening in the gap distribution. For the fit in Fig.6.7 (blue line) we have used $\Delta_1 = 0.78\,meV$ and $\Delta_2 = 1\,meV$ with a broadening parameters $\sigma_{1,2} = 0.12\,meV$ [Fente *et al.*, 2016]. We should note that these two gap values are much closer to each other than the values found in the pure compound [gaps distributions with values between $0.7\,meV$ and $1.4\,meV$ were used by Rodrigo and Vieira, 2004; Guillamón *et al.*, 2008a]. This shows that S acts as scattering center that reduces the gap anisotropy, leaving however a considerably broadened distribution of values of the superconducting gap.

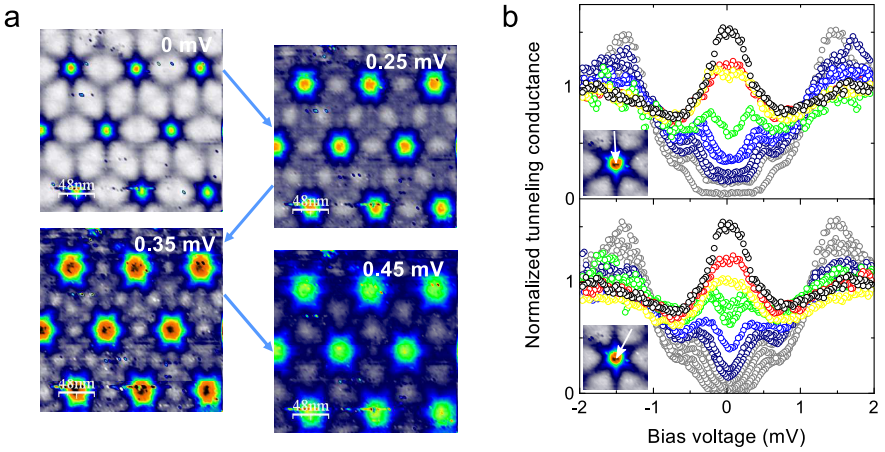

Figure 6.8: Adapted from Guillamón [2009]. a) Conductance maps taken at different bias voltages at $0.1\,K$ and $0.15\,T$ in pure 2H-$NbSe_2$. b) Normalized conductance curves taken at $0.1\,K$ and $0.03\,T$ in the same material along a $60\,nm$ line going into the vortex core center from the outside over one of the *star-shaped* arms of the vortex and in between them (as indicated by the arrows in the insets). Color scale is the same for all panels in the figure. Vortex shape and conductance curves reflect the strong anisotropy existing in this material.

6.2.4 Vortex lattice and vortex core

STM can be used as a tool study anisotropies in superconducting materials. Information about these anisotropies can be extracted, for example, from the shape of the vortex cores [see Guillamón *et al.*, 2008a; Herrera, 2016]. In the case of 2H-$NbSe_2$, vortices have a star shape reflecting an in plane gap anisotropy [Hess *et al.*, 1989; Hess, Robinson, and Waszczak, 1990; Guillamón, 2009]. Fig.6.8.a shows the vortex lattice for this compound and how the star rotates as the energy increases.

In order to compare 2H-$NbSe_{1.8}S_{0.2}$ with the pure compound we have imaged the vortex lattice for different applied fields in the c axis. We have found that they arrange in a well ordered triangular Abrikosov lattice as can be seen from images in Fig.6.9. The evolution of the intervortex distance with the magnetic field is displayed in the lower right graph of Fig.6.9 finding good agreement with the expected distance for a triangular lattice (black line). For all fields, vortices in Fig.6.9 have round cores and show no signature of the in-plane anisotropy found in the pure compound (right panel of Fig.6.8).

Fig.6.10.a shows a detailed image of a vortex core for an applied field of $0.05\,T$. It remains perfectly round as the bias voltage is changed in contrast to what is seen in Fig.6.8.a. A closer look into the vortex core reveals a peak corresponding to CaroliDeGennes-Matricon localized states. Conductance curves show no signature of the in-plane gap anisotropy. Fig.6.10.b shows a profile of conductance curves going away from the vortex core.

We associate the reduction of the gap anisotropy to the effect of scattering caused by the substitution of Se by S on the CDW order. Note that at the experimental temper-

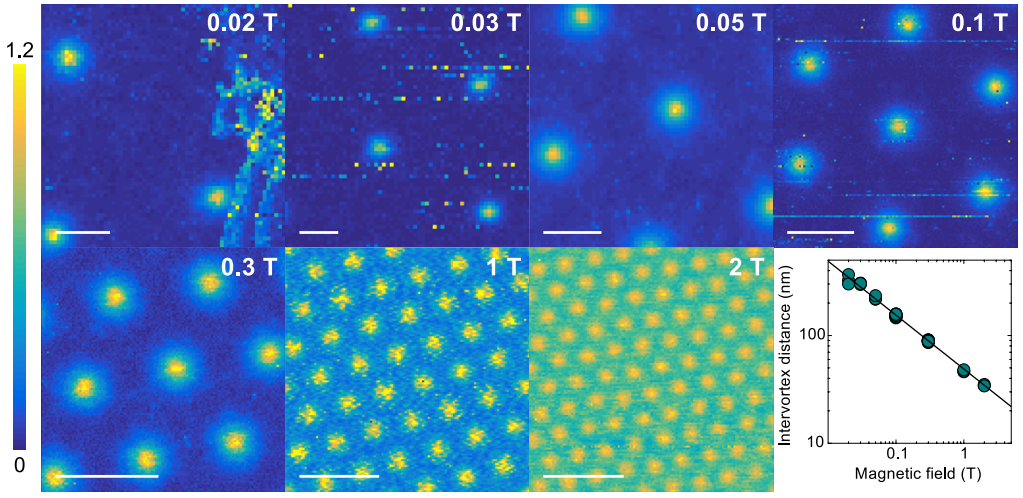

Figure 6.9: Vortex lattice imaged for different fields in 2H-$NbSe_{1.8}S_{0.2}$. Vortex cores are round and show no in-plane anisotropy. The lattice is ordered at all fields and the intervortex distances match the distance expected for a triangular Abrikosov lattice (lower right panel in the figure). White scale bars are of $100\,nm$.

ature ($800\,mK$), pure 2H-$NbSe_2$ clearly shows star shaped vortex cores, so the smearing observed in the experiment is due to impurity scattering introduced by S substitution. Studying magnetic impurities in this material will allow us to avoid the intrinsic anisotropies of 2H-$NbSe_2$ and give a new insight to the behavior of embedded magnetic atoms in an isotropic superconductor.

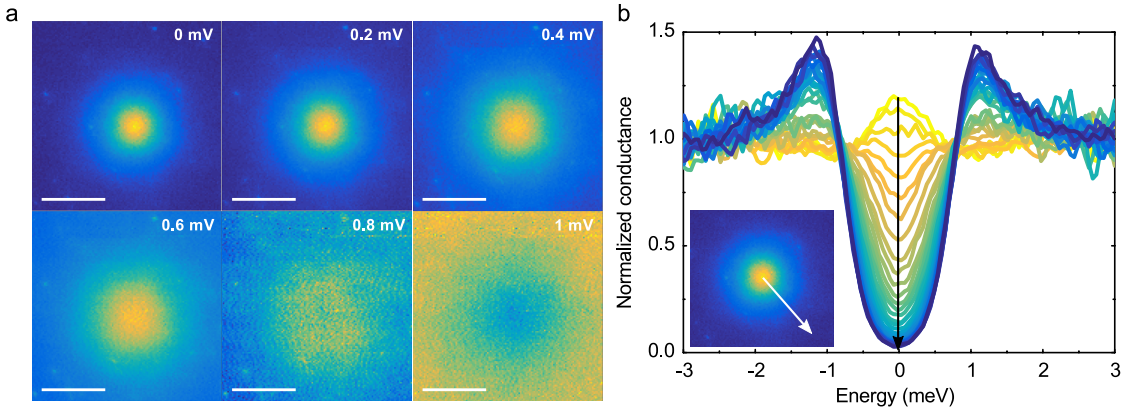

Figure 6.10: a) Normalized conductance maps of a superconducting vortex at $0.05\,T$ taken at different bias voltages. No sign of anisotropy is seen as the voltage is risen. White scale bars are of $20\,nm$. b) Normalized conductance curves taken in a line from the vortex core center to the outside. Vortex cores are round and show no signature of the *star* shape seen in the pure compound. Vortices show Caroli-deGennes-Matricon states states that split and disappear as we move away from the vortex core center as in 2H-$NbSe_2$.

6.3 Fe impurities at zero field

We first characterize the magnetic impurities at zero field. We have thus magnetic impurities in an in-plane isotropic superconducting system. The in-plane anisotropy present in pure 2H-$NbSe_2$ has been reduced due to the substitution of $10\,\%$ of the Se by S, as shown in the previous sections. Distribution of the magnetic impurities over the sample is, as seen in conductance maps, random (see Fig.6.11.b). Regarding the nature of our impurities, we can assure, given the precision of the ICP analysis, that all magnetic impurities we see are Fe atoms. Conductance map in Fig.6.11 has around 25 impurities and the whole window is of $102\,nm$ of lateral size, meaning there are around 9×10^4 atoms. A rough calculation gives $25/9 \times 10^4 \approx 2.7 \times 10^{-4}$ which is in the same order of magnitude of the 165 ppm found in the ICP analysis for Fe atoms. This reinforces the assumption that all our impurities are coming from Fe atoms.

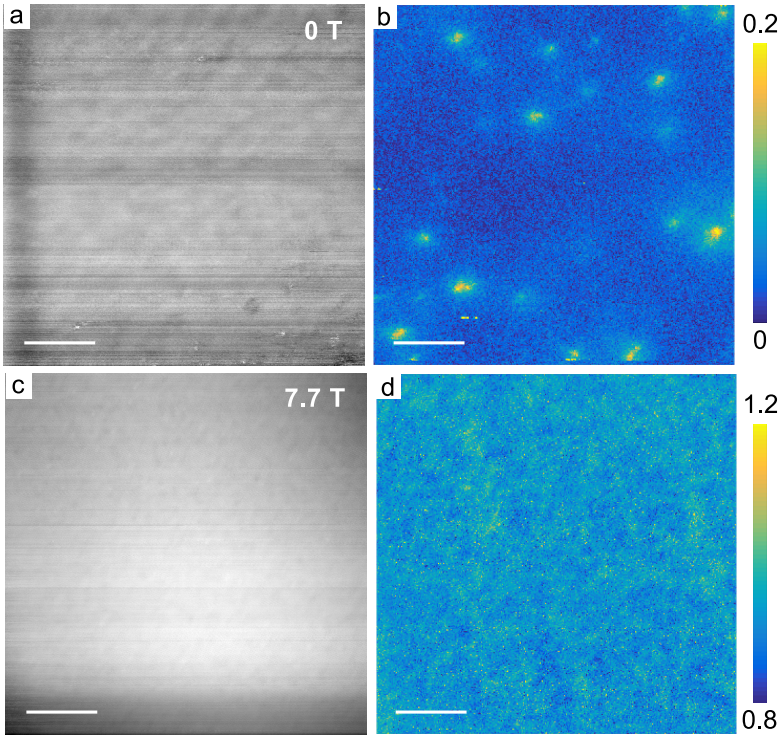

Figure 6.11: a) Topographic image taken at $2\,nA$ with $10\,mV$ of bias voltage. b) Zero bias normalized conductance map corresponding to the same window. Up to 25 impurities can be distinguished in the $102\,nm \times 102\,nm$ image. c) Topographic image taken in similar conditions as (a) with an applied field of $7.7\,T$. d) Zero bias normalized conductance map taken simultaneously with (c). Scale bars are of $20\,nm$.

When we apply a magnetic field above the upper critical field, we do not find any signature for the magnetic impurities. This shows that there is no strong exchange coupling between the magnetic impurities and the host. In particular, there is no Kondo effect, indicating that the interaction between magnetic impurities and the host is not very strong, with the scattering phase shift likely being different from unitary scattering with $\delta = \pi/2$.

In general, the spatial extension of the excited states is of $\approx 5-6\,nm$ which is comparable to the sizes given in Menard *et al.* [2015]. We should note that the location of the impurities is generally unknown. It is rather difficult to assume that they would simply be at the surface as adatoms or substitute a Se or a S atom. Instead, it seems much more likely that Fe substitutes a Mn atom or sits in the van der Waals gap. In both cases, this occurs below the surface. Given the crystalline structure of 2H-$NbSe_{1.8}S_{0.2}$, and the fact that the observed behavior is 2D, we can say that we are essentially observing the density of states of the outermost Nb-Se block. The exchange coupling of a Fe atom substituting a Mn atom, or of a Fe atom located below the layers in the van der Waals gap might be different. But the main result should remain changes in the density of states of the outermost Nb-Se layer.

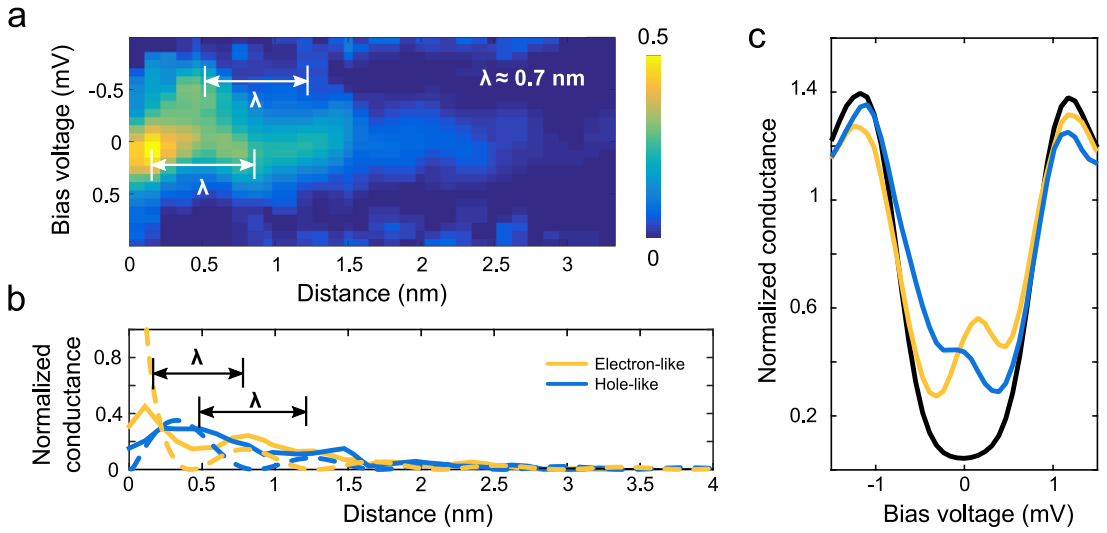

Figure 6.12: a) Normalized conductance profile going away from the center of the impurity showing the alternance between electron and hole excitations. b) Decay of the excited state showing the alternance of electron and hole-like states. c) Conductance curves corresponding to the electron-like and hole-like excitations.

We find that the reduced in-plane anisotropy shown in the vortex core manifests itself also in the impurity excited states (see Fig.6.11). Typical conductance curves over the impurities are different from those seen in previous works. Analyzing a large number of impurities in our measurements we mostly find two excitation peaks of nearly the same height as shown in conductance curves in Fig.6.12.c. Furthermore, we see that for most cases, Fe impurities show a higher peak for the electron-like excitation that for the hole-like.

Fig.6.12.b shows the change between hole and electron-like excitations as a function of the distance. Typical conductance curves in the profile are presented in Fig.6.12.c. We can extract from that change a $\lambda \approx 0.7\,nm$. The observed vector is of about two times the interatomic distance $a \approx 0.35\,nm$ which is of the order of the first Brillouin zone size. It therefore corresponds to a $\vec{k}$ of two times the k_F of the sheet centered in

the Γ point (see black arrow in Fig.6.13.b). These two sheets have small warping and are the main FS sheets of this compound.

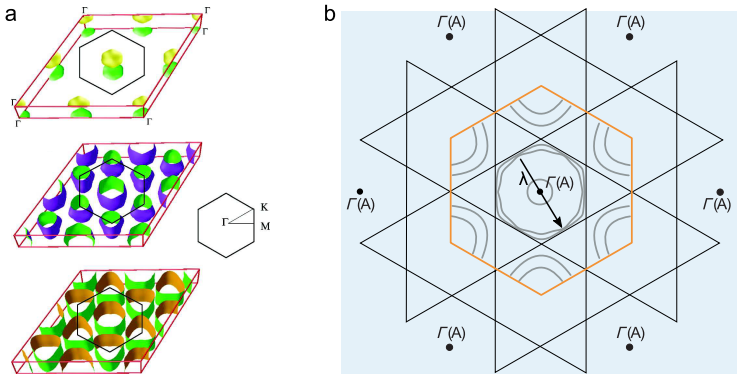

Figure 6.13: a) From Johannes, Mazin, and Howells [2006]. Calculations of the 3D Fermi surface of 2H-$NbSe_2$. Each panel corresponds to different sheets of the band structure. b) Adapted from Kiss *et al.* [2007]. Schematic 2D Fermi surface of 2H-$NbSe_2$. Black arrow labeled as λ in the center of the image indicates the size of the observed wave vector of the oscillation.

We can also compare the decay of the excitation as a function of the distance to the expected form for the 2D and the 3D cases. Fig.6.12.d shows how the variation of the excitations with the distance is compared to the 2D and the 3D models (dashed and complete black lines). The decay distance is of some nanometers, in the same order of magnitude of the mentioned work. We found this decay consistent with the 2D as shown in Fig.6.12.d.

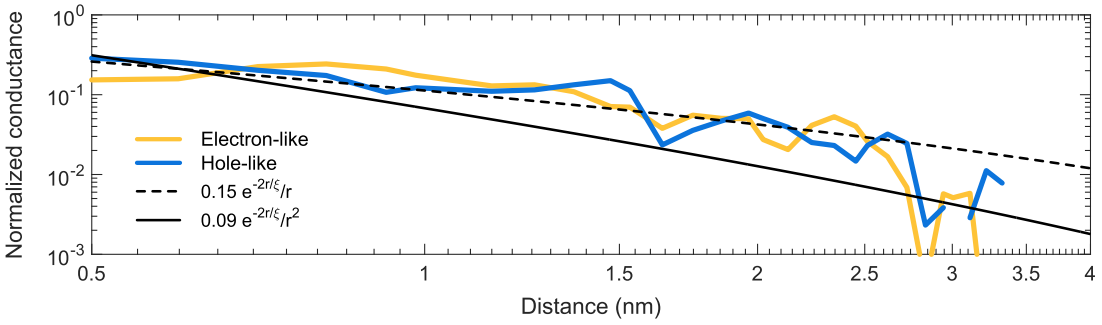

Figure 6.14: Decay of the excited state showing the alternance of electron and hole-like compared to the expected decays for 2D (dashed line) and 3D models (straight line).

We have shown in the previous section how the substitution of 10 % the Se for S strongly suppresses the in-plane anisotropy present in 2H-$NbSe_2$. This effect is also seen in the magnetic impurities that display no star shaped form. Nevertheless, we find that the impurity excited states decay is better described with the 2D model. This suggests that 2H-$NbSe_{1.8}S_{0.2}$ still behaves as a layered superconductor and that the out of plane anisotropy is of importance in this compound.

2H-$NbSe_2$ doped with concentrations of 5000 ppm of Fe and larger has been studied in the past [Whitney, Fleming, and Coleman, 1977]. With 5000 ppm, the critical temperature decreases by approximately $1\,K$ and the resistance shows a minimum, evidencing a Kondo effect. It was shown that, for concentrations in excess of $30\,\%$, the Fe enters the octahedral holes in the van der Waals gap [van den Berg and Cossee, 1968], and it is suggested that the same occurs for concentrations of 5000 ppm, because the behavior observed is generally different from the one observed in substitutional alloys.

It is important to highlight that we do not observe, in our work, any Kondo effect on the magnetic impurities. However, the studies of Whitney, Fleming, and Coleman [1977] clearly evidence Kondo-like spin-exchange, which should considerably influence the local density of states. This suggests that Fe is located, at the concentrations we have studied, in a totally different position. Much likely, Fe is substituting a Nb atom and is not in the van der Waals gap.

From the temperature and magnetic field dependence of the resistivity, Whitney, Fleming, and Coleman [1977] obtain a scattering potential V and J of ≈ 0.2 and $-0.1\,eV$ respectively. By using the classical pair breaking expression, they further obtain $J = -0.13\,eV$, in agreement with their result in resistivity. Furthermore, from the susceptibility, they obtain $g\,S(S+1)^{1/2} \approx 3.2$, which gives $S(S+1) = 2.6$.

Taking into account that Fe is likely located at another position in our case, it is unclear to us which of these parameters can be applied to our case. The absence of Kondo effect in our case suggests an RKKY interaction and a weaker scattering potential.

6.4 Different impurity configurations

6.4.1 Close-by impurities

Having realized that we can obtain Shiba states in 2H-$NbSe_2$ with a certain control over the impurity states, one interesting goal is to try to achieve some interaction, through the superconducting condensate, among impurities. We have found several situations in which impurities that are close-by show variations that seem to be related to each other. We are yet unsure, however, if this is just by having caught, by chance, an impurity with a different coupling to the superconductor, or if there is indeed some interaction. Here we discuss the different configurations that we have studied.

First, we discuss impurities that are very close to each other. In Fig.6.15 we show a pair of impurities showing Shiba states at opposite bias voltage. Note that the height of the peaks strongly depends on the bias voltage (Fig.6.15.a). We observe that close to zero bias, the peaks are at opposite bias voltages. Their height thus oscillates with the position in antiphase to each other. We can determine the decay length by plotting the height of the peaks vs distance (see Fig.6.15.d). Using the behavior found in Fig.6.14 we can extrapolate the intensity of the impurities at each others' site (dotted

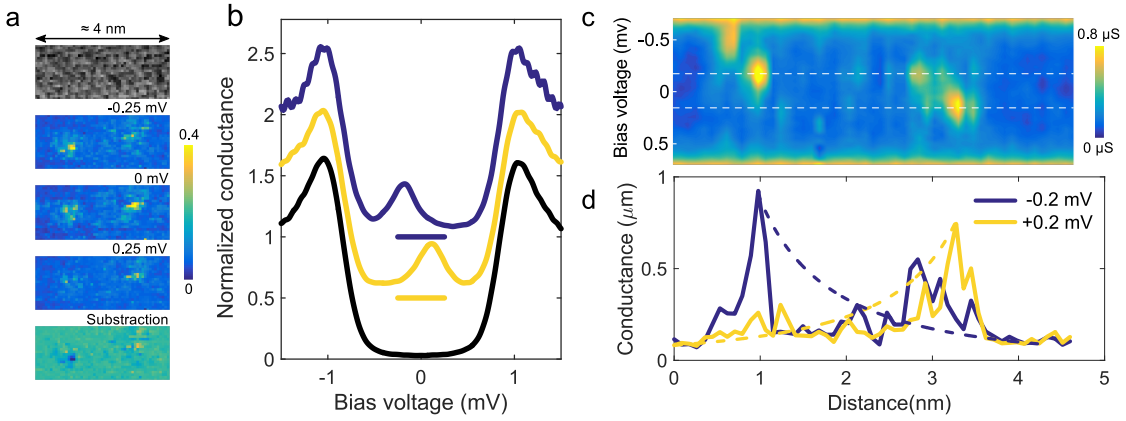

Figure 6.15: a) Atomic resolution topography taken in similar tunneling conditions as previous figures in the chapter and normalized conductance maps taken at the bias voltages indicated in the image over the same scanning window. Lowest panel contains the subtraction of the conductance maps at $\pm 0.25\,mV$ showing how in one of the impurities is the electron-like excitation that dominates while the hole-like dominates in the other. b) Conductance curves take over the impurities. Color code of the curve matches the subtraction image. c) Conductance profile along a line connecting the two impurities seen in (a). d) Conductance profile taken over the lines highlighted in (c) showing the spatial decay of the impurity states. Dashed lines represent the expected decay from the impurity state as extracted from in Fig.6.12

lines in Fig.6.15.d.) finding a value of around $15\,\%$ of the initial impurity peak intensity.

Given the small distance between the impurities in Fig.6.15 one might consider the opposite sign situation as result of a coupling between impurities. Trying to address this we look for impurities in similar configurations.

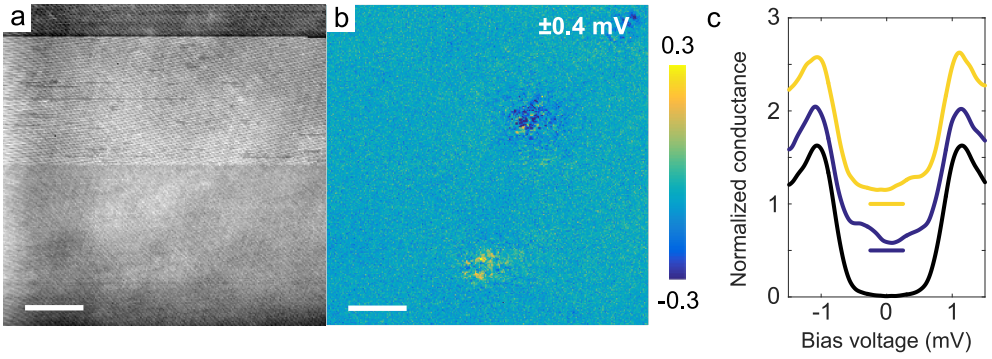

Figure 6.16: a) Topographic image taken in similar tunneling conductance as in Fig.6.11. b) Subtraction of the maps at $\pm 0.4\,mV$ showing the asymmetry of the excited states in the impurities. Scale bars are of $6\,nm$ c) Conductance curves found over the impurities in (b). Curves are shifted for clarity.

Further examples, where impurities appear to be close by, are shown in Fig.6.16. In this case, however, impurities are separated around $15\,nm$, which is an order of magnitude larger than in Fig.6.15 (see panels in Fig.6.16.a). It is clear from the subtracted

image that, as in the situation in Fig.6.15, the sign of the impurity state is inverted. Impurity states appear here as broad peaks inside the gap as shown in tunneling conductance curves in Fig.6.16.c. In this case, the impurities are too far away to each other and the height of the wavefunctions at each other site's is just less than a per cent of its value on top of the impurity.

It is difficult to associate in this case the difference in the sign of the excited state to an interaction between impurities. They are separated $15\,nm$ and we have seen in Fig.6.12 that the distance over which the signal decays is of only $\approx 2\,nm$. Furthermore, the drop in conductance between them is too pronounced to consider that they are interacting. This does not exclude that there might be some interaction in the Fig.6.15, but it is, at present difficult to quantify.

6.4.2 Impurities near to a vortex

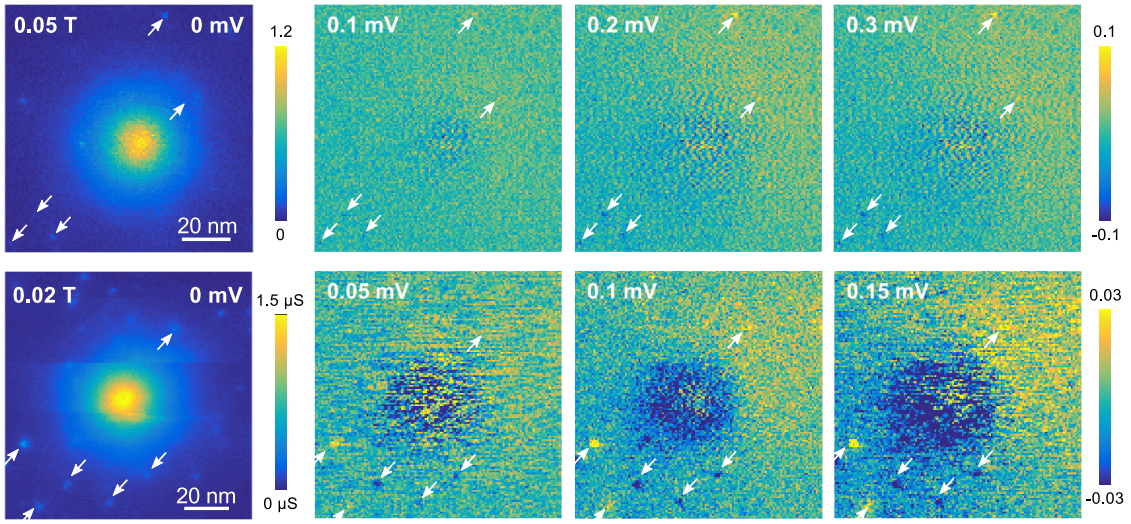

Figure 6.17: Zero bias conductance map and subtraction of symmetric – with respect to the Fermi level – conductance maps at the voltages indicated in each image. By this subtraction we remove the effect of the vortex core on the conductance, enhancing changes induced by impurities in the conductance. Figure contains these plots for a vortex at $0.05\,T$ (top panels) and a vortex at $0.02\,T$ (lower panels).

In order to visualize impurities near a vortex we subtract positive and negative bias images to remove the effect of the vortex in the conductance. Asymmetric peaks inside the gap will be enhanced in the resulting image since the influence of the vortex is electron-hole symmetric.

Fig.6.17 shows two different superconducting vortices at $0.05\,T$ and $0.02\,T$ at zero bias together with the subtraction of the conductance maps at different voltages for the same spectroscopic measurement. Subtraction of the vortex is not perfect, nevertheless, we are able to clearly see some impurities in the image. We have marked each impurity

with a white arrow indicating also its position at the zero bias map.

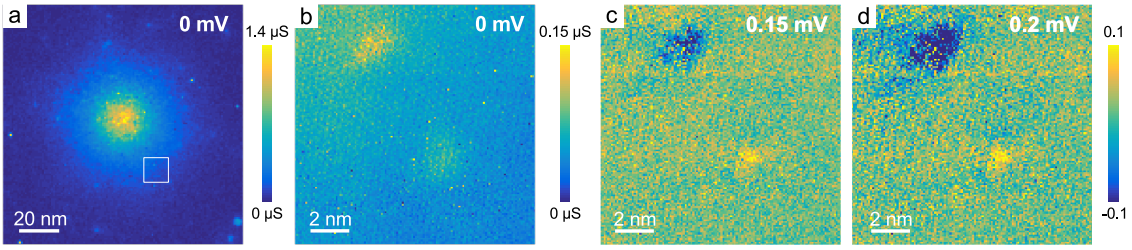

Figure 6.18: a) Zero bias conductance map a vortex at $0.05\,T$. b) Zero bias conductance map in the area highlighted in (a). Two impurities can be seen aligned as moving away from the vortex core. Like in Fig.6.17, in (c) and (d) we present the subtraction of the Fermi level symmetric conductance maps at different energies ($\pm\,0.15\,mV$ and $\pm\,0.2\,mV$). Yellow and blue in the color scale indicate positive and negative position of the peak, respectively. It can be seen that one of the impurities show hole-like excitation while the other is electron-like.

Looking into the impurities near a vortex an interesting situation appears. Very often, we find, under magnetic fields, impurities with peaks at opposite signs. This is shown in Fig.6.17. The difference with respect to zero field is the presence of a current and a strongly reduced superconducting order parameter when reaching the core (see chapter 3). There have been theoretical calculations showing quantized currents surrounding impurities in presence of Rashba spin orbit coupling. It is certain, nevertheless, that the gap suppression indeed modifies the interaction strength.

In Fig.6.18 we show a detailed image of two close impurities (separated by a few nm) near a vortex. Their relative position with respect to the vortex is depicted in Fig.6.18.a. The impurities are located in a radial direction with respect to the vortex core, one farther away than the other. The figure contains the zero bias conductance map and the subtraction of the maps at $\pm\,0.15\,mV$ and $\pm\,0.2\,mV$. It is clear from the subtracted images that the impurity located closer to the vortex has the peak at negative bias while that located farther away from the vortex has the peak at positive bias values.

Impurities in Fig.6.18 are located about $7\,nm$ away from each other as in the case of Figs.6.15 and 6.16. In this situation, as discussed earlier, there might be some coupling.

In all, there is a need of theoretical calculations asserting the expected behavior close to the vortex core.

We study now the case of two impurities separated by $10\,nm$ and located at the same distance from the vortex core. Fig.6.19.a illustrates this situation showing the relative position of the impurities with respect to the vortex. Fig.6.19.b shows the zero bias map in the area highlighted with a white square in (a). Fig.6.19.c contains the subtraction of the conductance maps at $\pm\,0.48\,mV$. Although in both cases the signal is small, it is clear that both impurities have the localized state at positive bias as indicated by the yellow color.

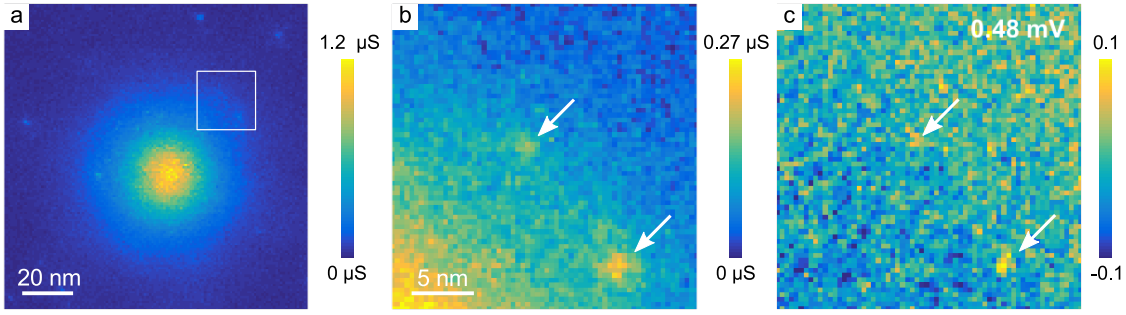

Figure 6.19: a) Zero bias conductance map of an area showing a superconducting vortex at $0.05\,T$. b) Zero bias conductance map of the area highlighted in (a) showing two impurities located at the same distance from the vortex core. c) Subtraction of the conductance maps at $\pm 0.48\,mV$ over the area in (b). Yellow and blue in the color scale indicate positive and negative position of the peak, respectively. In this case both impurities have increased conductance at positive voltages.

6.5 Conclusions

- We have characterized the effects of substituting Se by S in 2H-$NbSe_{1.8}S_{0.2}$. As a consequence of this substitution, CDW order in this material is considerably suppressed with respect to the pure compound. We have also seen that the superconducting gap is isotropic, providing round vortices that arrange in a triangular Abrikosov lattice.

- Introducing a small amount of Fe impurities we have imaged Yu-Shiba-Rusinov states in spectroscopic measurements. Excited states give a two peak structure with asymmetric peaks, being the electron-like excitation usually larger than the hole-like excitation.

- Spatial dependence of the excited state reveals a 2D-like behavior, suggesting that superconductivity in 2H-$NbSe_{1.8}S_{0.2}$ has a strong 2D character. This points that the effect of S substitution reduces the in-plane anisotropy but has little effect out of the plane.

- We have investigated situations where impurities are at distances where they overlap. In those cases the sign of the excited state is found to be opposite in both impurities. It is tempting to think that the interaction between them might have some influence on the sign of the excited state. We have seen, however, a similar situation involving impurities located at larger distances, which is not consistent with the interaction picture. More measurements and statistics are needed to clarify this point.

- Under magnetic field we find a larger number of impurities showing hole-like excitation. We speculate that the presence of supercurrents might have some influence in this outcome. Hopefully, further research will also clarify this point.

General conclusions

In this project we have used scanning tunneling microscopy and spectroscopy at very low temperatures to study three different superconducting compounds. We have focused our research in the study of superconducting vortices and the effect of impurities and defects in the superconducting density of states.

Regarding the experimental system, we implemented an *in situ* cleaving system in order to cleave our samples in cryogenic ultra high vacuum conditions. The method, suitable for layered materials, was successfully used in all samples measured giving large and flat surfaces. We have also improved mechanical isolation of the system, substituting the Dewar vessel and the isolation system itself.

Following a proposal by Dr. V. Kogan, we have analyzed the vortex core in a variety of materials. We find that in superconductors close to the clean limit, the vortex core shrinks with the magnetic field. Furthermore, the length scale governing spatial variations of the density of states around vortex cores is the same for superconductors that have different gaps opening on the Fermi surface. Finally, we have shown that the proposal of Kogan can be used to extract relevant length scales for the size of vortices. This helps to establish a connection between pair breaking and vortex pinning in the iron based superconductors.

In $Ca(Fe_{0.965}Co_{0.035})_2As_2$ we have characterized the effects of strain and the surface reconstruction on the superconducting properties. We have identified the different crystalline boundaries present in the sample and found that in the ORTH/T boundaries between orthorhombic and tetragonal domains superconductivity is enhanced. In those areas where superconductivity is better seen, we have imaged the vortex lattice finding round vortices arranging in a triangular disordered lattice. We have also characterize the pair breaking effect of the surface reconstruction and imaged, through quasi-particle interference, a nematic hole band with enhanced mass in the orthorhombic phase of the superconducting sample.

We have performed the first tunneling experiments in the recently discovered stoichiometric FeBSC $CaKFe_4As_4$, characterizing the gap structure which can be described with a model of two gaps. He have also shown how defects in the material provoke breaking of Cooper pairs, leading to a finite density of states at zero bias. The study of the vortex lattice reveals a triangular disordered lattice at all imaged fields that is strongly affected by the pinning potential produced by the pair breaking. Our results

are consistent with sign changing $s_{\pm}$ pairing in FeBSC.

Finally, we have characterized the effect of the substitution of Se by S in 2H-$NbSe_{1.8}S_{0.2}$. We found that the in-plane gap anisotropy present in pure 2H-$NbSe_2$ is suppressed through the reduction of the CDW order. In this isotropic superconductor we have studied the effect of Fe magnetic impurities by investigating the so called Yu-Shiba-Rusinov excited states. We conclude that the decay of the excited states follows a 2D behavior and investigate different impurity configurations to see the effect of close impurities and vortex shielding currents on the impurity state.

Conclusiones generales

En esta tesis hemos usado el microscopio túnel de barrido a muy bajas temperaturas para estudiar a través de medidas espectroscópicas tres sistemas superconductores distintos. Hemos centrado nuestra investigación en el estudio de los vórtices superconductores y los effectos de las impurezas y los defectos en la densidad de estados superconductora.

En cuanto al sistema experimental, hemos implementado un sistema de rotura *in situ* para poder romper las muestras en condiciones de ultra alto vacío criogénico. Este método, adecuado para materiales por capas, fue usado con éxito en todos los materiales estudiados, proporcionando grandes superficies planas. Hemos mejorado también el sistema de aislamiento de ruido mecánico, sustituyendo el Dewar y el propio sistema de aislamiento.

Siguiendo una propuesta del Dr. V. Kogan, hemos analizado el núcleo de los vórtices en varios materiales. Vemos que en superconductores cercanos al límite limpio, el núcleo del vórtice se reduce con el campo magnético. Además, la escala de longitud que gobierna las variaciones espaciales de la densidad de estados alrededor de los núcleos de los vórtices es la misma para superconductores que tienen distintas bandas con gaps en la superficie de Fermi. Finalmente, hemos demostrado que la propuesta de Kogan puede ser utilizada para extraer escalas de longitud relevantes para el tamaño de los vórtices. Esto permite establecer una conexión entre la rotura de pares y el anclaje de los vórtices en superconductores basados en hierro.

In $Ca(Fe_{0.965}Co_{0.035})_2As_2$ hemos caracterizado los efectos de la tensión y de la reconstrucción de superficie sobre la densidad de estados superconductora. Hemos identificado las diferentes fronteras de dominio existentes en el material y descubierto que en las las fronteras entre dominios tetragonales y ortorómbicos la superconductividad está potenciada. En esas zonas, donde la superconductividad es más clara, hemos hecho imágenes de la red de vórtices, encontrando vórtices redondos que se distribuyen formado una red triangular desordenada. Hemos caracterizado también los effectos de rotura de pares de la reconstrucción de superficie y visto, a través de medidas de interferencia de quasi-partícula, una banda nemática de huecos en la fase ortorómbica con una masa efectiva mayor en la muestra superconductora.

Hemos hecho las primeras medidas de espectroscopia túnel en el $CaKFe_4As_4$, caracterizando la estructura del gap en el mismo. Hemos mostrado que dicha estructura puede describirse con un modelo de dos gaps enseñando también cómo defectos en la

superficie producen rotura de pares de Cooper. El estudio de la red de vórtices revela una red triangular desordenada a todos los campos que se ve muy afectada por el potencial de anclaje producido por la rotura de pares. Nuestros resultados son consistentes con formación de pares con simetría $s_{\pm}$ con cambio de signo en superconductores de hierro.

Finalmente, hemos caracterizado los efectos de la sustitución de Se por S en 2H-$NbSe_{1.8}S_{0.2}$. Vemos que la anisotropía del gap en el plano y el orden de carga presente en 2H-$NbSe_2$ puro, se suprimen por el desorden introducido por el S. En este superconductor isótropo, hemos estudiado los effectos de impurezas magnéticas de hierro investigando los llamados estados de Yu-Shiba-Rusinov. Vemos que el decaimiento de estos estados excitados sigue un comportamiento bidimensional e investigamos diferentes configuraciones de impurezas para ver el efecto de otras impurezas cercanas y de las supercorrientes de apantallamiento de los vórtices en los estados excitados.

Publications

T. Pérez-Castañeda, J. Azpeitia, J. Hanko, A. Fente, H. Suderow and M. A. Ramos, "Low-temperature specific heat of graphite and $CeSb_2$: validation of a quasi-adiabatic continuous method", J. Low. Temp. Phys., 173, 4 (2013).

A. Fente, H. Suderow, S. Vieira, N. Nemes, M. García-Hernández, S. L. Bud'ko, and P. C. Canfield, "Low temperature magnetic transitions of single crystal HoBi", Solid State Comm., 171, 59–63 (2013).

A. Fente, I. Guillamón, S. Ran, S. Vieira, H. Suderow, S. L. Bud'ko and P. C. Canfield, "Observation of unreconstructed square atomic square lattice in $Ca(Fe_{0.965}Co_{0.035})_2As_2$ cleaved at very low temperatures", Jour. Phys.: Conf. Series 568, 022046 (2014).

R. F. Luccas, A. Fente, J. Hanko, A. Correa-Orellana, E. Herrera, E. Climent-Pascual, J. Azpeitia, T. Pérez-Castañeda, M. R. Osorio, E. Salas-Colera, N. M. Nemes, F. J. Mompean, M. García-Hernández, J. G. Rodrigo, M. A. Ramos, I. Guillamón, S. Vieira, and H. Suderow, "Charge density wave in layered $La_{1-x}Ce_xSb_2$", Phys. Rev. B 92, 235153 (2015).

E. Herrera, I. Guillamón, J. A. Galvis, A. Correa, A. Fente, R. F. Luccas, F. J. Mompean, M. García-Hernández, S. Vieira, J. P. Brison, and H. Suderow, "Magnetic field dependence of the density of states in the multiband superconductor β-Bi_2Pd", Phys. Rev. B 92, 054507 (2015).

A. Fente, E. Herrera, I. Guillamón, H. Suderow, S. Mañas-Valero, M. Galbiati, E. Coronado, and V. G. Kogan, "Field dependence of the vortex core size probed by scanning tunneling microscopy", Phys. Rev. B, 94, 014517 (2016).

A. Fente, W. R. Meier, T. Kong, V. G. Kogan, S. L. Bud'ko, P. C. Canfield, I. Guillamon, H. Suderow, "Vortices in two-effective-band, stoichiometric high T_c $CaKFe_4As_4$ superconductor", arXiv:1608.00605v1 [cond-mat.supr-con] (2016).

"Nodeless multiband superconductivity in stoichiometric single crystalline $CaKFe_4As_4$", K. Cho, A. Fente, S. Teknowijoyo, M. A. Tanatar, T. Kong, W. R. Meier, U. Kaluarachchi, I. Guillamón, H. Suderow, S. L. Bud'ko, P. C. Canfield, and R. Prozorov, "Nodeless multiband superconductivity in stoichiometric single crystalline $CaKFe_4$ As_4", Phys. Rev. B 95, 100502 (2017).

E. Herrera, I. Guillamón, J. A. Galvis, A. Correa, A. Fente, S. Vieira, H. Suderow, A. Yu. Martynovich and V. G. Kogan, "Surface bending and reorientation of tilted vortex lattices in the bulk due to Coulomb-like repulsion at the surface," *(in preparation)*.

A. Fente, I. Guillamón, S. Ran, W. R. Meier, T. Kong, A. Böhmer, S. Vieira, H. Suderow, S. L. Bud'ko and P. C. Canfield, "Strain induced coexistence of superconductivity and nematicity in Co-doped $CaFe_2As_2$," *(in preparation)*.

A. Fente, I. Guillamón, S. Mañas-Valero, S. Vieira, E. Coronado, A. Levy and H. Suderow, "Superconducting vortices and impurities in dichalcogenide systems," *(in preparation)*.

Bibliography

A. A. Abrikosov, "On the magnetic properties of superconductors of the second group," Zh. Eksp. Teor. Fiz. **32**, 1442–1452 (1957), english translation: J. Exptl. Theoret. Phys., **5**, 1174 (1957).

A. A. Abrikosov and L. P. Gor'kov, "Contribution to the theory of superconducting alloys with paramagnetic impurities," Zh. Eksp. Teor. Fiz. **39**, 1781–1796 (1961), english translation: J. Exptl. Theoret. Phys., **12**, 1243 (1961).

M. P. Allan, T.-M. Chuang, F. Massee, Y. Xie, N. Ni, S. L. Bud/'ko, G. S. Boebinger, Q. Wang, D. S. Dessau, P. C. Canfield, M. S. Golden, and J. C. Davis, "Anisotropic impurity states, quasiparticle scattering and nematic transport in underdoped $Ca(Fe_{1-x}Co_x)_2As_2$," Nat. Phys. **9**, 220–224 (2013).

J. G. Analytis, R. D. McDonald, S. C. Riggs, J.-H. Chu, G. S. Boebinger, and I. R. Fisher, "Two-dimensional surface state in the quantum limit of a topological insulator," Nat Phys **6**, 960–964 (2010).

P. W. Anderson, "Theory of dirty superconductors," Journal of Physics and Chemistry of Solids **11**, 26 – 30 (1959).

A. F. Andreev, "The thermal conductivity of the intermediate state in superconductors," Zh. Eksp. Teor. Fiz. **46**, 1823 (1964), english translation: J. Exptl. Theoret. Phys., **19**, 1228 (1964).

M. Angst, R. Puzniak, A. Wisniewski, J. Jun, S. M. Kazakov, J. Karpinski, J. Roos, and H. Keller, "Temperature and field dependence of the anisotropy of MgB_2," Phys. Rev. Lett. **88**, 167004 (2002).

J. Bardeen, "Tunnelling from a many-particle point of view," Phys. Rev. Lett. **6**, 57–59 (1961).

J. Bardeen, L. N. Cooper, and J. R. Schrieffer, "Microscopic theory of superconductivity," Phys. Rev. **106**, 162–164 (1957a).

J. Bardeen, L. N. Cooper, and J. R. Schrieffer, "Theory of superconductivity," Phys. Rev. **108**, 1175–1204 (1957b).

V. Barrena, *Single crystal growth and characterization of the pnictide superconductor* $LaRu_2P_2$, Master's thesis, Universidad Autónoma de Madrid, Spain (2016).

E. Bascones, B. Valenzuela, and M. J. Calderón, "Magnetic interactions in iron superconductors: a review," Comptes Rendus Physique **17**, 36 – 59 (2016), iron-based superconductors / Supraconducteurs à base de fer.

J. G. Bednorz and K. A. Müller, "Possible highTc superconductivity in the Ba-La-Cu-O system," Zeitschrift für Physik B Condensed Matter **64**, 189–193 (1986).

J. van den Berg and P. Cossee, "Structural aspects and magnetic behaviour of NbS_2 and TaS_2 containing extra metal atoms of the first transition series," Inorganica Chimica Acta **2**, 143 – 148 (1968).

G. Binnig and H. Rohrer, "Scanning tunneling microscopy," Surface Science **126**, 236 – 244 (1983).

G. Binnig, H. Rohrer, C. Gerber, and E. Weibel, "Surface studies by scanning tunneling microscopy," Phys. Rev. Lett. **49**, 57–61 (1982a).

G. Binnig, H. Rohrer, C. Gerber, and E. Weibel, "Tunneling through a controllable vacuum gap," Applied Physics Letters **40**, 178–180 (1982b).

G. Binnig, H. Rohrer, C. Gerber, and E. Weibel, "Vacuum tunneling," Physica B+C **109**, 2075 – 2077 (1982c).

G. Binning and H. Rohrer, "Scanning tunneling microscopy," Helv. Phys. Acta **55**, 726–735 (1982).

E. Boaknin, M. A. Tanatar, J. Paglione, D. Hawthorn, F. Ronning, R. W. Hill, M. Sutherland, L. Taillefer, J. Sonier, S. M. Hayden, and J. W. Brill, "Heat conduction in the vortex state of $NbSe_2$: evidence for multiband superconductivity," Phys. Rev. Lett. **90**, 117003 (2003).

A. E. Böhmer and A. Kreyssig, Private communication (2017).

A. E. Böhmer, A. Sapkota, A. Kreyssig, S. L. Bud'ko, G. Drachuck, S. M. Saunders, A. I. Goldman, and P. C. Canfield, "Effect of biaxial strain on the phase transitions of $Ca(Fe_{1-x}Co_x)_2As_2$," (2016), arXiv:1612.07341v1 [cond-mat.supr-con].

M. C. Boyer, K. Chatterjee, W. D. Wise, G. F. Chen, J. L. Luo, N. L. Wang, and E. W. Hudson, "Scanning tunneling microscopy of the 32 K superconductor $(Sr_{1-x}K_x)Fe_2As_2$," (2008), arXiv:0809.4400v2 [cond-mat.supt-con].

E. H. Brandt and M. P. Das, "Attractive vortex interaction and the intermediate-mixed state of superconductors," Journal of Superconductivity and Novel Magnetism **24**, 57–67 (2011).

B. Braunecker and P. Simon, "Interplay between classical magnetic moments and superconductivity in quantum one-dimensional conductors: toward a self-sustained topological Majorana phase," Phys. Rev. Lett. **111**, 147202 (2013).

P. Cai, W. Ruan, X. Zhou, C. Ye, A. Wang, X. Chen, D.-H. Lee, and Y. Wang, "Doping dependence of the anisotropic quasiparticle interference in $NaFe_{1-x}Co_xAs$ iron-based superconductors," Phys. Rev. Lett. **112**, 127001 (2014).

M. J. Calderón, B. Valenzuela, and E. Bascones, "Effect of tetrahedral distortion on the electronic properties of iron pnictides," New Journal of Physics **11**, 013051 (2009).

P. C. Canfield, *Solution Growth of Intermetallic Single Crystals: A Beginner's Guide*, E. Belin-Ferré ed., Book Series on Complex Metallic Alloys, Vol. 2 (World Scientific, Singapore, 2010).

P. C. Canfield and S. L. Bud'ko, "FeAs-based superconductivity: a case study of the effects of transition metal doping on $BaFe_2As_2$," Annual Review of Condensed Matter Physics **1**, 27–50 (2010).

P. C. Canfield and I. R. Fisher, "High-temperature solution growth of intermetallic single crystals and quasicrystals," Journal of Crystal Growth **225**, 155 – 161 (2001), proceedings of the 12^{th} American Conference on Crystal Growth and Epitaxy.

P. C. Canfield and Z. Fisk, "Growth of single crystals from metallic fluxes," Philosophical Magazine Part B **65**, 1117–1123 (1992).

P. C. Canfield, P. L. Gammel, and D. J. Bishop, "New magnetic superconductors: a toy box for solid-state physicists," Physics Today **51**, 40–46 (1998).

L. Capriotti, D. J. Scalapino, and R. D. Sedgewick, "Wave-vector power spectrum of the local tunneling density of states: ripples in a *d*-wave sea," Phys. Rev. B **68**, 014508 (2003).

C. Caroli, P. G. deGennes, and J. Matricon, "Bound fermion states on a vortex line in a type II superconductor," Physics Letters **9**, 307 – 309 (1964).

X. Chen, V. Mishra, S. Maiti, and P. J. Hirschfeld, "Effect of nonmagnetic impurities on $s_\pm$ superconductivity in the presence of incipient bands," Phys. Rev. B **94**, 054524 (2016).

K. Cho, A. Fente, S. Teknowijoyo, M. A. Tanatar, K. R. Joshi, N. M. Nusran, T. Kong, W. R. Meier, U. Kaluarachchi, I. Guillamón, H. Suderow, S. L. Bud'ko, P. C. Canfield, and R. Prozorov, "Nodeless multiband superconductivity in stoichiometric single-crystalline $CaKFe_4As_4$," Phys. Rev. B **95**, 100502 (2017).

K. Cho, M. Kończykowski, S. Teknowijoyo, M. A. Tanatar, Y. Liu, T. A. Lograsso, W. E. Straszheim, V. Mishra, S. Maiti, P. J. Hirschfeld, and R. Prozorov, "Energy gap evolution across the superconductivity dome in single crystals of $(Ba_{1-x}K_x)Fe_2As_2$," Science Advances **2**, e1600807 (2016).

H. J. Choi, D. Roundy, H. Sun, M. L. Cohen, and S. G. Louie, "The origin of the anomalous superconducting properties of MgB_2," Nature **418**, 758–760 (2002).

J.-H. Chu, J. G. Analytis, K. De Greve, P. L. McMahon, Z. Islam, Y. Yamamoto, and I. R. Fisher, "In-plane resistivity anisotropy in an underdoped iron arsenide superconductor," Science **329**, 824–826 (2010).

T.-M. Chuang, M. P. Allan, J. Lee, Y. Xie, N. Ni, S. L. Bud'ko, G. S. Boebinger, P. C. Canfield, and J. C. Davis, "Nematic electronic structure in the "parent" state of the iron-based superconductor $Ca(Fe_{1-x}Co_x)_2As_2$," Science **327**, 181–184 (2010).

A. Chubukov and P. J. Hirschfeld, "Iron-based superconductors, seven years later," Physics Today **68**, 46–52 (2015).

J. R. Clem, "Simple model for the vortex core in a type II superconductor," Journal of Low Temperature Physics **18**, 427–434 (1975).

L. N. Cooper, "Bound electron pairs in a degenerate Fermi gas," Phys. Rev. **104**, 1189–1190 (1956).

M. F. Crommie, C. P. Lutz, and D. M. Eigler, "Imaging standing waves in a two-dimensional electron gas," Nature **363**, 524–527 (1993).

J. C. Cuevas, A. Martín-Rodero, and A. L. Yeyati, "Hamiltonian approach to the transport properties of superconducting quantum point contacts," Phys. Rev. B **54**, 7366–7379 (1996).

P. G. deGennes, "Behavior of dirty superconductors in high magnetic fields," Physik der kondensierten Materie **3**, 79–90 (1964).

P. G. deGennes, *Superconductivity of metals and alloys*, 3rd ed. (Westview Press, New York, 1966) 1999 edition.

D. van Delft and P. Kes, "The discovery of superconductivity," Europhysics News **42**, 21–25 (2011).

Z. Deng, X. C. Wang, Q. Q. Liu, S. J. Zhang, Y. X. Lv, J. L. Zhu, R. C. Yu, and C. Q. Jin, "A new "111" type iron pnictide superconductor LiFeP," EPL (Europhysics Letters) **87**, 37004 (2009).

D. O. Edwards, D. F. Brewer, P. Seligman, M. Skertic, and M. Yaqub, "Solubility of He^3 in liquid He^4 at $0°K$," Phys. Rev. Lett. **15**, 773–775 (1965).

D. V. Efremov, M. M. Korshunov, O. V. Dolgov, A. A. Golubov, and P. J. Hirschfeld, "Disorder-induced transition between $s_{\pm}$ and s_{++} states in two-band superconductors," Phys. Rev. B **84**, 180512 (2011).

M. Eskildsen, M. Kugler, G. Levy, S. Tanaka, J. Jun, S. Kazakov, J. Karpinski, and Ø. Fischer, "Scanning tunneling spectroscopy on single crystal MgB_2," Physica C: Superconductivity **385**, 169 – 176 (2003a).

M. R. Eskildsen, N. Jenkins, G. Levy, M. Kugler, Ø. Fischer, J. Jun, S. M. Kazakov, and J. Karpinski, "Vortex imaging in magnesium diboride with $H \perp c$," Phys. Rev. B **68**, 100508 (2003b).

M. R. Eskildsen, M. Kugler, S. Tanaka, J. Jun, S. M. Kazakov, J. Karpinski, and Ø. Fischer, "Vortex imaging in the π band of magnesium diboride," Phys. Rev. Lett. **89**, 187003 (2002).

U. Essmann and H. Träuble, "The direct observation of individual flux lines in type II superconductors," Physics Letters A **24**, 526 – 527 (1967).

A. Fente, I. Guillamón, S. Ran, S. Vieira, H. Suderow, S. L. Bud'ko, and P. C. Canfield, "Observation of unreconstructed square atomic square lattice in $Ca(Fe_{0.965}Co_{0.035})_2As_2$ cleaved at very low temperatures," Journal of Physics: Conference Series **568**, 022046 (2014).

A. Fente, E. Herrera, I. Guillamón, H. Suderow, S. Mañas Valero, M. Galbiati, E. Coronado, and V. G. Kogan, "Field dependence of the vortex core size probed by scanning tunneling microscopy," Phys. Rev. B **94**, 014517 (2016).

A. Fente, H. Suderow, S. Vieira, N. Nemes, M. García-Hernández, S. Bud'ko, and P. Canfield, "Low temperature magnetic transitions of single crystal HoBi," Solid State Communications **171**, 59 – 63 (2013).

Ø. Fischer, M. Kugler, I. Maggio-Aprile, C. Berthod, and C. Renner, "Scanning tunneling spectroscopy of high-temperature superconductors," Rev. Mod. Phys. **79**, 353–419 (2007).

Z. Fisk and J. P. Remeika, *Growth of single crystals from molten metal fluxes*, Handbook on the Physics and Chemistry of Rare Earths, Vol. 12 (Elsevier, 1989) pp. 53 – 70.

M. E. Flatté and J. M. Byers, "Local electronic structure of a single magnetic impurity in a superconductor," Phys. Rev. Lett. **78**, 3761–3764 (1997).

H. Fröhlich, "Theory of the superconducting state. I. The ground state at the absolute zero of temperature," Phys. Rev. **79**, 845–856 (1950).

M. Gao, F. Ma, Z.-Y. Lu, and T. Xiang, "Surface structures of ternary iron arsenides AFe_2As_2 (A = Ba, Sr, or Ca)," Phys. Rev. B **81**, 193409 (2010).

E. Gati, S. Köhler, D. Guterding, B. Wolf, S. Knöner, S. Ran, S. L. Bud'ko, P. C. Canfield, and M. Lang, "Hydrostatic-pressure tuning of magnetic, nonmagnetic, and superconducting states in annealed $Ca(Fe_{1-x}Co_x)_2As_2$," Phys. Rev. B **86**, 220511 (2012).

T. Giamarchi and P. Le Doussal, "Elastic theory of pinned flux lattices," Phys. Rev. Lett. **72**, 1530–1533 (1994).

L. P. Gor'kov, "Microscopic derivation of the Ginzburg-Landau equations in the theory of superconductivity," Zh. Eksp. Teor. Fiz. **36**, 1442–1452 (1959), english translation: J. Exptl. Theoret. Phys., **36**, 1918 (1959).

S. Grothe, S. Chi, P. Dosanjh, R. Liang, W. N. Hardy, S. A. Burke, D. A. Bonn, and Y. Pennec, "Bound states of defects in superconducting LiFeAs studied by scanning tunneling spectroscopy," Phys. Rev. B **86**, 174503 (2012).

I. Guillamón, *Orden y desorden en superconductividad*, Ph.D. thesis, Universidad Autónoma de Madrid, Madrid, ES-28049, Spain (2009), http://lbtuam.es/?p=910.

I. Guillamón, R. Córdoba, J. Sesé, J. M. D. Teresa, M. R. Ibarra, S. Vieira, and H. Suderow, "Enhancement of long-range correlations in a 2D vortex lattice by an incommensurate 1D disorder potential," Nature Physics **10**, 851–856 (2015).

I. Guillamón, H. Suderow, F. Guinea, and S. Vieira, "Intrinsic atomic-scale modulations of the superconducting gap of 2H-$NbSe_2$," Phys. Rev. B **77**, 134505 (2008a).

I. Guillamón, H. Suderow, S. Vieira, L. Cario, P. Diener, and P. Rodière, "Superconducting density of states and vortex cores of 2H-NbS_2," Phys. Rev. Lett. **101**, 166407 (2008b).

J. Hamlin, R. Baumbach, D. Zocco, T. Sayles, and M. Maple, "Superconductivity in single crystals of LaFePO," Journal of Physics: Condensed Matter **20**, 365220 (2008).

T. Hanaguri, K. Kitagawa, K. Matsubayashi, Y. Mazaki, Y. Uwatoko, and H. Takagi, "Scanning tunneling microscopy/spectroscopy of vortices in LiFeAs," Phys. Rev. B **85**, 214505 (2012).

L. Harnagea, S. Singh, G. Friemel, N. Leps, D. Bombor, M. Abdel-Hafiez, A. U. B. Wolter, C. Hess, R. Klingeler, G. Behr, S. Wurmehl, and B. Büchner, "Phase diagram of the iron arsenide superconductors $Ca(Fe_{1-x}Co_x)_2As_2$ $(0 \leqslant x \leqslant 0.2)$," Phys. Rev. B **83**, 094523 (2011).

J. M. E. Harper, T. H. Geballe, and F. J. DiSalvo, "Thermal properties of layered transition-metal dichalcogenides at charge-density-wave transitions," Phys. Rev. B **15**, 2943–2951 (1977).

U. Hartmann, A. Golubov, T. Drechsler, M. Kupriyanov, and C. Heiden, "Measurement of the vortex-core radius by scanning tunneling microscopy," Physica B: Condensed Matter **194–196, Part 1**, 387 – 388 (1994).

Y. Hasegawa and P. Avouris, "Direct observation of standing wave formation at surface steps using scanning tunneling spectroscopy," Phys. Rev. Lett. **71**, 1071–1074 (1993).

K. Hashimoto, K. Cho, T. Shibauchi, S. Kasahara, Y. Mizukami, R. Katsumata, Y. Tsuruhara, T. Terashima, H. Ikeda, M. A. Tanatar, H. Kitano, N. Salovich, R. W. Giannetta, P. Walmsley, A. Carrington, R. Prozorov, and Y. Matsuda, "A sharp peak of the zero-temperature penetration depth at optimal composition in $BaFe_2(As_{1-x}P_x)_2$," Science **336**, 1554–1557 (2012).

K. Hashimoto, Y. Mizukami, R. Katsumata, H. Shishido, M. Yamashita, H. Ikeda, Y. Matsuda, J. A. Schlueter, J. D. Fletcher, A. Carrington, D. Gnida, D. Kaczorowski, and T. Shibauchi, "Anomalous superfluid density in quantum critical superconductors," Proceedings of the National Academy of Sciences **110**, 3293–3297 (2013).

N. Hayashi, T. Isoshima, M. Ichioka, and K. Machida, "Low-lying quasiparticle excitations around a vortex core in quantum limit," Phys. Rev. Lett. **80**, 2921–2924 (1998).

E. Herrera, *Visualizing the influence of the Fermi surface on superconductivity*, Ph.D. thesis, Universidad Autónoma de Madrid, Madrid, ES-28049, Spain (2016), http://lbtuam.es/TesisEd.

E. Herrera, I. Guillamón, J. A. Galvis, A. Correa, A. Fente, R. F. Luccas, F. J. Mompean, M. García-Hernández, S. Vieira, J. P. Brison, and H. Suderow, "Magnetic field dependence of the density of states in the multiband superconductor β-Bi_2Pd," Phys. Rev. B **92**, 054507 (2015).

H. Hess, R. Robinson, and J. Waszczak, "STM spectroscopy of vortex cores and the flux lattice," Physica B: Condensed Matter **169**, 422 – 431 (1991).

H. F. Hess, R. B. Robinson, R. C. Dynes, J. M. Valles, and J. V. Waszczak, "Scanning-tunneling-microscope observation of the Abrikosov flux lattice and the density of states near and inside a fluxoid," Phys. Rev. Lett. **62**, 214–216 (1989).

H. F. Hess, R. B. Robinson, and J. V. Waszczak, "Vortex-core structure observed with a scanning tunneling microscope," Phys. Rev. Lett. **64**, 2711–2714 (1990).

E. van Heumen, J. Vuorinen, K. Koepernik, F. Massee, Y. Huang, M. Shi, J. Klei, J. Goedkoop, M. Lindroos, J. van den Brink, and M. S. Golden, "Existence, character, and origin of surface-related bands in the high temperature iron pnictide superconductor $BaFe_{2-x}Co_xAs_2$," Phys. Rev. Lett. **106**, 027002 (2011).

P. J. Hirschfeld, "Using gap symmetry and structure to reveal the pairing mechanism in Fe-based superconductors," Comptes Rendus Physique **17**, 197 – 231 (2016), iron-based superconductors / Supraconducteurs à base de fer.

P. J. Hirschfeld, D. Altenfeld, I. Eremin, and I. I. Mazin, "Robust determination of the superconducting gap sign structure via quasiparticle interference," Phys. Rev. B **92**, 184513 (2015).

P. J. Hirschfeld, M. M. Korshunov, and I. I. Mazin, "Gap symmetry and structure of Fe-based superconductors," Reports on Progress in Physics **74**, 124508 (2011).

J. E. Hoffman, *A search for alternative electronic order in the high temperature superconductor $Bi_2Sr_2CaCu_2O_{8+\delta}$ by scanning tunneling microscopy*, Ph.D. thesis, University of California, Berkeley, Ca, USA (2003), http://users.physics.harvard.edu/~jhoffman/thesis/HoffmanThesis.pdf.

J. E. Hoffman, "Spectroscopic scanning tunneling microscopy insights into Fe-based superconductors," Reports on Progress in Physics **74**, 124513 (2011).

H. Hosono and K. Kuroki, "Iron-based superconductors: current status of materials and pairing mechanism," Physica C: Superconductivity and its Applications **514**, 399 – 422 (2015).

D. Hsieh, Y. Xia, L. Wray, D. Qian, K. Gomes, A. Yazdani, G. F. Chen, J. L. Luo, N. L. Wang, and M. Z. Hasan, "Experimental determination of the microscopic origin of magnetism in parent iron pnictides," (2008), arXiv:0812.2289v1[cond-mat.supr-con].

F.-C. Hsu, J.-Y. Luo, K.-W. Yeh, T.-K. Chen, T.-W. Huang, P. M. Wu, Y.-C. Lee, Y.-L. Huang, Y.-Y. Chu, D.-C. Yan, and M.-K. Wu, "Superconductivity in the PbO-type structure α-FeSe," Proceedings of the National Academy of Sciences **105**, 14262–14264 (2008).

R. Hu, S. Ran, W. E. Straszheim, S. L. Bud'ko, and P. C. Canfield, "Single crystal growth and superconductivity of $Ca(Fe_{1-x}Co_x)_2As_2$," Philosophical Magazine **92**, 3113–3120 (2012).

A. Iyo, K. Kawashima, T. Kinjo, T. Nishio, S. Ishida, H. Fujihisa, Y. Gotoh, K. Kihou, H. Eisaki, and Y. Yoshida, "New-structure-type Fe-based superconductors: $CaAFe_4As_4$ (A = K, Rb, Cs) and $SrAFe_4As_4$ (A = Rb, Cs)," Journal of the American Chemical Society **138**, 3410–3415 (2016).

W. Jeitschko, R. Glaum, and L. Boonk, "Superconducting $LaRu_2P_2$ and other alkaline earth and rare earth metal ruthenium and osmium phosphides and arsenides with $ThCr_2Si_2$ structure," Journal of Solid State Chemistry **69**, 93 – 100 (1987).

S.-H. Ji, T. Zhang, Y.-S. Fu, X. Chen, X.-C. Ma, J. Li, W.-H. Duan, J.-F. Jia, and Q.-K. Xue, "High-resolution scanning tunneling spectroscopy of magnetic impurity induced bound states in the superconducting gap of Pb thin films," Phys. Rev. Lett. **100**, 226801 (2008).

M. D. Johannes, I. I. Mazin, and C. A. Howells, "Fermi-surface nesting and the origin of the charge-density wave in $NbSe_2$," Phys. Rev. B **73**, 205102 (2006).

S. de Jong, Y. Huang, R. Huisman, F. Massee, S. Thirupathaiah, M. Gorgoi, F. Schaefers, R. Follath, J. B. Goedkoop, and M. S. Golden, "High-resolution, hard x-ray photoemission investigation of $BaFe_2As_2$: moderate influence of the surface and evidence for a low degree of Fe 3d - As 4p hybridization of electronic states near the Fermi energy," Phys. Rev. B **79**, 115125 (2009).

B. Kalisky, J. R. Kirtley, J. G. Analytis, J.-H. Chu, I. R. Fisher, and K. A. Moler, "Behavior of vortices near twin boundaries in underdoped $Ba(Fe_{1-x}Co_x)_2As_2$," Phys. Rev. B **83**, 064511 (2011).

B. Kalisky, J. R. Kirtley, J. G. Analytis, J.-H. Chu, A. Vailionis, I. R. Fisher, and K. A. Moler, "Stripes of increased diamagnetic susceptibility in underdoped superconducting $Ba(Fe_{1-x}Co_x)_2As_2$ single crystals: evidence for an enhanced superfluid density at twin boundaries," Phys. Rev. B **81**, 184513 (2010).

Y. Kamihara, H. Hiramatsu, M. Hirano, R. Kawamura, H. Yanagi, T. Kamiya, and H. Hosono, "Iron-based layered superconductor: LaOFeP," Journal of the American Chemical Society **128**, 10012–10013 (2006).

Y. Kamihara, T. Watanabe, M. Hirano, and H. Hosono, "Iron-based layered superconductor $La[O_{1-x}F_x]FeAs$ (x = 0.05–0.12) with $T_c = 26\,K$," Journal of the American Chemical Society **130**, 3296–3297 (2008).

J. R. Kirtley, B. Kalisky, L. Luan, and K. A. Moler, "Meissner response of a bulk superconductor with an embedded sheet of reduced penetration depth," Phys. Rev. B **81**, 184514 (2010).

T. Kiss, T. Yokoya, A. Chainani, S. Shin, T. Hanaguri, M. Nohara, and H. Takagi, "Charge-order-maximized momentum-dependent superconductivity," Nat. Phys. **3**, 720–725 (2007).

J. Klinovaja, P. Stano, A. Yazdani, and D. Loss, "Topological superconductivity and Majorana fermions in RKKY systems," Phys. Rev. Lett. **111**, 186805 (2013).

V. G. Kogan, "Pair breaking in iron pnictides," Phys. Rev. B **80**, 214532 (2009).

V. G. Kogan and N. V. Zhelezina, "Field dependence of the vortex core size," Phys. Rev. B **71**, 134505 (2005).

W. Kohn and J. M. Luttinger, "New mechanism for superconductivity," Phys. Rev. Lett. **15**, 524–526 (1965).

K. Kuroki, H. Usui, S. Onari, R. Arita, and H. Aoki, "Pnictogen height as a possible switch between high-T_c nodeless and low-T_c nodal pairings in the iron-based superconductors," Phys. Rev. B **79**, 224511 (2009).

X. Lai, H. Zhang, Y. Wang, X. Wang, X. Zhang, J. Lin, and F. Huang, "Observation of superconductivity in tetragonal FeS," Journal of the American Chemical Society **137**, 10148–10151 (2015).

L. D. Landau and V. L. Ginzburg, "On the theory of superconductivity," Zh. Eksp. Teor. Fiz. **20**, 1064 (1950), in *Collected Papers of L.D. Landau*, Pergamon (1965).

A. I. Larkin and Y. N. Ovchinnikov, "Pinning in type II superconductors," Journal of Low Temperature Physics **34**, 409–428 (1979).

B. Li, P. Lu, J. Liu, J. Sun, S. Li, X. Zhu, and H.-H. Wen, "Pressure induced enhancement of superconductivity in $LaRu_2P_2$," Scientific Reports **6**, 24479 (2016).

G. Li, X. He, J. Zhang, R. Jin, A. S. Sefat, M. A. McGuire, D. G. Mandrus, B. C. Sales, and E. W. Plummer, "Coupled structural and magnetic antiphase domain walls on $BaFe_2As_2$," Phys. Rev. B **86**, 060512 (2012).

F. London and H. London, "The electromagnetic equations of the supraconductor," Proceedings of the Royal Society of London A: mathematical, physical and engineering sciences **149**, 71–88 (1935).

H. London, ed., *Proceedings of the 2nd International Conference on Low Temperature Physics* (Oxford Univ. Press, Oxford, UK, 1951).

H. London, G. R. Clarke, and E. Mendoza, "Osmotic pressure of He^3 in liquid He^4, with proposals for a refrigerator to work below $1^\circ K$," Phys. Rev. **128**, 1992–2005 (1962).

O. Lounasmaa, *Experimental principles and methods below 1 K* (Academic Press: London and New York, 1974).

R. F. Luccas, A. Fente, J. Hanko, A. Correa-Orellana, E. Herrera, E. Climent-Pascual, J. Azpeitia, T. Pérez-Castañeda, M. R. Osorio, E. Salas-Colera, N. M. Nemes, F. J. Mompean, M. García-Hernández, J. G. Rodrigo, M. A. Ramos, I. Guillamón, S. Vieira, and H. Suderow, "Charge density wave in layered $La_{1-x}Ce_xSb_2$," Phys. Rev. B **92**, 235153 (2015).

P. Martinez-Samper, J. G. Rodrigo, G. Rubio-Bollinger, H. Suderow, S. Vieira, S. Lee, and S. Tajima, "Scanning tunneling spectroscopy in MgB_2," Physica C: Superconductivity **385**, 233 – 243 (2003).

F. Massee, *A tunneler's view on correlated oxides and iron based superconductors*, Ph.D. thesis, Van der Waals - Zeeman Institute of the University of Amsterdam, The Netherlands (2011), http://dare.uva.nl/record/1/337519.

F. Massee, Y. Huang, R. Huisman, S. de Jong, J. B. Goedkoop, and M. S. Golden, "Nanoscale superconducting-gap variations and lack of phase separation in optimally doped $BaFe_{1.86}Co_{0.14}As_2$," Phys. Rev. B **79**, 220517 (2009a).

F. Massee, S. de Jong, Y. Huang, J. Kaas, E. van Heumen, J. B. Goedkoop, and M. S. Golden, "Cleavage surfaces of the $BaFe_{2-x}Co_xAs_2$ and $Fe_ySe_{1-x}Te_x$ superconductors: a combined STM plus LEED study," Phys. Rev. B **80**, 140507 (2009b).

F. Massee, P. O. Sprau, Y.-L. Wang, J. C. S. Davis, G. Ghigo, G. D. Gu, and W.-K. Kwok, "Imaging atomic-scale effects of high-energy ion irradiation on superconductivity and vortex pinning in Fe(Se,Te)," Science Advances **1**, e1500033 (2015).

B. T. Matthias, "Superconductivity and ferromagnetism," IBM Journal of Research and Development **6**, 250–255 (1962).

B. T. Matthias, H. Suhl, and E. Corenzwit, "Spin exchange in superconductors," Phys. Rev. Lett. **1**, 92–94 (1958).

B. T. Matthias, H. Suhl, and E. Corenzwit, "Further experiments concerning the spin-electron interactions in superconductors," Journal of Physics and Chemistry of Solids **13**, 156 – 159 (1960).

E. Maxwell, "Isotope effect in the superconductivity of mercury," Phys. Rev. **78**, 477–477 (1950).

I. I. Mazin and J. Schmalian, "Pairing symmetry and pairing state in ferropnictides: theoretical overview," Physica C: Superconductivity **469**, 614 – 627 (2009).

I. I. Mazin, D. J. Singh, M. D. Johannes, and M. H. Du, "Unconventional superconductivity with a sign reversal in the order parameter of $LaFeAsO_{1-x}F_x$," Phys. Rev. Lett. **101**, 057003 (2008).

A. Meerschaut and C. Deudon, "Crystal structure studies of the 3R-$Nb_{1.09}S_2$ and the 2H-$NbSe_2$ compounds: correlation between nonstoichiometry and stacking type (= polytypism)," Materials Research Bulletin **36**, 1721 – 1727 (2001).

W. R. Meier, T. Kong, U. S. Kaluarachchi, V. Taufour, N. H. Jo, G. Drachuck, A. E. Böhmer, S. M. Saunders, A. Sapkota, A. Kreyssig, M. A. Tanatar, R. Prozorov, A. I. Goldman, F. F. Balakirev, A. Gurevich, S. L. Bud'ko, and P. C. Canfield, "Anisotropic thermodynamic and transport properties of single-crystalline $CaKFe_4As_4$," Phys. Rev. B **94**, 064501 (2016).

W. Meissner and R. Ochsenfeld, "Ein neuer Effekt bei Eintritt der Supraleitfähigkeit," Naturwissenschaften **21**, 787–788 (1933).

G. C. Menard, S. Guissart, C. Brun, S. Pons, V. S. Stolyarov, F. Debontridder, M. V. Leclerc, E. Janod, L. Cario, D. Roditchev, P. Simon, and T. Cren, "Coherent long-range magnetic bound states in a superconductor," Nat. Phys. **11**, 1013–1016 (2015).

R. Mittal, S. K. Mishra, S. L. Chaplot, S. V. Ovsyannikov, E. Greenberg, D. M. Trots, L. Dubrovinsky, Y. Su, T. Brueckel, S. Matsuishi, H. Hosono, and G. Garbarino, "Ambient- and low-temperature synchrotron x-ray diffraction study of $BaFe_2As_2$ and $CaFe_2As_2$ at high pressures up to 56 GPa," Phys. Rev. B **83**, 054503 (2011).

K. Miyake and N. K. Sato, "Unconventional cooper pairing in the superconducting state of UPd_2Al_3," Phys. Rev. B **63**, 052508 (2001).

S. Mizusaki, Y. Adachi, T. Ohnishi, T. Taniguchi, Y. Nagata, T. Ozawa, Y. Noro, and H. Samata, "Synthesis and properties of $LnRu_2P_2$ (Ln = lanthanides) crystals," Journal of Alloys and Compounds **468**, 28 – 33 (2009).

D. Mou, T. Kong, W. R. Meier, F. Lochner, L.-L. Wang, Q. Lin, Y. Wu, S. L. Bud'ko, I. Eremin, D. D. Johnson, P. C. Canfield, and A. Kaminski, "Enhancement of the superconducting gap by nesting in $CaKFe_4As_4$: a new high temperature superconductor," Phys. Rev. Lett. **117**, 277001 (2016).

N. Nakai, M. Ichioka, and K. Machida, "Field dependence of electronic specific heat in two-band superconductors," Journal of the Physical Society of Japan **71**, 23–26 (2002).

V. B. Nascimento, A. Li, D. R. Jayasundara, Y. Xuan, J. O'Neal, S. Pan, T. Y. Chien, B. Hu, X. B. He, G. Li, A. S. Sefat, M. A. McGuire, B. C. Sales, D. Mandrus, M. H. Pan, J. Zhang, R. Jin, and E. W. Plummer, "Surface geometric and electronic structures of $BaFe_2As_2$(001)," Phys. Rev. Lett. **103**, 076104 (2009).

N. Ni, S. L. Bud'ko, A. Kreyssig, S. Nandi, G. E. Rustan, A. I. Goldman, S. Gupta, J. D. Corbett, A. Kracher, and P. C. Canfield, "Anisotropic thermodynamic and transport properties of single-crystalline $Ba_{1-x}K_xFe_2As_2$ (x = 0 and 0.45)," Phys. Rev. B **78**, 014507 (2008a).

N. Ni, S. Nandi, A. Kreyssig, A. I. Goldman, E. D. Mun, S. L. Bud'ko, and P. C. Canfield, "First-order structural phase transition in $CaFe_2As_2$," Phys. Rev. B **78**, 014523 (2008b).

F. C. Niestemski, V. B. Nascimento, B. Hu, W. Plummer, J. Gillett, S. Sebastian, Z. Wang, and V. Madhavan, "Unveiling the atomic and electronic structure at the surface of the parent pnictide $SrFe_2As_2$," (2009), arXiv:0906.2761v1 [cond-mat.supr-con].

H. Okamoto, "Comment on bi-ho (bismuth-holmium)," Journal of Phase Equilibria **15**, 651–652 (1994).

J. Paglione and R. L. Greene, "High-temperature superconductivity in iron-based materials," Nat Phys **6**, 645–658 (2010).

T. Pérez-Castañeda, J. Azpeitia, J. Hanko, A. Fente, H. Suderow, and M. A. Ramos, "Low-temperature specific heat of graphite and $CeSb_2$: validation of a quasi-adiabatic continuous method," Journal of Low Temperature Physics **173**, 4–20 (2013).

L. Petersen, P. T. Sprunger, P. Hofmann, E. Lægsgaard, B. G. Briner, M. Doering, H.-P. Rust, A. M. Bradshaw, F. Besenbacher, and E. W. Plummer, "Direct imaging of the two-dimensional Fermi contour: fourier-transform STM," Phys. Rev. B **57**, R6858–R6861 (1998).

C. Putzke, P. Walmsley, J. D. Fletcher, L. Malone, D. Vignolles, C. Proust, S. Badoux, P. See, H. E. Beere, D. A. Ritchie, S. Kasahara, Y. Mizukami, T. Shibauchi, Y. Matsuda, and A. Carrington, "Anomalous critical fields in quantum critical superconductors," Nature Communications **5**, 5679 (2014).

S. Ran, *Combined effects of post-growth thermal treatment and chemical substitution on physical properties of $CaFe_2As_2$*, Ph.D. thesis, Iowa State University, Ames (IA), USA (2014), http://lib.dr.iastate.edu/etd/14274.

S. Ran, S. L. Bud'ko, D. K. Pratt, A. Kreyssig, M. G. Kim, M. J. Kramer, D. H. Ryan, W. N. Rowan-Weetaluktuk, Y. Furukawa, B. Roy, A. I. Goldman, and P. C. Canfield, "Stabilization of an ambient-pressure collapsed tetragonal phase in $CaFe_2As_2$ and tuning of the orthorhombic-antiferromagnetic transition temperature by over 70 K via control of nanoscale precipitates," Phys. Rev. B **83**, 144517 (2011).

S. Ran, S. L. Bud'ko, W. E. Straszheim, J. Soh, M. G. Kim, A. Kreyssig, A. I. Goldman, and P. C. Canfield, "Control of magnetic, nonmagnetic, and superconducting states in annealed $Ca(Fe_{1-x}Co_x)_2As_2$," Phys. Rev. B **85**, 224528 (2012).

C. A. Reynolds, B. Serin, W. H. Wright, and L. B. Nesbitt, "Superconductivity of isotopes of mercury," Phys. Rev. **78**, 487–487 (1950).

J. G. Rodrigo, H. Suderow, S. Vieira, E. Bascones, and F. Guinea, "Superconducting nanostructures fabricated with the scanning tunnelling microscope," Journal of Physics: Condensed Matter **16**, R1151 (2004).

J. G. Rodrigo and S. Vieira, "STM study of multiband superconductivity in $NbSe_2$ using a superconducting tip," Physica C: Superconductivity **404**, 306 – 310 (2004), proceedings of the Third European Conference on Vortex Matter in Superconductors at Extreme Scales and Conditions.

F. Ronning, T. Klimczuk, E. D. Bauer, H. Volz, and J. D. Thompson, "Synthesis and properties of $CaFe_2As_2$ single crystals," Journal of Physics: Condensed Matter **20**, 322201 (2008).

E. P. Rosenthal, E. F. Andrade, C. J. Arguello, R. M. Fernandes, L. Y. Xing, X. C. Wang, C. Q. Jin, A. J. Millis, and A. N. Pasupathy, "Visualization of electron nematicity and unidirectional antiferroic fluctuations at high temperatures in NaFeAs," Nat. Phys. **10**, 225–232 (2014).

M. Rotter, M. Pangerl, M. Tegel, and D. Johrendt, "Superconductivity and crystal structures of $(Ba_{1-x}K_x)Fe_2As_2$ (x = 0–1)," Angewandte Chemie International Edition **47**, 7949–7952 (2008).

A. I. Rusinov, "Superconductivity near a paramagnetic impurity," J. Exptl. Theoret. Phys Lett. **9**, 85–87 (1968).

D. Saint-James, G. Sarma, and E. J. Thomas, *Type-II superconductivity*, International series of monographs in natural philosophy, Vol. 17 (Pergamon Press, Oxford, 1969) eq. 6.83.

A. Schmid, "A time dependent Ginzburg-Landau equation and its application to the problem of resistivity in the mixed state," Physik der kondensierten Materie **5**, 302–317 (1966).

V. V. Schmidt, *The physics of superconductors: introduction to fundamentals and applications*, 1st ed. (Springer - Verlag, Berlin-Heidelberg-New York, 1997) original russian edition published by Nauka Publishers, Moscow, (1982).

A. S. Sefat, R. Jin, M. A. McGuire, B. C. Sales, D. J. Singh, and D. Mandrus, "Superconductivity at 22 K in Co-doped $BaFe_2As_2$ crystals," Phys. Rev. Lett. **101**, 117004 (2008).

G. Seyfarth, J. P. Brison, M.-A. Méasson, D. Braithwaite, G. Lapertot, and J. Flouquet, "Superconducting $PrOs_4Sb_{12}$: a thermal conductivity study," Phys. Rev. Lett. **97**, 236403 (2006).

L. Shan, Y. L. Wang, B. Shen, B. Zeng, Y. Huang, A. Li, D. Wang, H. Yang, C. Ren, Q. H. Wang, S. H. Pan, and H. H. Wen, "Observation of ordered vortices with andreev bound states in $Ba_{0.6}K_{0.4}Fe_2As_2$," Nature Physics **7**, 325–331 (2011).

H. Shiba, "Classical spins in superconductors," Progress of Theoretical Physics **40**, 435–451 (1968).

J. I. Shimoyama, "Potentials of iron-based superconductors for practical future materials," Superconductor Science and Technology **27**, 044002 (2014).

U. R. Singh, S. C. White, S. Schmaus, V. Tsurkan, A. Loidl, J. Deisenhofer, and P. Wahl, "Evidence for orbital order and its relation to superconductivity in $FeSe_{0.4}Te_{0.6}$," Science Advances **1**, e1500206 (2015).

S. Skalski, O. Betbeder-Matibet, and P. R. Weiss, "Properties of superconducting alloys containing paramagnetic impurities," Phys. Rev. **136**, A1500–A1518 (1964).

A. V. Sologubenko, J. Jun, S. M. Kazakov, J. Karpinski, and H. R. Ott, "Thermal conductivity of single-crystalline MgB_2," Phys. Rev. B **66**, 014504 (2002).

C.-L. Song, Y.-L. Wang, P. Cheng, Y.-P. Jiang, W. Li, T. Zhang, Z. Li, K. He, L. Wang, J.-F. Jia, H.-H. Hung, C. Wu, X. Ma, X. Chen, and Q.-K. Xue, "Direct observation of nodes and twofold symmetry in FeSe superconductor," Science **332**, 1410–1413 (2011).

C.-L. Song, Y.-L. Wang, Y.-P. Jiang, L. Wang, K. He, X. Chen, J. E. Hoffman, X.-C. Ma, and Q.-K. Xue, "Suppression of superconductivity by twin boundaries in FeSe," Phys. Rev. Lett. **109**, 137004 (2012).

C.-L. Song, Y. Yin, M. Zech, T. Williams, M. M. Yee, G.-F. Chen, J.-L. Luo, N.-L. Wang, E. W. Hudson, and J. E. Hoffman, "Dopant clustering, electronic inhomogeneity, and vortex pinning in iron-based superconductors," Phys. Rev. B **87**, 214519 (2013).

A. Soumyanarayanan, M. M. Yee, Y. He, J. van Wezel, D. J. Rahn, K. Rossnagel, E. W. Hudson, M. R. Norman, and J. E. Hoffman, "Quantum phase transition from triangular to stripe charge order in $NbSe_2$," Proceedings of the National Academy of Sciences **110**, 1623–1627 (2013).

H. Suderow, I. Guillamón, J. G. Rodrigo, and S. Vieira, "Imaging superconducting vortex cores and lattices with a scanning tunneling microscope," Superconductor Science and Technology **27**, 063001 (2014).

H. Suderow, I. Guillamón, and S. Vieira, "Compact very low temperature scanning tunneling microscope with mechanically driven horizontal linear positioning stage," Review of Scientific Instruments **82**, 033711 (2011).

H. Suderow, S. Kambe, J. P. Brison, A. Huxley, J. Flouquet, and F. Rullier-Albenque, "Controlled creation of structural defects in the heavy fermion superconductor UPt_3 and its influence on the superconducting properties," Journal of Low Temperature Physics **116**, 393–405 (1999).

H. Suhl, B. T. Matthias, and L. R. Walker, "Bardeen-Cooper-Schrieffer theory of superconductivity in the case of overlapping bands," Phys. Rev. Lett. **3**, 552–554 (1959).

M. A. Tanatar, A. Kreyssig, S. Nandi, N. Ni, S. L. Bud'ko, P. C. Canfield, A. I. Goldman, and R. Prozorov, "Direct imaging of the structural domains in the iron pnictides AFe_2As_2 (A=Ca,Sr,Ba)," Phys. Rev. B **79**, 180508 (2009).

J. Tersoff and D. R. Hamann, "Theory and application for the scanning tunneling microscope," Phys. Rev. Lett. **50**, 1998–2001 (1983).

J. Tersoff and D. R. Hamann, "Theory of the scanning tunneling microscope," Phys. Rev. B **31**, 805–813 (1985).

M. Tinkham, *Introduction to superconductivity*, 2nd ed., International series in pure and applied physics (McGraw-Hill, Inc., 1996).

M. M. Vazifeh and M. Franz, "Self-organized topological state with Majorana fermions," Phys. Rev. Lett. **111**, 206802 (2013).

P. Walmsley, C. Putzke, L. Malone, I. Guillamón, D. Vignolles, C. Proust, S. Badoux, A. I. Coldea, M. D. Watson, S. Kasahara, Y. Mizukami, T. Shibauchi, Y. Matsuda, and A. Carrington, "Quasiparticle mass enhancement close to the quantum critical point in $BaFe_2(As_{1-x}P_x)_2$," Phys. Rev. Lett. **110**, 257002 (2013).

X. Wang, Q. Liu, Y. Lv, W. Gao, L. Yang, R. Yu, F. Li, and C. Jin, "The superconductivity at 18 K in LiFeAs system," Solid State Communications **148**, 538 – 540 (2008).

T. Watanabe, H. Yanagi, T. Kamiya, Y. Kamihara, H. Hiramatsu, M. Hirano, and H. Hosono, "Nickel-based oxyphosphide superconductor with a layered crystal structure, LaNiOP," Inorganic Chemistry **46**, 7719–7721 (2007).

D. A. Whitney, R. M. Fleming, and R. V. Coleman, "Magnetotransport and superconductivity in dilute Fe alloys of $NbSe_2$, $TaSe_2$, and TaS_2," Phys. Rev. B **15**, 3405–3423 (1977).

M. A. Woolf and F. Reif, "Effect of magnetic impurities on the density of states of superconductors," Phys. Rev. **137**, A557–A564 (1965).

G. Wu, H. Chen, T. Wu, Y. L. Xie, Y. J. Yan, R. H. Liu, X. F. Wang, J. J. Ying, and X. H. Chen, "Different resistivity response to spin-density wave and superconductivity at 20 K in $Ca_{1-x}Na_xFe_2As_2$," Journal of Physics: Condensed Matter **20**, 422201 (2008).

Y. Xia, F. Huang, X. Xie, and M. Jiang, "Preparation and superconductivity of stoichiometric β-FeSe," EPL (Europhysics Letters) **86**, 37008 (2009).

A. Yazdani, B. A. Jones, C. P. Lutz, M. F. Crommie, and D. M. Eigler, "Probing the local effects of magnetic impurities on superconductivity," Science **275**, 1767–1770 (1997).

J.-X. Yin, Z. Wu, J.-H. Wang, Z.-Y. Ye, J. Gong, X.-Y. Hou, L. Shan, A. Li, X.-J. Liang, X.-X. Wu, J. Li, C.-S. Ting, Z.-Q. Wang, J.-P. Hu, P.-H. Hor, H. Ding, and S. H. Pan, "Observation of a robust zero-energy bound state in iron-based superconductor Fe(Te,Se)," Nature Physics **11**, 543–546 (2015).

Y. Yin, M. Zech, T. L. Williams, X. F. Wang, G. Wu, X. H. Chen, and J. E. Hoffman, "Scanning tunneling spectroscopy and vortex imaging in the iron pnictide superconductor $BaFe_{1.8}Co_{0.2}As_2$," Phys. Rev. Lett. **102**, 097002 (2009).

J. J. Ying, Y. J. Yan, R. H. Liu, X. F. Wang, A. F. Wang, M. Zhang, Z. J. Xiang, and X. H. Chen, "Isotropic superconductivity in $LaRu_2P_2$ with the $ThCr_2Si_2$ -type structure," Superconductor Science and Technology **23**, 115009 (2010).

L. Yu, "Bound state in superconductors with paramagnetic impurities," Acta Physica Sinica **21**, 75 (1965).

W. Yu, A. A. Aczel, T. J. Williams, S. L. Bud'ko, N. Ni, P. C. Canfield, and G. M. Luke, "Absence of superconductivity in single-phase $CaFe_2As_2$ under hydrostatic pressure," Phys. Rev. B **79**, 020511 (2009).

H. Zhang, J. Dai, Y. Zhang, D. Qu, H. Ji, G. Wu, X. F. Wang, X. H. Chen, B. Wang, C. Zeng, J. Yang, and J. G. Hou, "$\sqrt{2}\times\sqrt{2}$ structure and charge inhomogeneity at the surface of superconducting $BaFe_{2-x}Co_xAs_2$ (x = 0–0.32)," Phys. Rev. B **81**, 104520 (2010).

X. Zhou, C. Ye, P. Cai, X. Wang, X. Chen, and Y. Wang, "Quasiparticle interference of C_2-symmetric surface states in a LaOFeAs parent compound," Phys. Rev. Lett. **106**, 087001 (2011).